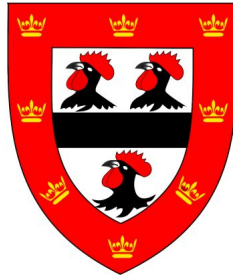




**Unconventional computing platforms  
and nature-inspired methods for solving  
hard optimisation problems**



**Kirill Kalinin**

Department of Applied Mathematics and Theoretical Physics  
University of Cambridge

This dissertation is submitted for the degree of  
*Doctor of Philosophy*

Jesus College

July 2021



## **Declaration**

I hereby declare that except where specific reference is made to the work of others, the contents of this dissertation are original and have not been submitted in whole or in part for consideration for any other degree or qualification in this, or any other university. This dissertation is my own work and contains nothing which is the outcome of work done in collaboration with others, except as specified in the text and Acknowledgements. This dissertation contains fewer than 65,000 words including appendices, bibliography, footnotes, tables and equations and has fewer than 150 figures.

Kirill Kalinin  
July 2021



## Acknowledgements

First and foremost I would like to sincerely and warmly acknowledge my scientific supervisor Natasha Berloff. We first met back in 2013, and since that time, we have been through so many adventures together. Thank you for the countless number of stimulating discussions that we have had, thank you for creating the fantastic, friendly atmosphere that made my learning a pleasure, thank you for sharing your infinite passion for science with me, and thank you for the opportunity to do research in one of the greatest universities. I will always stay in touch, and I am very much looking forward to continuing to work with you throughout my future academic career.

I am grateful to our experimental collaborators. Thank you, Pavlos Lagoudakis, for a chance to study a polaritonic graph simulator from scratch and for helping to get a postdoctoral position. Thank you, Alexis Askitopoulos and Julian Topfer, for the exciting discussions we had in conferences and beyond.

I wish to thank Carleton Coffrin for insightful discussions. I am grateful for your help and support in securing my postdoctoral position. Hopefully, I will have a chance to work with you and Andrey Lokhov on some projects in future.

I feel fortunate to have worked with Christos Gkantsidis, Francesca Parmigiani, and Hitesh Ballani as a Microsoft research intern. You were all very welcoming and made me quickly feel like a part of your Microsoft family. Thank you very much, Christos, for the great number of discussions we have had, for giving a different perspective on research, and for helping to improve my software skills. It would be great to work together again in future.

I am grateful to Cambridge Trust and EPSRC for wholly funding my PhD. I am also thankful for the generous conference travelling funding which, regardless of the pandemic, I used to almost full extent to present our research results in five international conferences.

I want to highlight the thriving environment in Jesus College. Quiet college walks, football fields, tennis courts, great food - I literally had everything for a good rest when not doing research. Thank you for providing my family with the best accommodation we could imagine. And thank you for supporting my conference expenses.

Thank you to Alexander Johnston and Samuel Alperin. It was pure fun to see where the conversations between Australian, American, and Russian students could lead to. The

considerable improvement in my academic writing is also thanks to you. Warmest thanks to Alex and his family for showing me the fantastic places in Sunshine Coast.

I have many lifelong friends thanks to Skoltech, the place where I got my MSc and where I started doing my PhD first. Thank you, Skoltech, for kickstarting my career and, hopefully, I will be back one day.

A warm thank you goes to all our friends who visited us during my PhD: Nastya and Zhenya, Vovchik, Sasha and Sasha, Max and Kristina, Andrii and Tanya, Sasha and Nastya. Thanks to you, we got to explore the beautiful nature of England, Wales, and Scotland.

And, of course, I am grateful to my family. To my mum, dad, and sister for your great support and encouragement throughout the years. To my wife, Kristina, for always caring and being there for me for over ten years. To my son, Peter, for being the greatest joy in my life. Thanks to you, we got to know the beautiful families of Katerina and Enrico, Asel and Vova, with their lovely kids.

## Abstract

The search for novel hardware beyond the traditional von Neumann architecture has given rise to a modern area of unconventional computing requiring the efforts of mathematicians, physicists and engineers. Many analogue physical systems, including networks of nonlinear oscillators, lasers, condensates, and superconducting qubits, are proposed and realised to address challenging computational problems from various areas of social and physical sciences and technology. Understanding the underlying physical process by which the system finds the solutions to such problems often leads to new optimisation algorithms. This thesis focuses on studying gain-dissipative systems and nature-inspired algorithms that form a hybrid architecture that may soon rival classical hardware.

Chapter 1 lays the necessary foundation and explains various interdisciplinary terms that are used throughout the dissertation. In particular, connections between the optimisation problems and spin Hamiltonians are established, their computational complexity classes are explained, and the most prominent physical platforms for spin Hamiltonian implementation are reviewed.

Chapter 2 demonstrates a large variety of behaviours encapsulated in networks of polariton condensates, which are a vivid example of a gain-dissipative system we use throughout the thesis. We explain how the variations of experimentally tunable parameters allow the networks of polariton condensates to represent different oscillator models. We derive analytic expressions for the interactions between two spatially separated polariton condensates and show various synchronisation regimes for periodic chains of condensates. An odd number of condensates at the vertices of a regular polygon leads to a spontaneous formation of a giant multiply-quantised vortex at the centre of a polygon. Numerical simulations of all studied configurations of polariton condensates are performed with a mean-field approach with some theoretically proposed physical phenomena supported by the relevant experiments.

Chapter 3 examines the potential of polariton graphs to find the low-energy minima of the spin Hamiltonians. By associating a spin with a condensate phase, the minima of the XY model are achieved for simple configurations of spatially-interacting polariton condensates. We argue that such implementation of gain-dissipative simulators limits their applicability to the classes of easily solvable problems since the parameters of a particular Hamiltonian

depend on the node occupancies that are not known a priori. To overcome this difficulty, we propose to adjust pumping intensities and coupling strengths dynamically. We further theoretically suggest how the discrete Ising and  $n$ -state planar Potts models with or without external fields can be simulated using gain-dissipative platforms. The underlying operational principle originates from a combination of resonant and non-resonant pumping. Spatial anisotropy of pump and dissipation profiles enables an effective control of the sign and intensity of the coupling strength between any two neighbouring sites, which we demonstrate with a two dimensional square lattice of polariton condensates. For an accurate minimisation of discrete and continuous spin Hamiltonians, we propose a fully controllable polaritonic XY-Ising machine based on a network of geometrically isolated polariton condensates.

In Chapter 4, we look at classical computing rivals and study nature-inspired methods for optimising spin Hamiltonians. Based on the operational principles of gain-dissipative machines, we develop a novel class of gain-dissipative algorithms for the optimisation of discrete and continuous problems and show its performance in comparison with traditional optimisation techniques. Besides looking at traditional heuristic methods for Ising minimisation, such as the Hopfield-Tank neural networks and parallel tempering, we consider a recent physics-inspired algorithm, namely chaotic amplitude control, and exact commercial solver, Gurobi. For a proper evaluation of physical simulators, we further discuss the importance of detecting easy instances of hard combinatorial optimisation problems. The Ising model for certain interaction matrices, that are commonly used for evaluating the performance of unconventional computing machines and assumed to be exponentially hard, is shown to be solvable in polynomial time including the Mobius ladder graphs and Mattis spin glasses.

In Chapter 5 we discuss possible future applications of unconventional computing platforms including emulation of search algorithms such as PageRank, realisation of a proof-of-work protocol for blockchain technology, and reservoir computing.

---

## Publications

Chapter 1 is based on a book chapter:

- **K. P. Kalinin** and N. G. Berloff, in *Emerging Frontiers in Nonlinear Science* (Springer, 2020) pp. 345–369.

Chapter 2 is based on four articles:

- **K. P. Kalinin** and N. G. Berloff, Polaritonic network as a paradigm for dynamics of coupled oscillators, *Phys. Rev. B* **100(24)**, 245306 (2019).
- **K. P. Kalinin**, P. G. Lagoudakis, and N. G. Berloff, Matter wave coupling of spatially separated and unequally pumped polariton condensates, *Phys. Rev. B* **97**, 094512 (2018).
- **K. P. Kalinin**, P. G. Lagoudakis, and N. G. Berloff, Exotic states of matter with polariton chains, *Phys. Rev. B* **97**, 161101(R) (2018).
- T. Cookson, **K. Kalinin**, H. Sigurdsson, J. D. Töpfer, S. Alyatkin, M. Silva, W. Langbein, N. G. Berloff, and P. G. Lagoudakis, Geometric frustration in polygons of polariton condensates creating vortices of varying topological charge, *Nat. Commun.* **12(1)**, 1-11 (2021).

Chapter 3 is based on five articles:

- N. G. Berloff, M. Silva, **K. P. Kalinin**, A. Askitopoulos, J. D. Topfer, P. Cilibizzi, W. Langbein, and P. G. Lagoudakis, Realizing the classical XY Hamiltonian in polariton simulators, *Nat. Mat.* **16 (11)**, 1120 (2017).
- **K.P. Kalinin** and N.G. Berloff, Networks of non-equilibrium condensates for global optimization, *New Journal of Physics* **20**, 113023 (2018).
- **K.P. Kalinin** and N.G. Berloff, Simulating Ising and Potts models and external fields with non-equilibrium condensates, *PRL* **121**, 235302 (2018).
- **K.P. Kalinin** and N.G. Berloff, Toward Arbitrary Control of Lattice Interactions in Nonequilibrium Condensates, *Adv. Quantum Technol.*, 1900065 (2019).
- **K. P. Kalinin**, A. Amo, J. Bloch, and N. G. Berloff, Polaritonic XY-Ising machine, *Nanophotonics* **9(13)**, 4127-4138 (2020).

Chapter 4 is based on one article and one unpublished manuscript:

- **K.P. Kalinin** and N.G. Berloff, Global optimization of spin Hamiltonians with gain-dissipative systems, *Scientific Reports* **8**, 17791 (2018).
- **K.P. Kalinin** and N.G. Berloff, Complexity continuum within Ising formulation of NP problems, arXiv preprint, arXiv:2008.00466 (2020).

Chapter 5 is based on two unpublished manuscripts:

- **K.P. Kalinin** and N.G. Berloff, Blockchain platform with proof-of-work based on analog Hamiltonian optimisers, arXiv preprint arXiv:1802.10091 (2018).
- **K.P. Kalinin** and N.G. Berloff, Large-scale Sustainable Search on Unconventional Computing Hardware, arXiv preprint, arXiv:2104.02553 (2021).

The results from all these articles are presented harmoniously in this thesis, with some of the earlier articles rewritten for better flow. I completed numerical simulations and analytical derivations presented in this thesis under the supervision of Prof. N. G. Berloff, while the presented experimental results are done by our collaborators.

Several articles are not included in this thesis:

- A. Johnston, **K. P. Kalinin**, and N. G. Berloff, Artificial polariton molecules, *Phys. Rev. B* **103(6)**, L060507 (2020).
- **K. P. Kalinin**, S. Alyatkin, P. G. Lagoudakis, A. Askitopoulos, and N. G. Berloff, Simulating the spectral gap with polariton graphs. *Phys. Rev. B* **102(18)**, 180303(R) (2020)
- L. Pickup, **K. P. Kalinin**, A. Askitopoulos, Z. Hatzopoulos, P. G. Savvidis, N. G. Berloff, and P. G. Lagoudakis, Optical bistability under non-resonant excitation in spinor polariton condensates, *PRL* **120(22)**, 225301 (2018)

# Table of contents

<b>List of figures</b>	<b>xv</b>
<b>List of tables</b>	<b>xxvii</b>
<b>Nomenclature</b>	<b>xxix</b>
<b>1 Introduction: Systems for unconventional computing</b>	<b>1</b>
1.1 Nonlinear physical systems . . . . .	2
1.2 Spin Hamiltonians . . . . .	4
1.3 P, NP, NP-complete problems . . . . .	5
1.4 Physical platforms for large-scale optimisation . . . . .	9
1.4.1 Cold atoms in optical lattices . . . . .	9
1.4.2 Superconducting qubits . . . . .	11
1.4.3 Complex laser networks . . . . .	11
1.4.4 Optical parametric oscillators . . . . .	13
1.4.5 Polariton and Photon networks . . . . .	15
1.5 Conclusions . . . . .	17
<b>2 Physics of polaritonic networks</b>	<b>19</b>
2.1 Polariton network as a paradigm for dynamics of coupled oscillators . . . . .	20
2.1.1 Mean-field description . . . . .	21
2.1.2 Fast reservoir relaxation limit . . . . .	23
2.1.3 Slow reservoir relaxation limit . . . . .	25
2.2 Matter-wave coupling of two spatially-separated polariton condensates . . . . .	27
2.2.1 Symmetric Heisenberg and asymmetric Dzyaloshinskii-Moriya interactions . . . . .	27
2.2.2 Analytical expressions for coupling strengths . . . . .	28
2.2.3 Loss of coherence in polariton dyad . . . . .	30
2.3 Exotic states of matter with polariton chains . . . . .	34

2.3.1	Linear periodic chain of equidistant polariton condensates . . . . .	34
2.3.2	Spin liquid states for equidistant polariton condensates along the circle	37
2.4	Giant vortices of controlled multiplicity in polariton lattices . . . . .	41
2.5	Conclusions . . . . .	46
<b>3</b>	<b>Gain-dissipative simulator with non-equilibrium condensates</b>	<b>47</b>
3.1	Signatures of minimising the XY model on simple graphs . . . . .	48
3.2	Density equilibration for minimising the XY model on arbitrary graphs . .	56
3.3	Signatures of minimising the Ising and Potts models on simple graphs . . .	63
3.4	Individual control of spatial lattice interactions by varying dissipation profile	69
3.5	Polaritonic XY-Ising Machine . . . . .	76
3.5.1	Remote coupling control . . . . .	77
3.5.2	Minimisation of the XY and Ising models on arbitrary graphs . . .	80
3.6	Conclusions . . . . .	88
<b>4</b>	<b>Nature-inspired algorithms for evaluating unconventional computing machines</b>	<b>89</b>
4.1	Gain-dissipative approach for minimising spin Hamiltonians . . . . .	90
4.1.1	Minimisation of the XY Hamiltonian . . . . .	92
4.1.2	Minimisation of the Ising Hamiltonian . . . . .	95
4.2	Computational complexity continuum within Ising formulation of NP problems	97
4.2.1	Optimisation simplicity criterion for the Ising model . . . . .	99
4.2.2	Minimising Ising model on Möbius ladder graphs . . . . .	101
4.2.3	Interpolating between simple Möbius ladders and hard 3-regular graphs	104
4.2.4	General applicability of the optimisation simplicity criterion . . . .	107
<b>5</b>	<b>Other applications for unconventional computing platforms</b>	<b>111</b>
5.1	Reservoir computing . . . . .	112
5.2	Proof-of-work protocol . . . . .	113
5.2.1	Introduction to blockchain technology . . . . .	113
5.2.2	Proof-of-work through minimisation of spin Hamiltonians . . . . .	115
5.3	PageRank algorithm . . . . .	119
5.3.1	Emulating PageRank algorithm with unconventional networks . . .	120
5.3.2	Alternative ranking through minimisation of the XY Hamiltonian .	127
<b>6</b>	<b>Conclusions</b>	<b>133</b>
	<b>References</b>	<b>137</b>

Table of contents	<b>xiii</b>
<b>Appendix A Parameters for numerical simulations of polaritonic networks</b>	<b>159</b>
<b>Appendix B Algorithms for Ising minimisation</b>	<b>161</b>
<b>Appendix C Ising models</b>	<b>165</b>
<b>Appendix D Details of PageRank simulations</b>	<b>167</b>



# List of figures

- 2.1 The polaritonic networks described by Eqs. (2.5, 2.6) can lead to the Lang-Kobayashi model in the absence of the nonlinear self-interaction term or to Kuramoto/Sakaguchi-Kuramoto/Stuart-Landau models of coupled oscillators in the limit of fast reservoir relaxation. The new regimes are expected to appear due to strong polariton-polariton interactions or once the experimental controls such as resonant excitation pump, spin polarisation, magnetic field, or combination of different sub-lattices are considered in polaritonic networks. . . . . 26
- 2.2 The strengths of (a) the symmetric Heisenberg exchange  $J$  and (b) the asymmetric Dzyaloshinskii-Moriya interactions  $D$  as functions of the separation distance  $d$ . The solid (dashed) lines show the normalised coupling strengths found numerically (analytically) from Eqs. (2.15, 2.16) (Eqs. (2.25, 2.26)). Colours correspond to the different population imbalances characterized by the percentage differences of the condensates' wave vectors,  $\Delta k = 0\%$ ,  $6\%$  and  $8\%$ , where  $\Delta k = 100\% \cdot (k_{c2} - k_{c1})/k_{c1}$ . The parameters are  $k_{c1} = 1.6\mu m^{-1}$ ,  $\beta = 0.2\mu m^{-1}$ . . . . . 31
- 2.3 (a) Contour plot of the phase difference  $\Delta\theta = \theta_1 - \theta_2$  in the polariton dyad as a function of the pumping imbalance  $\Delta P = 100\% \cdot (P_2 - P_1)/P_1$  and the separation distance  $d$ . The pumping corresponding to  $P_1$  is kept fixed. The phase difference is measured either for the steady state or at a fixed moment of time for time-dependent oscillations that characterise the loss of phase locking between the condensates. Fragmentation of the contour plot, therefore, represents the region with the loss of the phase locking (coherence) between the condensates. (b) Density cross-sections of the polariton dyad along the line connecting the condensate centers positioned at the distance  $d = 6.4\mu m$  apart and pumped with  $\Delta P = \{-28, 0, 45\}\%$ . . . . . 32

- 2.4 The contour plot shows the frustration parameter  $J_2/J_1$  as a function of  $k_c d$  and  $\beta/k_c$ , where  $k_c$  is the polariton wave vector,  $\beta$  is the width of the polariton spot,  $d$  is the distance between the two adjacent spots. The coupling strengths  $J_1$  and  $J_2$  are calculated from Eq. (2.39) for the distances  $d$  and  $2d$ , respectively. Solid black lines show lines of the sign change for  $J_1$ . The inset shows the different regimes of the XY model on  $J_2 - J_1$  plane: ferromagnetic, antiferromagnetic and frustrated. . . . . 36
- 2.5 Polariton densities (solid blue line) and velocities (dashed red lines) are shown for twelve condensates obtained by numerical integration of one-dimensional cGLE with periodical boundary conditions. Pumping profiles are shown with solid green lines. Panel (a) shows the ferromagnetic state, (b) corresponds to the antiferromagnetic state with  $\pi$  phase difference between the adjacent sites, and panel (c) shows the frustrated state. The distances between the nearest condensates are  $d = 5.4\mu m$ ,  $d = 6.9\mu m$ , and  $d = 6.5\mu m$  for (a), (b), and (c), respectively. . . . . 38
- 2.6 Density snapshots (left panel) and the far-field emission (central panel) are shown at a fixed time for twelve condensates arranged in a circle obtained by numerical integration of Eqs. (2.1, 2.2). The right panels show the evolution of the phases (relative to one fixed spin) between adjacent spots with  $12ps$  (c) and  $10ps$  (f) time steps between spin configurations. The highlighted with blue circles spin configurations in (c) and (f) correspond to the density profiles (a,d) and the far-field emissions (b,e). The stable spins of the spots are marked with orange circles in (c,f). The distances between the adjacent sites are  $6.4\mu m$  (a-c) and  $7\mu m$  (d-f). Other simulation parameters can be found in Appendix A. . . . . 39
- 2.7 The spectral weight plots are shown for  $k_y = 0$  of the two-dimensional non-stationary spin wave states from Figure 2.6(a-c) in (a) and from Figure 2.6(d-f) in (b). Both plots are saturated at the same level of 0.2 to make the energy levels more visible and to provide an easier comparison between the states . . . . . 39
- 2.8 A schematic of the density profile of an heptagon of polariton condensates with antiferromagnetic coupling between its vertices is shown. Within the inner ring visible at the centre of the heptagon, a sinkhole giant vortex occurs that is fully contained within the inner ring. . . . . 41

- 2.9 Normalised real-space photoluminescence intensity at condensation threshold for an octagon and a nonagon with ferromagnetic couplings between nearest neighbours are shown in a false-grey scale. The first column (a,b) shows the experimental results and the second column (c,d) shows the numerical simulations of the density profiles; (a) is saturated at 0.5, and (b) is saturated at 0.4 to increase the visibility of the low-intensity fringes between the vertices. In (c,d) the centres of the pumping spots are shown by the black dashed circles. The parameters of the numerical simulations are listed in Appendix A. . . . . 43
- 2.10 The first column (a-c) shows the normalised real-space photoluminescence intensity at condensation threshold for a heptagon, nonagon and a hendecagon with antiferromagnetic couplings between nearest neighbours in a false-grey scale. The second column (d-f) shows the corresponding normalised photoluminescence intensity of the two-dimensional Fourier-space at condensation threshold for the polygons of (a-c). The absence of nodal radial lines indicates the presence of a central vortex. The third column (g-i) shows the velocity stream-lines and the zeros of the real and imaginary parts of the wave functions with solid red and black lines respectively for the polygons of (a-c). The black filled area in (g-i) indicates the areas where the polariton density is less than  $10^{-5}$  of its maximum. The parameters of the numerical simulations are listed in Appendix A. . . . . 45
- 3.1 (a) A schematic of the condensate density map is shown for a five-vertex polariton graph. Depending on the separation distance between the sites and the outflow wave vector, the interactions between sites can be ferromagnetic (solid-blue lines) or antiferromagnetic (dashed-red lines). At each vertex  $\mathbf{x}_i$  of the graph polaritons have a local phase  $\theta_i$  that is mapped to a classical vector spin  $\mathbf{s}_i = (\cos \theta_i, \sin \theta_i)$ . (b) The vertices (blue solid-circles) and edges of the polariton density map depicted in (a), showing the sign of the coupling and the spin vector  $\mathbf{s}_i$  of each vertex. . . . . 49

- 3.2 (a) The maximum number of particles,  $N$ , of a polariton condensate dyad formed under incoherent pumping of two nodes as the function of the product  $k_c d$  between the nodes obtained by numerical integration of the cGLE for a fixed  $k_c$  starting with random initial conditions and choosing the realisation that maximises  $N$ . The solid black line corresponds to the maximum number of particles in the in-phase ferromagnetic configuration and the dashed black line to the antiferromagnetic configuration with  $\pi$ -phase difference. The switching occurs with the periodicity  $2\pi/k_c$  as the superimposed graph of  $\cos(k_c d + \phi)$  illustrates in red, where  $\phi \approx 225^\circ$ . (b-e) Experimental realisation of the chain of five equidistant polariton nodes with lattice constants of  $\sim 9\mu m$ ,  $\sim 11.1\mu m$ ,  $\sim 11.4\mu m$ , and  $\sim 13.4\mu m$  respectively. The false-grey scale images show the normalised real-space photoluminescence intensity. The corresponding  $k_c d$  are shown by solid circles in (a). . . . . 50
- 3.3 Spin configurations are shown for square polariton lattices. The diagrams of the numerically calculated spins vectors at the pumping sites  $\mathbf{s}_i = (\cos \theta_i, \sin \theta_i)$ , the real-space energy tomography of the experimental realisations, and the averaged condensate densities of the numerically simulated condensate wavefunctions for several realisations are shown on the left, central and right columns respectively. Solid and dashed blue lines on the spin vector diagrams (left column) indicate ferromagnetic and antiferromagnetic coupling, respectively. The false-grey scale images of the middle column show the normalised real-space photoluminescence intensity at the energy of the condensate at the condensation threshold; (c) is saturated at 0.5 to increase the visibility of the low-intensity fringes between the vertices. The configurations shown are some elementary building blocks of square lattices such as (a,c) antiferromagnetic, (b) ferromagnetic, (d)  $90^\circ$ -compass. The centres of the pumping spots are shown by white dashed circles on the numerical density profiles (right column). The parameters of the numerical simulations of Eqs. (2.1, 2.2) are listed in the Appendix A. . . . . 52

- 3.4 Spin configurations are shown for the diamond-shaped polariton lattices. The columns of images are as described in the caption to Figure 3.3. The configurations shown are some elementary building blocks of triangular lattices such as (a,c) antiferromagnetic and (b) ferromagnetic rhombuses. The false-grey scale images of the middle column show the normalised real-space photoluminescence intensity at the energy of the condensate at condensation threshold saturated at 0.5 to increase the visibility of the low-intensity fringes between the vertices. . . . . 53
- 3.5 Spin configurations are shown for a random polariton graph. The panels of images are as described in the caption to Figure 3.3. The false-grey scale image of the middle column show the normalised real-space photoluminescence intensity at the energy of the condensate at condensation threshold saturated at 0.5 to increase the visibility of the low intensity fringes between the vertices. . . . . 54
- 3.6 The first row shows the normalised real-space photoluminescence intensity at the energy of the condensate at condensation threshold in a false-grey scale for (a,c) antiferromagnetic and (b) ferromagnetic configuration of 45 coherently coupled polariton condensates arranged at the vertices of a square lattice. The second row (d-f) shows the normalised photoluminescence intensity of the two-dimensional Fourier-space corresponding to the lattices of (a-c). . . . . 55
- 3.7 (a) The operational schematics of the gain-dissipative simulator is shown. Initially, all CCs are equally pumped (green bars) below the threshold, and all have negligible number densities at  $t = t_1$ . As the pumping intensities increase, the different CCs emerge (red bars) with different number densities depending on the connectivity between CCs, as shown at some  $t = t_2$ . The individual control of the pumping intensity as described by Eq. (3.4) leads to the steady-state with all the densities reaching the threshold at  $t = t_3$ . (b-c) The ground state spin configurations of the XY Hamiltonian for problem size  $N = 100$  found by (b) the numerical evolution of Eqs. (3.1, 3.4, 3.8) and (c) by the basin-hopping optimisation algorithm. The found energies agree to 10 significant digits between methods. The coupling matrix is fully connected with interactions randomly distributed in  $[-10, 10]$ . . . . . 59

- 3.8 (a) The contour plot is shown for the number density of polariton condensates formed by non-resonant pumping with equal intensities. Red lines show the particle fluxes between the sites: the central site experiences the inflow of the particles from eight neighbouring sites whereas the sites on margins have only four or five neighbours. Dashed figures embrace the condensates with densities lower than the central condensates. (b,d,f) Contour plots of the steady state number density function  $|\psi|^2$  obtained by the numerical integration of the full dynamical governing equations for  $7 \times 7$  lattice and for the parameters used in previous Section. Contour plots of the pumping profiles at the steady state are shown in (c,e). Panels (c,d) are obtained by applying the density adjustments according to Eq. (3.4). Panels (e,f) are obtained by applying both the density adjustments and coupling adjustments according to Eq. (3.4) and Eq. (3.8). The resulting pumping intensities at the lattice sites are indicated for the top right quarter of (c,e) as the factor of the pumping at the lattice centre. The coupling strength adjustments are achieved by shifting the lattice sites as shown in red for the bottom left corner only in (e). . . . . 62
- 3.9 Contour plots of the density  $|\psi(\mathbf{r})|^2$  of the polariton condensates with antiferromagnetic nearest neighbour interactions show the ground states of the XY (a,c), the Ising (b), and the 3-state planar Potts (d) Hamiltonians at the condensation threshold. The densities for the Ising and 3-state planar Potts models are shown in log scale to emphasise the standing matter waves between condensates and, therefore, the phase differences. The densities are obtained by numerical integration of Eqs. (3.16, 3.17) with the parameters given in Appendix A. . . . . 65
- 3.10 Contour plots of the density  $|\psi(\mathbf{r})|^2$  of the polariton condensates in the corners of quadraterial show the ground state of the XY (a), the Ising (b), and the 3-state planar Potts (c) Hamiltonians without the external fields. The Ising and the 3-state planar Potts Hamiltonians with the external fields forcing the bottom condensates to acquire phase  $\theta_i$  are shown in (d) and (e), respectively. The densities are obtained by numerical integration of Eqs. (3.17) with the parameters given in Appendix A are shown in log scale for the Ising and Potts models. . . . . 68

- 3.11 The schematic is shown for the spatially dependent dissipation profile with nine condensates (yellow balls) arranged in a 2D lattice in a semiconductor microcavity. The condensates interact via channels of low dissipation (light grey). Dissipative barriers (brown areas) show an increased dissipation that prevents the coupling between the condensates across the diagonals. Dissipative gates (dark blue areas) show the regions where the dissipation is increased or decreased to control the couplings between neighbouring condensates. . . . . 70
- 3.12 (a) The transitions from the ferromagnetic state with 0 phase difference to the antiferromagnetic state with  $\pi$  phase difference between two polariton condensates by varying the amplitude of the dissipative gate are shown for three dissipative barriers (solid lines). The condensates remain synchronised though the small phase fluctuations appear for higher dissipative gates. The amplitude of such fluctuations is contained within the colour dashed lines. (b) The pumping profile for a  $3 \times 3$  square lattice of polariton condensates. (c) The structure of a dissipation profile  $\gamma(\mathbf{r})$  consisting of dissipative channels (black), dissipative barriers (pink), and dissipative gates (purple) being horizontally placed between vertical stripes of condensates. (d-g) The phase differences of all condensates are shown with black arrows with respect to the central condensate, the background is the normalised polariton density  $|\psi(\mathbf{r})|^2$ . (d) In the absence of dissipative gates, the initial state is prepared to be ferromagnetic with all spins aligned in the same direction. (e-g) With a dissipative gate of  $\gamma_{\text{gate}} = \{3, 5, 7\}$ , the coupling strengths between vertical stripes of condensates are continuously changed from ferromagnetic to antiferromagnetic coupling. . . . . 72
- 3.13 (a) A dissipation profile structure is similar to that of Fig. 3.12(b) but with only one dissipative gate. This dissipative gate makes the particular link antiferromagnetic while all other links remain ferromagnetic and, thus, frustration is created in the network. The resulting spin configuration is shown in (b). (c) The addition of another dissipative gate removes frustration from the system and leads to the spin configuration which is shown in (d). The dissipative gate's amplitude is  $\gamma_{\text{gate}} = 7$ . . . . . 73

- 3.14 The  $20 \times 25$  square lattice of polariton condensates is shown for the lowest energy state in (a) and for one of the excited energy states in (b). The polariton densities are shown with black-and-white colour scheme, the phase differences are plotted with a cyclic green-grey colour scheme. The dissipative gates  $\gamma_{\text{gate}} = 7$  are placed between the condensates constituting letters "Sk" and other condensates to create antiferromagnetic couplings, while all other couplings are ferromagnetic. The lowest energy state spin configuration (a) resembles "Sk" letters while the excited energy state (b) is blurred. The energies are in dimensionless units. . . . . 74
- 3.15 Top: Phase difference as a function of coupling strength for a polariton dyad. The Eqs. (3.24, 3.25) are simulated for 50 random initial conditions for each coupling value. The coherence occurs for the absolute values of strengths greater than 0.02 leading to ferromagnetic state with 0 phase difference for positive couplings and to antiferromagnetic state with  $\pi$  phase difference for negative couplings. The slowly decaying unstable solutions are shown in grey. Bottom: Phase difference as a function of time delay for a polariton dyad. The time delay percentage is defined with respect to the time required to reach a steady state in the absence of delay. The scatter point size indicates how many states out of 50 initial conditions end with a particular phase difference. The coupling strength between condensates is chosen to be  $J_0 = -0.1$ . The expected antiferromagnetic state is observed for time delays  $\tau < 2\%$  and followed by the region with decoupled condensates. The further phase-locking of condensates becomes possible for bigger time delays due to the global phase presence. . . . . 81

- 3.16 The XY Hamiltonian is minimised for a problem of size  $N = 9$  with a  $3 \times 3$  polariton lattice by simulating Eqs. (3.24, 3.25). The intensity distribution of the incoherent pumping profile  $P(\mathbf{r})$  is shown in (a). The condensate emissions within the black circles are used for couplings between condensates. The dissipative profile for realising spatially isolated polariton pillars are presented in (b). The fully connected coupling matrix  $J$ , which is randomly constructed from  $J_1 = 0.05$  and  $J_2 = 0.1$  of random signs, is shown in (c). The polariton density profiles and phase configurations are plotted for *relative* and *absolute* coupling models in (d-e), respectively. The white arrows represent the phase difference relative to the central condensate (the vertical arrow). The corresponding energy values of the XY Hamiltonian are shown in the top-right corner. The XY Hamiltonian ground state solution is verified by the gain-dissipative and the basin-hopping algorithms in (f). . . . . 83
- 3.17 Optimal amplitude range is studied for *relative* and *absolute* coupling models on the unweighted MaxCut problems of size  $N = 16$  with degrees 5, 9, and 13. The median accuracy is shown for the XY Hamiltonian in (a-b) and the Ising Hamiltonian in (c-d). Both models are simulated with Eqs. (3.24, 3.25) for 20 random initial conditions per each coupling strength. Shading indicates 25th and 75th percentile range of instances. . . . . 85
- 4.1 The operational principle of the gain-dissipative algorithm: the number densities  $\rho$  (a), the phases  $\theta$  (b), and the injection rates  $\gamma$  (c) are shown as functions of time for all network elements by simulating Eqs. (4.4, 4.5) with  $f_{\text{Res}} = 0$ . The interactions between elements are given by the fully connected matrix with random coupling strengths taken from the range  $[-10, 10]$ . . . . 92
- 4.2 The count number dependence on the proximity to the optimal solutions of the XY Hamiltonian is shown for several methods: (a,e) Monte-Carlo sampling, (b,f) basin-hopping, (c,g) gain-dissipative algorithm (GD) based on Eqs. (4.4, 4.5), and (d,h) the modified gain-dissipative algorithm (GD-mod) based on Eqs. (4.1-4.3). The results of 500 runs are averaged over 50 real symmetric coupling matrices  $J$  of size  $N = 50$  for (a-d) dense and (e-h) sparse matrices described in the main text. The number of internal BH iterations is set to ten. . . . . 94

- 4.3 The gain-dissipative algorithm, governed by Eqs. (4.1-4.2), is applied to the MaxCut optimisation problem formulated on  $G$ -Set instances  $\{G_1 - G_{10}\}$  of size  $N = 800$ . The found optimal values are shown with scatter plots for 100 runs on each  $G_i$ . The best known optimal values are plotted with coloured rectangles for each  $G_i$ . . . . . 96
- 4.4 (A) Illustration of the Möbius ladder graph on Möbius strip (left) and on circular graph (right). Two possible frustrated edges in the ground state are highlighted in red. (B) The evolution of amplitudes  $v_i$  (top) for the Möbius ladder graph of size  $N = 1000$  over  $N_{\text{iter}} = 3000$  time iterations of the Hopfield-Tank algorithm with the corresponding proximity to the ground state shown below. All low energy levels  $E_{\lambda_i}$  correspond to the projected eigenvectors  $\text{sign}(\mathbf{e}_i)$  of the distinct largest eigenvalues  $\lambda_i$ . (C) The number of time iterations  $N_{\text{iter}}$  of the Hopfield-Tank algorithm for optimising Möbius ladder graphs of sizes up to  $N = 10000$  with desired ground state probability ranges of  $p_{\text{gs}} \in \{50 - 55\%, 75 - 80\%, 99 - 100\%\}$  are shown on the left panel. The solid lines correspond to a quadratic fit confirming that the Ising model on Möbius ladder graphs can be solved in polynomial time. The number of algorithm runs per each graph size is fixed to 250. The ground state probabilities as a function of Möbius ladder size are shown for the fixed number of time iterations  $N_{\text{iter}} \in \{10000, 50000, 250000\}$  on the right panel. 102
- 4.5 (A) The rewiring procedure of two edges for violating the optimisation simplicity criterion in the Möbius ladder graphs of size  $N = 2n$  for any even  $N$  (left) and most even  $N$  (right). The removed and added edges are shown with red solid and dashed green lines, respectively. (B) The relative computational hardness of the unweighted Ising model on the rewired Möbius ladder graphs is evaluated by the median time required for reaching zero optimality gap with Gurobi solver for problem sizes 100, 200, and 300. The 100 random graphs are optimised for each problem size for every percentage of rewired edges with shaded regions indicating an interquartile range. The median time to solution metric as a function of the percentage of rewired edges in the Möbius ladder graphs is shown at the bottom for chaotic amplitude control and parallel tempering methods. (C) The average computational hardness is evaluated by the median time required for reaching zero optimality gap with Gurobi solver for the Möbius ladder graphs of sizes up to 500000 with couplings from the unweighted, bimodal, and Gaussian distributions. The 10 random graphs are optimised for each problem size. . . . . 106

- 4.6 **Probability of finding easy instances for various Ising models.** Fraction of instances, satisfying the optimisation simplicity criterion, is shown as a function of problem size  $N$  for Gaussian, bimodal, and unweighted coupling distributions. The considered Ising models include Sherrington-Kirkpatrick, 3-regular maximum cut, Mattis spin glass, spin glass on a torus, Möbius ladder graphs, biased ferromagnet on Chimera graph, planar spin glass within a magnetic field. The red dashed line represents models which are polynomially easy to optimise across all problem sizes. For each model, 1000 random matrices are generated per each size, and the ground states are verified with the exact Gurobi solver. . . . . 108
- 5.1 The schematic for blockchain generation by computational nodes in bitcoin cryptocurrency is shown. The block is added to a blockchain with an average interval of ten minutes. The output of each block serves as the name for the next block, thus forming a chain. . . . . 114
- 5.2 The scheme shows how to use purposely built quantum simulators based on superconducting qubits, optical parametric oscillators, polariton and photon condensates for solving QUBO or QCO problems in the proof-of-work protocol. 115
- 5.3 (a) The schematics of mapping the block's information to a coupling matrix  $J$  for solving QUBO or QCO problems as a proof-of-work is shown. Each node is placed around the circle and represents a financial party that transfers (blue dots) or receives (red dots) the money with the nodes being clustered in a few regions, i.e. six regions for 200 nodes shown. The nodes are randomly connected with red or blue lines with respect to positive or negative  $J_{ij}$ , respectively. (b) A typical structure of a random matrix  $J$  of size  $N = 800$  constructed as described in the main text, the positive and negative elements of  $J$  are marked with red and blue colours, respectively. (c) The global and the low energy excited states of QUBO problem for three such randomly generated coupling matrices of size  $N = 800$  denoted by  $J_1$  (dark green),  $J_2$  (green),  $J_3$  (light green). The results show that classical algorithms can often result in finding excited states for such coupling matrices. The inset shows the average time to find a steady-state solution by the GD algorithm as a function of the problem size  $N$  (dashed green line). The projected time of the GD simulator (solid green line) is obtained by multiplying the number of time iterations of the GD algorithm for each size  $N$  with the pumping adjustment time  $0.1ms$ , which is a realistic time for current physical platforms. 117

- 
- 5.4 The schematics of running ranking algorithms on unconventional hardware is shown. The link-structure of pages is represented as the Google matrix of the web network (top image). This web network is then mapped to unconventional hardware (middle image) that could be based on a variety of physical platforms, including optical parametric oscillators, lasers, polariton and photon condensates. The time-evolution of unconventional networks can mimic the traditional PageRank algorithm and find the principal eigenvector (PageRank) of the Google matrix or offer alternative rankings based on the minimisation of spin Hamiltonians. . . . . 121
- 5.5 (A) Kendall’s tau, as a measure of the agreement between the PageRank order computed with the power method and the rankings obtained using unconventional networks, is shown as a function of the number of iterations for a variety of web graphs. The sizes of graphs vary from  $N = 500$  for the university network (‘harvard’) to  $N = 3.5$  million for the Wikipedia database (‘wikipedia’). The unconventional networks are represented by Hopfield networks and networks of optical parametric oscillators (OPOs), condensates (polariton and photon), and lasers. (B) Kendall’s tau distribution is shown as a function of the highest-ranked elements for the PageRank order (top) and the PageRank vector (bottom). The teleportation parameter is fixed across all datasets to  $\alpha = 0.85$ . . . . . 126
- 5.6 The schematic distribution of the processing power as a function of energy efficiency is shown for several conventional computing devices, including CPUs, GPUs, FPGAs, and supercomputers. Unconventional computing devices based on optical systems could provide orders of magnitude improvements in time and energy performance. . . . . 128

# List of tables

3.1	The Ising and XY spin Hamiltonians are minimised with <i>relative</i> and <i>absolute</i> coupling models on unweighted MaxCut problems of size 25 and 49 with edge density 0.5. The median accuracy of both models is calculated for 20 random initial conditions per each coupling matrix which was further averaged over 20 random coupling matrices with coupling strength $J_0 = 0.04$ . The number in parentheses indicates how many problems with different coupling matrices were globally optimised. The ground state solutions are calculated with the gain-dissipative and the basin-hopping algorithms for the XY Hamiltonians and the gain-dissipative and CIM algorithms for the Ising Hamiltonians. . . . .	86
5.1	The highest 10 PageRank positions are shown for datasets ‘ <i>harvard</i> ’, ‘ <i>california</i> ’, ‘ <i>facebook</i> ’, and ‘ <i>wiki-topcats</i> ’ of size $N = 500$ , $N = 9664$ , $N = 22470$ , and $N = 1791489$ . The identical PageRank distributions are found between the original PageRank algorithm based on the power method and simulations of Hopfield networks and networks based on optical parametric oscillators, lasers, polariton and photon condensates. The alternative ranking (XYRank) is computed by minimising the XY Hamiltonian. The difference between the two ratings is indicated by green (red) arrows showing the shift in the XYRank towards a higher (lower) rating by a certain number of positions with respect to the PageRank. . . . .	131
B.1	Optimal parameters for chaotic amplitude control method are shown. The individual sets of parameters are selected for each rewiring of 3-regular graphs in Fig. 5.5 by optimising time to solution for ten rewired graphs with the m-loop method. The presented values are averaged over the percentage of rewired edges for each problem size. . . . .	163

---

B.2	Optimal parameters for parallel tempering are shown. The individual sets of parameters are selected for each rewiring of 3-regular graphs in Fig. 5.5 by optimising time to solution for ten rewired graphs with the m-loop method. The presented values are averaged over the percentage of rewired edges for each problem size. . . . .	164
D.1	The highest 10 alternative ranking positions (XYRank) are shown for datasets ‘harvard’, ‘california’, ‘facebook’, and ‘wiki-topcats’ of size $N = 500$ , $N = 9664$ , $N = 22470$ , and $N = 1791489$ . The XYRank is calculated by minimising the XY Hamiltonian for the Google matrices. The difference between the XYRank and PageRank distributions is indicated by green (red) arrows showing the shift in the PageRank towards a higher (lower) rating by a certain number of positions with respect to the XYRank. . . . .	174

# Nomenclature

## Acronyms / Abbreviations

1D One-Dimensional

2D Two-Dimensional

BEC Bose-Einstein Condensate

BH Basin-Hopping

CC Coherent Centre

cGLE Complex Ginzburg-Landau Equation

CIM Coherent Ising Machine

DNLS Discrete Nonlinear Schrödinger

DOPO Degenerate Optical Parametric Oscillator

FPGA Field-Programmable Gate Array

GD Gain-Dissipative

HT Hopfield-Tank

L-BFGS-B Quasi-Newton method of Broyden, Fletcher, Goldfarb, and Shanno

MaxCut Maximum Cut

MC Monte Carlo

OPO Optical Parametric Oscillator

OSC Optimisation Simplicity Criterion

POW Proof-of-Work

PUBO Polynomial Unconstrained Binary Optimisation

QCO Quadratic Continuous Optimisation

QUBO Quadratic Unconstrained Binary Optimisation

RC Reservoir Computing

SLM Spatial Light Modulator

TPU Tensor Processing Unit

# **Chapter 1**

## **Introduction: Systems for unconventional computing**

## 1.1 Nonlinear physical systems

We live in a world dominated by information. Systems that enable faster information processing and decision making are becoming more integrated into our daily lives. This data-intensive science relies on continual improvements in hardware for solving ever growing in number of variables and constraints optimisation problems. Digital electronics can no longer satisfy this trend as exponential hardware scaling (Moore's law) and the von Neumann architecture are reaching their limits [1, 2].

Looking beyond the traditional computing one turns to physical platforms that with their superior speed and reconfigurability and internal parallel processing can provide faster alternatives to solving a specialised class of nonlinear problems. Despite a number of physical systems that were proposed as quantum or analogue simulators and further elucidated in active applied research, significant challenges still remain before scalable analogue processors can be realised and show the superior performance in comparison with the von Neumann computing architecture. Over the years, various unconventional computing techniques were proposed that enable simultaneous communication, computation, and memory access throughout their architecture with the purpose to alleviate the device and system architectural challenges faced by conventional computing platforms.

Neuromorphic computing based on neural networks promises to make processors that use low energies while integrating massive amounts of information. Quantum annealer devices promise to find the global minimum of a combinatorial optimisation problem faster than classical computers. Physical (natural) systems aim to become analogue machines by bridging the physics of a particular system with hardware platforms to enhance the performance of machine learning algorithms.

A central challenge is in the development of mathematical models – system-inspired computing – linking physical platforms to models of complex analogue information processing. Among such models, those based on principles of neural networks and quantum annealing are perhaps the most widely studied.

A large class of problems that can be solved on physical platforms includes nonlinear programming problems. They seek to minimise some nonlinear objective function  $E(\mathbf{x})$  of real or complex variables  $\mathbf{x}$  subject to a series of constraints represented by equalities or inequalities. Numerous applications in social sciences and telecommunications, finance and aerospace, biological and chemical industries can be described in this basic framework [3–5].

Nonlinear optimisation problems are notoriously difficult to solve, and often involve specialised techniques such as genetic algorithms, particle swarm optimisation, simulation and population annealing. Around the vicinity of the optimal solution nonlinear optimisation problems are quadratic to second order, and therefore, quadratic programming for minimising

quadratic functions subject to linear constraints is a usual simplification to such problems that can be used with a wide array of applications. Quadratic programming occurs in various machine learning problems, such as the support vector machine training and least squares regression. At the same time, quadratic programming and other nonlinear optimisation problems can be mapped to spin Hamiltonians which can be emulated by real physical systems: the degrees of freedom  $\mathbf{x}$  become ‘spins,’ the cost function  $E(\mathbf{x})$  is a ‘Hamiltonian’ that specifies the interaction pattern between spins. In this Chapter we discuss two possible ways by which the system can find the optimal solution – the ground state of the corresponding spin Hamiltonian – depending on the nature of the system.

The system in thermodynamic equilibrium may find the optimal solution by quantum annealing which is executed with the time-dependent Hamiltonian

$$H(t) = \left(1 - \frac{t}{\tau}\right)H_0 + \frac{t}{\tau}H_{\text{objective}}, \quad (1.1)$$

where  $H_0$  is the initial trivial Hamiltonian whose ground state is known, and  $H_{\text{objective}}$  is the final Hamiltonian at  $t = \tau$  which encodes an original objective function  $E(\mathbf{x})$ . If the system is in thermal equilibrium at all times then it stays close to the ground state, as Hamiltonian parameters are adiabatically varied. A linear time dependence in Eq. (1.1) is assumed for simplicity but more complex annealing schedules can be used. The time  $\tau$  for obtaining the result of optimisation is much larger than that defined by the inverse of the spectral gap [6]. When spectral gap is large, the coupling to the environment helps the annealer by cooling the system towards its ground state, however, as the system becomes larger and the spectral gap shrinks (typically exponentially fast with the system size) the excited states lead to large errors at the same time slowing down the annealing procedure.

Non-equilibrium systems rely on a different principle of approaching the ground state from below rather than via quantum tunnelling during the adiabatic annealing. The principle of the gain-dissipative simulator is based on a two-stage process: gain increase below the threshold and the coherence of operations at the threshold. Ramping up the gain allows system to overcome its linear losses and to stabilise by the nonlinearity of the gain saturation. The emergent coherent state minimises the losses and, therefore, maximises the total number of particles as it will be explained further below, which leads to minimising a particular functional that can be written as the objective spin Hamiltonian. Close to the threshold, the resulting evolution of the system elements resembles the dynamics of Hopfield networks which were shown to be able to solve quadratic optimisation problems more than thirty years ago [7, 8]. Various modifications of Hopfield networks were proposed and studied [9], however, the optimisers based on Hopfield networks were surpassed by other computational

methods. This is largely due to the high connectivity between neurons that neural networks require and the concomitant time it takes to evolve large networks on classical hardware. The recent interest in Hopfield networks re-emerged as it became possible to create them in analogue physical systems such as electronic circuits or photonic neural networks. Photonic systems have an advantage over their electronic counterparts due to the picosecond to femtosecond time scale of their operation and as hundreds of high bandwidth signals can flow through a single optical waveguide. This means that a photonic implementation of Hopfield networks as optimisers can have a large dimensionality and dense connectivity as well as a fast convergence time. However, the evolution of Hopfield networks does not necessarily lead to the optimal solution.

In this Chapter we review recent progress in building the analogue devices that implement either quantum annealing or gain-dissipative principle in their architecture.

## 1.2 Spin Hamiltonians

The majority of optimisation problems are computationally impractical for traditional computers with classic examples of a so-called “hard optimisation task” being the travelling salesman problem, the dynamic analysis of financial markets, the prediction of new chemical materials, and machine learning applications [10]. Mathematically, it is possible to reformulate many of these optimisation problems from vastly different areas into the problem of finding the ground state of a particular spin Hamiltonian with discrete or continuous degrees of freedom. Throughout this Chapter, we will refer to this spin Hamiltonian optimisation simply as solving spin model. The spin Hamiltonian can be emulated with a given simulator, e.g. solid-state system, that would need to have an easy mapping of the variables of the desired Hamiltonian into the elements (spins, currents etc.) of the simulator, independently tunable short and long range interactions between them, and would allow one to perform measurements to obtain the answer with the required precision. Such spin model Hamiltonians are experimentally challenging to implement and control but their possible advantageous performance over classical computers, which struggle solving sufficiently large problem sizes, leads to an intensive search for a superior simulator. Such simulators have been proposed and realised to a various extent in disparate physical systems. Among these systems, two classes of spin Hamiltonians are more common: Ising and XY Hamiltonians. For instance, the Ising Hamiltonian is widely used for a vast variety of hard discrete combinatorial optimisation problems, so that travelling salesman, graph colouring, graph partitioning, and others can be mapped into it with a polynomial overhead [11]. This model is formulated for  $N$  classical “spin”  $s_j$  that take discrete values  $\{-1, 1\}$  to minimise the quadratic unconstrained binary

optimisation (QUBO) problem:

$$\min - \sum_{\substack{i,j=1 \\ i < j}}^N J_{ij} s_i s_j + \sum_{i=1}^N h_i s_i \quad \text{subject to} \quad s_i \in \{-1, 1\} \quad (1.2)$$

where  $h_i$  represents external (magnetic) field. This term can be incorporated in  $\mathbf{J}$  matrix by considering  $N + 1$  spins and thus will be omitted. Experimental realisation of the nonlinear terms beyond quadratic in the Ising Hamiltonian would lead to a  $k$ -local spin Hamiltonian with  $k > 2$  and would allow for a direct mapping of polynomial unconstrained binary optimisation (PUBO) problems including Max-SAT [12] or number factorisation [13]:

$$\min - \sum_{i_1, i_2, \dots, i_k}^N Q_{i_1, i_2, \dots, i_k} s_{i_1} s_{i_2} \dots s_{i_1} \dots s_{i_k} \quad \text{subject to} \quad s_{i_l} \in \{-1, 1\}. \quad (1.3)$$

In the XY model “spins” are continuous  $s_j = \cos \theta_j + i \sin \theta_j$  and the corresponding quadratic continuous optimisation (QCO) problem can be formulated as

$$\min - \sum_{i < j} J_{ij} \mathbf{s}_i \cdot \mathbf{s}_j = \min - \sum_{i < j} J_{ij} \cos(\theta_i - \theta_j) \quad \text{subject to} \quad \theta_i \in [0, 2\pi). \quad (1.4)$$

When possible phases  $\theta_j$  are limited to discrete values  $2\pi/n$  with an integer  $n > 2$  the model (1.4) recovers the  $n$ -state Potts model (Clock model) with applications in protein folding [14].

QCO, QUBO, and PUBO problems are all examples of NP-hard problems. The corresponding spin models are universal. The connection between these notions are detailed in the next section.

### 1.3 P, NP, NP-complete problems

The computational complexity of a problem can be revealed by looking at the dependence of the problem size on time or the number of operations required to solve it. In a simple case of such polynomial dependence, i.e. when a polynomial time algorithm exists, a problem belongs to a  $\mathbb{P}$  class. If a polynomial time algorithm of finding a solution is not known but there exists a polynomial algorithm for verifying a solution when presented, then a problem belongs to non-deterministic polynomial-time (NP) class that clearly includes the  $\mathbb{P}$  class. Whether  $\mathbb{P} = \text{NP}$  is true or not is a major unsolved problem in computer science although it is widely believed to be untrue [15]. Most difficult decision problems in NP are called NP-complete. These problems are equivalent in a sense that either all of them or none of

them admit a polynomial-time algorithm. Examples include the travelling salesman problem, spin glass models, and integer linear programming. A problem is called  $\text{NP}$ -hard if the existence of an efficient algorithm for its solution implies the existence of such an algorithm for all the  $\text{NP}$ -complete problems.

In general, if a decision problem with a yes or no answer, e.g. does a particular Ising Hamiltonian have a ground state energy less than some value, is  $\text{NP}$ -complete then its corresponding optimisation problem, e.g. what is the ground state energy of this Ising Hamiltonian, is said to be  $\text{NP}$ -hard meaning that  $\text{NP}$ -hard problems are not any easier to solve than the corresponding  $\text{NP}$ -complete decision problems. The computational complexity of the Ising model on finite lattices has been studied before [16] where the two-dimensional Ising model with a magnetic field and equal antiferromagnetic couplings has been shown to be  $\text{NP}$ -hard for planar graphs. In addition,  $\text{NP}$ -hardness was demonstrated for the three-dimensional Ising model with nearest neighbour interactions and coupling strengths from  $\{-1, 0, 1\}$  [16]. Consequently, the above mentioned hierarchy of complexity classes allows one to conclude the impossibility of existence of a polynomial algorithm for computing the ground state energy of the Ising model without the existence of a polynomial algorithm for all  $\text{NP}$ -complete problems.

The existence of universal spin Hamiltonians has been established. Universality means that all classical spin models with any range of interactions can be reproduced within such a model, and certain simple Hamiltonians such as the Ising model on a square lattice with transverse fields and nearest neighbour interactions are universal [17]. Thus, due to  $\text{NP}$ -hardness of the Ising model, there should exist a polynomial time mapping of many practically relevant  $\text{NP}$ -complete problems to the Ising Hamiltonian, whose decision version solves the  $\text{NP}$ -complete problem of interest. The mapping of various  $\text{NP}$  problems, including Karp's 21  $\text{NP}$ -complete problems [18], to Ising models with a polynomial overhead was demonstrated [11]. For example, the travelling salesman problem for  $N$  cities, that are connected with weighted edges  $w_{uv} \geq 0$  from the set  $E$  (distances between cities), can be formulated as the following Ising problem of size  $N^2$ :

$$\begin{aligned}
 H_{\text{TSP}} = & A \sum_{i=1}^N \left( 1 - \sum_{v=1}^N x_{v,i} \right)^2 + A \sum_{v=1}^N \left( 1 - \sum_{i=1}^N x_{v,i} \right)^2 + A \sum_{(uv) \notin E} \sum_{i=1}^N x_{u,i} x_{v,i+1} \\
 & + B \sum_{(uv) \in E} w_{u,v} \sum_{i=1}^N x_{u,i} x_{v,i+1}.
 \end{aligned} \tag{1.5}$$

Each spin  $x_{v,i} \in \{0, 1\}$  in Eq. (1.5) represents the vertex  $v$  and its order  $i$  in a path. All valid routes in this representation are regulated by the first three terms: each city should be in the

route (first term) and should appear in it only once (second term), any adjacent cities in the route should be connected (third term), while the search for the optimal route is realised by minimising the sum of weights of all cities in a route (forth term). The reasonable choice of constants  $A$  and  $B$  (e.g.  $A$  should be big enough with respect to  $B > 0$ ) guarantees that only the space of valid routes is explored. Reshaping this two-dimensional spin matrix with elements  $x_{v,i}$  to a spin vector of size  $N^2$  allows one to recover the coupling matrix  $\mathbf{J}$  and magnetic field  $\mathbf{h}$  to formulate the corresponding Ising Hamiltonian. The size of the Ising problem can be reduced to  $(N - 1)^2$  by fixing a particular city to be the first in the route. Note, that the Hamiltonian  $H_{\text{TSP}}$  can represent both directed and undirected graphs, and the generalisation for the cycles optimisation problem is straightforward. We also note that a polynomial overhead does not always apply and some combinatorial optimisation problems can be mapped to the Ising model of the same size  $N$ . For example, the maximum cut (MaxCut) problem

$$\max_{S^+, S^-} \sum_{i \in S^+, j \in S^-} w_{ij} \quad (1.6)$$

seeks for the cut of a graph into two subsets with a largest sum of their connecting weighted edges. By assigning  $+1$  and  $-1$  spins to all vertices in subsets  $S^+$  and  $S^-$ , respectively, this optimisation problem can be formulated as

$$\max_{s_i} \frac{1}{2} \sum_{i < j} w_{ij} (1 - s_i s_j) = \frac{1}{2} \sum_{i < j} w_{ij} + \min_{s_i} \frac{1}{2} \sum_{i < j} w_{ij} s_i s_j \quad (1.7)$$

and thus a maximum cut of any graph can be converted to minimisation of the corresponding Ising Hamiltonian with the coupling matrix  $J_{ij} = -w_{ij}$  with an addition of an offset. A well-known standardised set of MaxCut type of problems often serve as a metric for comparison of newly proposed simulators and algorithms [19–21].

Another example of a universal spin model is the XY model which is directly related to the notoriously hard to solve phase retrieval problem. The problem's objective is to recover a general signal (or image) from the magnitude of its Fourier transform [22–24]. This problem arises from the fact that the signal detectors can usually record only modulus of the diffraction pattern, therefore, losing the information about the phase of the optical wave. Mathematically, one needs to recover a signal  $\mathbf{x} \in \mathbb{C}^m$  from the amplitude  $\mathbf{b} = |\mathbf{A}\mathbf{x}|$ , where  $\mathbf{A} \in \mathbb{C}^{n \times m}$ ,  $\mathbf{b} \in \mathbb{R}^n$ . Then the phase recovery problem [25] can be formulated as:

$$\min_{x_j, u_i} \sum_i \left( \sum_j A_{ij} x_j - b_i u_i \right)^2 \quad (1.8)$$

where  $\mathbf{u} \in \mathbb{C}^n$  is a phase vector that satisfies  $\mathbf{A}\mathbf{x} = \text{diag}(\mathbf{b})\mathbf{u}$ ,  $|u_i| = 1$  for  $i = \overline{1, n}$ . This optimisation problem can be further rewritten as

$$\min \sum_{ij} M_{ij} u_i u_j \quad \text{subject to} \quad |u_i| = 1, i = \overline{1, n}, \quad (1.9)$$

where  $\mathbf{M} = \text{diag}(\mathbf{b})(\mathbf{I} - \mathbf{A}\mathbf{A}^\dagger)\text{diag}(\mathbf{b})$  is the Hermitian matrix,  $\mathbf{I}$  is the identity matrix, and  $\mathbf{A}^\dagger$  is the Moore-Penrose pseudoinverse of a matrix  $\mathbf{A}$ .

It is important to note that when we refer to a spin problem as  $\mathbb{NP}$ -complete we understand that for some specific coupling matrix  $\mathbf{J}$  (‘problem instances’) finding the solution can be easy (belong to  $\mathbb{P}$  class). The term  $\mathbb{NP}$ -completeness reflects worst case behaviour and may allow a polynomial time to solution for most instances on average. This leads to the cornerstone question of how to distinguish hard instances from simple ones. The answer is especially important for the rivalry between classical computing machines and unconventional hardware which have to compete on problems of known complexity. It is believed that the way to create “hard” instances for spin Hamiltonians resides at the intersection of computational complexity and physics, e.g. the hardness of problems can be connected to the existence of a first-order phase transition in a system (see [26] and references therein). If an instance is indeed hard then it would be difficult to solve even for a medium size on a classical computer since the number of operations grows as an exponential function with the matrix size. Thus, the time required to find reliably the ground state energy should highly depend on the coupling matrix structure  $\mathbf{J}$  and the way it was constructed. For instance, finding the global minimum of the XY model for positive definite matrices remains  $\mathbb{NP}$ -hard due to the non-convex constraints but can be effectively approximated using a semidefinite programming (SDP) relaxation with some performance guarantee [27, 28]. Sparsity also plays an important role and for sufficiently sparse matrices fast methods exist [29]. For spin models, the generation of matrix instances  $\mathbb{J}$  with tunable algorithmic hardness and, preferably, with a specifiable ground state, is an ongoing problem studied by many research teams [26]. Having a unified set of optimisation problems with a tunable hardness and known solutions would allow for an objective benchmark of quantum simulators on various physical platforms as well as for classical algorithms. Otherwise, announcements of state-of-the-art platforms and methods, which demonstrate their performance on some random and not necessarily hard instances, would continue to happen.

## 1.4 Physical platforms for large-scale optimisation

Rather than trying to model nature one can consider a reverse idea of exploiting physical phenomena for solving  $\text{NP}$ -complete problems. Such problems can be tackled by quantum computers or simulators to produce solutions in reasonable time. In the last five years we have seen a competition of different physical platforms in solving classical optimisation problems faster than it can be achieved on a classical hardware for a given problem size. This rivalry resulted in the rapid emergence of a new field at the intersection of laser and condensed matter physics, engineering and complexity theories, which aims to develop quantum or classical analogue devices to simulate spin Hamiltonians. Next we discuss the achieved success in such simulations for a range of physical systems.

### 1.4.1 Cold atoms in optical lattices

Ultra-cold atoms in optical lattices constitute a well-controlled experimental setting to realise various spin Hamiltonians [30, 31]. Optical lattices are formed by directing several laser beams to interfere and to create standing wave configurations. Such waves provide practically loss-free external potentials in which ultra-cold atoms may condense, move and interact with one another [32, 33]. The unprecedented control and precision with which one can engineer such lattices and load the atoms there led to many suggestions to consider such systems as possible candidates for unconventional computing in quantum information processing and quantum simulations.

Here we will only discuss a weakly interacting Bose gas in an optical lattice. The description of particles in the strongly-correlated regime is possible with Bose- and Fermi-Hubbard models as well as with extended Hubbard models with nearest-neighbour and next nearest-neighbour interactions [34]. If the bosonic gas is dilute, the time evolution of the condensate wave function  $\psi$  is governed by the Gross-Pitaevskii equation (GPE) [35–37]

$$i\hbar \frac{d}{dt} \psi(\mathbf{r}, t) = -\frac{\hbar^2}{2m} \nabla^2 \psi(\mathbf{r}, t) + V_{\text{ext}}(\mathbf{r}) \psi(\mathbf{r}, t) + g |\psi(\mathbf{r}, t)|^2 \psi(\mathbf{r}, t), \quad (1.10)$$

where  $g$  is the strength of the delta-function interactions and the external potential  $V_{\text{ext}}$  describes an optical lattice (periodic potential) usually combined with a weak harmonic trapping potential.

The condensate evolution and particles' interactions at different local minima of the optical lattice can be described with the tight-binding approximation, which is valid when the barrier between the neighbouring sites is much higher than the chemical potential. In this approximation the condensate wave function  $\psi$  is written as a sum of normalised wave

functions  $\phi_i = \phi(\mathbf{r} - \mathbf{r}_i)$  localised in each minimum of the periodic potential, i.e.  $\mathbf{r} = \mathbf{r}_i$ :

$$\psi(\mathbf{r}, t) = \sum_i \Psi_i(t) \phi(\mathbf{r} - \mathbf{r}_i), \quad (1.11)$$

where  $\Psi_i(t) = \sqrt{\rho_i(t)} e^{i\theta_i(t)}$  is the complex amplitude of the  $i$ -th lattice site,  $\rho_i$  and  $\theta_i$  are the number of particles and the phase in the  $i$ -th site, respectively. The amplitude  $\Psi_i$  describes the state of the so-called ‘coherent centre’ located at  $\mathbf{r}_i$ . By inserting this ansatz into Eq. (1.10) and integrating the spatial degrees of freedom out one obtains the discrete nonlinear Schrödinger (DNLS) equation [38]

$$i\hbar \frac{\partial \Psi_i}{\partial t} = -J(\Psi_{i+1} + \Psi_{i-1}) + \varepsilon_i \Psi_i + U |\Psi_i|^2 \Psi_i, \quad (1.12)$$

where  $J$  is the nearest-neighbour tunnelling rate,

$$J = - \int d\mathbf{r} \left[ \frac{\hbar^2}{2m} \nabla \phi_i \cdot \nabla \phi_{i+1} + \phi_i V_{\text{ext}} \phi_{i+1} \right], \quad (1.13)$$

$\varepsilon_i$  is the on-site energy given by

$$\varepsilon_i = \int d\mathbf{r} \left[ \frac{\hbar^2}{2m} (\nabla \phi_i)^2 + V_{\text{ext}} \phi_i^2 \right], \quad (1.14)$$

and  $U$  is the nonlinear coefficient given by

$$U = g \int d\mathbf{r} \phi_i^4. \quad (1.15)$$

Such classical lattice models described by DNLS equations represent the mean-field limit of Bose-Hubbard models [39]. The mean-field limit of the non-standard Bose-Hubbard models includes the interactions beyond the nearest neighbours which leads to a generalised DNLS

$$i\hbar \frac{\partial \Psi_i}{\partial t} = -\frac{1}{2} \sum_{\langle i,j \rangle} J_{ij} \Psi_j + (\varepsilon_i + U |\Psi_i|^2) \Psi_i, \quad (1.16)$$

where  $J_{ij}$  is the coupling strength between the  $i$ -th and  $j$ -th coherent centres. If one loads an equal number of particles in each site of the lattice, the ground state of Eq. (1.16) realises the minimum of the XY Hamiltonian  $-\sum_{\langle i,j \rangle} J_{ij} \cos(\theta_i - \theta_j)$ . This has been experimentally demonstrated in triangular lattices using the atoms motional degrees of freedom and tunable artificial gauge fields [40, 41].

The quantum annealing protocol can in principle be implemented in such a system by using Eq. (1.1) with  $H_0 = \sum_{\langle i,j \rangle} \cos(\theta_i - \theta_j)$  and  $H_{\text{objective}} = -\sum_{\langle i,j \rangle} J_{ij} \cos(\theta_i - \theta_j)$ . A similar principle of adiabatic quantum annealing has been realised in the D-Wave machine that we discuss below.

### 1.4.2 Superconducting qubits

D-Wave is a first commercially available quantum annealer that is built on superconducting qubits with programmable couplings and specifically designed to solve QUBO problems [42]. By specifying the interactions  $J_{ij}$  between qubits, a desired QUBO problem is solved [43] via a quantum annealing process as in Eq. (1.1). Adiabatic (slow) transition in time from an initial state of a specially prepared “easy” Hamiltonian to the objective Ising Hamiltonian guarantees that the system remains in the low energy state, which gives the final energy that corresponds to the optimal solution of the QUBO problem.

Many benchmarks on different QUBO problems were performed on a D-Wave One and D-Wave Two machines without a solid demonstration of quantum speedup of annealer over classical algorithms [44–46]. A better performance was shown for the last 2000-qubit D-Wave machine released in 2017 on a newly proposed synthetic problem class in which the computational hardness is created through frustrated global interactions. The major limitations of D-wave simulators is that each qubit can be connected to maximum of six other qubits which is the consequence of creating chips with Chimera structure. The last generation of D-Wave quantum computer is announced in 2020 with Pegasus architecture, allowing one to have 15 connections per qubit. Together with reverse annealing and virtual graphs features a significant performance improvement could be possibly demonstrated.

### 1.4.3 Complex laser networks

A new generation of complex lasers such as degenerate cavity lasers, multimode fibre amplifiers, large-aperture VCSEL, random lasers have many advantages in comparison with the relatively simple traditional laser resonators in terms of their computing properties [47]. They have a large number of spatial degrees of freedom, their nonlinear interactions within the gain material can be controlled by adjusting the spatial structures of lasing modes, the spatial coherence of emission can be tuned over a wide range, and the output beams may have arbitrary profiles. These properties allow the complex lasers to be used for reservoir computing [48] or for solving hard computational problems.

In laser networks the coupling can be engineered by mutual light injection from one laser to another. This introduces losses that depend on the relative phases between the lasers.

Such dissipative coupling drives the system to a phase locking and therefore to a steady state solution of QCO described by Eq. (1.4), i.e. to the minimum of the XY Hamiltonian [49–51]. Degenerate cavity lasers are particularly useful as solvers as all their transverse modes have nearly identical quality factor. This implies that a large number of transverse modes lase simultaneously since they all have similar lasing thresholds [47].

The evolution of the  $N$  single transverse and longitudinal modes class-B lasers can be described by the rate equations [52, 53] on the amplitude  $A_i$ , phase  $\theta_i$ , and gain  $G_i$  of the  $i$ -th laser

$$\frac{dA_i}{dt} = (G_i - \alpha_i) \frac{A_i}{\tau_p} + \sum_j J_{ij} \frac{A_j}{\tau_p} \cos(\theta_i - \theta_j), \quad (1.17)$$

$$\frac{d\theta_i}{dt} = \Omega_i - \sum_j J_{ij} \frac{A_j}{\tau_p A_i} \sin(\theta_i - \theta_j), \quad (1.18)$$

$$\frac{dG_i}{dt} = \frac{1}{\tau_c} [P_i - G_i(1 + A_i^2)], \quad (1.19)$$

where  $P_i$ ,  $\alpha_i$ ,  $\Omega_i$  represent the pump strength, loss, frequency detuning of laser  $i$ , respectively, whereas  $\tau_p$  and  $\tau_c$  denote the cavity round trip time and the carrier lifetime, respectively. The coupling strengths between  $i$ -th and  $j$ -th lasers are represented by  $J_{ij}$ . If the amplitudes of all lasers are equal, Eq. (1.18) reduces to system of coupled phase oscillators with  $\Omega_i = \Omega$ :

$$\frac{d\theta_i}{dt} = \Omega_i - \frac{1}{\tau_p} \sum_j J_{ij} \sin(\theta_i - \theta_j). \quad (1.20)$$

This Eq. (1.20) is a celebrated Kuramoto model of identical oscillators which is widely used to describe the emergence of coherent behaviour in complex systems [54, 55]. By LaSalle Invariance Principle [56] every trajectory of the Kuramoto model converges to a minimum of the XY Hamiltonian.

It was shown that the probability of finding the global minimum of the XY Hamiltonian agrees between experimental realisations of the laser array and numerical simulations of Eqs. (1.17-1.19). However, simulating the Kuramoto model of Eq. (1.20) on the same matrix of coupling strengths gives a much lower probability of finding the global minimum. The conclusion was made that the amplitude dynamics described by Eq. (1.17) provides a mechanism to reach the global minimum [53] by pumping from below. This suggested that the cavity lasers can be used as an efficient physical simulator for finding the global minimum of the XY Hamiltonian, and therefore, for solving phase retrieval problems.

A digital degenerate cavity laser has recently been shown to solve phase retrieval problems rapidly [57]. It is an all-optical system that uses nonlinear lasing process to find a solution

that best satisfies the constraint on the Fourier magnitudes of the light scattered from an object. To make sure that the solution to the phase retrieval problem is found the compact support aperture is introduced inside the cavity that ensures that different configurations of laser phases compete to find the one with the minimal losses. The system combines the advantages of short round-trip times of the order of 20 ns and high parallelism in selecting the winning mode.

#### 1.4.4 Optical parametric oscillators

Network of coupled optical parametric oscillators (OPOs) is an alternative physical system for solving the Ising problem ([58] and references therein). Each OPO is a nonlinear oscillator with two possible phase states above the threshold that can be interpreted as binary spin states  $\{-1, 1\}$  with respect to the reference beam. The OPO is stimulated with pulses of light which are then loaded into a loop of optical fibre. Below threshold, pulses of low intensity have random phase fluctuations. Depending on the enforced pulse interactions, the intensities are continuously modulated so that after multiple runs around the loop the final binary phases are formed for all OPOs at about the same time. Driving the system close to this near-threshold regime, the lowest loss configuration state can be found. This state corresponds to the optimal solution of the Ising Hamiltonian and, therefore, the OPO-based simulator is known as the coherent Ising Machine (CIM).

The currently most successful implementations of CIMs have been realised using a fibre-based degenerate optical parametric oscillators (DOPOs) and a measurement based feedback coupling, in which a matrix-vector multiplication is performed on a field-programmable gate array (FPGA) embedded in the feedback loop. The computational performance of such scalable optical processor, that is bounded by the electronic feedback, was demonstrated for various large-scale Ising problems [58–60], while a speedup over classical algorithms is an ongoing study [61, 62]. The ability to implement arbitrary coupling connections between any two spins [58] was apparently the main reason to claim a better scalability of the CIM than the quantum annealer, i.e. D-Wave machine [59].

In a Coherent Ising Machine each Ising spin corresponds to a DOPO that is described by a stochastic equation for the complex amplitude of the signal field  $a_i$ :

$$\frac{da_i}{dt} = pa_i^* - a_i - |a_i|^2 a_i + \sum_j J_{ij} a_j, \quad (1.21)$$

where the dynamics is defined by a linear pump term  $p$ , normalised linear and nonlinear losses, and mutual couplings  $J_{ij}$ . To experimentally realise these couplings, a portion of

light is extracted from the cavity after each round trip. That light is then homodyned against a reference pulse to produce  $a_i$  that is next supplied to FPGA where a feedback signal is computed for each pulse. Lastly, an optical modulator is applied to convert the signal back to light that can be used for the next round trip. The Eq. (1.21) is often reformulated in terms of the in-phase and quadrature components  $a_i = c_i + is_i$  giving the equations in real terms:

$$\frac{dc_i}{dt} = \left( p - 1 - (c_i^2 + s_i^2) \right) c_i + \sum_j J_{ij} c_j \quad (1.22)$$

$$\frac{ds_i}{dt} = \left( -p - 1 - (c_i^2 + s_i^2) \right) s_i + \sum_j J_{ij} s_j. \quad (1.23)$$

The computational effectiveness of these equations has been demonstrated [63] by tackling small size Ising type problems of order up to 20. In a part devoted to polariton condensates we will show that for achieving the global minimum the realisation of an individual pump variation  $p_i$  for equalising all signal amplitudes  $|a_i|$  is crucial.

Phase-stability for the whole length of the cavity is required which makes the DOPOs system highly susceptible to external perturbations that can affect performance [59]. Furthermore, the nonlinear DOPO generation process demands powerful laser systems and temperature-controlled nonlinear materials, which result in large and complex optical setups. These issues lead to recent proposals of other physical platforms for implementing a CIM-like machine. A CIM based on opto-electronic oscillators with self-feedback was suggested to be more stable and cheaper based on solving Ising optimisation problems on regular and frustrated graphs with up to 100 spins and similar or better performance compared to the original DOPO-based CIM [64]. An analogue all-optical implementation of a CIM based on a network of injection-locked multicore fibre lasers [65] demonstrated a possibility to solve Ising Hamiltonians for up to thirteen nodes. The dynamics of a network of injection-locked lasers was based on nonlinear coupled photon rate equations and the couplings were implemented using spatial light modulators (SLMs). The couplings were reported to be dependent on the photon numbers that are not known beforehand, which can be a major obstacle on the way of solving a given Ising Hamiltonian with the proposed photonic CIM. To solve this issue, approaches similar to gain variation that we discuss in Section 3.2 may be considered in the future. Another large-scale optical Ising machine based on the use of an SLM was experimentally demonstrated by using the binary phases in separated spatial points of the optical wave front of an amplitude-modulated laser beam and realising configurations with thousands of spins with tunable all-to-all pairwise interactions [66].

### 1.4.5 Polariton and Photon networks

Microcavity exciton-polaritons, or simply polaritons, are mixed light-matter quasi-particles that form due to the strong coupling of photons in a microcavity and excitons in a semiconductor quantum well. Polaritons are bosons and obey Bose-Einstein statistics and can, therefore, form a condensed (coherent) state above a critical density [67]. These bosonic quasi-particles have a tiny effective mass which is typically 4 – 5 orders of magnitude smaller than the electron’s mass. Polariton condensates are intrinsically non-equilibrium systems with the steady states set by the balance between pumping and losses due to the short lifetime of polaritons as photons leak through the confining mirrors. Their energy-momentum dispersion curves can be controlled by appropriate detuning and their properties and dynamics can be readily accessed by angular-resolved photo- or electroluminescence spectroscopy. This is possible due to finite cavity lifetimes: polaritons decay in the form of photons that carry all information of the corresponding polariton state (energy, momentum, spin and phase). The continuous coupling of polaritons to free photons allows for the in-situ characterisation of static polariton graphs, and for the dynamic control of an arbitrary set of sites, whilst measuring in real time the kinetics and phase configuration of the modulated polariton graph. Polariton condensates can be imprinted into any two-dimensional graph by spatial modulation of the pumping source, offering straightforward scalability. Optically injected polariton condensates can potentially be imprinted in multi-site configurations with arbitrary polarisation and density profiles offering the possibility to control the separation distance between sites. The design and choice of material allows one to control the polariton mass and to realise such solid state non-equilibrium condensates not only at cryogenic temperatures but even at room temperature in organic structures. The weak coupling at high temperatures and high pumping intensities transitions continuously to strong coupling at lower temperatures and lower pumping intensities. In the limit of a small gain, i.e. small losses, solid state condensates resemble equilibrium Bose-Einstein condensates (BECs) and in the regime of high gain, i.e. high losses, they approach the lasers. This transition from the equilibrium BECs to normal lasers was described with a unified approach via polariton condensates [68]. A wealth of experimental results have been demonstrated with polaritons including polariton lasers [69], polariton parametric amplifiers [70], and cavity quantum electrodynamics [71]. The polariton BEC or lasing have been demonstrated in various materials such as CdTe [67], GaAs [72, 73], GaN [74], organic polymers [75] and using optical pumping or electrically pumped exciton-polariton emitters [76].

In another system, closely resembling the physics of polariton condensates, macroscopic occupation of the lowest mode for a gas of photons confined in a dye-filled optical microcavity was recently shown [77–80]. The rapid thermalisation of rovibrational modes of the dye

molecules by their collisions with the solvent and phonon dressing of the absorption and emission by the dye molecules leads to the thermal equilibrium distribution of photons and concomitant accumulation of low-energy photons. Such systems resemble micro-lasers [81], but unlike micro-lasers exhibit a sharp threshold which occurs far below inversion.

To realise the lattices of polariton or photon condensates many techniques have been proposed and realised in experiments. Polariton lattices can be optically engineered by injecting polaritons in specific areas of the sample using a spatial light modulator [82–86]. A variety of potential landscapes to confine polariton or photons have also been engineered [87–89]. As it will be derived in the next Chapter, the evolution of gain-dissipative condensates in a lattice can be described by the Stuart-Landau equations:

$$\dot{\Psi}_i = -iU|\Psi_i|^2\Psi_i + (\gamma_i - |\Psi_i|^2)\Psi_i + \sum_{j \neq i} \mathcal{C}_{ij}\Psi_j, \quad (1.24)$$

where  $\Psi_i = \sqrt{\rho_i} \exp[i\theta_i]$  is the complex amplitude of the  $i$ -th condensate,  $U$  is the strength of self-interactions between the quasi-particles,  $\gamma_i$  is the effective injection rate (the difference between the pumping of the quasi-particles into the system and linear losses). The coupling strength  $\mathcal{C}_{ij} = J_{ij} + iG_{ij}$  is generally a complex number and consists of the Heisenberg coupling  $J_{ij}$  mediated by the injection reservoir and the Josephson part  $G_{ij}$  that comes from exchange interactions between the condensates. We will show in Chapter 3, that the system described by Eq. (1.24) reaches the fixed point when  $J_{ij} \gg G_{ij}$  and the pumping feedback is introduced in the system. The feedback on the pumping intensity ensures that all the occupations are the same at the fixed point, by adjusting the pumping if the occupation exceeds the set threshold value  $|\Psi_i|^2 = \rho_{\text{th}}$ . The total injection of the particles in the system of  $N$  condensates at the fixed point is given by

$$\sum_{i=1}^N \gamma_i = N\rho_{\text{th}} - \sum_{i=1}^N \sum_{j < i}^N J_{ij} \cos(\theta_i - \theta_j). \quad (1.25)$$

Choosing the lowest possible total particle injection  $\sum \gamma_i$  that leads to the occupation  $\rho_{\text{th}}$  for each condensate guarantees that the minimum of the XY Hamiltonian is reached. In order to find the true global minimum the system has to slowly be brought to the condensation threshold while spending enough time in its neighbourhood to span various phase configurations driven by the system noise (classical and quantum fluctuations). When the system reaches a phase configuration in the vicinity of the minimum of the XY Hamiltonian

it quickly converges to it by the gradient decent given by the imaginary part of Eq. (1.24):

$$\dot{\theta}_i = -U\rho_{\text{th}} - \sum_{j \neq i}^N J_{ij} \sin(\theta_i - \theta_j). \quad (1.26)$$

This idea will be explained in more details in Chapter 3. When the resonant excitation is combined with a non-resonant one, the spins are forced to take the discrete values aligning with the directions set by the resonant excitation. If  $n : 1$  resonant drive is added to the system, the dynamics of the coherent centres obeys

$$\dot{\Psi}_i = -iU|\Psi_i|^2\Psi_i + (\gamma_i - |\Psi_i|^2)\Psi_i + \sum_{j \neq i} J_{ij}\Psi_j + h(t)\Psi_i^{*(n-1)}, \quad (1.27)$$

where  $h(t)$  is an increasing function that reaches some value  $H > \max_i \sum_j |J_{ij}|$  at the threshold. At the fixed point, Eq. (1.25) is replaced with

$$\sum_{i=1}^N \gamma_i = N\rho_{\text{th}} - \sum_{i=1}^N \sum_{j < i}^N J_{ij} \cos(\theta_i - \theta_j) - H\rho_{\text{th}}^{n/2-1} \cos(n\theta_i). \quad (1.28)$$

At  $n = 2$ , the last term on the right-hand side provides the penalty to phases deviating from 0 or  $\pi$  reducing the optimisation problem to QUBO. For  $n > 2$ , the  $n$ -state Potts Hamiltonian is minimised. More details will be given about minimising such discrete spin Hamiltonians in Chapter 3.

## 1.5 Conclusions

The physical systems that we described aim at finding the global minimum of challenging optimisation problems. They offer the potential to find a better solution for a fixed time, find a solution of a given precision faster, or solve more complex problems at fixed and limited cost. All these platforms have advantages and limitations. They vary in scalability, ability to engineer the required couplings, flexibility of tuning the interactions, precision of read-out, factors facilitating the approach to global rather than local minima. However, all of them have specific operational components that promise increased performance over the classical computations. With the advancement of system-inspired computational algorithms, these physical platforms may indeed one day revolutionise our computing. The next Chapter will focus on the physics of one of such platforms in more detail, namely polariton condensates.



## **Chapter 2**

# **Physics of polaritonic networks**

## 2.1 Polariton network as a paradigm for dynamics of coupled oscillators

Complex dynamic behaviour of networks of coupled oscillators arises in various scientific disciplines ranging from biology, physics, and chemistry to social and neural networks. Such networks served as paradigmatic models for understanding the mechanism of various collective phenomena. The reason for such power of networks of coupled oscillators in describing vastly different setups lies in their underlying symmetries: all these physical platforms are characterised by similar universal order parameter equations [90]. Such symmetries allow one to classify the physical systems into various universality classes that differ only by the nature of the dynamics [91]. In turn, such classification helps not only to draw similarities between very different physical platforms but also predict the behaviour of the new systems that fall into previously known universality class [68].

Traditionally, at the other end of the spectrum of nonlinear dynamical studies lie the complex many-body solid-state systems. Lattices of various physical origin have been realised, including neutral atoms, ions, electrons in semiconductors, polar molecules, superconducting circuits, nuclear spins [92]. These are typically equilibrium systems that realise ground or excited states of their structure Hamiltonians. Recently, photonic and polaritonic lattices have emerged as promising platforms for many-body quantum and classical simulations [93, 94]. These systems are typically gain-dissipative, capable of symmetry breaking and spontaneous pattern formation, and have constant nonzero particle fluxes even at the steady-state. As we will discuss shortly, the gain-dissipative lattice elements evolve, interact and synchronise, resembling the coupled oscillators dynamics governed by the universal order parameter equations. As a result, many classical phenomena found in such lattices can be explained or predicted by the behaviour of the corresponding system of coupled oscillator networks from the same universality class.

In the last decade, it emerged that strong light-matter interactions in semiconductor microcavities offer a versatile platform to realise nontrivial states. They consist of exciton-polaritons, or simply polaritons, that are quasi-particles resulting from the hybridisation of light confined inside semiconductor microcavities and bound electron-hole pairs (excitons). In this Section, we will consider networks of polariton condensates that can be engineered with a variety of experimental techniques [87, 88]. Polariton can be confined by strain-induced traps [73], surface acoustic waves [95], direct fabrication with the gold deposition technique [96], by using hybrid air gap microcavities [97], or by coupled mesas etched during the growth of the microcavity [98], by micropillars [99]. With these techniques, polariton graphs of various geometries can be created including square [96], triangular [100],

hexagonal [101], fully etched honeycomb [102], Kagome [103] and quasi-periodic lattices [104]. However, the flow dynamics could be highly nontrivial even in the steady-state for some geometries due to the potential traps. Another option is to optically engineer polariton lattices by exploiting interactions between polaritons and reservoir excitons that can be injected in specific areas of the sample. Excitons can barely move from where they are excited as they are orders of magnitude heavier than polaritons. In experiments, any prescribed graph of polariton condensates can be created by using an SLM [82–86]. With this technique, the intensities of individual sites can also be controlled depending on the density of the polariton condensate at the site.

Next, we will investigate the behaviour of networks of exciton-polaritons (*polaritonic networks*) and argue that they can be viewed as a flexible universal platform to realise a vast array of known and extensively studied systems of coupled oscillators.

### 2.1.1 Mean-field description

The mean-field behaviour of polariton condensates is described by the generalised complex Ginzburg-Landau equation (cGLE) (often also referred to as a driven-dissipative Gross-Pitaevskii equation) coupled to the reservoir dynamics [105–107]. Although the process of Bose-Einstein condensation includes quantum effects, once the condensate is formed, it can be accurately described by the mean-field equations as was shown in numerous experimental works [84, 85, 108–114]. The equation on the wave function  $\psi(\mathbf{r}, t)$  of the condensed system is coupled to the rate equation on the density of the hot reservoir  $\mathcal{R}(\mathbf{r}, t)$  so that

$$i \frac{\partial \psi}{\partial t} = -\frac{1}{2m} (1 - i\hat{\eta}\mathcal{R}) \nabla^2 \psi + U_0 |\psi|^2 \psi + g_R \mathcal{R} \psi + \frac{i}{2} [R_R \mathcal{R} - \gamma_C] \psi, \quad (2.1)$$

$$\frac{\partial \mathcal{R}}{\partial t} = -(\gamma_R + R_R |\psi|^2) \mathcal{R} + P(\mathbf{r}, t), \quad (2.2)$$

where  $\hbar = 1$ ,  $U_0$  and  $g_R$  are the polariton-polariton and polariton-exciton interaction strengths respectively,  $\hat{\eta}$  is the energy relaxation,  $R_R$  is the rate of scattering from the hot reservoir into the condensates [68, 115]. The condensate ( $\gamma_C$ ) and the reservoir ( $\gamma_R$ ) relaxation rates describe photon losses in the cavity and hot exciton losses other than scattering into condensates. The incoherent pump source is described by the pumping intensity  $P(\mathbf{r}, t)$ . These equations can be nondimensionalised by  $\psi \rightarrow \sqrt{\gamma_C/2U_0} \psi$ ,  $t \rightarrow 2t/\gamma_C$ ,  $\mathbf{r} \rightarrow \sqrt{1/m\gamma_C} \mathbf{r}$ ,  $\mathcal{R} \rightarrow \gamma_C \mathcal{R}/R_R$ ,  $P \rightarrow P\gamma_C^2/2R_R$ . With the dimensionless parameters  $g = 2g_R/R_R$ ,  $b_0 = 2\gamma_R/\gamma_C$ ,  $b_1 = R_R/U_0$ ,

$\eta = \hat{\eta}\gamma_C/R_R$ , the resulting model yields

$$i\frac{\partial\psi}{\partial t} = -(1 - i\eta\mathcal{R})\nabla^2\psi + |\psi|^2\psi + g\mathcal{R}\psi + i(\mathcal{R} - 1)\psi, \quad (2.3)$$

$$\frac{\partial\mathcal{R}}{\partial t} = -(b_0 + b_1|\psi|^2)\mathcal{R} + P(\mathbf{r}, t). \quad (2.4)$$

A unique property of the exciton-polariton system is the flexibility with which the parameters  $g$ ,  $b_0$ ,  $b_1$ ,  $\eta$  can be controlled and changed to allow the system to span various regimes bridging lasers or other non-equilibrium systems with equilibrium condensates. The lifetime of polaritons  $\gamma_C$  is governed by the accuracy of the cavity distributed Bragg reflectors and spans two orders of magnitude [67, 116]. The detuning between the cavity photon energy and the exciton resonance determines the proportion of photon and exciton in the polariton and, therefore, the strength of the polariton-polariton and polariton-exciton interactions and effective mass [107]. The pumping geometry allows one to tune further the repulsive interactions between excitons and polaritons  $g_R$  by creating, for example, trapped condensates [108].

A polaritonic network building block is a single stationary condensate described by a wave function  $\psi = \phi(r)$ , created by a spatially localised radially symmetric incoherent pumping source  $P = p(r)$ . For instance, a Gaussian pump  $p(r) = A \exp[-wr^2]$  where  $w$  determines the inverse width has been widely used in experiments [85, 86]. In what follows, the pumping intensity  $A$  can be chosen so that  $\phi$  is normalised and  $\int_Q |\phi|^2 d\mathbf{r} = 1$ , where  $Q$  is the entire plane of the cavity. The corresponding stationary reservoir profile is then defined as the steady state of Eq. (2.4) which is  $\mathcal{R}(r) = n(r) = p/(b_0 + b_1|\phi|^2)$ . The networks of  $N$  polariton condensates are created at lattice sites  $i$  using a time and space varying pumping profile  $P(\mathbf{r}, t) = \sum_{i=1}^N f_i(t)p(|\mathbf{r} - \mathbf{r}_i|)$ . The total wave function  $\psi$  and the reservoir density  $\mathcal{R}$  can be approximated by  $\psi(\mathbf{r}, t) \approx \sum_{i=1}^N a_i(t)\phi(|\mathbf{r} - \mathbf{r}_i|)$  and  $\mathcal{R}(\mathbf{r}, t) \approx \sum_{i=1}^N k_i(t)n(|\mathbf{r} - \mathbf{r}_i|)$  respectively. Such approximation is valid if the distance between the lattice sites exceeds the width of the condensate and reservoir [117]. With the shorthand notation  $p_i \equiv p(|\mathbf{r} - \mathbf{r}_i|)$  and similarly for  $\phi$  and  $n$ , the spatial degrees of freedom are eliminated by multiplying Eq. (2.3) by  $\phi_i^*$ , Eq. (2.4) by  $|\phi_i|^2$  and integrating both equations over the plane of cavity  $Q$ . To show how systems of different universality classes become relevant to polaritonic networks, we use the smallness of the overlap integrals for the wave functions of the different lattice sites [118] so that  $l_{ij} \equiv \int_Q n_i \phi_j \phi_i^* d\mathbf{r} \gg \int_Q \phi_j \phi_i^* d\mathbf{r}$ ,  $l = l_{ii} \gg \int_Q n_i |\phi_j|^2 d\mathbf{r}$ , and  $H = \int_Q n \nabla^2 \phi \phi^* d\mathbf{r} \gg \int_Q n_i \nabla^2 \phi_j \phi_i^* d\mathbf{r}$  if  $i \neq j$ . Condensate profiles are also assumed to be sufficiently smooth  $\int_Q n_i \nabla^2 \phi_j \phi_i^* d\mathbf{r} \ll l_{ij}$ . The dynamical equations

on  $\Psi_i(t) = a_i(t) \exp[-idt]$  and  $R_i(t) = lk_i$  become

$$\dot{\Psi}_i = -i|\Psi_i|^2\Psi_i - \Psi_i + hR_i\Psi_i + (1 - ig)[R_i\Psi_i + \sum_{j \neq i} \mathcal{C}_{ij}\Psi_j], \quad (2.5)$$

$$\dot{R}_i = b_0(\gamma_i - R_i - \xi R_i|\Psi_i|^2), \quad (2.6)$$

where  $d = \int_Q \phi^* \nabla^2 \phi d\mathbf{r}$ ,  $h = \eta H/l$ ,  $\gamma_i = f_i \int_Q p |\phi|^2 d\mathbf{r} / b_0$ ,  $\xi = b_1 \int_Q n |\phi|^4 d\mathbf{r} / lb_0$ ,  $\mathcal{C}_{ij} = (R_i l_{ij} + R_j l_{ji}^*)/l$ . The energy relaxation parameter is small  $\eta \ll 1$  and, therefore,  $|H| < l$ , so the term  $|h|R_i\Psi_i$  will be neglected in comparison with  $R_i\Psi_i$ , whereas the imaginary part of  $h$  will be assumed be absorbed by  $g$ . The coupling strength  $\mathcal{C}_{ij}$  is generally a complex number and can be written as  $\mathcal{C}_{ij} \equiv J_{ij} \exp[iv_{ij}]$  for real  $J_{ij}$  and  $v_{ij}$ . In deriving Eqs. (2.5, 2.6), higher order nonlinearities in  $\Psi_i$  are neglected in the view of their smallness close to the condensation threshold. Several special cases of Eqs. (2.5, 2.6) are considered below.

### 2.1.2 Fast reservoir relaxation limit

In fast reservoir relaxation limit, when  $b_0 \gg 1$ , the reservoir dynamics can be replaced with its steady state as  $R_i = \gamma_i / (1 + \xi |\Psi_i|^2) \approx \gamma_i - \xi \gamma_i |\Psi_i|^2$ , which reduces the system of Eqs. (2.5, 2.6) to the single equation

$$\dot{\Psi}_i = i(g\xi\gamma_i - 1)|\Psi_i|^2\Psi_i - \xi\gamma_i|\Psi_i|^2\Psi_i - \Psi_i + (1 - ig)[\gamma_i\Psi_i + \sum_{j \neq i} \mathcal{C}_{ij}\Psi_j]. \quad (2.7)$$

For uniform pumping  $\gamma_i = \gamma$ , this is a Stuart-Landau system of coupled oscillators [119, 120]. This model represents the normal form of the Andronov-Hopf bifurcation. Consequently, it can approximate a wide range of different oscillatory systems including lasers operating close to an instability threshold. Substituting  $\Psi_i(t) = \sqrt{\rho_i(t)} \exp[i\theta_i(t)]$  into Eq. (2.7) and separating real and imaginary parts allows one to get

$$\frac{1}{2}\dot{\rho}_i(t) = (\gamma - 1 - \xi\gamma\rho_i)\rho_i + \sum_{j:j \neq i} \tilde{J}_{ij} \sqrt{\rho_i \rho_j} \cos(\theta_{ij} - v_{ij} + \alpha), \quad (2.8)$$

$$\dot{\theta}_i(t) = (g\xi\gamma - 1)\rho_i - g\gamma - \sum_{j:j \neq i} \tilde{J}_{ij} \frac{\sqrt{\rho_j}}{\sqrt{\rho_i}} \sin(\theta_{ij} - v_{ij} + \alpha), \quad (2.9)$$

where  $\theta_{ij} = \theta_i - \theta_j$ ,  $\tan(\alpha) = g$  and  $\tilde{J}_{ij} = J_{ij} / \cos \alpha$ . Note, that for the Gaussian pumping profile and wide reservoir the relation  $|v_{ij}| \ll |J_{ij}|$  is valid and the term  $v_{ij}$  can be neglected since  $l_{ij} \approx l_{ji}^*$  [117]. For other network geometries such assumption may not be valid in which case  $v_{ij}$  can be absorbed into  $\alpha_{ij} = \alpha - v_{ij}$ .

Experimentally, the feedback can be applied to bring all the sites to the same density  $\rho_i(t) = |\Psi_i(t)|^2 = \rho_{\text{th}}$  by combining Eq. (2.7) with an equation on the pumping adjustments

$$\dot{\gamma}_i(t) = \varepsilon[\rho_{\text{th}} - \rho_i(t)], \quad (2.10)$$

where the parameter  $\varepsilon$  characterises the rate of such adjustment or its discrete version applied at discrete times  $t_n$  (more appropriate for the current experimental control techniques), so that  $\gamma_i(t_n < t \leq t_{n+1}) = \gamma_i(t_n) + \varepsilon(t_{n+1} - t_n)(\rho_{\text{th}} - \rho_i(t_n))$ . Under this control, the Eqs. (2.8-2.9) can be reduced to a single equation near the threshold  $\rho_i \approx \rho_{\text{th}}$ :

$$\dot{\theta}_i(t) = (g\xi\gamma_i - 1)\rho_{\text{th}} - g\gamma_i - \sum_{j:j \neq i} \tilde{J}_{ij} \sin(\theta_{ij} + \alpha). \quad (2.11)$$

This is the Sakaguchi-Kuramoto model of coupled oscillators [121] with  $\alpha$  representing a phase lag. Synchronisation of such phase oscillators has been extensively studied in vastly different contexts including networks of Wien-bridge oscillators [122], power grids of many generators [123], and earthquake sequences [124]. The phase lag appears due to synaptic organisations in neuroscience systems, time delays in sensor networks, or transfer conductances in power networks. The Sakaguchi-Kuramoto model is a special case of the Winfree model with delta-function pulse shape  $W_1(\theta)$  and a sinusoidal response curve  $W_2(\theta)$ , so that  $\dot{\theta}_i = \omega_i + W_2(\theta_i) \sum_{j=1}^N W_1(\theta_j)$ . If the coupling is sufficiently weak and the oscillators are nearly identical, the phase can be replaced by its average over an entire period of oscillations leading to the Sakaguchi-Kuramoto model.

The Eq. (2.11) is reduced to the paradigmatic Kuramoto model, i.e. the first tractable mathematical model describing how coherent behaviour emerges in complex systems, when  $g = 0$  (or equivalently  $\alpha = 0$ ) [54, 55]. This model exhibits a phase transition at a critical coupling, beyond which a collective behaviour is achieved. In our case, natural frequencies are identical and equal to  $\rho_{\text{th}}$ , so the model describes the negative gradient flow  $\dot{\theta} = -\partial U(\theta)/\partial \theta$  for the smooth function  $U(\theta) = -\sum_{i,j} \tilde{J}_{ij} \cos \theta_{ij}$ . Therefore, every trajectory converges to a minimum of the XY Hamiltonian  $H_{XY} = -\sum_{i=1}^N \sum_{j=1}^N \tilde{J}_{ij} \cos(\theta_i - \theta_j)$  by the LaSalle invariance principle [56]. Such minimisation happens for the type of couplings represented by the negative gradient flow of real function  $U$ . For example, this is true when the coupling matrix  $\mathcal{C}_{ij}$  in Eq. (2.7) is self-adjoint ( $J_{ij} = J_{ji}$  and  $v_{ij} = -v_{ji}$ ). In contrast, if the couplings in Eq. (2.7) are of a pure Josephson type (e.g.  $\Psi_i = \dots + i \sum_j K_{ij} \Psi_j$  with real couplings  $K_{ij}$ ) or have a non-negligible  $g$ , such a network will not necessarily minimise any spin Hamiltonian.

In addition, the parameter  $g$  has a destabilising effect on the fixed points of Eq. (2.11). Different  $\gamma_i$  that have to be maintained to allow all densities to reach the same value  $\rho_{\text{th}}$ ,

provide each lattice element with its own “natural frequency”  $\omega_i = (g\xi\gamma_i - 1)\rho_{\text{th}} - g\gamma_i$ , and, therefore, favour desynchronisation. In the network described by Eq. (2.11), synchronisation occurs when the coupling dominates the dissimilarity introduced by natural frequencies and the phase lag. The smaller is  $g$ , the more likely the global synchronisation will be achieved. Concise results for complex networks are known for specific topologies such as, for instance, complete graphs, highly symmetric ring or linear graphs, acyclic graphs, and complete bipartite graphs with uniform weights. Also, Sakaguchi phase lag parameter  $\alpha$  contributes to desynchronisation as it provides attraction and repulsion between the oscillator phases similar to the coupling time delay. The dependence of synchronisation and desynchronisation in polariton condensates on  $g$  has been noted experimentally, but the reasons have not been previously identified [82–84, 125]. Such a behaviour, however, is easily explained from the point of view of the dynamics of coupled oscillators.

### 2.1.3 Slow reservoir relaxation limit

Eq. (2.7) describes the direct coupling scheme when pumping at the mean-field, calculated algebraically from the states of all oscillators, enters the coupling. The coupling scheme of Eqs. (2.5-2.6) is more complex: the mean-field acts on the reservoir densities that obey its own nonlinear differential equations, and the acting force is a function of the reservoir state. This is similar to the famous example of synchrony on London’s Millennium Bridge where equations for the swinging mode of the bridge are coupled to the equations on individual pedestrians [126], or to electronic or electrochemical oscillators that are coupled through the common macroscopic current or voltage, which obeys macroscopic equations describing the coupling circuit [127]. By tuning the photonic component of polaritons one can change the polariton-polariton interactions up to 4 orders of magnitude [125] which allows one to neglect the term  $|\Psi_i|^2\Psi_i$ , so that Eqs. (2.5-2.6) become similar to the Lang-Kobayashi equations (with  $\Psi_i$  replaced by the electric field and  $R_i$  by the population inversion of the  $i$ -th laser) obtained using Lamb’s semiclassical laser theory and capable of describing the dynamical behaviour of coupled lasers [128, 129]. We summarise all the regimes and models described above schematically in Figure 2.1.

The flexibility to tune the system parameters, the shape and geometry of the polariton lattice [86], existence and tunability of the nonlocal couplings beyond the next neighbour interactions [130], strong self-interactions of polariton condensates allow one to not only recreate the intriguing patterns, states and structures that fascinated the nonlinear dynamics community in the last couple of decades but also to enter novel regimes. These regimes are discussed in subsequent parts of this Chapter, with a detailed analysis of interactions between two polariton condensates presented first.

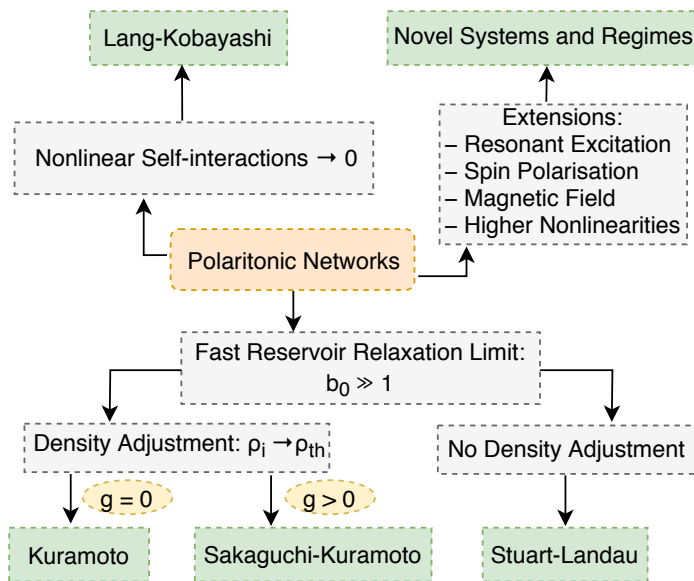


Fig. 2.1 The polaritonic networks described by Eqs. (2.5, 2.6) can lead to the Lang-Kobayashi model in the absence of the nonlinear self-interaction term or to Kuramoto/Sakaguchi-Kuramoto/Stuart-Landau models of coupled oscillators in the limit of fast reservoir relaxation. The new regimes are expected to appear due to strong polariton-polariton interactions or once the experimental controls such as resonant excitation pump, spin polarisation, magnetic field, or combination of different sub-lattices are considered in polaritonic networks.

## 2.2 Matter-wave coupling of two spatially-separated polariton condensates

In this Section, the coupling of driven-dissipative condensates is studied. The closed-form expression for the coupling interactions between equally pumped polariton condensates is analytically derived, assuming an exponential profile of the individual polariton densities. The coupling strength is derived from a series expansion for the outflow wave vector difference in unequally populated polariton condensates. The limit under which two condensates remain coherently coupled is discussed. It is shown that the phase configuration maximising the polariton occupancy across a dyad corresponds to the minimisation of the sum of the symmetric Heisenberg exchange and asymmetric Dzyaloshinskii-Moriya interactions.

### 2.2.1 Symmetric Heisenberg and asymmetric Dzyaloshinskii-Moriya interactions

We start by considering the case of two unequally pumped exciton reservoirs with Gaussian pumping profiles. For two spatially separated condensates, the system's wave function can be approximated as the sum of the two wave functions of the individually created condensates:

$$\psi(\mathbf{r}) \approx \psi_1(|\mathbf{r} - \mathbf{r}_1|) + \psi_2(|\mathbf{r} - \mathbf{r}_2|), \quad (2.12)$$

where the wave function of a condensate located at  $\mathbf{r} = \mathbf{r}_i$  can be approximated [118] by

$$\psi_i(|\mathbf{r} - \mathbf{r}_i|) \approx \sqrt{\rho_i(|\mathbf{r} - \mathbf{r}_i|)} \exp[ik_{ci}|\mathbf{r} - \mathbf{r}_i| + i\theta_i]. \quad (2.13)$$

Here  $\theta_i$  is the space independent part of the phase,  $k_{ci}$  is the maximum wave vector  $k(\mathbf{r})$  that polaritons reach within their lifetime by converting their potential to kinetic energy [107], and  $\rho_i(|\mathbf{r} - \mathbf{r}_i|)$  is the density of the isolated condensate created by a single pumping source centered at  $\mathbf{r}_i$ ; for an approximate expression for  $\rho_i$  as a function of the system parameters see [118]. Note that the assumption of a linear superposition does not account for the nonlinearity of the system.

The total number of polaritons across the dyad is given by  $\mathcal{N} = \int |\psi(\mathbf{r})|^2 d\mathbf{r}$ , where integration is over the entire area of the microcavity and

$$\begin{aligned}
\mathcal{N} &\approx \int |\psi_1(|\mathbf{r} - \mathbf{r}_1|) + \psi_2(|\mathbf{r} - \mathbf{r}_2|)|^2 d\mathbf{r} = \\
&= \int d\mathbf{r} [|\psi_1(|\mathbf{r} - \mathbf{r}_1|)|^2 + |\psi_2(|\mathbf{r} - \mathbf{r}_2|)|^2] + \\
&+ \int d\mathbf{r} [\psi_1(|\mathbf{r} - \mathbf{r}_1|)\psi_2^*(|\mathbf{r} - \mathbf{r}_2|) + c.c.] = \\
&= \mathcal{N}_1 + \mathcal{N}_2 + J \cos \Delta\theta + D \sin \Delta\theta,
\end{aligned} \tag{2.14}$$

where  $\Delta\theta = \theta_1 - \theta_2$  is the phase difference between two polariton condensates,  $\mathcal{N}_i = \int |\psi_i(|\mathbf{r} - \mathbf{r}_i|)|^2 d\mathbf{r}$  is the number of polaritons of an individual condensate indexed by  $i$ , and the interaction strengths  $J$  and  $D$  are expressed as

$$\begin{aligned}
J &= 2 \int \sqrt{\rho_1(|\mathbf{r} - \mathbf{r}_1|)} \sqrt{\rho_2(|\mathbf{r} - \mathbf{r}_2|)} \\
&\times \cos[k_{c1}|\mathbf{r} - \mathbf{r}_1| - k_{c2}|\mathbf{r} - \mathbf{r}_2|] d\mathbf{r},
\end{aligned} \tag{2.15}$$

$$\begin{aligned}
D &= 2 \int \sqrt{\rho_1(|\mathbf{r} - \mathbf{r}_1|)} \sqrt{\rho_2(|\mathbf{r} - \mathbf{r}_2|)} \\
&\times \sin[k_{c1}|\mathbf{r} - \mathbf{r}_1| - k_{c2}|\mathbf{r} - \mathbf{r}_2|] d\mathbf{r}.
\end{aligned} \tag{2.16}$$

From all the possible phase differences  $\Delta\theta = [0, 2\pi)$ , the one that maximises the number of particles in Eq. (2.14) will condense first for the equally pumped polariton dyad [131]. Equivalently, in the generic case of a polariton dyad with unequal populations, the system will reach the threshold at the phase difference configuration  $\Delta\theta$  that minimises

$$H_T = -(J \cos \Delta\theta + D \sin \Delta\theta), \tag{2.17}$$

where  $H_T$  is the sum of the symmetric Heisenberg exchange and the asymmetric Dzyaloshinskii-Moriya interactions [132, 133], that are usually studied in the context of a contribution to the total magnetic exchange interaction between two neighbouring magnetic spins [134].

## 2.2.2 Analytical expressions for coupling strengths

Analytical expressions of the coupling strengths  $J$  and  $D$  can be obtained by positioning the condensates at  $\mathbf{r}_1 = (-d/2, 0)$  and  $\mathbf{r}_2 = (d/2, 0)$ , where  $d = |\mathbf{r}_1 - \mathbf{r}_2|$  is the separation

distance, and transforming into elliptic coordinates  $(\mu, \nu)$  with

$$x = \frac{d}{2} \cosh \mu \cos \nu, \quad (2.18)$$

$$y = \frac{d}{2} \sinh \mu \sin \nu, \quad (2.19)$$

$$d^2 \mathbf{r} = \frac{d^2}{4} (\sinh^2 \mu + \sin^2 \nu) d\mu d\nu. \quad (2.20)$$

Here  $\mu$  is a positive real number and  $\nu \in [0, 2\pi)$ . The expressions for the absolute values can be further simplified to

$$|\mathbf{r} - \mathbf{r}_1| = \frac{d}{2} (\cosh \mu + \cos \nu), \quad (2.21)$$

$$|\mathbf{r} - \mathbf{r}_2| = \frac{d}{2} (\cosh \mu - \cos \nu). \quad (2.22)$$

Assuming an exponential decay of the amplitude for an individual condensate  $\sqrt{\rho_i(|\mathbf{r} - \mathbf{r}_i|)} = A_i \exp(-\beta|\mathbf{r} - \mathbf{r}_i|)$ , where  $A_i$  and  $\beta$  correlate with the shape of the pumping profile [118], and substituting Eqs. (2.21, 2.22) we obtain

$$J = \frac{1}{2} A_1 A_2 d^2 \int_0^\infty e^{-\beta d \cosh \mu} \int_0^{2\pi} (\sinh^2 \mu + \sin^2 \nu) \times \cos(\delta k_c^- d \cosh \mu - \delta k_c^+ d \cos \nu) d\nu d\mu, \quad (2.23)$$

$$D = \frac{1}{2} A_1 A_2 d^2 \int_0^\infty e^{-\beta d \cosh \mu} \int_0^{2\pi} (\sinh^2 \mu + \sin^2 \nu) \times \sin(\delta k_c^- d \cosh \mu - \delta k_c^+ d \cos \nu) d\nu d\mu, \quad (2.24)$$

where we denoted  $\delta k_c^\pm = (k_{c1} \pm k_{c2})/2$ . After integrating over  $\nu$  and expanding the integrand for small  $\delta k_c^-$  up to the third order, analytical expressions for the coupling strengths of the two unequally pumped condensates are obtained in terms of the Bessel functions  $J_n$  and the modified Bessel functions of the second kind  $K_n$ :

$$J = \pi A_1 A_2 d \left[ \frac{1}{\beta} J_0(\delta k_c^+ d) K_1(\beta d) + \frac{1}{\delta k_c^+} J_1(\delta k_c^+ d) K_0(\beta d) - (\delta k_c^-)^2 F \right], \quad (2.25)$$

$$D = \pi A_1 A_2 d^2 \delta k_c^- \left[ \frac{1}{\beta} J_0(\delta k_c^+ d) K_2(\beta d) + \frac{1}{\delta k_c^+} J_1(\delta k_c^+ d) K_1(\beta d) - (\delta k_c^-)^2 G \right], \quad (2.26)$$

where

$$F = \frac{d}{2\beta^2} J_0(\delta k_c^+ d) \{ \beta d K_1(\beta d) + 3K_2(\beta d) \} + \frac{d}{2\beta} \frac{J_1(\delta k_c^+ d)}{\delta k_c^+} \{ (\beta d K_0(\beta d) + K_1(\beta d)) \}, \quad (2.27)$$

$$G = \frac{d}{6\beta^2} J_0(\delta k_c^+ d) \{ \beta d K_2(\beta d) + 3K_3(\beta d) \} + \frac{d}{6\beta} \frac{J_1(\delta k_c^+ d)}{\delta k_c^+} \{ (\beta d K_1(\beta d) + K_2(\beta d)) \}, \quad (2.28)$$

We note here that the integrals can be analytically calculated up to any desired precision of  $(\delta k_c^-)^n$ . An exact analytical expression for two equally pumped polariton condensates with  $A_1 = A_2 = A$  and  $k_{c1} = k_{c2} = k_c$  ( $D = 0$ ) reads as

$$J = \pi A^2 d \left[ \frac{1}{\beta} J_0(k_c d) K_1(\beta d) + \frac{1}{k_c} J_1(k_c d) K_0(\beta d) \right]. \quad (2.29)$$

If the pumping width is large ( $\beta$  is small) the sign of the interactions is determined by  $J_0(k_c d)$  as was found in [131].

Figure 2.2 shows the analytically and numerically calculated  $J$  and  $D$  as functions of the distance separating two condensates for small differences between the outflow wave vectors. The agreement improves even further when higher orders of  $\delta k_c^-$  in Eqs. (2.25, 2.26) are taken into account. Note that a discrepancy between the polariton wave vectors  $k_{c1}$  and  $k_{c2}$  may lead to significant non-zero values of the coupling strength  $D$  that may even exceed values of  $J$ . In particular, for the range of experimental parameters it is possible to obtain a continuous phase transition between antiferromagnetic coupling for equal pumping ( $\Delta\theta = \pi$ ,  $J < 0$  and  $D = 0$ ) and ferromagnetic coupling for unequal pumping ( $\Delta\theta = 0$ ,  $J \approx 0$  and  $D > 0$ ).

### 2.2.3 Loss of coherence in polariton dyad

To determine the levels of the pumping imbalance and the distances for which polariton condensates in a polariton dyad remain coherently coupled, we use the cGLE for a polariton wave function  $\psi$  in two-dimensional (2D) with a saturable nonlinearity as written in Eqs. (2.1, 2.2). The simulation parameters were calibrated using an extensive set of experimental data [86].

For the range of pumping parameters where there is a mutual coherence across the polariton dyad, the condensates share the same global chemical potential  $\mu_{\text{coh}}$ , which can be

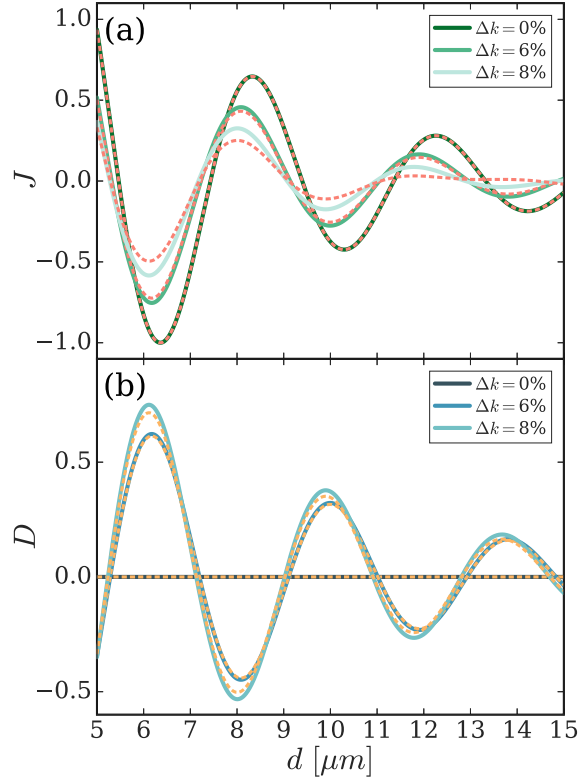


Fig. 2.2 The strengths of (a) the symmetric Heisenberg exchange  $J$  and (b) the asymmetric Dzyaloshinskii-Moriya interactions  $D$  as functions of the separation distance  $d$ . The solid (dashed) lines show the normalised coupling strengths found numerically (analytically) from Eqs. (2.15, 2.16) (Eqs. (2.25, 2.26)). Colours correspond to the different population imbalances characterized by the percentage differences of the condensates' wave vectors,  $\Delta k = 0\%$ ,  $6\%$  and  $8\%$ , where  $\Delta k = 100\% \cdot (k_{c2} - k_{c1}) / k_{c1}$ . The parameters are  $k_{c1} = 1.6 \mu\text{m}^{-1}$ ,  $\beta = 0.2 \mu\text{m}^{-1}$ .

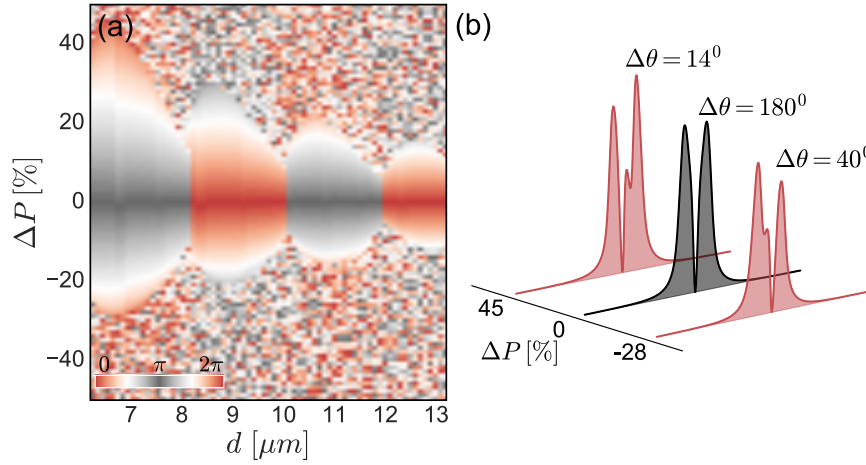


Fig. 2.3 (a) Contour plot of the phase difference  $\Delta\theta = \theta_1 - \theta_2$  in the polariton dyad as a function of the pumping imbalance  $\Delta P = 100\% \cdot (P_2 - P_1)/P_1$  and the separation distance  $d$ . The pumping corresponding to  $P_1$  is kept fixed. The phase difference is measured either for the steady state or at a fixed moment of time for time-dependent oscillations that characterise the loss of phase locking between the condensates. Fragmentation of the contour plot, therefore, represents the region with the loss of the phase locking (coherence) between the condensates. (b) Density cross-sections of the polariton dyad along the line connecting the condensate centers positioned at the distance  $d = 6.4\mu\text{m}$  apart and pumped with  $\Delta P = \{-28, 0, 45\}\%$ .

found from Eq. (2.1) by substituting  $\psi \rightarrow \psi \exp(-i\mu_{\text{coh}}t/\hbar)$ . For each separation distance  $d$ , we numerically integrate Eq. (2.2) starting with many random phase difference configurations and choosing the one that maximises the total number of particles as this corresponds to the state that will lase first [131]. The resulting phase differences are depicted in Figure 2.3(a). Here the phase difference  $\Delta\theta$  in the polariton dyad is shown in a colour scale as a function of the pumping imbalance  $\Delta P$  and the separation distance  $d$ . If two condensates in a dyad are coherently coupled, they share the same chemical potential and achieve a steady state. Above some critical pumping imbalance, which is different for different separation distances, the coherence is lost: condensates have different chemical potentials and their phase difference oscillates in time. This region is shown as fragmented in Figure 2.3(a). Figure 2.3(a) demonstrates that phase differences from 0 to  $\pi$  are achievable in a polariton dyad without losing coherence by adjusting the pumping imbalance or the distance between condensates. Figure 2.3(b) depicts the density cross-sections of the polariton dyad along the line connecting the condensate centres. The variation in the pumping imbalance changes the phase-locking from  $\pi$  phase difference to almost ferromagnetic configurations.

Once arranged in a graph, the population imbalance plays a crucial role in the ability of polariton networks to minimise any given spin Hamiltonian. If all condensates have the same

density, they are phase-locked through symmetric Heisenberg interactions and can achieve the minima of the XY Hamiltonian. For some simple configurations, such as the chains of polariton condensates that we consider next, one can realise the XY model's classical ground states with nearest- and next-to-nearest-neighbour interactions and exotic spin states. The ability to suppress the asymmetric Dzyaloshinskii-Moriya interactions for an arbitrary graph would lead to the minimisation of the XY Hamiltonian on a broader range of problems, as we will discuss later in Chapter 3.

## 2.3 Exotic states of matter with polariton chains

Here we explore properties of various frustrated phase states that can be generated with polariton graphs. In particular, we show that polariton condensates establish the relative phases that correspond to the classical ferromagnetic, antiferromagnetic, frustrated states and the novel exotic states that can be associated with a spin-wave.

### 2.3.1 Linear periodic chain of equidistant polariton condensates

For simplicity, a periodic chain of polariton condensates in a one-dimensional (1D) case is considered first. The steady-state of cGLE with a saturable nonlinearity (see Eqs. (2.1, 2.2)) can be written for the polariton wave function  $\psi$  in one-dimension as

$$\mu\Psi = -(1 - i\eta\mathcal{R})\Psi_{xx} + |\Psi|^2\Psi + g\mathcal{R}(x)\Psi + i(\mathcal{R}(x) - \gamma)\Psi, \quad (2.30)$$

$$\mathcal{R} = \frac{p(x)}{(1 + b|\Psi|^2)}, \quad (2.31)$$

where the non-dimensionalisation is done with  $\psi \rightarrow \sqrt{\hbar^2/2mU_0l^2}\Psi$ ,  $\mathbf{r} \rightarrow l\mathbf{r}$ ,  $t \rightarrow 2mtl^2/\hbar$  and the notations  $g = 2g_R/R_R$ ,  $\gamma = m\gamma_C l^2/\hbar$ ,  $p = ml^2 R_R P(\mathbf{r})/\hbar\gamma_R$ ,  $\eta = \eta_d \hbar/mR_R l^2$ , and  $b = R_R \hbar^2/2ml^2 \gamma_R U_0$  are introduced. We choose the unit length as  $l = 1\mu m$ . When pumped into several spots with the outflows from each spot reaching its neighbours the system establishes a global coherence with a chemical potential  $\mu$  if the characteristics of the pump (intensity, spatial shape) are not vastly different from one spot to another. The Madelung transformation  $\Psi = \sqrt{\rho} \exp[iS]$  relates the wave function to density  $\rho = |\Psi|^2$  and velocity  $u = S_x$ . To derive the coupling strength, we consider a single pumping spot given by  $p(x) = p_0 \exp[-\sigma x^2]$ . At large  $x$ , where  $p(x) = 0$ , the velocity  $u$  is given by the outflow wave number  $k_c = \text{const}$  with  $\rho_x/\rho = -\gamma/k_c$ , which after integration leads to  $\rho \sim \exp[-x\gamma/k_c]$ . Therefore, we obtain  $\mu = k_c^2 - \gamma^2/4k_c^2$  at infinity from Eq. (2.30).

In previous Section, the coupling strength between two equally-pumped condensates was derived in 2D (see Eq. (2.29)). Here to study spin configurations in a periodic chain of polariton condensates, we obtain a similar analytical expression for the coupling strength in 1D. The polariton wave function is approximated as a sum of identical spots  $\Psi(x) \approx \sum_{i=1}^{\ell} \Psi_i(x - x_i)$ . The wave function of a single pumping spot centred at  $x = x_i$  can be approximated by  $\Psi_i(x - x_i) = \sqrt{\rho(x - x_i)} \exp[(ik_c|x - x_i|) + i\theta_i]$ , where  $\theta_i$  is a space independent part of the phase. Depending on the pumping parameters, the system will lock with the relative phases  $\theta_{ij} = \theta_i - \theta_j$  between the sites  $i$  and  $j$  to achieve the highest occupation number, i.e. the total amount of matter given by  $\mathcal{N} = \int_{-\infty}^{\infty} |\Psi|^2 dx$ . To evaluate  $\mathcal{N}$ , we work in the Fourier space

and rewrite it as

$$\begin{aligned}\mathcal{N} &= \frac{1}{2\pi} \int |\widehat{\Psi}(k)|^2 dk \approx \frac{1}{2\pi} \int \left| \sum_i \widehat{\Psi}_i(k) \right|^2 dk = \\ &= \ell \mathcal{N}_0 + \frac{1}{\pi} \sum_{i < j} \int \left( \widehat{\Psi}_i \widehat{\Psi}_j^* + c.c. \right) dk\end{aligned}\quad (2.32)$$

where  $\mathcal{N}_0$  is the number of particles of a single isolated condensate and

$$\begin{aligned}\widehat{\Psi}_i(k) &= \int_{-\infty}^{\infty} \Psi_i(x - x_i) \exp(-ikx) dx = \\ &= \exp(-ikx_i) \int_{-\infty}^{\infty} \Psi_i(\alpha) \exp(-ik\alpha) d\alpha = \\ &= \exp(-ikx_i + i\theta_i) \widehat{\psi}(k),\end{aligned}\quad (2.33)$$

$$\widehat{\psi}(k) = 2 \int_0^{\infty} \sqrt{\rho(\alpha)} \exp(ik_c \alpha) \cos(k\alpha) d\alpha. \quad (2.34)$$

Denoting the distances between the spots as  $x_{ij} = x_i - x_j$ , we substitute Eq. (2.33) into the integral in Eq. (2.32) to get:

$$\mathcal{N} = \ell \mathcal{N}_0 + \frac{2}{\pi} \sum_{i < j} \cos \theta_{ij} \int_0^{\infty} |\widehat{\psi}(k)|^2 \cos(kx_{ij}) dk. \quad (2.35)$$

This expression implies that polariton condensates establish the phase difference in a way minimising the XY Hamiltonian, where the coupling strengths are given by

$$J_{ij} = \frac{2}{\pi} \int_0^{\infty} |\widehat{\psi}(k)|^2 \cos(kx_{ij}) dk. \quad (2.36)$$

Similarly to 2D case, the amplitude of the condensate is parametrised by the width  $\beta$  and the height  $A$  as  $\sqrt{\rho(x)} \approx A \exp[-\beta|x|]$ . We expect the condensate's width and height to correlate with the width and intensity of the pumping profile, respectively. For this shape of the amplitude, the integrals in Eqs. (2.35, 2.36) can be evaluated exactly:

$$\begin{aligned}\widehat{\psi}(k) &= 2A \int_0^{\infty} \exp(-\beta\alpha + ik_c\alpha) \cos(k\alpha) d\alpha \\ &= \frac{2A(\beta - ik_c)}{\beta^2 + k^2 - 2i\beta k_c - k_c^2}.\end{aligned}\quad (2.37)$$

$$J_{ij} = \frac{8A^2}{\pi} \int_0^{\infty} \frac{(\beta^2 + k_c^2) \cos(kx_{ij}) dk}{\beta^4 + (k^2 - k_c^2)^2 + 2\beta^2(k^2 + k_c^2)}. \quad (2.38)$$

Applying the residue theorem for evaluating the last integral, we obtain the closed-form expression for the coupling constants in 1D

$$J_{ij} = 2A^2 \left[ \frac{1}{\beta} \cos(k_c x_{ij}) + \frac{1}{k_c} \sin(k_c x_{ij}) \right] e^{-\beta x_{ij}}. \quad (2.39)$$

This expression determines the switching of ferro- and antiferromagnetic coupling between the neighbours since the sign of  $J_{ij}$  is set by the expression in brackets. If the pumping profile is wide ( $\beta$  is small), the sign of the interactions is determined by  $\cos(k_c x_{ij})$ , which is what we expect directly from Eq. (2.36) since  $|\hat{\psi}(k)|^2 \sim \delta(k - k_c)$  for a wide pumping spot.

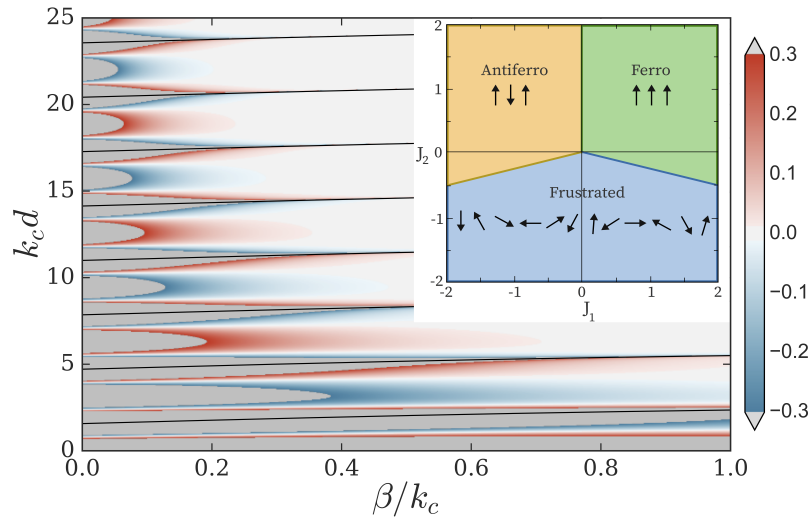


Fig. 2.4 The contour plot shows the frustration parameter  $J_2/J_1$  as a function of  $k_c d$  and  $\beta/k_c$ , where  $k_c$  is the polariton wave vector,  $\beta$  is the width of the polariton spot,  $d$  is the distance between the two adjacent spots. The coupling strengths  $J_1$  and  $J_2$  are calculated from Eq. (2.39) for the distances  $d$  and  $2d$ , respectively. Solid black lines show lines of the sign change for  $J_1$ . The inset shows the different regimes of the XY model on  $J_2 - J_1$  plane: ferromagnetic, antiferromagnetic and frustrated.

Now we consider a linear periodic chain of  $\ell$  equidistant polariton condensates separated by  $x_{ij} = d$ . This chain can be created experimentally by pumping condensates around a circle [86, 135]. The corresponding XY model takes form  $H = -J_1 \sum_i \mathbf{s}_i \cdot \mathbf{s}_{i+1} - J_2 \sum_i \mathbf{s}_i \cdot \mathbf{s}_{i+2}$ , where the sum is over all  $\ell$  condensates with periodic boundary conditions. In case of  $J_2 = 0$  the model is integrable [136], whereas for  $J_2 \neq 0$  the exact solutions were found for a limited set of values of  $J_2/J_1$ . Frustrated phases of the classical, as well as quantum spin-1/2 system with nearest-neighbour and next-nearest-neighbour isotropic exchange known as the Majumdar-Ghosh Hamiltonian, have been extensively studied [137–139]. Classically, three regimes were identified for  $\ell \rightarrow \infty$ : ferromagnetic for  $J_1 > 0, J_2 > -J_1/4$ , antiferromagnetic

for  $J_1 < 0, J_2 > J_1/4$  and frustrated (spiral) phase otherwise, as the inset to Figure 2.4 illustrates. In frustrated phase the pitch angle of the spiral is  $\phi = \cos^{-1}(-J_1/4J_2)$  [139]. Quantum fluctuations lower the ground state and shift the phase transition from spin liquid state at  $J_2 = 0$  to a dimerized regime with a gap to the excited states at  $J_2 = 0.2411J_1$ ; the transition from antiferromagnetic phase to dimerized singlets takes place at  $J_2 = J_1/2$  [137, 138]. Consequently, we elucidate if a polariton linear periodic chain can reproduce the characteristics of classical regimes and what new physics arises due to nonlinear interactions of polaritons.

Based on the derived above expression for the coupling strengths in Eq. (2.39), we plot the frustration parameter  $J_2/J_1$  in Figure 2.4. As evident, the frustration parameters from  $-0.3$  to  $0.3$  can be achieved for the feasible values of polariton spot widths and wave vectors. Hence, we insinuate that all three of the classical regimes that are depicted in the inset of the Figure 2.4 should be accessible in a linear periodic chain unless the hot exciton reservoirs,  $\mathcal{R}$ , of the polariton spots shield the interactions between the next-nearest-neighbours.

To verify our analytical results, we consider twelve condensates in a linear periodic chain and numerically integrate the cGLE for several distances in the presence of white noise. For each configuration, we start from 100 random initial distribution of phases to find the ground state configurations. Figure 2.5 identifies ferromagnetic, antiferromagnetic and spiral spin-wave phases that represent the ground states of the one-dimensional XY model. The polariton densities (solid blue lines) are displaced from the pumping profiles (solid green lines) in the case of the spin-wave state, which is depicted in Figure 2.5(c). In addition, this state has a distinguished velocity pattern (red dashed lines) compared to the other two classic states in Figure 2.5(a,b).

### 2.3.2 Spin liquid states for equidistant polariton condensates along the circle

Here we consider the full 2D system of Eqs. (2.1, 2.2). The same classical phases are obtained for pumping intensities just above the threshold. As the pumping intensity increases, the nonlinearity of the system destabilises the frustrated state and produces spin fluctuations as illustrated in Figure 2.6(a-c). The formation of a non-stationary spin-wave can probably be related to a spin liquid (for review of spin liquids see [140, 141]). Direct observation of liquid spin states in experiments would require time-resolved measurements on time scales challenging with current experimental configurations. Figure 2.6(d-f) demonstrates a non-stationary state of two spin waves of different periods with respect to the condensates

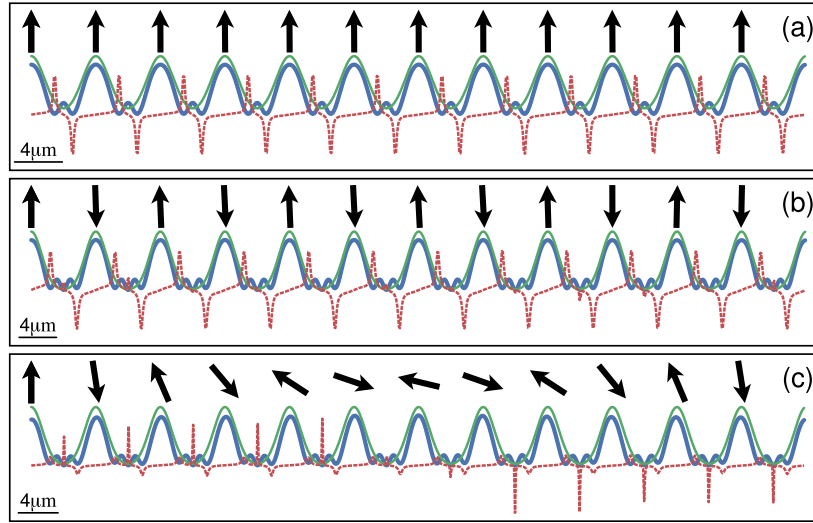


Fig. 2.5 Polariton densities (solid blue line) and velocities (dashed red lines) are shown for twelve condensates obtained by numerical integration of one-dimensional cGLE with periodical boundary conditions. Pumping profiles are shown with solid green lines. Panel (a) shows the ferromagnetic state, (b) corresponds to the antiferromagnetic state with  $\pi$  phase difference between the adjacent sites, and panel (c) shows the frustrated state. The distances between the nearest condensates are  $d = 5.4\mu m$ ,  $d = 6.9\mu m$ , and  $d = 6.5\mu m$  for (a), (b), and (c), respectively.

across the circle. The spectral weights at a fixed time in Figure 2.6(b,e) reflect the symmetry of the lattice.

Non-stationary spin-wave states and, perhaps, spin liquid states can be detected in the momentum- and energy-resolved photoluminescence spectrum, which can be directly measured in the far-field. Figure 2.7 shows the spectral weight

$$I(\omega, \mathbf{k}) = \left| \iint \Psi(\mathbf{r}, t) \exp[-i\mathbf{k} \cdot \mathbf{r} - i\omega t] dt d\mathbf{r} \right|^2,$$

as a function of  $(\omega, k_x, k_y = 0)$ . In the case of the non-stationary state depicted in Figure 2.6(a-c), spins reorient themselves randomly with time, cycling through different microstates whose density distributions are shown in Figure 2.7(a). The state shown in Figure 2.6(d-f) is a more periodic state which is proved by the energy spectrum in Figure 2.7(b), showing several well-separated energy levels. In contrast, the stationary state would show only one energy level [142, 143].

Frustrated states that we found in the linear periodic chain of polariton graphs correspond to superfluids at nonzero quasi-momentum and exhibit nontrivial long-range phase order. The spiral phases spontaneously break time-reversal symmetry by generating bosonic currents

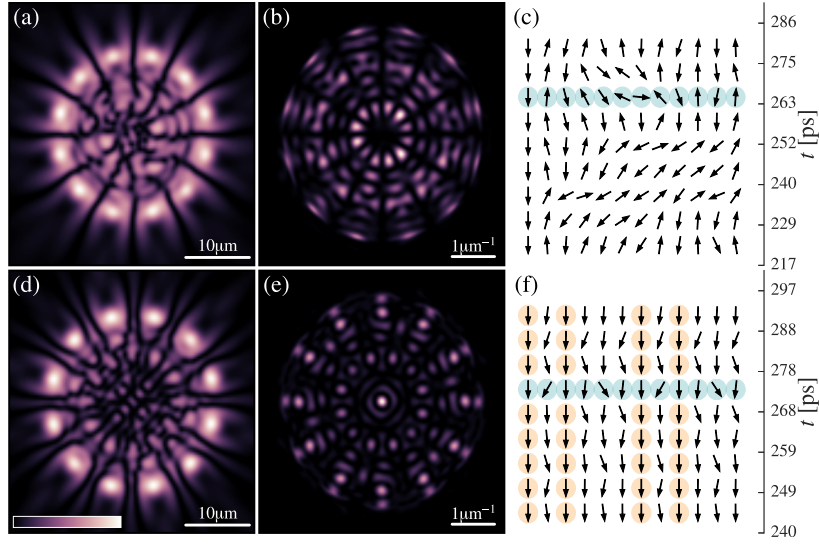


Fig. 2.6 Density snapshots (left panel) and the far-field emission (central panel) are shown at a fixed time for twelve condensates arranged in a circle obtained by numerical integration of Eqs. (2.1, 2.2). The right panels show the evolution of the phases (relative to one fixed spin) between adjacent spots with  $12ps$  (c) and  $10ps$  (f) time steps between spin configurations. The highlighted with blue circles spin configurations in (c) and (f) correspond to the density profiles (a,d) and the far-field emissions (b,e). The stable spins of the spots are marked with orange circles in (c,f). The distances between the adjacent sites are  $6.4\mu m$  (a-c) and  $7\mu m$  (d-f). Other simulation parameters can be found in Appendix A.

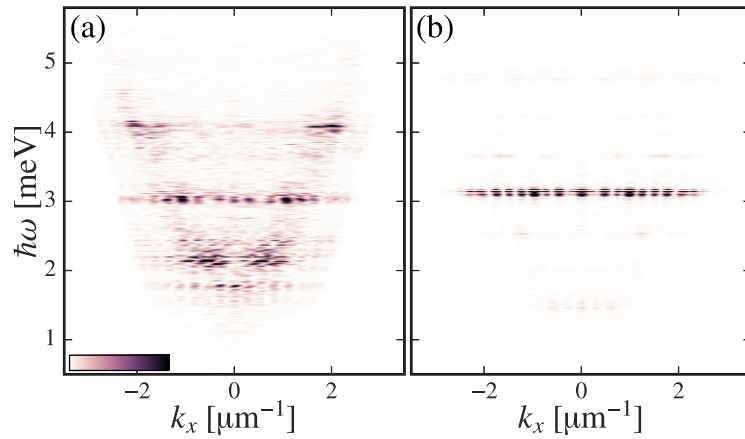


Fig. 2.7 The spectral weight plots are shown for  $k_y = 0$  of the two-dimensional non-stationary spin wave states from Figure 2.6(a-c) in (a) and from Figure 2.6(d-f) in (b). Both plots are saturated at the same level of 0.2 to make the energy levels more visible and to provide an easier comparison between the states

around the sites of polariton graphs. The observations of such spin waves open a new path for studying novel states of matter. One of such states, namely the giant vortices, can be formed by controlling the distances between the condensates and the number of condensates along the circle, as we discuss next.

## 2.4 Giant vortices of controlled multiplicity in polariton lattices

Quantised vortices are fundamental topological objects that play an important role in diverse areas ranging from superfluids and superconductors to high energy physics and optics. They exist in classical matter fields described by a classical smooth complex-valued field  $\Psi = \sqrt{\rho} \exp[iS]$  signifying the points in 2D or lines in 3D, where the amplitude of  $\psi$  becomes zero and the phase  $S$  winds around in multiples of  $2\pi$ . The winding of a quantised vortex, also called topological charge, is the integer defined as the integral  $k = (m/2\pi\hbar) \oint_C \nabla S \cdot d\mathbf{l}$ , where  $C$  is the closed contour around the zero of the amplitude. Although the formation, structure, dynamics, and turbulence of quantised vortices have been the subjects of intense research [144, 145], many fundamental aspects of the vortex dynamics are still not fully understood [146–148]. Vortex motions, even in the simplest configurations, such as the advection of a single vortex of unit charge by a constant super flow, have challenged the scientific community [149].

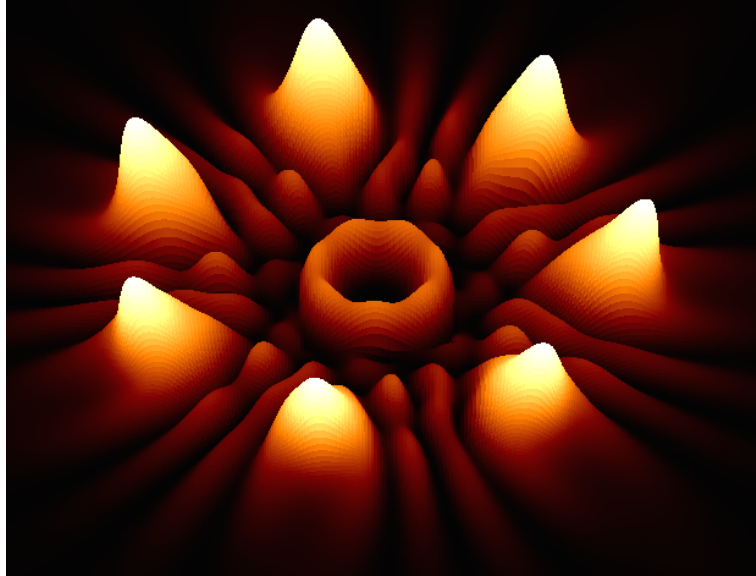


Fig. 2.8 A schematic of the density profile of an heptagon of polariton condensates with antiferromagnetic coupling between its vertices is shown. Within the inner ring visible at the centre of the heptagon, a sinkhole giant vortex occurs that is fully contained within the inner ring.

In this Section, crossbreeds of the discrete vortex solitons and giant vortices are theoretically proposed and experimentally realised in a graph of polariton condensates. The unprecedented control over the properties of these vortices, including the winding, density

and velocity profiles, is achieved. Unlike discrete vortex solitons in purely optical systems or photonic crystals, where the phase winding comes from the laser, giant vortices can form under non-resonant pumping in polariton graphs. In this respect, they are closer to vortices in atomic condensates but do not require any external rotation, and even multiply-charged vortices are fully stabilised by the polariton outflow from the pumping sites. Also, unlike vortices in ultra-cold atomic BECs, polariton giant vortices generate spiral velocity profiles towards the vortex centre. Each node of polariton graphs that are considered here occupies the vertex of a regular polygon. Figure 2.8 shows a schematic of the expected density profile of an heptagon of polariton condensates. The coupling between the condensates is such that a giant vortex is formed in the centre of the polygon.

In a polariton graph, relative phases are chosen by stimulated relaxation of polaritons to the configuration with the highest overall occupation. The measurement of the condensate phase is always made with respect to a reference phase; that is, only phase differences are measurable of the system. As we discussed earlier in this Chapter, the phase configuration with the highest polariton occupancy of  $N$  spatially separated condensates can correspond to the minimum of the XY Hamiltonian:  $H_{XY} = -\sum J_{ij} \cos \theta_{ij}$ , where  $\theta_{ij}$  is the phase difference between two vertices. By varying the pumping intensity and the distances between sites, one can control the sign and strength of the coupling. By arranging an odd number of condensates along the circle with antiferromagnetic interactions, frustration is created: the spins can no longer alternate their direction and are forced to acquire non-trivial phase winding patterns. In the simplest case of three condensates, and for an element of a triangular lattice, phase differences between vertices of an equilateral triangle are measured to be  $2\pi/3$  [86, 131].

In the following, we generalise the above discussion and analyse the spin configurations obtained by minimising the XY Hamiltonian for  $N$  polariton condensates arranged at the vertices of a regular polygon. When only nearest neighbour interactions are taken into account, the XY Hamiltonian becomes  $H_{XY} = -J \sum_{i=1}^N \cos \theta_{i+1}$ , where the summation is cyclic. For a regular polygon, the XY Hamiltonian can be written as  $H_{XY} = -JN \cos(2\pi k/N)$ , where  $k$  is an integer. If  $J > 0$ , the global minimum is at  $\theta_{i+1} = 0$ ; if  $J < 0$  and  $N$  is even, the global minimum is achieved by  $\theta_{i+1} = \pi$ ; finally if  $J < 0$  and  $N$  is odd, the frustration described above gives rise to a non-trivial phase winding with  $\theta_{i+1} = \pm\pi(N-1)/N$ . The latter case corresponds to the formation of the central vortex with winding  $k = \pm(N-1)/2$ . Therefore, by engineering antiferromagnetic coupling between nearest-neighbour condensates at the vertices of an odd-sided regular polygon, we build frustration into the system and force it to form a central vortex of multiplicity that relates to the number of vertices  $N$ . As the central region contains particle fluxes coming from the condensates, these vortices exist on a nonzero density background, which allows for the full manifestation of their nonlinear nature.

*Condensates along the circle with ferromagnetic interactions.* The spin configurations are experimentally accessed by injecting equidistant polariton condensates in a circle. From the XY Hamiltonian minimisation perspective, the trivial spin configuration occurs in the case of ferromagnetic couplings when the condensates lock in phase. For an even and an odd number of vertices, we illustrate the all-in-phase configuration by tuning the nearest neighbour distances to obtain ferromagnetic couplings at the condensation threshold. Figure 2.9(a,b) shows experimental results of real-space photoluminescence intensity for an octagon and a nonagon of polariton condensates at condensation threshold. The ferromagnetic coupling is distinguishable by an odd number of fringes between vertices and their symmetry. Local maxima of the photoluminescence intensity are observed in the centre of both polygons, indicating the absence of a vortex.

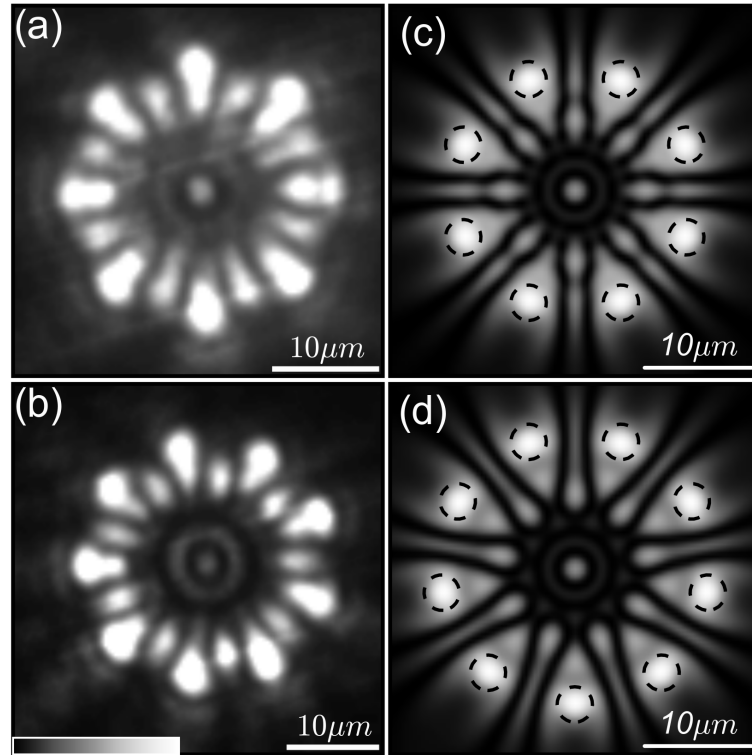


Fig. 2.9 Normalised real-space photoluminescence intensity at condensation threshold for an octagon and a nonagon with ferromagnetic couplings between nearest neighbours are shown in a false-grey scale. The first column (a,b) shows the experimental results and the second column (c,d) shows the numerical simulations of the density profiles; (a) is saturated at 0.5, and (b) is saturated at 0.4 to increase the visibility of the low-intensity fringes between the vertices. In (c,d) the centres of the pumping spots are shown by the black dashed circles. The parameters of the numerical simulations are listed in Appendix A.

The phase dynamics of polariton condensates is numerically simulated across regular polygons using the cGLE coupled to a rate equation for the hot exciton reservoir, Eqs. (2.1, 2.2). The experimental excitation conditions for the pumping profile are mimicked using  $N$  Gaussian functions:  $P(\mathbf{r}, t) = \sum_{i=1}^N P_0 \exp(-\alpha |\mathbf{r} - \mathbf{r}_i|^2)$  centred at the positions  $\mathbf{r}_i$ . Figure 2.9(c,d) shows the result of the numerical simulations that are in good agreement with the experimental observations, where the centres of the pumping spots are annotated by black dashed circles on the theoretical density profiles.

*Condensates along the circle with antiferromagnetic interactions.* For even numbers of condensates arranged at the vertices of the regular polygon with antiferromagnetic couplings between nearest neighbours ( $J < 0$ ), the condensates will simply lock in anti-phase. The most exciting spin configuration is observed for an odd number of condensates. In this case, frustration gives rise to non-trivial phase windings that correspond to the formation of multiply-charged vortices. Figure 2.10 summarises the experimental results and numerical simulations for seven (top row), nine (middle row), and eleven (bottom row) condensates, respectively. The first column shows the experimental results of the real-space photoluminescence intensity. The antiferromagnetic coupling is imposed by tuning the distance between nearest neighbours and is distinguishable by the even number of fringes between vertices. In all three cases, the photoluminescence intensity depletion is observed at the centre of polygons, indicative of a central vortex.

To investigate polariton flows in these polygons, the Fourier-spaces of the photoluminescence intensities are presented in the second column of Figure 2.10. We do not observe the minima of the photoluminescence intensity that cross the Fourier-space centre. The absence of nodal radial lines shows a continuum of wave vectors' distribution versus the azimuthal angle of the Fourier-space, which is a further indication of the presence of a central vortex. In the third column of Figure 2.10, we further visualise the presence of core vortices by plotting the velocity streamlines. In addition, zeros of the real and imaginary parts of the numerically simulated polariton wave functions show the velocity circulation around the centre of the polygons. The presence of a central vortex displaces a significant amount of polariton fluid away from the centre and forces the fluid to circulate along a spiral trajectory. In principle, by tuning the geometry and the profile of the excitation density, we can effectively control the amount of the circulating fluid, its tangential and inward radial velocities and the volume of the displaced fluid from the central region. Such control over the dynamics of giant vortices may offer a unique test-bed for “Analogue” gravity studies.

These experimental observations and numerical simulations provide strong evidence for the presence of multiply-charged vortices of winding numbers  $k = \pm 3, \pm 4$  and  $\pm 5$  for the case of negative couplings in the heptagon, nonagon and hendecagon, respectively. Note

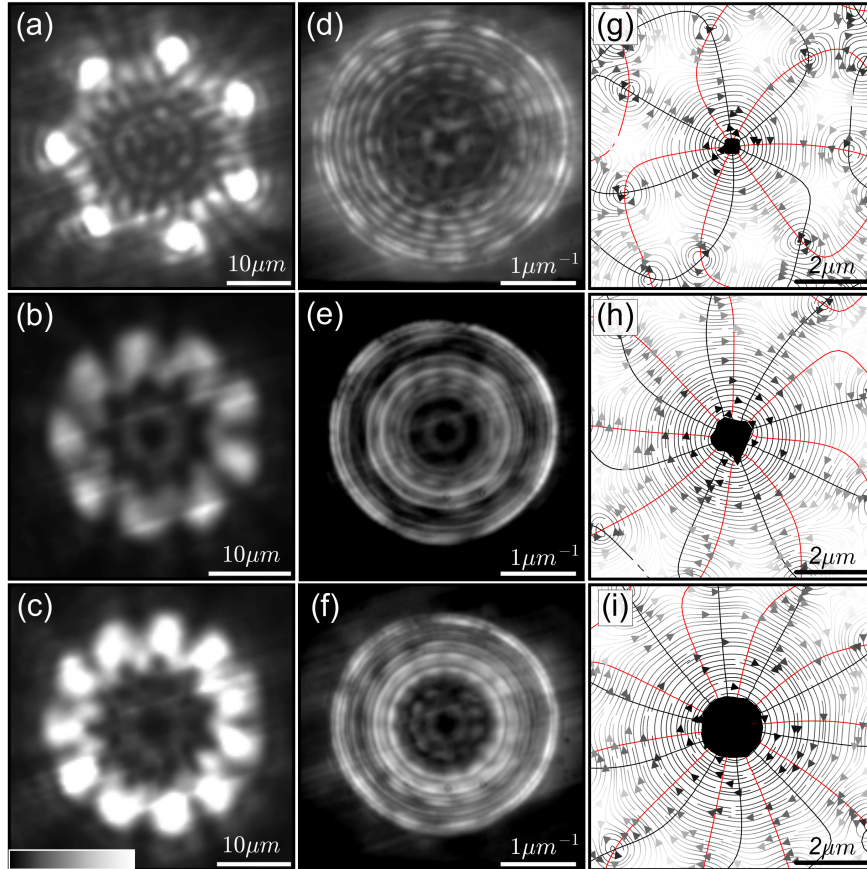


Fig. 2.10 The first column (a-c) shows the normalised real-space photoluminescence intensity at condensation threshold for a heptagon, nonagon and a hendecagon with antiferromagnetic couplings between nearest neighbours in a false-greyscale. The second column (d-f) shows the corresponding normalised photoluminescence intensity of the two-dimensional Fourier-space at condensation threshold for the polygons of (a-c). The absence of nodal radial lines indicates the presence of a central vortex. The third column (g-i) shows the velocity stream-lines and the zeros of the real and imaginary parts of the wave functions with solid red and black lines respectively for the polygons of (a-c). The black filled area in (g-i) indicates the areas where the polariton density is less than  $10^{-5}$  of its maximum. The parameters of the numerical simulations are listed in Appendix A.

that in these configurations, we do not externally imprint the phases [150–154]. Instead, we control the dynamics of the coupling between condensates, which leads to the spontaneous formation of giant vortices.

## 2.5 Conclusions

Spatially coupled polariton condensates can represent different oscillator models, including the Kuramoto, Sakaguchi-Kuramoto, Lang-Kobayashi and Stuart-Landau models for different experimental parameters. Some of these parameters are easier to adjust, e.g. exciton-polariton interactions, while others are harder, e.g. polariton lifetime. This apparent flexibility of a polariton system is both a blessing and a curse. On one side, it allows us to observe fascinating nonlinear dynamics phenomena with exotic spin states and topological giant vortices discussed in this Chapter. On the other side, such flexibility makes it harder to isolate a particular optimisation model to address with polariton networks and, consequently, limits the optimisation accuracy of any objective function. Nevertheless, we confirm the possibility of achieving the XY model's ground states for simple configurations of condensates in a circle. Spatially coupled polariton condensates may require an instrumental calibration of experimental parameters for addressing a given optimisation problem, even for nearest neighbour interactions. In addition, one needs to control the couplings beyond nearest neighbours for arbitrary graphs of polariton condensates to tackle non-trivial discrete and continuous optimisation problems. We focus on the optimisation perspectives of non-equilibrium condensates in the next Chapter.

## **Chapter 3**

### **Gain-dissipative simulator with non-equilibrium condensates**

### 3.1 Signatures of minimising the XY model on simple graphs

A large variety of computationally intractable systems can be mapped into certain universal classical spin models characterised by the given degrees of freedom, i.e. spins, by their interactions, i.e. couplings, and by the associated cost function, i.e. Hamiltonian [17]. As a result, there has been much interest in the possibility of devising a physical system, an analogue simulator, to solve such spin models:  $n$ -vector models of classical unit vector spins  $\mathbf{s}_i$  with the Hamiltonian  $H = -\sum_{ij} J_{ij} \mathbf{s}_i \cdot \mathbf{s}_j$ , where  $J_{ij}$  are real numbers specifying the coupling strengths between the sites labelled  $i$  and  $j$  [92]. The Ising model corresponds to the  $n = 1$  case of the  $n$ -vector model, with  $\mathbf{s}_i \in \{-1, 1\}$ . For  $n = 2$  the  $n$ -vector Hamiltonian becomes  $H_{XY} = -\sum_{ij} J_{ij} \cos(\theta_i - \theta_j)$ , where we have parameterised unit planar vectors using the polar coordinates  $\mathbf{s}_i = (\cos \theta_i, \sin \theta_i)$ . As it was discussed in the Introduction, these spin Hamiltonians belong to the  $\text{NP-hard}$  complexity class.

With increasing excitation power, polariton condensation occurs at the state with the phase configuration that carries the highest polariton occupation. This is due to the condensate bosonic nature: the quasi-particles probability to relax in a particular state grows with the population of that state. A macroscopic coherent state is formed at the condensation threshold and can be described by the wave function  $\psi_g$ . To the leading order,  $\psi_g$  can be written as a superposition of the wavefunctions  $\psi_j$  at the sites  $\mathbf{x}_j$  with phase  $\theta_j$ ; that is  $\psi_g \approx \sum_j \psi_j \exp[i\theta_j]$ . Under the conditions discussed in Section 2.1, the system of an arbitrary polariton graph can condense into the minima of the XY Hamiltonian  $H_{XY} = -\sum J_{ij} \cos \theta_{ij}$ , where  $\theta_{ij}$  is the phase difference between two sites. The bottom-up approach for searching the global minimum of the XY Hamiltonian is achievable within the line width of the corresponding state. This approach is different from classical and quantum annealing techniques, where the global minimum is reached through transitions over metastable excited states (local minima).

In Section 2.2 we established analytically that the coupling between two equally-pumped spots could be either in-phase with zero phase difference or anti-phase with a  $\pi$  phase difference. In general, the coupling strength and the relative phase depend on the density of the sites  $i$  and  $j$ , the distance between them,  $d_{ij} = |\mathbf{x}_i - \mathbf{x}_j|$ , and the outflow condensate wavenumber  $k_c$ , which under non-resonant optical excitation depends on the pumping intensity and profile. The state with the phase configuration that carries the highest number of particles corresponds to the solution that minimises the XY Hamiltonian. Experimentally, phase differences can be verified for more complex geometries through interferometry and Fourier-space analysis. In Figure 3.1(a), we plot the density of a polariton graph. The interactions are either ferromagnetic or antiferromagnetic depending on the separation distance between the vertices and the outflow wave vector. Polaritons have a local phase  $\theta_i$  at each vertex  $\mathbf{x}_i$  of the graph (always with respect to a reference vertex), which we map to a

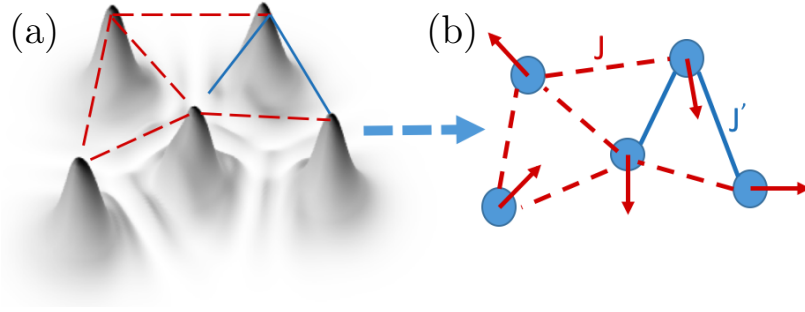


Fig. 3.1 (a) A schematic of the condensate density map is shown for a five-vertex polariton graph. Depending on the separation distance between the sites and the outflow wave vector, the interactions between sites can be ferromagnetic (solid-blue lines) or antiferromagnetic (dashed-red lines). At each vertex  $\mathbf{x}_i$  of the graph polaritons have a local phase  $\theta_i$  that is mapped to a classical vector spin  $\mathbf{s}_i = (\cos \theta_i, \sin \theta_i)$ . (b) The vertices (blue solid-circles) and edges of the polariton density map depicted in (a), showing the sign of the coupling and the spin vector  $\mathbf{s}_i$  of each vertex.

classical vector spin  $\mathbf{s}_i = (\cos \theta_i, \sin \theta_i)$ . In Figure 3.1(b), we show spin vectors  $\mathbf{s}_i$  that could minimise the XY Hamiltonian of the graph given in Figure 3.1(a).

Following the theoretical investigation of 1D periodic polariton chains in Section 2.3, here we theoretically describe and experimentally address several lattice configurations that may resemble the minimisation of the XY Hamiltonian.

*Polariton chain.* We first consider a linear chain of polariton condensates with equal spacing  $d = d_{ij}$  between neighbours. For a given wave vector, the coupling strength  $J_{ij}$  between the neighbour sites oscillates between negative and positive values with increasing separation distance. We approximate the switching of the coupling sign with  $\cos(k_c d + \phi)$ , where  $\phi$  is fixed by the system parameters. In the steady-state excitation regime, we can calculate the maximum particle number of a polariton dyad as a function of the separation distance  $d$  by numerically integrating the cGLE to find the solutions of Eqs. (2.1, 2.2) that maximise  $N$  for a given pumping profile  $p(\mathbf{r}) = p_0[\exp(-\alpha|\mathbf{r} - \mathbf{d}/2|^2) + \exp(-\alpha|\mathbf{r} + \mathbf{d}/2|^2)]$  of a characteristic width  $\alpha$ ; the results are shown in Figure 3.2(a). The relative phases that realise the maximum particle number switch periodically between 0 and  $\pi$  with the period  $2\pi/k_c$  as shown by superimposing the function  $\cos(k_c d + \phi)$  in Figure 3.2(a). Figure 3.2(b-e) shows the real-space photoluminescence intensity of the linear chain condensate for several lattice constants. The relative phase difference realised between neighbours in the chain is either  $\pi$  or zero. The patterns are distinguishable by the number of fringes (density maxima) between the sites: zero or even for antiferromagnetic and odd for ferromagnetic coupling. In Figure 3.2(a), we have annotated the abscissa with solid circles for each of the two separation

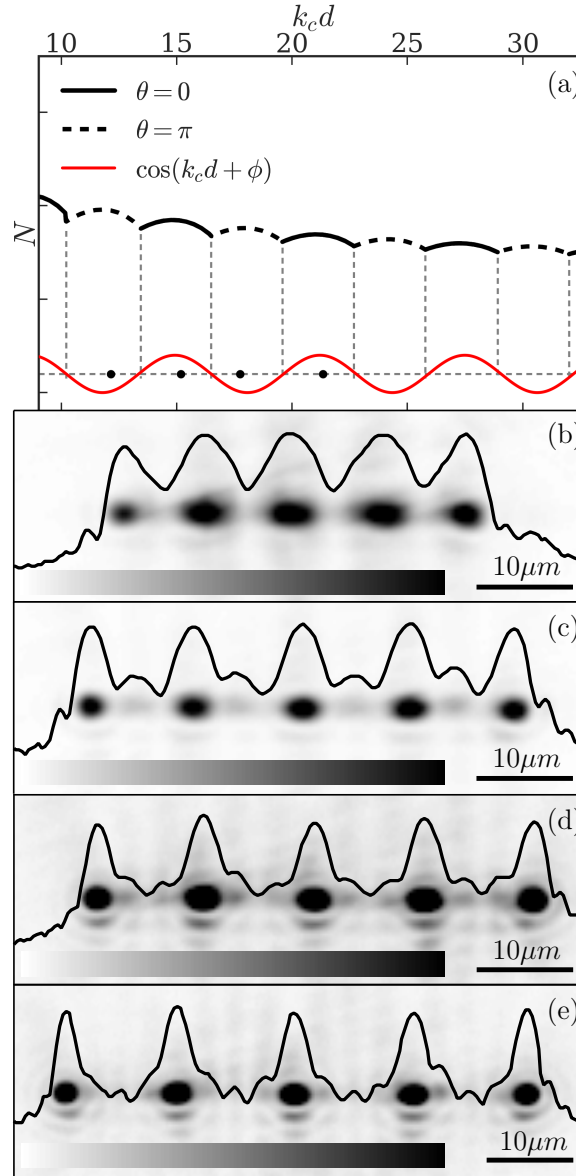


Fig. 3.2 (a) The maximum number of particles,  $N$ , of a polariton condensate dyad formed under incoherent pumping of two nodes as the function of the product  $k_c d$  between the nodes obtained by numerical integration of the cGLE for a fixed  $k_c$  starting with random initial conditions and choosing the realisation that maximises  $N$ . The solid black line corresponds to the maximum number of particles in the in-phase ferromagnetic configuration and the dashed black line to the antiferromagnetic configuration with  $\pi$ -phase difference. The switching occurs with the periodicity  $2\pi/k_c$  as the superimposed graph of  $\cos(k_c d + \phi)$  illustrates in red, where  $\phi \approx 225^\circ$ . (b-e) Experimental realisation of the chain of five equidistant polariton nodes with lattice constants of  $\sim 9 \mu m$ ,  $\sim 11.1 \mu m$ ,  $\sim 11.4 \mu m$ , and  $\sim 13.4 \mu m$  respectively. The false-grey scale images show the normalised real-space photoluminescence intensity. The corresponding  $k_c d$  are shown by solid circles in (a).

distances from which the expected sign of coupling is depicted, showing good agreement with the experiment.

*Square lattice.* We consider a geometry of  $N$  incoherently pumped equidistant polariton vertices positioned on the circumference of a circle. For equal separation distances  $d = d_{ij}$  between adjacent sites, the XY Hamiltonian becomes  $H_{XY} = -J \sum_{i=1}^N \cos(\theta_{i,i+1})$ , where  $J = J_{ij}$ , the summation is cyclic and we took into account only nearest neighbour interactions. If  $J$  is positive, then all sites lock in-phase with  $\theta_{i,i+1} = 0$ . If  $J$  is negative, the minimum of  $H_{XY}$  occurs for  $\theta_{i,i+1} = \pm\pi$ , when  $N$  is even and for  $\theta_{i,i+1} = \pm\pi(N-1)/N$  when  $N$  is odd ( $N > 1$ ). For the odd number of vertices, therefore, the configurations bring about topological vortices of winding  $\pm(N-1)/2$ . These are spontaneously formed discrete vortex solitons, whose properties we discussed in Chapter 2.4.

We experimentally access these regimes through incoherent injection of polaritons at the vertices of a square. Figure 3.3(a,b,c) shows the experimental and numerical results for lattice constants that lead to antiferromagnetic, ferromagnetic and the next antiferromagnetic coupling respectively. Similar to the polariton chain, the type of coupling is distinguishable by the number and symmetry of fringes between the vertices.

*90° compass model.* Apart from the trivial all ferromagnetic or antiferromagnetic coupling configurations in a square geometry, we consider the compass models where the coupling between the internal spin components is inherently directionally dependent. Such compass-type coupling appears in various physical systems, where the interactions are sensitive to the spatial orientation of the involved orbitals. In polariton graphs, the compass models with direction-dependent coupling or glassy spin models with random couplings can be realised by changing the pumping intensity and preserving the square geometry or by tuning the separation distances so that each vertex has one ferromagnetic and one antiferromagnetic coupling with its nearest neighbours. In Figure 3.3(c), we have realised the 90° compass model, where each vertex has one ferromagnetic and one antiferromagnetic coupling with its neighbours.

*Triangular lattice.* The XY Hamiltonian has been simulated on a triangular lattice of atomic condensates, discovering a variety of magnetic phases and frustrated spin configurations [40]. For an antiferromagnetically coupled polariton triad, the energy flux that minimises the XY Hamiltonian corresponds to  $\pm 1$  winding ( $2\pi/3$  phase difference between the condensates) [131]. Here, we experimentally realise an equidistant triangular lattice of two lattice cells (rhombus configuration). Figure 3.4(a-c) shows the experimental results and numerical simulations for a rhombus with lattice constants that lead to antiferromagnetic, ferromagnetic and the next antiferromagnetic coupling, respectively. In the case of ferromagnetic coupling between nearest neighbours and neglecting opposite neighbours in-

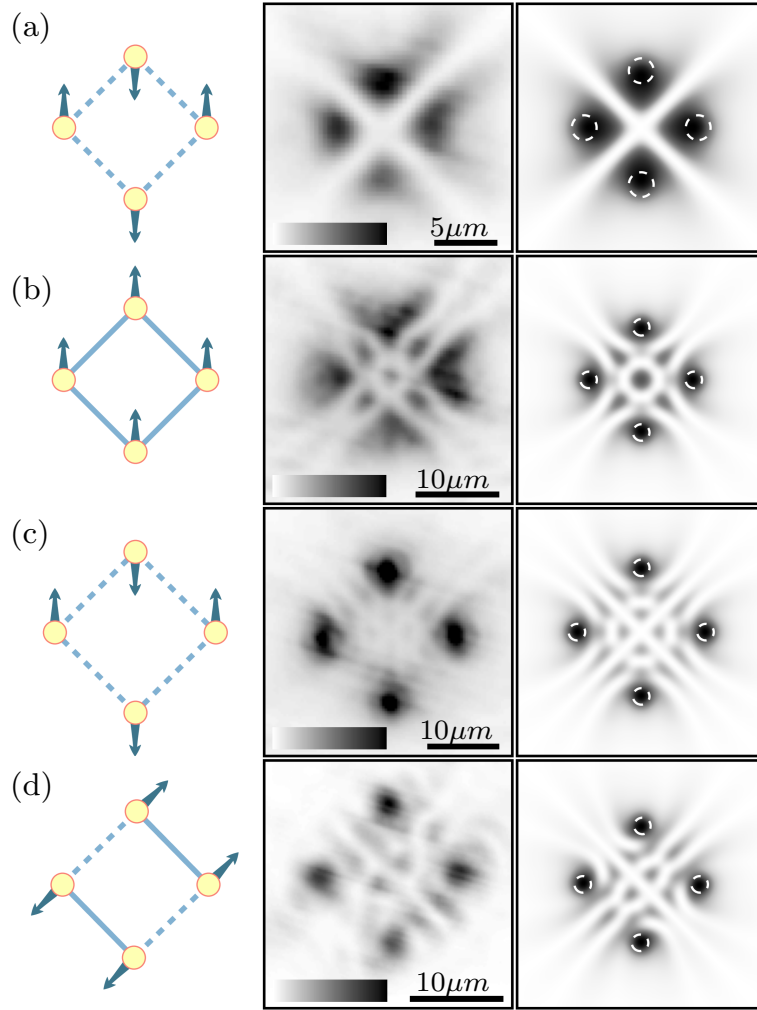


Fig. 3.3 Spin configurations are shown for square polariton lattices. The diagrams of the numerically calculated spins vectors at the pumping sites  $\mathbf{s}_i = (\cos \theta_i, \sin \theta_i)$ , the real-space energy tomography of the experimental realisations, and the averaged condensate densities of the numerically simulated condensate wavefunctions for several realisations are shown on the left, central and right columns respectively. Solid and dashed blue lines on the spin vector diagrams (left column) indicate ferromagnetic and antiferromagnetic coupling, respectively. The false-grey scale images of the middle column show the normalised real-space photoluminescence intensity at the energy of the condensate at the condensation threshold; (c) is saturated at 0.5 to increase the visibility of the low-intensity fringes between the vertices. The configurations shown are some elementary building blocks of square lattices such as (a,c) antiferromagnetic, (b) ferromagnetic, (d) 90°-compass. The centres of the pumping spots are shown by white dashed circles on the numerical density profiles (right column). The parameters of the numerical simulations of Eqs. (2.1, 2.2) are listed in the Appendix A.

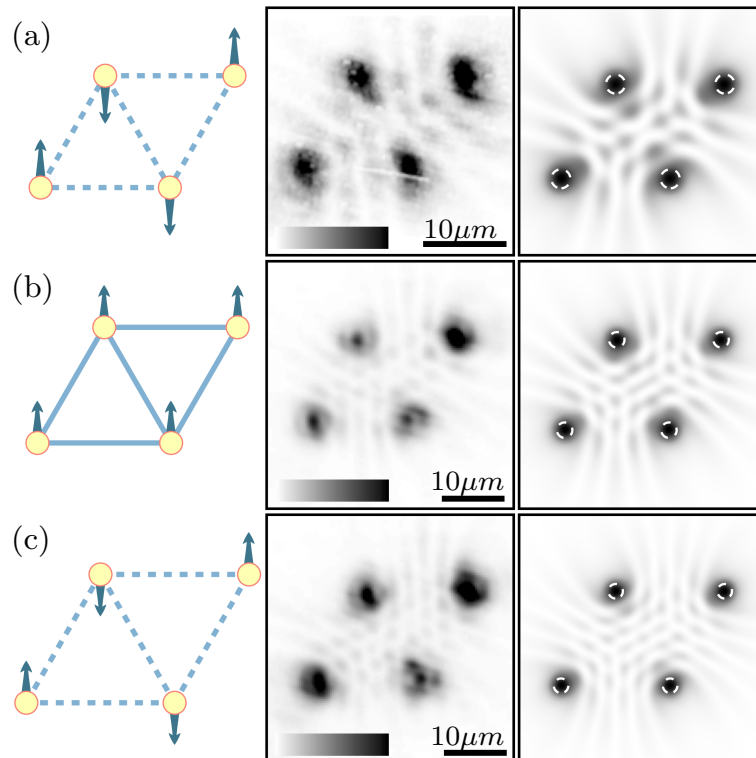


Fig. 3.4 Spin configurations are shown for the diamond-shaped polariton lattices. The columns of images are as described in the caption to Figure 3.3. The configurations shown are some elementary building blocks of triangular lattices such as (a,c) antiferromagnetic and (b) ferromagnetic rhombuses. The false-grey scale images of the middle column show the normalised real-space photoluminescence intensity at the energy of the condensate at condensation threshold saturated at 0.5 to increase the visibility of the low-intensity fringes between the vertices.

interactions across the long diagonal axis of the rhombus, the XY Hamiltonian is minimised at  $H_{XY} \sim -5J$  when all polariton sites lock in phase. Similarly, in the case of antiferromagnetic coupling between nearest neighbours, the XY Hamiltonian is minimised at  $H_{XY} \sim -3J$  when there is  $\pm\pi$  phase difference between the outer edges of the rhombus. This configuration forces the rhombus in a frustrated state wherein opposite vertices have the same phase. This type of frustrated spin configuration is experimentally realised in Figure 3.4(a,c). These configurations belong to two different bands of antiferromagnetic regions separated by a ferromagnetic band, which are consistent with the alternating bands shown in Figure 3.2(a).

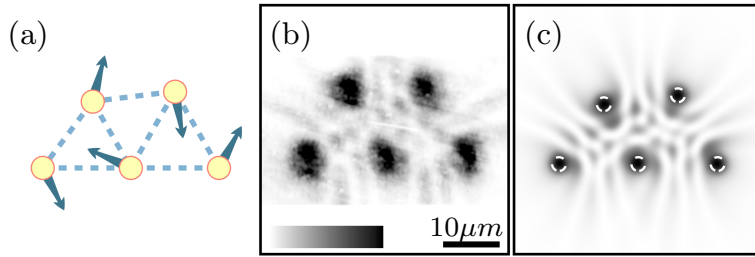


Fig. 3.5 Spin configurations are shown for a random polariton graph. The panels of images are as described in the caption to Figure 3.3. The false-grey scale image of the middle column show the normalised real-space photoluminescence intensity at the energy of the condensate at condensation threshold saturated at 0.5 to increase the visibility of the low intensity fringes between the vertices.

*Random polariton graph.* Finally, we test our platform on a disordered polariton graph of five vertices. We take a graph of three equidistant triangular unit cells for a lattice constant that leads to antiferromagnetic coupling and break the symmetry by slightly displacing one vertex in Figure 3.5. For the symmetric configuration of three equidistant triangular cells and considering only nearest neighbours interactions, the XY Hamiltonian is minimised at  $H_{XY} \sim -3.86J$  with an alternating winding around each cell slightly deviating from  $2\pi/3$  difference reported for a single equilateral triangle. Breaking the symmetry leads to a different phase distribution while maintaining the winding around each cell. The analysis of the fringes on the experimental image (with different rows of local maxima along the two long diagonals) shows that the symmetry is explicitly broken.

*Extended polariton lattices.* The photoluminescence intensities for a square lattice of 45 polariton condensates are shown in Figure 3.6(a-c) for several lattice constants. Figure 3.6(d-f) shows the corresponding normalised photoluminescence intensity of the two-dimensional Fourier-space. The contrast of the interference pattern observed in the Fourier-space images is indicative of the degree of coherence across the lattice. In particular, the dark centre surrounded by sharp intense “Bragg peaks” in Figure 3.6(a,c) indicates antiferromagnetic

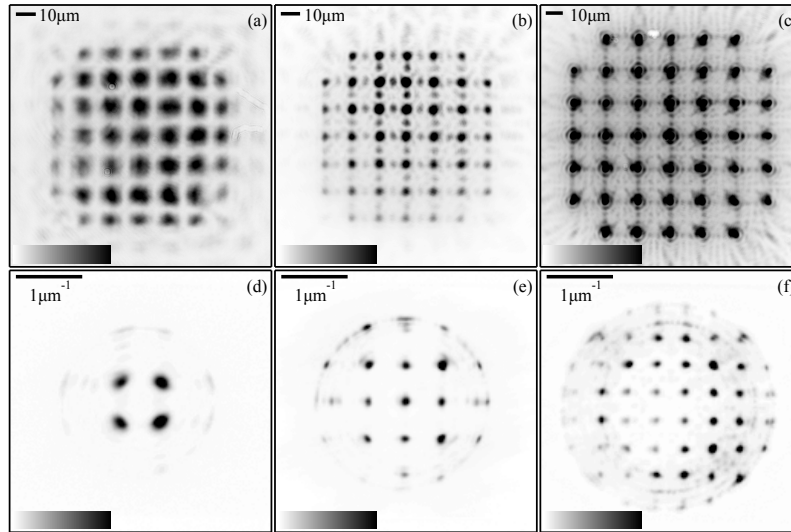


Fig. 3.6 The first row shows the normalised real-space photoluminescence intensity at the energy of the condensate at condensation threshold in a false-grey scale for (a,c) antiferromagnetic and (b) ferromagnetic configuration of 45 coherently coupled polariton condensates arranged at the vertices of a square lattice. The second row (d-f) shows the normalised photoluminescence intensity of the two-dimensional Fourier-space corresponding to the lattices of (a-c).

coupling, whereas a bright centre in the two-dimensional Fourier-space of Figure 3.6(b) indicates ferromagnetic coupling.

The optical approach of imprinting two-dimensional polariton lattices of arbitrary geometries and density profiles allows for tunable coupling strengths between vertices and can offer the potential for rapid scalability. For a few simple configurations of condensates, the observed phase configurations realise the ferromagnetic and antiferromagnetic configurations, which could be a signature of minimising the XY Hamiltonian. The obstacles to using such a polariton simulator to minimise an arbitrary XY coupling matrix and ways to overcome these obstacles are discussed in the remainder of this Chapter.

## 3.2 Density equilibration for minimising the XY model on arbitrary graphs

In gain-dissipative simulators, the ‘spin’ (or node or ‘bit’) of the simulators can be represented by the condensate phase at a particular spatial position [86, 89] or by the phase of coherent state generated in a laser cavity [155, 156], so by the phase of the so-called *coherent centre* (CC). Proposals to use gain-dissipative simulators to find the absolute minima of spin Hamiltonians suffer from a severe limitation. As we show below, the coupling strengths  $J_{ij}$  in such systems are modified by the occupations (number densities) of CCs  $i$  and  $j$ . However, the densities are not known a priori and could be different from one CC to another for a general matrix  $\mathbf{J}$ . In previous experimental realisations of gain-dissipative simulators, an explicit or implicit assumption was made about the smallness of coupling terms so that each laser or condensate is stabilised independently at the same steady-state amplitude [86, 155–158]. Such belief is justified only for the simplest structures of the coupling matrix, where all CCs are almost equally connected with about the same coupling strengths. The found solution for a more general matrix is bound to be either approximate or invalid.

Here we formulate the technological requirements for gain-dissipative platforms to be used as analogue Hamiltonian optimisers. A general framework is developed for the operation of gain-dissipative analogue simulators based on the Langevin gain-dissipative equations written for a set of CCs. We derive the rate equations for geometrically coupled CCs based on polariton or photon condensates. We show that by establishing a feedback connection between the gain mechanism and the CC density, we can drive the system to the coherent ground state of the XY model. The minimisers of this ground state will give the valid minimum for the externally provided coupling strengths.

The operation of gain-dissipative simulators consists of two stages: bosonic stimulation below the threshold and the coherence of operations at and above the threshold. As one increases the power of the gain mechanism (e.g. laser intensity), the nonlinear gain saturation stabilises the emergent coherent state. In this state, the total number of particles is maximised while losses are minimised. To derive the governing equations, one can describe each CC at a position  $\mathbf{r} = \mathbf{r}_i$  by a classical complex function  $\Psi_i(t)$ . Depending on the system, the couplings  $K_{ij}$  between CCs can have a different origin: they can be geometrically induced by the particle outflow from other CCs, as we have shown for polariton condensates earlier, or induced by the mutual injection rate between lasers [155, 159] or spatially separated condensates. Hence, we exploit the rate equations for the CCs valid for polariton condensates considered in the previous Chapter or photon condensates. These equations were derived in Section 2.1 starting from the mean-field description by the cGLE and integrating out spatial

degrees of freedom. The time evolution of the complex amplitudes describing individual condensates in the lattice can be written as

$$\frac{d\Psi_i}{dt} = \Psi_i(\gamma_i^{\text{inj}} - \gamma_c - (iU + \sigma)|\Psi_i|^2) + \sum_{j,j \neq i}^N \Delta_{ij}^{\text{inj}} K_{ij} \Psi_j + \text{noise}(t), \quad (3.1)$$

that is valid for polariton condensates under the following assumptions: negligible blue-shift due to interactions of polaritons with the reservoir, short lifetime sample, fast reservoir relaxation, near-threshold pumping intensity (the notations are taken from [20]). These equations can be recovered from Eq. (2.7) assuming  $g \ll 1$ ,  $\xi \gamma_i = \sigma$ ,  $\mathcal{C}_{ij} = \Delta_{ij}^{\text{inj}} K_{ij}$ , and denoting the polariton-polariton interactions as  $U$ . The noise term here represents the intrinsic system's fluctuations which become negligible at the threshold.

In other platforms such as the OPOs, the injection does not have to be symmetric between nodes. This asymmetry can be modelled by introducing a parameter  $\delta$  so that  $\Delta_{ij} = \gamma_i^{\text{inj}}(t) + (1 - \delta)\gamma_j^{\text{inj}}(t)$ , where  $\delta = 0$  for symmetrically coupled CCs. The Eq. (3.1) is the rate equation on the CCs coupled with the strengths  $\Delta_{ij} K_{ij}$ . By writing the coupling strength in such form, we separated the effect of what is not known a priori, e.g. pumping intensity or energy at the threshold, from  $K_{ij}$  that are known and for geometrically coupled condensates depend on the characteristics of the system, e.g. the distance between CCs  $i$  and  $j$ . To show how Eq. (3.1) leads to the XY model minimisation, we suppress noise and use the Madelung transformation  $\Psi_i = \sqrt{\rho_i} \exp[i\theta_i]$  to rewrite it in terms of the number densities  $\rho_i$  and phases  $\theta_i$ :

$$\frac{1}{2}\dot{\rho}_i(t) = (\gamma_i^{\text{inj}} - \gamma_c - \sigma\rho_i)\rho_i + \sum_{j,j \neq i} \Delta_{ij}^{\text{inj}} K_{ij} \sqrt{\rho_i \rho_j} \cos \theta_{ij}, \quad (3.2)$$

$$\dot{\theta}_i(t) = -U\rho_i - \sum_{j,j \neq i} \Delta_{ij}^{\text{inj}} K_{ij} \frac{\sqrt{\rho_j}}{\sqrt{\rho_i}} \sin \theta_{ij}, \quad (3.3)$$

where  $\theta_{ij} = \theta_i - \theta_j$ . The first term on the right-hand side of Eq. (3.3) tends to provide  $\theta_i$  with its own frequency of oscillations, whereas the second term couples the phases to each other and so tends to synchronise them. This synchronisation is analogous to the Kuramoto model discussed earlier in Section 2.1 allowing CCs to have constant (but not necessarily zero) phase differences. Phase synchronisation in such a system has been extensively studied, especially in the context of semiconductor laser arrays [160, 161]. To guarantee the XY model minimisation, one needs to ensure that the gain mechanism equalises all densities  $\rho_i$  at the near-threshold steady-state. Only under this condition does the second term on the right-hand side of Eq. (3.3) describe the gradient descent to the minimum of the XY model.

The earlier demonstrations of the XY model with laser systems and non-equilibrium condensates were based on the assumption that all lasers (condensates) have the same steady-state photon (particle) number [155, 160, 161]. Unfortunately, this assumption limits the problems such a framework can address to trivial ones where all CCs have an almost equal number of connections with nearly the same pumping rate. When phase synchronisation is achieved, the variations of CC densities imply that the steady-state configuration realises the minimum of the XY Hamiltonian with modified couplings  $\Delta_{ij}^{\text{inj}} K_{ij} \sqrt{\rho_j/\rho_i}$ , where  $\rho_i$  and  $\rho_j$  are not known a priori. To implement any couplings and connectivities, one needs to be able to control the pumping rate of individual CCs and bring all densities to the same value near the threshold so that the term  $\sqrt{\rho_j/\rho_i}$  is cancelled out. The operational principle of such a control mechanism is schematically illustrated in Figure 3.7(a). When a system is below the threshold at some  $t = t_1$ , all CCs are equally pumped. Depending on the node connectivity, the non-zero densities emerge at different rates for each CC as the pumping intensity increases and takes some of them above the specified threshold  $\rho = \rho_{\text{th}}$  as illustrated in Figure 3.7(a) for  $t = t_2$ . The pumping mechanism must be adjusted for each CC to enable the saturation at the same density: decreased for CCs with densities above the threshold and increased for CCs below the threshold. The feedback mechanism can be implemented via optical delay lines in a network of OPOs or by adjusting the injection via the SLM in polariton and photon condensates. The mathematical description of such a feedback mechanism is

$$\frac{d\gamma_i^{\text{inj}}}{dt} = \varepsilon(\rho_{\text{th}} - \rho_i), \quad (3.4)$$

where  $\varepsilon$  is a parameter that can be tuned to control the speed of approaching the threshold. The fixed point of Eqs. (3.2, 3.4) is

$$\rho_i = \rho_{\text{th}} = (\gamma_i^{\text{inj}} - \gamma_c + \sum_{j:j \neq i} \Delta_{ij}^{\text{inj}} K_{ij} \cos \theta_{ij}) / \sigma, \quad (3.5)$$

with the total particle number given by

$$\mathcal{N} = (\sum_i \gamma_i^{\text{inj}} - N\gamma_c + \sum_{i,j:j \neq i} \Delta_{ij}^{\text{inj}} K_{ij} \cos \theta_{ij}) / \sigma. \quad (3.6)$$

By gradually increasing the gain until the threshold density value is reached, the condensation takes place at the minimum of  $\sum_i \gamma_i^{\text{inj}}$  for a given set of coupling coefficients since the pumping of each of the CCs is controlled independently from others. Given that  $\mathcal{N} = N\rho_{\text{th}}$  and  $N\gamma_c$  are fixed, the minimum of  $\sum_i \gamma_i^{\text{inj}}$  is achieved at the maximum of  $\sum_{i,j:j \neq i} \Delta_{ij}^{\text{inj}} K_{ij} \cos \theta_{ij}$  so at the minimum of the XY Hamiltonian  $H_{\text{XY}} = -\sum_{i,j:j \neq i} \Delta_{ij}^{\text{inj}} K_{ij} \cos \theta_{ij}$ .

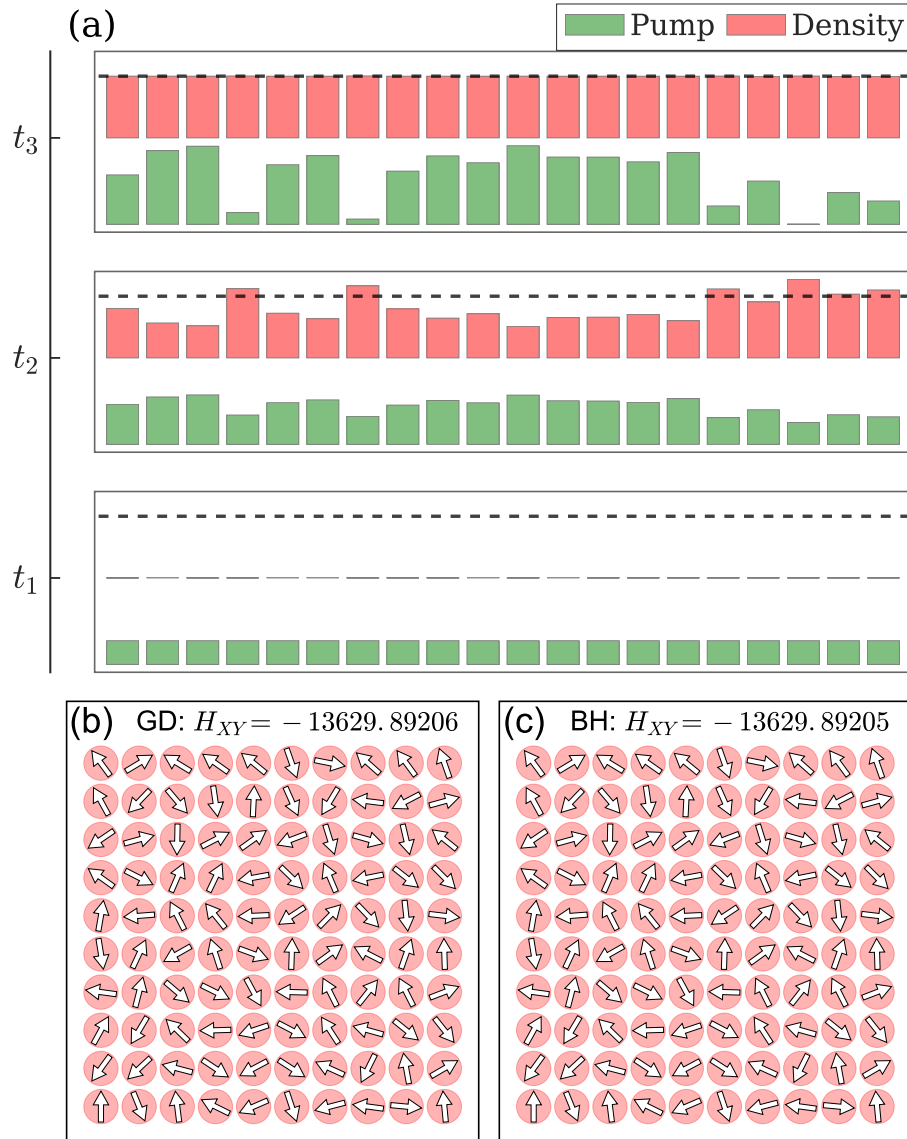


Fig. 3.7 (a) The operational schematics of the gain-dissipative simulator is shown. Initially, all CCs are equally pumped (green bars) below the threshold, and all have negligible number densities at  $t = t_1$ . As the pumping intensities increase, the different CCs emerge (red bars) with different number densities depending on the connectivity between CCs, as shown at some  $t = t_2$ . The individual control of the pumping intensity as described by Eq. (3.4) leads to the steady-state with all the densities reaching the threshold at  $t = t_3$ . (b-c) The ground state spin configurations of the XY Hamiltonian for problem size  $N = 100$  found by (b) the numerical evolution of Eqs. (3.1, 3.4, 3.8) and (c) by the basin-hopping optimisation algorithm. The found energies agree to 10 significant digits between methods. The coupling matrix is fully connected with interactions randomly distributed in  $[-10, 10]$ .

For non-equilibrium condensates, the nonlinear dissipation term  $\sigma$  can be proportional to the pumping intensity  $\sigma = \xi \gamma_i = \xi \gamma_i^{\text{inj}}$ , where  $\xi$  is a system dependent parameter that for polariton condensates depends on the decay rate of the particles in the exciton reservoir (see Section 2.1 for details). The steady state of Eqs. (3.2, 3.4) becomes

$$\rho_i = \rho_{\text{th}} = (1 - \gamma_c / \gamma_i^{\text{inj}} + \sum_{j:j \neq i} \Delta_{ij}^{\text{inj}} K_{ij} \cos \theta_{ij}) / \xi, \quad (3.7)$$

with  $\Delta_{ij}^{\text{inj}} = 1 + \gamma_j^{\text{inj}} / \gamma_i^{\text{inj}}$ . In this case, each of  $1/\gamma_i^{\text{inj}}$  (and so  $\sum_i 1/\gamma_i^{\text{inj}}$ ) is maximised at the threshold, so again the system reaches the minimum of the XY Hamiltonian.

If one removes the density heterogeneity, the global minimum of the XY model can be achieved. However, the coupling terms  $\Delta_{ij}^{\text{inj}}(t) K_{ij}$  now depend on the particle injection rates  $\gamma_i^{\text{inj}}$  that are not known a priori under the condition of equal densities at the threshold. Therefore, not only  $\gamma_i^{\text{inj}}(t)$  has to be adjusted in time to equalise the densities using Eq. (3.4) but also the coupling coefficients  $K_{ij}$  have to be modified in time to bring the required couplings  $J_{ij}$  at the steady-state by

$$\frac{dK_{ij}}{dt} = \hat{\varepsilon} (J_{ij} - \Delta_{ij}^{\text{inj}} K_{ij}), \quad (3.8)$$

where  $\hat{\varepsilon}$  controls the rate of the coupling strengths adjustment. Since  $\hat{\varepsilon} \ll \varepsilon$  such adjustments do not significantly slow down the operation of the simulator as they have to be performed much more rarely than adjustments of the gain. The couplings need to be reconfigured depending on the injection rate as described by Eq. (3.8): if the coupling strength scaled by the gain at time  $t$  is lower (higher) than the objective coupling  $J_{ij}$ , it has to be increased (decreased). We have verified that Eqs. (3.1, 3.4, 3.8) find not just the value of the global minimum of the XY Hamiltonian for a variety of couplings and sizes of the system, but also the minimisers as Figure 3.7(b,c) shows.

Next, we illustrate the density and coupling adjustments for simulating the XY model on the square lattice of polariton condensates that we discussed in Section 3.1. Figure 3.8(a) shows the density profile of 45 polariton condensates that interact by the outflow of the particles from neighbouring CCs. All CCs are equally pumped (with, say,  $\gamma^{\text{inj}} \equiv \gamma_i^{\text{inj}}$ ) and, therefore, the CCs away from the margins have the largest occupation: they are fed by the particles coming from the eight neighbours. On the other hand, the CCs at the margins have the lowest occupation as they interact with only four or five neighbours. Such density heterogeneity between the lattice sites is observed in Figure 3.8(a), where the condensates on the margins are barely visible. The resulting configuration could realise the minimum of the XY model, but for the coupling strengths between  $i$ -th and  $j$ -th condensates given

by  $2\gamma^{inj}K_{ij}\sqrt{\rho_i\rho_j}$  with number densities  $\rho_i$  and  $\rho_j$  that are not known before the system reaches the configuration shown in Figure 3.8(a). In agreement with experimental results, the numerical simulation of the  $7 \times 7$  polariton lattice suggests not only the density variation between the sites but indicates the formation of a spin-wave state (Figure 3.8(b)), which manifests the presence of various couplings in the lattice.

To realise the XY model for the given couplings  $J_{ij}$ , we need to implement the feedback mechanisms described above and that we illustrate step by step. First, we remove the density heterogeneity by adjusting the gain mechanism described by Eq. (3.4). The resulting pumping profile is shown in Figure 3.8(c) with the corresponding steady-state number densities and phases in Figure 3.8(d). In the presence of equal densities between the lattice sites, the spin-wave is due to the different pumping intensities, and therefore, different couplings  $\Delta_{ij}K_{ij}$  between the CCs across the lattice. We adjust  $K_{ij}$  according to Eq. (3.8) by changing the distances between the sites as Figure 3.8(e) illustrates. The final steady-state has equal densities and equal antiferromagnetic coupling strength between the nearest neighbours with phases alternating between 0 and  $\pi$ , giving the expected global minimum of the XY model.

The developed procedure for the dynamical adjustment of the gain and coupling strengths, which is reflected in Eqs. (3.1, 3.4, 3.8), can be simulated on a classical computer leading to a new class of optimisation algorithms that we will explore in the next Chapter. In the next Section, the developed scheme for minimising the XY Hamiltonian is extended to discrete spin Hamiltonians, including the Ising and Potts models.

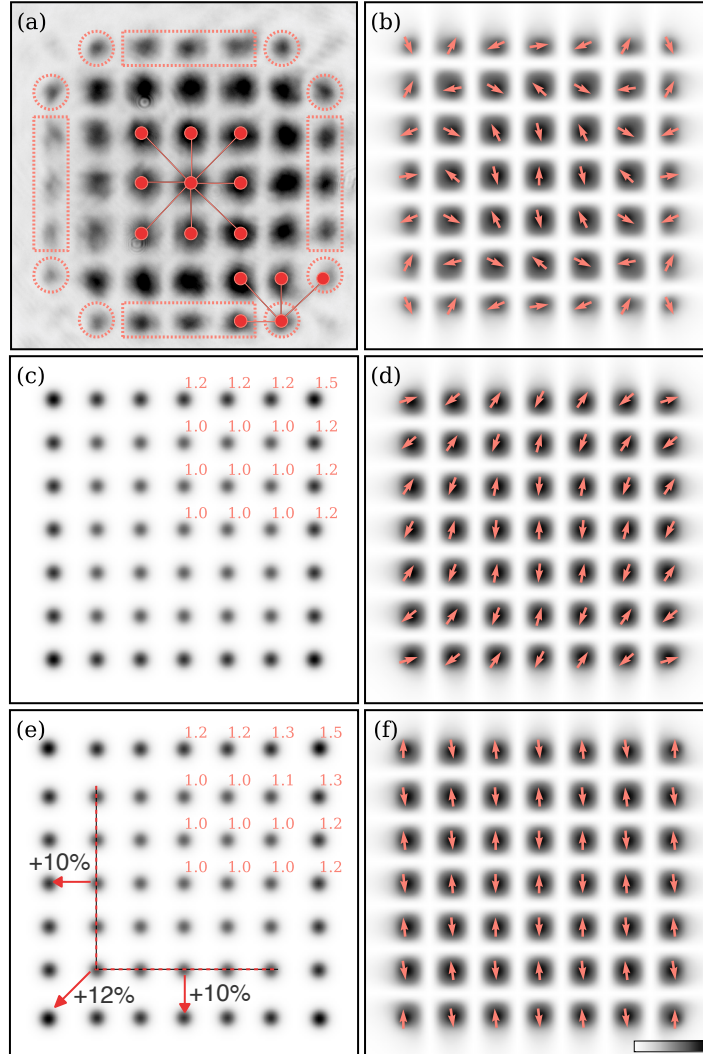


Fig. 3.8 (a) The contour plot is shown for the number density of polariton condensates formed by non-resonant pumping with equal intensities. Red lines show the particle fluxes between the sites: the central site experiences the inflow of the particles from eight neighbouring sites whereas the sites on margins have only four or five neighbours. Dashed figures embrace the condensates with densities lower than the central condensates. (b,d,f) Contour plots of the steady state number density function  $|\psi|^2$  obtained by the numerical integration of the full dynamical governing equations for  $7 \times 7$  lattice and for the parameters used in previous Section. Contour plots of the pumping profiles at the steady state are shown in (c,e). Panels (c,d) are obtained by applying the density adjustments according to Eq. (3.4). Panels (e,f) are obtained by applying both the density adjustments and coupling adjustments according to Eq. (3.4) and Eq. (3.8). The resulting pumping intensities at the lattice sites are indicated for the top right quarter of (c,e) as the factor of the pumping at the lattice centre. The coupling strength adjustments are achieved by shifting the lattice sites as shown in red for the bottom left corner only in (e).

### 3.3 Signatures of minimising the Ising and Potts models on simple graphs

In all considered lattice configurations of non-equilibrium condensates so far, the phases of CCs could have taken any value between 0 and  $2\pi$ . Many real-life optimisation tasks can be formulated as discrete combinatorial optimisation problems, while mapping them to continuous Hamiltonians is not practical. Therefore, it is crucial to reduce the overhead by mapping discrete problems into discrete spin Hamiltonians directly. This section describes the procedure for implementing the discrete Hamiltonians, namely the Ising and  $n$ -state planar Potts Hamiltonians, in the geometrically coupled non-equilibrium condensates that can be adapted to other gain-dissipative systems. The result is a flexible model system that allows one to find the time and pumping-dependent behaviour and interplay of the discrete and continuous order parameters with different symmetry breaking properties.

The operation of gain-dissipative simulators follows from the cGLE described by Eq. (2.1) that governs the time evolution of the system of  $N$  spatially separated non-equilibrium condensates. As we have shown earlier, the spatial degrees of freedom can be integrated out so that the coupled rate equations describe the time evolution of the complex amplitudes  $\Psi_i(t)$  of these CCs. For such a system to reach the global minimum of the XY Hamiltonian, one needs to establish a feedback connection between the condensates' gain, coupling strengths, and densities. The resulting system is

$$\frac{d\Psi_i}{dt} = \Psi_i(\gamma_i - \sigma|\Psi_i|^2) - iU|\Psi_i|^2\Psi_i + \sum_{j, j \neq i}^N \mathcal{C}_{ij}\Psi_j + \text{noise}(t), \quad (3.9)$$

$$\frac{d\gamma_i^{\text{inj}}}{dt} = \varepsilon(\rho_{\text{th}} - \rho_i), \quad \frac{d\mathcal{C}_{ij}}{dt} = \hat{\varepsilon}(J_{ij} - \mathcal{C}_{ij}), \quad (3.10)$$

where  $\Psi_i(t) = \sqrt{\rho_i(t)} \exp[i\theta_i(t)]$ ,  $\rho_i$  is the number density and  $\theta_i$  is the phase of the  $i$ -th CC,  $\gamma_i = \gamma_i^{\text{inj}} - \gamma_c$  is the effective gain where  $\gamma_i^{\text{inj}}$  is the pumping rate,  $\gamma_c$  and  $\sigma$  are the rates of linear and nonlinear dissipation respectively,  $U$  is the strength of the in-site particle interactions,  $\rho_{\text{th}}$  is the specified threshold number density. For simplicity, the coupling strength between  $i$ -th and  $j$ -th CCs is denoted by  $\mathcal{C}_{ij}$  compared to  $\Delta_{ij}^{\text{inj}} K_{ij}$  from the previous Section. The constants  $\varepsilon$  and  $\hat{\varepsilon}$  characterise the rates of the density and coupling adjustments respectively: if the number density (the coupling strength) of the  $i$ -th CC is below (above)  $\rho_{\text{th}}$  ( $J_{ij}$ ) it has to be increased (decreased).

The system described by Eqs. (3.9, 3.10) has stable fixed points  $\rho_i = \rho_{\text{th}}$  at which the phases acquire the global frequency  $\omega_0 = U\rho_{\text{th}}$  and minimise the XY Hamiltonian. To

implement external fields and discrete versions of the XY model, such as the Ising and  $n$ -state planar Potts models, we need to break the symmetry of Eq. (3.9) to phase rotations. This symmetry breaking can be achieved by forcing the system parametrically at a frequency  $\omega_c$  resonant with  $\omega_0$ . In polariton condensates, such resonant forcing has recently been used in combination with a non-resonant pumping [162]. In analogy with [163, 164], the Eq. (3.9) becomes for an integer ratio  $n = \omega_c/\omega_0$

$$\frac{d\Psi_i}{dt} = \Psi_i(\gamma_i - \sigma|\Psi_i|^2) - iU|\Psi_i|^2\Psi_i + \sum_{j:j \neq i}^N \mathcal{C}_{ij}\Psi_j + h_{ni}\Psi_i^{*(n-1)} + \text{noise}(t), \quad (3.11)$$

where  $h_{ni}$  is the pumping strength of  $i$ -th CC at the resonant frequency  $n$ . We substitute  $\Psi_i(t) = \sqrt{\rho_i(t)} \exp[i\theta_i(t)]$  in Eq. (3.11), separate real and imaginary parts, and drop the noise term to get

$$\frac{1}{2}\dot{\rho}_i(t) = (\gamma_i - \sigma\rho_i)\rho_i + \sum_{j:j \neq i} \mathcal{C}_{ij}\sqrt{\rho_i\rho_j} \cos \theta_{ij} + h_{ni}\rho_i^{\frac{n}{2}} \cos(n\theta_i), \quad (3.12)$$

$$\dot{\theta}_i(t) = -U\rho_i - \sum_{j:j \neq i} \mathcal{C}_{ij} \frac{\sqrt{\rho_j}}{\sqrt{\rho_i}} \sin \theta_{ij} - h_{ni}\rho_i^{\frac{n}{2}-1} \sin(n\theta_i), \quad (3.13)$$

where  $\theta_{ij} = \theta_i - \theta_j$ . The fixed point of the dynamical system given by the Eqs. (3.12, 3.13, 3.10) satisfies

$$\rho_i = \rho_{\text{th}} = [\gamma_i + \sum_{j:j \neq i} J_{ij} \cos \theta_{ij} + h_{ni}\rho_{\text{th}}^{\frac{n}{2}-1} \cos(n\theta_i)]/\sigma. \quad (3.14)$$

Since for each CC we choose the smallest  $\gamma_i$  by raising it slowly from below the threshold, the global minimum of

$$H = - \sum_{i=1}^N \sum_{j=1:j \neq i}^N J_{ij} \cos \theta_{ij} - \rho_{\text{th}}^{\frac{n}{2}-1} \sum_{i=1}^N h_{ni} \cos(n\theta_i) \quad (3.15)$$

is achieved while Eq. (3.13) describes the gradient decent to that minimum. By taking the resonance  $n = 1$  we introduce the effective external ‘‘magnetic’’ field  $\mathbf{F} = \{h_{1i}/\sqrt{\rho_{\text{th}}}\}$  into the model. For  $n > 1$  the forcing term in Eq. (3.11) reduces the invariance to a global phase shift to a discrete symmetry  $\theta_i = 2\pi i/n$  and for a sufficiently large  $h_{ni}\rho_{\text{th}}^{\frac{n}{2}-1} > \sum_j |J_{ij}|$  introduces the penalty term in the Hamiltonian  $H$  for the deviation of phases from the discrete values  $2\pi i/n$ . For  $n = 2$  and a uniform strength of the resonant pumping  $h_2 = h_{2i}$ , Eqs. (3.11, 3.10) realise the minimum of Eq. (3.15) with  $\theta_i$  restricted to 0 or  $\pi$ , and therefore, the minimum of the Ising Hamiltonian, whereas for  $n > 2$  and  $h_n = h_{ni}\rho_{\text{th}}^{\frac{n}{2}-1}$  Eqs. (3.11, 3.10) realise the  $n$ -state planar Potts Hamiltonian with  $\theta_i = 2\pi i/n$  [165].

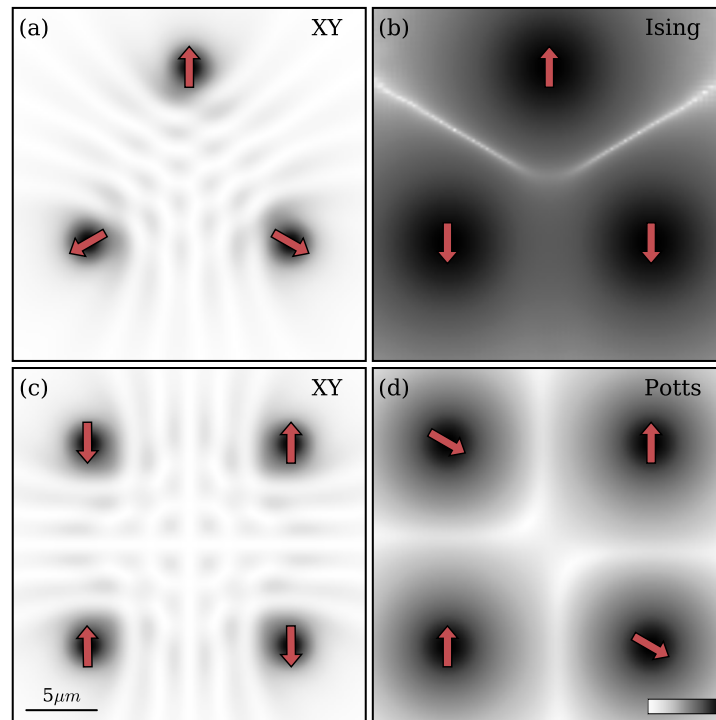


Fig. 3.9 Contour plots of the density  $|\psi(\mathbf{r})|^2$  of the polariton condensates with antiferromagnetic nearest neighbour interactions show the ground states of the XY (a,c), the Ising (b), and the 3-state planar Potts (d) Hamiltonians at the condensation threshold. The densities for the Ising and 3-state planar Potts models are shown in log scale to emphasise the standing matter waves between condensates and, therefore, the phase differences. The densities are obtained by numerical integration of Eqs. (3.16, 3.17) with the parameters given in Appendix A.

One can use Eqs. (3.11, 3.10) to simulate the behaviour of gain-dissipative systems. However, since simplified assumptions were made to arrive at Eq. (3.11), it is important to verify that a real system shows the transition from achieving the minimum of the continuous XY model to the minimum of the discrete model when the resonant forcing is introduced. As an illustrative example, we consider the polariton condensates modelled by the cGLE coupled to the rate equation describing the exciton reservoir as given in Eqs. (2.1, 2.2). The resonant drive can be achieved by an additional single-mode continuous wave laser tuned to the multiple of the frequency of the system at the Hopf bibrucation [163, 54]. The resulting equations read

$$i\hbar \frac{\partial \psi}{\partial t} = -\frac{\hbar^2}{2m} (1 - i\eta_d \mathcal{R}) \nabla^2 \psi + U_0 |\psi|^2 \psi + \hbar g_R \mathcal{R} \psi + i\frac{\hbar}{2} \left( R_R \mathcal{R} - \gamma_C \right) \psi + iP_n(\mathbf{r}, t) \psi^{*(n-1)}, \quad (3.16)$$

$$\frac{\partial \mathcal{R}}{\partial t} = -(\gamma_R + R_R |\psi|^2) \mathcal{R} + P_0(\mathbf{r}), \quad (3.17)$$

where  $\psi(\mathbf{r}, t)$  is the condensate wave function,  $\mathcal{R}(\mathbf{r}, t)$  is the density profile of the hot exciton reservoir, the last term on the right-hand side of Eq. (3.16) is the resonant forcing with resonance  $n$ , and all other parameters are described in Section 2.1. Here the polariton lattice of  $N$  condensates at the positions  $\mathbf{r} = \mathbf{r}_i$  is formed by taking the non-resonant pumping profile as  $P_0(\mathbf{r}, t) = \sum_{i=1}^N f_i(t) p(|\mathbf{r} - \mathbf{r}_i|)$ , where  $p(r) = \exp(-\alpha r^2)$ ,  $\alpha$  characterises the inverse width of the incoherent pumping profile and  $f_i$  describes the strength of the pumping centred at the position  $\mathbf{r} = \mathbf{r}_i$ . The resonant pumping profile  $P_n(\mathbf{r}, t) = \sum_{i=1}^N \tilde{h}_{ni} p(|\mathbf{r} - \mathbf{r}_i|)$ ,  $n > 0$  follows the lattice spatial profile but with different pumping intensities  $\tilde{h}_{ni} \ll f_i$ . As we have discussed above and shown in detail in Section 2.1 and Section 3.2, the spatial degrees of freedom of Eqs. (3.16, 3.17) without the resonant terms can be integrated out to yield the rate equations on the complex amplitudes of the CCs leading to Eqs. (3.9). Similarly, Eqs. (3.16, 3.17) with the resonant forcing yield Eqs. (3.11) with  $h_{ni} = \tilde{h}_{ni} \text{Re}[\int p(|\mathbf{r} - \mathbf{r}_i|) \phi^{*n}(|\mathbf{r} - \mathbf{r}_i|) d\mathbf{r}] / \int |\phi(|\mathbf{r} - \mathbf{r}_i|)|^2 d\mathbf{r}$ , where  $\phi(r)$  is the wave function of a single condensate pumped with  $p(r)$ .

To illustrate how the polariton lattice minimises the discrete Ising or n-state planar Potts models with or without external fields, we study the behaviour of the unit polariton lattice cells when they are subjected to the effect of the resonant forcing. In what follows, we explore the behaviour of the system without density and coupling adjustments described by Eqs. (3.10) to see how the introduction of the resonant forcing changes the couplings. First, we consider a simple lattice of three condensates arranged at the corners of the equilateral triangle coupled antiferromagnetically with  $J = J_{ij} < 0$ . Without the resonant

forcing,  $P_n = 0$ ,  $n > 0$ , the phases arrange themselves with  $2\pi/3$  phase differences to minimise  $H_{XY} = -J(\cos \theta_{12} + \cos \theta_{23} + \cos \theta_{31})$  as Figure 3.9(a) illustrates. This agrees with the experimental findings [131]. When the resonant forcing is introduced at  $n = 2$ , the system described by Eqs. (3.16, 3.17) finds the global minimum of the Ising Hamiltonian  $H_{\text{Ising}} = -\tilde{J}(s_1 s_2 + s_2 s_3 + s_1 s_3)$ ,  $s_i = \cos \theta_i = \pm 1$  for  $\tilde{J} < 0$ ,  $\tilde{J} \neq J$ . Such configuration is frustrated with spins  $0, \pi, \pi$  or  $0, 0, \pi$  depicted in Figure 3.9(b).

To illustrate the transition from solving the XY model to the  $n$ -state planar Potts model, we consider four condensates arranged at the corners of a square with antiferromagnetic coupling between the nearest neighbours and ferromagnetic coupling along the diagonal. Figure 3.9(c) shows the solution of Eqs. (3.16, 3.17) without the resonant terms ( $P_n = 0$ ,  $n > 0$ ). Four condensates realise the global minimum of the XY model with  $0, \pi, 0, \pi$  phase differences as been shown in Section 3.1 and as been also observed in experiments [85]. The same configuration would result from the Ising model, but the 3-state planar Potts model with  $\theta_i$  restricted to  $0, 2\pi/3$  and  $4\pi/3$  is minimised by  $0, z, 0, z, 0$  configurations where  $z = 2\pi/3$  or  $z = 4\pi/3$ . As Figure 3.9(d) illustrates, this is what we observe by implementing  $n = 3$  resonant forcing in Eqs. (3.16, 3.17).

Finally, we combine two resonant forcing terms: the resonance  $n = 1$  and either resonance  $n = 2$  or  $n = 3$  in Eq. (3.16) to simulate the effect of an external ‘‘magnetic’’ field in the Ising or 3-state planar Potts models. We take  $\tilde{h}_{11} = \tilde{h}_{12} > \max|J_{ij}|$  and  $\tilde{h}_{13} = \tilde{h}_{14} = 0$ . Such external field penalises the objection function if the phases of the bottom two condensates in Figure 3.10(b-c) are not zeros and leads to the phase configurations as shown in Figure 3.10(d-e).

This approach opens rather exciting possibilities for simulating complex physical systems, solving combinatorial optimisation problems and developing new computational algorithms. With spatially varied dissipation profiles, which we propose in the next Section for realising independent control of individual coupling strengths, exciting opportunities are open to study collective quantum phenomena and exotic phase configurations and transitions.

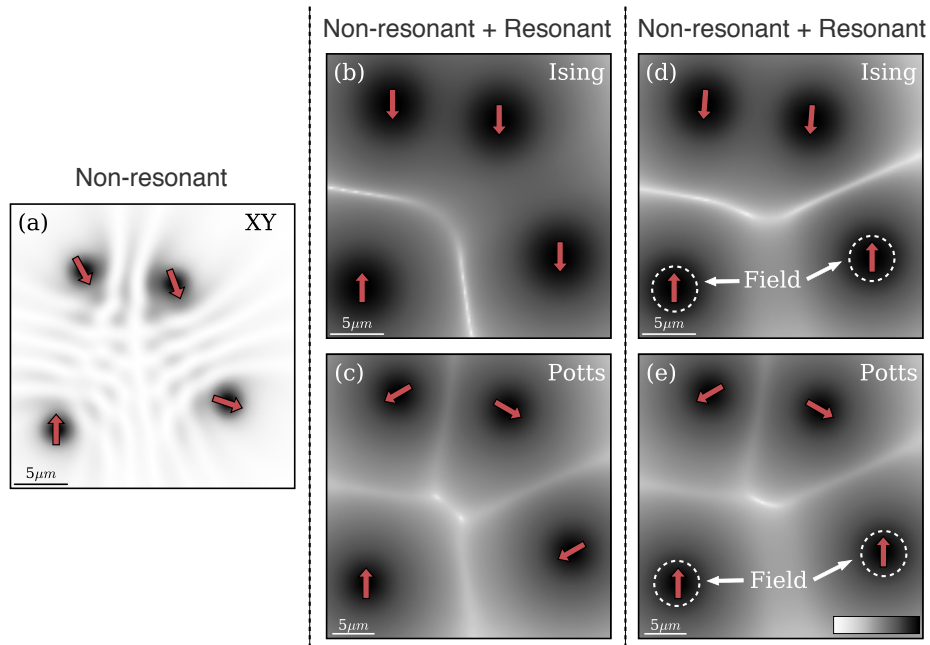


Fig. 3.10 Contour plots of the density  $|\psi(\mathbf{r})|^2$  of the polariton condensates in the corners of quadrilateral show the ground state of the XY (a), the Ising (b), and the 3-state planar Potts (c) Hamiltonians without the external fields. The Ising and the 3-state planar Potts Hamiltonians with the external fields forcing the bottom condensates to acquire phase  $\theta_i$  are shown in (d) and (e), respectively. The densities are obtained by numerical integration of Eqs. (3.17) with the parameters given in Appendix A are shown in log scale for the Ising and Potts models.

### 3.4 Individual control of spatial lattice interactions by varying dissipation profile

In previous Sections, the new subclass of simulators was proposed based on networks of polariton and photon condensates and lasers. These are gain driven systems with dissipation: when gain exceeds the threshold and overcomes the losses, a phase transition to a coherent state occurs. The gain should occur at various localised spatial positions within the decoherence length of neighbouring condensates to create a network of condensates. Initially, each gain centre is seeded with a random phase and is evolved independently of other centres. As the occupation of each gain centre grows with an increased pumping intensity, different centres start interacting while exchanging particles. Finally, the dissipative nonlinearity saturates the gain and the system can settle to a steady-state with a particular distribution of phase differences between the network elements.

In this Section, we study a model of a fully controllable polaritonic network of a fixed geometry by spatially varying dissipation. In this network, the desired interactions between any nodes can be supported by creating channels of low dissipation and further controlled individually by dissipative gates. At the same time, high-dissipative barriers can eliminate undesired interactions. We justify how such dissipative channels, gates, and barriers, can be experimentally implemented for a few physical platforms, including polariton and coupled laser systems.

*Individual control of pairwise interactions.* As it was shown earlier, polaritonic networks can be accurately modelled with the cGLE coupled to the reservoir dynamics which are described by Eqs. (2.1, 2.2). For a purpose of spatially varying dissipation, we nondimensionalise these equations here in a different way by  $\psi \rightarrow \sqrt{\hbar R_R / 2U_0 l_0^2} \psi$ ,  $t \rightarrow 2l_0^2 t / R_R$ ,  $\mathbf{r} \rightarrow \sqrt{\hbar l_0^2 / (m R_R)} \mathbf{r}$ ,  $\mathcal{R} \rightarrow \mathcal{R} / l_0^2$ ,  $P \rightarrow R_R P / 2l_0^2$  and introduce the dimensionless parameters  $g = 2g_R / R_R$ ,  $b_0 = 2\gamma_R l_0^2 / R_R$ ,  $b_1 = \hbar R_R / U_0$ ,  $\eta = \hat{\eta} / l_0^2$ ,  $\gamma = \gamma_C l_0^2 / R_R$ , where  $l_0 = 1 \mu m$ . The resulting model yields

$$i \frac{\partial \psi}{\partial t} = -(1 - i\eta \mathcal{R}) \nabla^2 \psi + |\psi|^2 \psi + g \mathcal{R} \psi + i(\mathcal{R} - \gamma) \psi, \quad (3.18)$$

$$\frac{\partial \mathcal{R}}{\partial t} = -(b_0 + b_1 |\psi|^2) \mathcal{R} + P(\mathbf{r}, t). \quad (3.19)$$

Spatially varying dissipation profile effectively creates an excitonic landscape of hills and valleys for polariton flows with excitons reservoirs occupying the regions of higher dissipation. Such an excitonic landscape can create barriers for polariton flow and, therefore, change the interaction depending on the height of the barriers. This relationship between density

modulations and spatially varying dissipation suggests to use a varying dissipation profile across the sample to establish pairwise interactions that can be independently tuned between any two condensates. For instance, this can be achieved by creating a spatially dependent dissipation profile  $\gamma(\mathbf{r})$ , as illustrated in Figure 3.11. With this scheme, a two-dimensional square grid is formed. It consists of narrow rectangular strips, i.e. channels, characterised by a constant low dissipation rate  $\gamma = \gamma_{\text{channel}}$ . Such small dissipation supports flows of polariton quasi-particles through these channels. Outside of the channels, the dissipation is strongly enhanced and equal to  $\gamma = \gamma_{\text{barrier}} \gg 1$ , thereby forming dissipative barriers. The condensates are pumped at the grid vertices (schematically shown as yellow spheres in Figure 3.11) and the high-dissipative barriers (brown areas) block the outflow of polaritons across the diagonals.

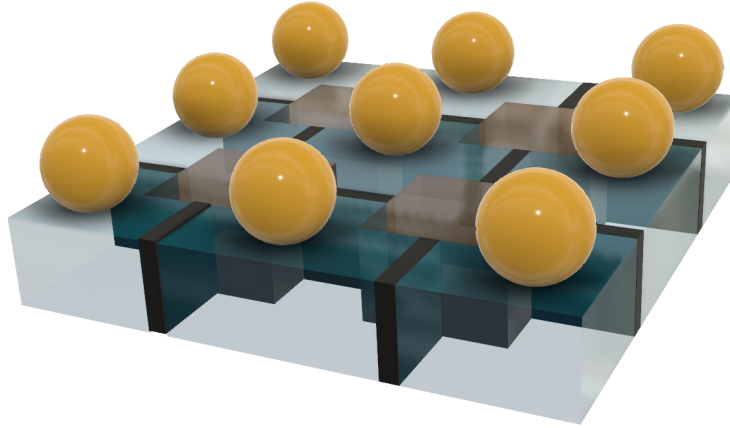


Fig. 3.11 The schematic is shown for the spatially dependent dissipation profile with nine condensates (yellow balls) arranged in a 2D lattice in a semiconductor microcavity. The condensates interact via channels of low dissipation (light grey). Dissipative barriers (brown areas) show an increased dissipation that prevents the coupling between the condensates across the diagonals. Dissipative gates (dark blue areas) show the regions where the dissipation is increased or decreased to control the couplings between neighbouring condensates.

The pairwise interactions between the neighbouring condensates are further controlled by another dissipative layer across the channel: dissipative gates (dark blue narrow blocks in the scheme) given by  $\gamma = \gamma_{\text{channel}} + \gamma_{\text{gate}}(\mathbf{r})$ . The amplitude of dissipative gates should be available for a dynamical adjustment and be large enough to change the sign of interactions from ferro- to antiferromagnetic. In contrast, the channel-barrier structure forms the stationary dissipative profile that can be conclusively imprinted in the sample.

*Two condensates.* To relate the characteristics of the dissipative control with the interaction between the condensates, we first study the configuration of two polariton condensates. The  $\pi$  phase modulation between geometrically fixed condensates is achieved by increasing

the amplitude of the dissipative gate between condensates, as shown in Figure 3.12(a). The complete transition to the  $\pi$  phase state happens at higher gates in the presence of higher dissipative barriers meaning that the excitonic landscape with deeper valleys supports stronger couplings between condensates. Here “strong coupling” means that the condensates have to remain synchronised after the dissipative gate of a particular amplitude is placed. Such strong coupling can be achieved by, for example, using a uniform pumping profile or by closely arranging the condensates with significant overlapping of their pumping shapes. If the external potential is used to control the coupling, the condensates become de-coupled before the  $\pi$  phase difference can be reached.

*Nine condensates.* Next, we consider the same close arrangement of pumpings for a  $3 \times 3$  square block of polariton condensates with the pumping profile as in Figure 3.12(b). In this case, the dissipative gates are placed between the vertical stripes of condensates (see Figure 3.12(c)). The initial gateless state is configured to be ferromagnetic, as shown in Figure 3.12(d). The amplitude of dissipative gates is then increased, which leads to spin configurations in Figure 3.12(e-g) with an antiferromagnetic coupling between vertical stripes of condensates in the final configuration. Here we note that both chosen dissipative and pump profiles serve the same purpose of preventing undesired interactions. The former destroys polaritons by decreasing their lifetime, i.e. increasing losses, and the latter creates exciton reservoirs that block polariton outflows due to repulsive exciton-polariton interactions.

To check the stability of an arbitrary network, we next demonstrate that the individual control of couplings can be realised. Figure 3.13(a) shows the dissipative profile with only one dissipative gate placed for the bottom-left condensate. This dissipative gate creates frustration in the network and makes this particular coupling antiferromagnetic while all the other couplings are ferromagnetic. The resulting spin configuration is depicted in Figure 3.13(b) and demonstrates how the frustration spreads across the network. The addition of another dissipative gate as in Figure 3.13(c) removes frustration from the system and leads to the spin configuration, which is shown in Figure 3.13(d).

*Arbitrary networks.* For a potential implementation of reservoir computing or analogue Hamiltonian optimisation, it is important to demonstrate the scalability of the polaritonic network with dissipative gates, channels, and barriers. In Figure 3.14 we show a configuration of 500 condensates with 92 dissipative gates, which are placed so that regions with antiferromagnetic couplings can form arbitrary symbols, in this case “Sk”. We simulate Eqs. (3.18, 3.19) starting with 500 random initial conditions and choose two lowest energy states to show in Figure 3.14. While the excited energy states do not maintain any recognisable spin configuration (see Figure 3.14(b)), the lowest found energy state indeed recovers the letters “Sk” (see Figure 3.14(a)).

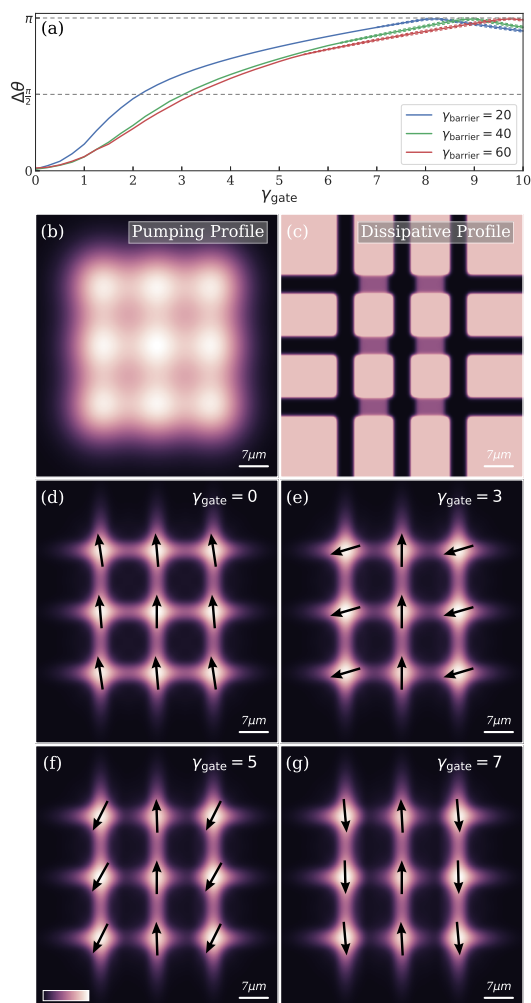


Fig. 3.12 (a) The transitions from the ferromagnetic state with 0 phase difference to the antiferromagnetic state with  $\pi$  phase difference between two polariton condensates by varying the amplitude of the dissipative gate are shown for three dissipative barriers (solid lines). The condensates remain synchronised though the small phase fluctuations appear for higher dissipative gates. The amplitude of such fluctuations is contained within the colour dashed lines. (b) The pumping profile for a  $3 \times 3$  square lattice of polariton condensates. (c) The structure of a dissipation profile  $\gamma(\mathbf{r})$  consisting of dissipative channels (black), dissipative barriers (pink), and dissipative gates (purple) being horizontally placed between vertical stripes of condensates. (d-g) The phase differences of all condensates are shown with black arrows with respect to the central condensate, the background is the normalised polariton density  $|\psi(\mathbf{r})|^2$ . (d) In the absence of dissipative gates, the initial state is prepared to be ferromagnetic with all spins aligned in the same direction. (e-g) With a dissipative gate of  $\gamma_{\text{gate}} = \{3, 5, 7\}$ , the coupling strengths between vertical stripes of condensates are continuously changed from ferromagnetic to antiferromagnetic coupling.

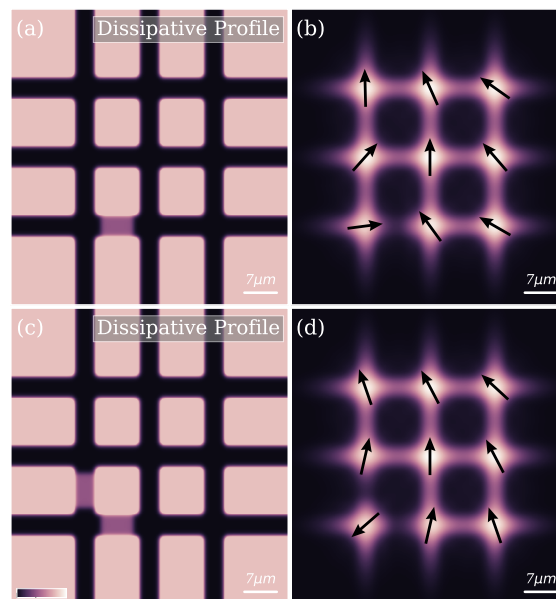


Fig. 3.13 (a) A dissipation profile structure is similar to that of Fig. 3.12(b) but with only one dissipative gate. This dissipative gate makes the particular link antiferromagnetic while all other links remain ferromagnetic and, thus, frustration is created in the network. The resulting spin configuration is shown in (b). (c) The addition of another dissipative gate removes frustration from the system and leads to the spin configuration which is shown in (d). The dissipative gate's amplitude is  $\gamma_{\text{gate}} = 7$ .

Figures 3.13 and 3.14 give the realistic spin distributions under the XY model. However, there are small deviations from the exact spin orientations of the global minimum of the XY model. In all considered configurations, dissipative gates remove particles from the system in an asymmetric way and create gentle density inhomogeneity that affects spins across lattice sites. The origin of this problem and possible solutions have been elucidated in Section 3.2. In particular, the injection rates could be adjusted and a weak dependence of polariton outflow velocity on the pumping intensity, which is a sample-dependent property of polaritons, could be ensured. Without such extensions, spins realise the stationary state of the Stuart-Landau model, which we discussed in Section 2.1. In the next Section, we propose a scheme for minimising the XY and Ising models on arbitrary graphs with non-equilibrium condensates.

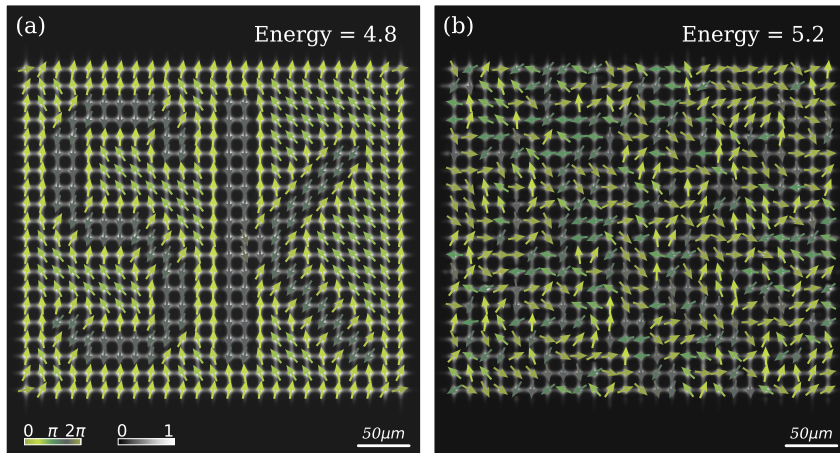


Fig. 3.14 The  $20 \times 25$  square lattice of polariton condensates is shown for the lowest energy state in (a) and for one of the excited energy states in (b). The polariton densities are shown with black-and-white colour scheme, the phase differences are plotted with a cyclic green-grey colour scheme. The dissipative gates  $\gamma_{\text{gate}} = 7$  are placed between the condensates constituting letters “Sk” and other condensates to create antiferromagnetic couplings, while all other couplings are ferromagnetic. The lowest energy state spin configuration (a) resembles “Sk” letters while the excited energy state (b) is blurred. The energies are in dimensionless units.

*Implementation feasibility.* The following experimental approaches may be promising to realise a fixed dissipative structure consisting of dissipative channels and barriers. Since polaritons are quasi-particles that exist in semiconductor microcavity environments, their excitonic or photonic components can be directly accessed by manipulating quantum wells or microcavities, respectively. The technique of implanting protons into the quantum wells or the top of distributed Bragg reflectors [87] makes independent spatial control of both the exciton and the cavity photon energies possible, which in turn leads to local control over

the polariton decay rate. The spatial control of the polariton lifetime, i.e. the dissipation profile  $\gamma(\mathbf{r})$ , can therefore be fabricated with the proton implant technique with a multi-layer mask [87]. Another way to access the exciton states alone is to create controlled stress by applying a pin to the backside of the substrate [73]. As a result, a spatial trap is formed directly under the stressor where polaritons have an energy minimum, and the cavity photon states and the exciton states are strongly coupled. However, away from the centre of the trap, the lowest polariton states are almost purely photon-like, making the coupling of the exciton states and cavity photon states weaker. This means that the lifetime of polaritons at high energy is shorter than the lifetime of those at the energy minimum. Thus, in principle, such strain-induced traps can be used to create a configuration of dissipative channels and barriers if the tip radius of the pin can be decreased to a micrometre or less.

The dynamic dissipation control for realising dissipative gates can be achieved by electrical carrier injection, which leads to localised losses due to excited state absorption and bimolecular annihilation involving polarons and long-lived triplets [166]. Alternatively, the local control of the dissipation can be achieved by increasing the biexciton formation rate. Biexcitons can be created by two-photon absorption, by exciton absorption, or by inducing polariton-biexciton transitions [167–170].

### 3.5 Polaritonic XY-Ising Machine

A system of polariton condensates has attracted considerable interest over the last few years by offering a gain-dissipative system for tackling both discrete and continuous optimisation problems. The macroscopic coherence of networks of polariton condensates is characterised by a complex classical field with well-defined condensates' relative phases  $\theta_i$ . These phases can be mapped into continuous 'spins'  $\mathbf{s}_i = (\cos \theta_i, \sin \theta_i)$  that can be further constrained to discrete values  $\theta_i \in \{0, \pi\}$  by employing the resonant excitation, as we have seen in Section 3.3. The idea underlying the polariton simulator for solving optimisation problems originates from the belief that huge combinatorial space of possible states can be sought in parallel near the condensation threshold, at which only the low-energy coherent states can form. These states may correspond to local or global minima of a particular spin Hamiltonian, and since condensation occurs on a picosecond time scale, such polariton simulators may be potentially attractive for optimisation tasks.

We have shown in Chapter 2 that the interactions between geometrically coupled condensates are generally of a complex nature and consist of the dissipative (Heisenberg) and Josephson couplings. The latter could prevent the system from achieving the minimum of a spin Hamiltonian. Moreover, even when the Josephson coupling is negligible compared to the dissipative coupling, the geometric coupling barely allows one to control the interactions beyond the nearest neighbours. Such a lack of control prevents the system from addressing complex, non-planar spin Hamiltonians.

Finding ways to dynamically control individual interactions between network nodes, such as the dissipative gates discussed in the previous Section, is a necessary step for addressing non-trivial spin Hamiltonians but not sufficient. In all proposed schemes, the nearest neighbour interactions are attempted to be controlled while the beyond nearest neighbour interactions are assumed to be negligible, which is rarely the case. A recent study has shown the synchronisation between condensates across distances over  $100 \mu m$  [171] noting that a typical lattice size constant is often in the range of  $5-15 \mu m$ . Moreover, spatially coupled polariton condensates are capable of representing different oscillator models for different ranges of experimental parameters (see Section 2.1 for details).

This Section focuses on a crucial and yet missing discussion of isolating a particular optimisation problem to address with polariton networks and controlling the couplings beyond nearest neighbours for arbitrary graphs of polariton condensates. We offer an alternative approach for simulating spin Hamiltonians with a network of spatially localised polariton condensates that do not interact with one another geometrically. For the network to become a spin Hamiltonian optimiser, we propose to couple any two condensates by redirecting the emission from one condensate to another or by exciting one condensate with an additional

resonant pump tuned to the phase of that condensate. The performance of the emulated polariton simulator is demonstrated for discrete, i.e. Ising, and continuous, i.e. XY, spin Hamiltonians for sparse and dense interaction matrices  $J$  of various sizes from 9 to 49 condensates.

### 3.5.1 Remote coupling control

To model polariton condensates, we start again with the dimensionless cGLE coupled to the exciton reservoir dynamics:

$$i\frac{\partial\psi}{\partial t} = -\nabla^2\psi + |\psi|^2\psi + g\mathcal{R}\psi + i(\mathcal{R} - \gamma)\psi + if_{\text{Res}}(\mathbf{r}, t)\psi^*, \quad (3.20)$$

$$\frac{\partial\mathcal{R}}{\partial t} = -(b_0 + b_1|\psi|^2)\mathcal{R} + P(\mathbf{r}, t). \quad (3.21)$$

Compared to Eqs. (3.18, 3.19), here we neglected  $\eta$  that is generally assumed to be small in experiments. Also, following the discussion of Section 3.3, we introduced the  $f_{\text{Res}}$  term that is an optional resonant pump at the double condensate frequency (second resonance) which forces phase differences between different condensates to be either 0 or  $\pi$ .

We use Eqs. (3.20, 3.21) to represent a network of isolated non-interacting polariton condensates which can be experimentally realised, for instance, with micropillars or with trapped polariton condensates. The former requires a lithographically modified sample and etching and leads to the formation of a polariton condensate, which coexists with the exciton reservoir density in each micropillar. The latter can be achieved without modifying the sample, e.g. by exciting each network's element with a Gaussian ring pump, which would form a polariton condensate separated from the exciton reservoir. Although the following analysis can be readily applied to either experimental configuration, for ease of reading, we will use an array of micropillars as our primary example of isolated condensates with occasional notes on the possible change in performance of the other.

The position, shape and size of micropillars can be accurately controlled during fabrication [99]. Hundreds of coupled micropillars etched in a planar semiconductor microcavity have been used to study a wealth of phenomena from the Dirac cones in a honeycomb geometry [102] to the gap solitons in 1D Lieb lattices [172]. To model the polariton condensation in a micropillar cavity, we introduce a spatially dependent dissipative profile

$$\gamma(\mathbf{r}) = \gamma_{\text{out}} - (\gamma_{\text{out}} - \gamma_{\text{in}}) \sum_i \exp(-\alpha|\mathbf{r} - \mathbf{r}_i|^{2n_{\text{SG}}}), \quad (3.22)$$

where  $\gamma_{\text{out}}$  and  $\gamma_{\text{in}}$  are the dissipation rates outside and inside of a micropillar, respectively. Here,  $\gamma_{\text{out}} \gg \gamma_{\text{in}}$ ,  $\mathbf{r}_i$  denotes the centre of the  $i$ -th micropillar, and  $n_{\text{SG}}$  is the degree of a supergaussian that models micropillars as flat low-dissipative discs. The dramatically increased dissipation between the discs ( $\gamma_{\text{out}} = 100\gamma_{\text{in}}$ ) effectively blocks all the polariton outflows which leads to non-interacting condensates even for short separation distances of a few micrometers as would be expected for the system of micropillars. The condensates at different micropillars are noninteracting unless either *relative* or *absolute* remote couplings are introduced. In the former case, a part of the light emitted by the  $j$ -th micropillar condensate is re-injected into the  $i$ -th micropillar condensate at the amount proportional to the occupation of the  $j$ -th condensate. In the case of the *absolute coupling*, the same amount of light is exchanged between the  $i$ -th and the  $j$ -th condensates. Both coupling models can be represented by

$$i\psi_t = -\nabla^2\psi + |\psi|^2\psi + g\mathcal{R}\psi + i(\mathcal{R} - \gamma)\psi + if_{\text{Res}}\psi^* + i\delta_{\gamma,\gamma_{\text{in}}}\sum_{j=1,j\neq i}^N \mathcal{J}_{ij}\psi(\mathbf{r} + \mathbf{r}_j - \mathbf{r}_i, t - \tau) \quad (3.23)$$

where  $\delta_{\gamma,\gamma_{\text{in}}}$  is the delta-function which is equal to one inside a micropillar, i.e when  $\gamma(\mathbf{r}) = \gamma_{\text{in}}$ , and zero outside,  $N$  is the number of micropillars, and  $\tau$  represents a possible time delay to supply couplings in an experimental setup. The coupling term represents the emission feedback when for each  $\psi(\mathbf{r})$  in a micropillar  $i$  the respective values  $\psi(\mathbf{r} + \mathbf{r}_j - \mathbf{r}_i)$  are added from the micropillar centred at  $j$ . For the *relative* coupling model we shall consider  $\mathcal{J}_{ij} = J_{ij}$  while for the *absolute* coupling model we will use  $\mathcal{J}_{ij} = |\psi_i|J_{ij}/|\psi_j|$ . The sign of the coupling strength can be made positive or negative by injecting the light with zero (ferromagnetic coupling) or  $\pi$  phase (antiferromagnetic coupling), respectively. For further derivations, we denote  $K(r) = \Theta(R - r)$  as the Heaviside function where  $R$  is the radius of the central part of the micropillar with a uniform phase distribution. In Eq. (3.23) we assume that the frequencies of each individual micropillar may be slightly different just below the condensation threshold. Nevertheless, the condensation process in presence of interpillar couplings locks these frequencies of different condensates resulting in a single energy condensate level. Recent experimental reports on two coupled micropillar lasers have demonstrated such frequency locking for detunings of up to 1 GHz in the few photons regime [173, 174]. For negligible time delay and geometric couplings between condensates, we can rewrite Eqs. (3.21, 3.23) for each micropillar  $i$  using  $\psi = \sum_i \psi_i$  and  $\mathcal{R} = \sum_i \mathcal{R}_i$  as  $N$  equations for the polariton condensates  $\psi_i = K(|\mathbf{r} - \mathbf{r}_i|)\psi(\mathbf{r} - \mathbf{r}_i, t)$  and  $N$  equations for reservoir densities  $\mathcal{R}_i = K(|\mathbf{r} - \mathbf{r}_i|)\mathcal{R}(\mathbf{r} - \mathbf{r}_i, t)$  noting that  $P(\mathbf{r}, t) = \sum_i P_i = \sum_i P(|\mathbf{r} - \mathbf{r}_i|, t)$ ,

$$f_{\text{Res}}(\mathbf{r}, t) = \sum_i f_{\text{Res}}^{(i)} = \sum_i f_{\text{Res}}(|\mathbf{r} - \mathbf{r}_i|, t):$$

$$i\partial_t \psi_i = -\nabla^2 \psi_i + |\psi_i|^2 \psi_i + g\mathcal{R}_i \psi_i + i(\mathcal{R}_i - \gamma_{in}) \psi_i + i f_{\text{Res}}^{(i)} \psi_i^* + i \sum_{\substack{j=1 \\ j \neq i}}^N \mathcal{J}_{ij} \psi_j \quad (3.24)$$

$$\partial_t \mathcal{R}_i = -(b_0 + b_1 |\psi_i|^2) \mathcal{R}_i + P_i. \quad (3.25)$$

The steady states of Eqs. (3.24, 3.25) correspond to the minima of the XY, when  $f_{\text{Res}}^{(i)} = 0$ , and Ising, when  $f_{\text{Res}}^{(i)} \neq 0$ , models as it becomes evident after we substitute  $\psi_i = \sqrt{\rho_i} \exp[i\theta_i]$  into Eq. (3.25) and separate the real and imaginary parts. The equations read as

$$\frac{1}{2} \partial_t \rho_i = (\mathcal{R}_i - \gamma_{in}) \rho_i + \sum_{j=1, j \neq i}^N \sqrt{\rho_i \rho_j} \mathcal{J}_{ij} \cos(\theta_{ji}) + \rho_i f_{\text{Res}}(\mathbf{r}, t) \cos(2\theta_i), \quad (3.26)$$

$$\partial_t \theta_i = \frac{\nabla^2 \sqrt{\rho_i}}{\sqrt{\rho_i}} - \rho_i - g\mathcal{R}_i + \sum_{j=1, j \neq i}^N \sqrt{\frac{\rho_j}{\rho_i}} \mathcal{J}_{ij} \sin(\theta_{ji}) - f_{\text{Res}}(\mathbf{r}, t) \sin(2\theta_i), \quad (3.27)$$

$$\partial_t \mathcal{R}_i = -(b_0 + b_1 \rho_i) \mathcal{R}_i + P_i(|\mathbf{r} - \mathbf{r}_i|, t), \quad (3.28)$$

where  $\theta_{ji} = \theta_j - \theta_i$ . Here we considered the uniform phase distribution  $\theta_i(|\mathbf{r} - \mathbf{r}_i|, t) \approx \theta_i(t)$  which is a valid assumption near the micropillar's centre, i.e.  $R < R_m$  with  $R_m$  being the micropillar's radius. In case of the *relative* coupling scheme, the fixed points of Eqs. (3.26-3.28) represent the minima of the XY or Ising spin Hamiltonians only for the equal polariton densities across all micropillars, that is, when the condition  $\rho_i(\mathbf{r}) = \rho_j(\mathbf{r})$  stands. Such density equilibration can be robustly achieved by iteratively updating pumping intensity  $P_i$  so that  $\int \rho_i d\mathbf{r} = \rho_0$  for all micropillars, where  $\rho_0$  is the predefined integral luminosity. In contrast, the *absolute* coupling model naturally optimises the XY and Ising models and doesn't require the equalised polariton densities due to the coupling coefficients  $\mathcal{J}_{ij} = |\psi_i| J_{ij} / |\psi_j|$  that represent the exchange of a fixed number of photons between sites. The steady state solution of Eqs. (3.26-3.28) is given for both coupling models by equations:

$$(\mathcal{R}_i - \gamma_{in}) = - \sum_{j=1, j \neq i}^N J_{ij} \cos(\theta_{ji}) - f_{\text{Res}}^{(i)} \cos(2\theta_i), \quad (3.29)$$

$$\mu - \frac{\nabla^2 \sqrt{\rho_i}}{\sqrt{\rho_i}} + \rho_i + g\mathcal{R}_i = \sum_{j=1, j \neq i}^N J_{ij} \sin(\theta_{ji}) - f_{\text{Res}}^{(i)} \sin(2\theta_i) \quad (3.30)$$

$$\mathcal{R}_i = P_i (b_0 + b_1 \rho_i)^{-1}, \quad (3.31)$$

where  $\mu$  is the global oscillation frequency shared between all condensates at a coherent state.

One can see from the Eq. (3.31) that for a fixed point solution the maximised total polariton density corresponds to the minimum of the total reservoir density, which together with Eq. (3.29) leads to the minimisation of the spin Hamiltonians:

$$\begin{aligned} \max \sum_{i=1}^N \int_{\Omega} \rho_i d\mathbf{r} &\Leftrightarrow \min \sum_{i=1}^N \int_{\Omega} \mathcal{R}_i d\mathbf{r} \Leftrightarrow \min H_{\text{XY|Ising}} \\ H_{\text{XY|Ising}} &= -\frac{1}{2} \sum_{i,j=1}^N J_{ij} \cos(\theta_{ij}) - \sum_{i=1}^N \left( \int_{\Omega} f_{\text{Res}}^{(i)} d\mathbf{r} \right) \cos(2\theta_i), \end{aligned}$$

where  $\Omega$  denotes the plane of the microcavity. The resonant force term  $f_{\text{Res}}^{(i)}$  acts as a penalty in the objective function and leads to optimisation of the Ising model. At the same time, the XY Hamiltonian is optimised for the zero penalty term. We note that the term  $g\mathcal{R}_i$  has a destabilising effect on the steady states solutions corresponding to minima of spin Hamiltonians meaning that small exciton-polariton interactions and/or small exciton reservoirs  $\mathcal{R}_i$  could possibly improve the optimisation accuracy. In experiments, a small reservoir density can be achieved for a high conversion rate of excitons into polaritons or by spatially separating polaritons from the reservoir by considering, for example, trapped condensates.

### 3.5.2 Minimisation of the XY and Ising models on arbitrary graphs

The validity of the proposed *relative* and *absolute* coupling models is verified by applying the two-dimensional Eqs. (3.24, 3.25) for optimisation of the XY and Ising Hamiltonians on various coupling matrices. Firstly, we determine the minimum value of the coupling strength required for the phase-locking of two condensates. Figure 3.15(top) shows the phase difference for a polariton dyad in the case of different interaction strengths with a zero time delay. We simulate 50 random initial conditions for each coupling strength and calculate the phase difference between the condensates in a final steady state. The region of decoupled condensates can be identified for coupling strengths  $|J_0| \lesssim 0.02$  by observing random phase differences between the condensates in Fig. 3.15(top). The condensates become phase-locked for bigger coupling strengths and can reach the ferromagnetic ground state for positive couplings or antiferromagnetic ground state for negative couplings. The local minima become unstable for coupling strengths bigger than 0.05 when the system finds the ground state regardless of the initial conditions. The demonstrated minimum coupling strengths for phase-locking of two condensates are similar for both *relative* and *absolute*

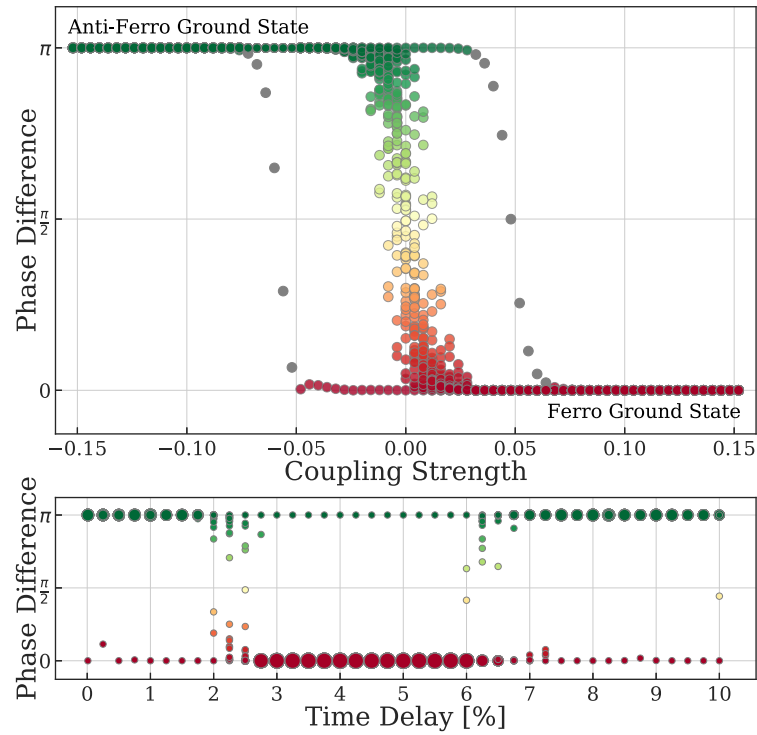


Fig. 3.15 Top: Phase difference as a function of coupling strength for a polariton dyad. The Eqs. (3.24, 3.25) are simulated for 50 random initial conditions for each coupling value. The coherence occurs for the absolute values of strengths greater than 0.02 leading to ferromagnetic state with 0 phase difference for positive couplings and to antiferromagnetic state with  $\pi$  phase difference for negative couplings. The slowly decaying unstable solutions are shown in grey. Bottom: Phase difference as a function of time delay for a polariton dyad. The time delay percentage is defined with respect to the time required to reach a steady state in the absence of delay. The scatter point size indicates how many states out of 50 initial conditions end with a particular phase difference. The coupling strength between condensates is chosen to be  $J_0 = -0.1$ . The expected antiferromagnetic state is observed for time delays  $\tau < 2\%$  and followed by the region with decoupled condensates. The further phase-locking of condensates becomes possible for bigger time delays due to the global phase presence.

coupling models in the case of the XY model. For the Ising Hamiltonian, the destabilisation of excited states (local minima) happens for bigger coupling strengths of about  $|J_0| \geq 0.07$ . This is, therefore, the minimum coupling strength needed for the system to find the dyad's ground state independently of the initial conditions. We note that the presence of intrinsic noise has a positive effect on destabilising such local minima.

In an experimental implementation of interactions, a possible time delay  $\tau$  may appear in constructing couplings between the network elements due to multiple reasons, including the phase readout time, the time required to re-route photons or the time for adjusting an SLM. As a result, the delayed phase information of condensates at time  $t - \tau$  will be used for creating couplings between the condensates at time  $t$  whose phases will be shifted due to the global oscillation frequency. To demonstrate this effect of a time delay in realising coupling strengths between different micropillars, we consider the *absolute* coupling model in optimising the XY Hamiltonian. Figure 3.15(bottom) shows the phase difference dependence on the time delay for the polariton dyad with the coupling strength  $J_0 = -0.1$ . The percentage time delay is defined as a ratio to the time  $T$  required for the dyad to reach a steady state without delay. We simulate 50 random initial conditions for each time delay value and show the resulting phase difference with scatter points of varied sizes proportional to the fraction of initial conditions that lead to this phase. The anticipated antiferromagnetic ground state is observed for time delays  $\tau$  up to 2%. The previously unstable local minimum, i.e. a ferromagnetic state with 0 phase difference for  $J_0 = -0.1$ , becomes now stable in the presence of time delay.

Interestingly, the subsequent de-synchronisation area is followed by a clear ferromagnetic coupling between condensates, followed by another antiferromagnetic area for  $\tau > 7\%$ . This peculiar synchronisation behaviour can be attributed to the global phase rotation with frequency  $\mu$  of each condensate, leading to phase-locking of condensates with an additional  $\pi$  phase difference for large time delay values. This time delay effect is similar for both coupling schemes in simulating either spin Hamiltonian. Although for networks of condensates, the presence of a time delay would result in a phase lag in Eqs. (3.29-3.31) which for significant  $\tau$  can decrease the optimisation accuracy of the XY Hamiltonian, but not Ising. For simplicity, in the following investigations, we will not consider any time delay in the couplings.

Having established the minimum coupling strength for phase-locking of two condensates, we now consider nine fully connected polariton condensates. Each condensate is created with a non-resonant Gaussian pump in a lattice of 3 by 3 condensates (see Fig. 3.16(a)). To realise spatially non-interacting polariton condensates we introduce a dissipative profile as shown in Fig. 3.16(b) where the absence of particle outflows is ensured by the high value of  $\gamma_{\text{out}} = 100$  outside nodes compared to low  $\gamma_{\text{in}} = 1$  values inside nodes. A random interaction

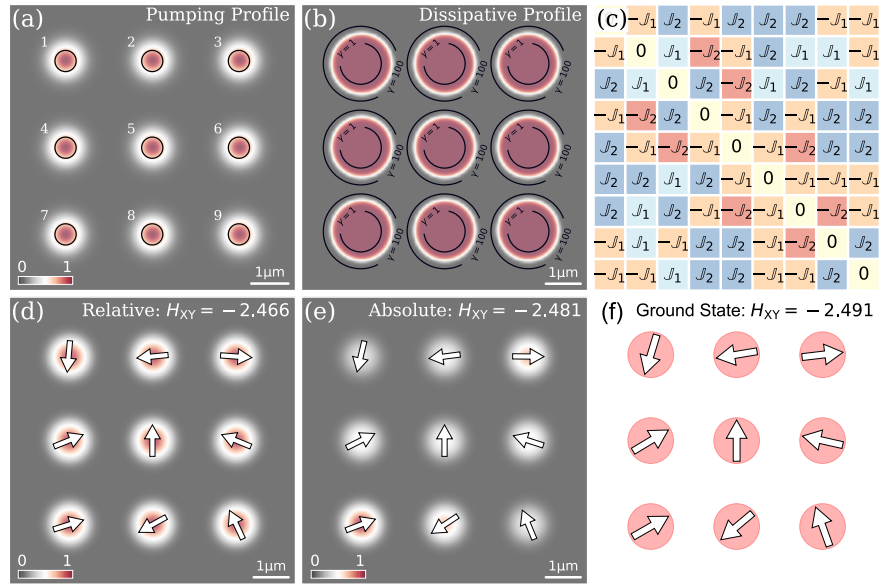


Fig. 3.16 The XY Hamiltonian is minimised for a problem of size  $N = 9$  with a  $3 \times 3$  polariton lattice by simulating Eqs. (3.24, 3.25). The intensity distribution of the incoherent pumping profile  $P(\mathbf{r})$  is shown in (a). The condensate emissions within the black circles are used for couplings between condensates. The dissipative profile for realising spatially isolated polariton pillars are presented in (b). The fully connected coupling matrix  $J$ , which is randomly constructed from  $J_1 = 0.05$  and  $J_2 = 0.1$  of random signs, is shown in (c). The polariton density profiles and phase configurations are plotted for *relative* and *absolute* coupling models in (d-e), respectively. The white arrows represent the phase difference relative to the central condensate (the vertical arrow). The corresponding energy values of the XY Hamiltonian are shown in the top-right corner. The XY Hamiltonian ground state solution is verified by the gain-dissipative and the basin-hopping algorithms in (f).

matrix is constructed of positive and negative couplings of amplitude  $\{0.05, 0.1\}$  as shown in Fig. 3.16(c). As an illustrative example, we apply the *relative* and *absolute* coupling models described by Eqs. (3.24-3.25) for optimising the XY Hamiltonian ( $f_{\text{Res}} = 0$ ). In the former case, the densities of condensates are iteratively equalised over time by individually adjusting pumping intensities  $P_i$ . On the other hand, the *absolute* coupling model does not require equal polariton densities at the steady-state and, consequently, non-equal densities can be realised in a final state. The phase configurations and corresponding density profiles are shown in Fig. 3.16(d-e) for the lowest energy states out of 10 runs for both models. To quantify the optimisation performance of coupling models, we consider the median accuracy that is defined by proximity to the ground state:

$$\text{Median Accuracy} = \left\langle \frac{H_{\text{Relative|Absolute}}}{H_{\text{Ground State}}} \right\rangle. \quad (3.32)$$

where  $H_{\text{Relative|Absolute}}$  is the spin Hamiltonian energy for the phase configurations obtained with the mean-field approach (Eqs. (3.24, 3.25)) in case of the *relative* or *absolute* coupling schemes,  $H_{\text{Ground State}}$  is the ground state energy found by the classical optimisation algorithms. In Fig. 3.16(d-e), the found minima are within 1% and 0.4% from the XY Hamiltonian ground state that was verified with the gain-dissipative [20] and the basin-hopping [175] algorithms (Fig. 3.16(f)). The median accuracy over 100 random fully-connected matrices of size  $N = 9$  generalises to 99.2% and 99.5% for the XY Hamiltonian in case of the *relative* and *absolute* coupling models, respectively.

To investigate the performance of the proposed polaritonic XY-Ising machine on the bigger size problems, an analysis of the optimal range of coupling values and edge density effects is required. In what follows we study the *relative* and *absolute* coupling models on the random unweighted MaxCut problems for the XY and Ising spin Hamiltonians. For the unweighted MaxCut problem, one seeks to divide the graph into two subgraphs with the maximised number of edges between them. As it was mentioned in Introduction, this problem is known to be NP-hard and can be mapped to the Ising Hamiltonian by assigning antiferromagnetic couplings  $J_{ij} = -1$  to the graph edges. We construct three such random adjacency matrices  $\mathcal{A}$  of size  $N = 16$  of degree 5, 9, and 13. Both coupling models are simulated on matrices  $J = -J_0\mathcal{A}$  with amplitudes  $J_0$  in the range  $[0.001, 0.3]$ . For each coupling strength amplitude, the Eqs. (3.24, 3.25) are simulated for 20 random initial conditions. Figure 3.17(a-b) shows the ground state proximity as a function of  $J_0$  amplitude for the XY Hamiltonian. The optimal range of couplings with the median accuracy over 90% can be identified for the amplitudes in the range  $[0.01, 0.11]$  for the *relative* coupling model and slightly smaller range of  $[0.02, 0.1]$  for the *absolute* coupling model. For the Ising model,

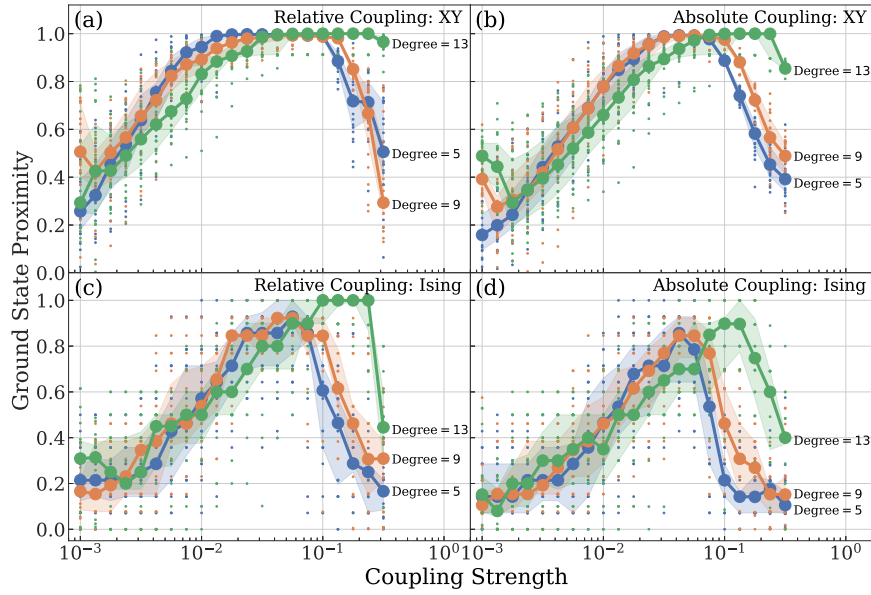


Fig. 3.17 Optimal amplitude range is studied for *relative* and *absolute* coupling models on the unweighted MaxCut problems of size  $N = 16$  with degrees 5, 9, and 13. The median accuracy is shown for the XY Hamiltonian in (a-b) and the Ising Hamiltonian in (c-d). Both models are simulated with Eqs. (3.24, 3.25) for 20 random initial conditions per each coupling strength. Shading indicates 25th and 75th percentile range of instances.

a smaller batch of coupling amplitudes allows one to achieve the median accuracy greater than 90% (see Fig. 3.17(c-d)). Such difference between the optimal coupling ranges can be possibly anticipated since the hard problems for the Ising Hamiltonian are not necessarily hard for the XY Hamiltonian optimisation. The clear shift to bigger optimal couplings for bigger edge densities ( $> 0.8$ ) is especially pronounced for the Ising Hamiltonian. This analysis confirms the lower bound and provides the upper bound of the coupling strength  $J_0$  for achieving higher optimisation accuracies for both models. We note that the ground states of the Ising Hamiltonians were verified with the gain-dissipative [20] and CIM [21] algorithms.

With the identified optimal range of coupling amplitudes, we apply the *relative* and *absolute* coupling models to the larger spin Hamiltonian problems. Table 3.1 shows the median accuracy for both coupling models simulated on 20 unweighted MaxCut instances of size 25 and 49 with edge density of 50%. For such connectivity, we pick the amplitude strength of  $J_0 = 0.04$  from the optimal range. The number of initial conditions is fixed to 20 per coupling matrix. We say that the coupling matrix  $J$  is globally optimised if the actual ground state is found at least once out of 20 runs for the Ising Hamiltonian. In the case of the XY Hamiltonian, we require at least one phase configuration that is closer than 98% to the

ground state for claiming global optimisation. This number of globally optimised interaction matrices is indicated in parentheses in Table 3.1. The *relative* coupling model shows consistently better performance on both the Ising and XY Hamiltonians than the *absolute* coupling model. The less accurate results for the Ising Hamiltonian, which are even more pronounced for the *absolute* coupling model, maybe due to the greater hardness of generated interaction matrices for discrete optimisation than continuous. The drastic difference between coupling models could be possibly mitigated with a better choice of  $J_0$  or may be a signal of a better local minima escape mechanism of the *relative* scheme. Nevertheless, the demonstration of the optimal performance of either of the proposed coupling methods is not the focus of this Section since standard heuristic algorithms can easily outperform both methods. Instead, the achieved results demonstrate a proof-of-principle for using polariton condensates, modelled with the mean-field approach governed by Eqs. (3.24-3.25), as the XY-Ising computing machine.

## Feasibility of experimental implementation

The spatially non-interacting condensates can be experimentally realised using lithographically etched micropillars or with trapped polariton condensates. The couplings are established remotely according to the elements of the coupling matrix  $J_{ij}$ . We envision two types of remote couplings. In the first scheme, couplings are constructed by redirecting the emission of each condensate with either free-space optics or optical fibres to an SLM. At the SLM, the signal from each node is multiplexed and redirected to other nodes with the desired coupling strength  $J_{ij}$  allowing one, in principle, to create an all-to-all coupled network. Each matrix of couplings  $J$  can be programmed on the SLM in advance. We refer to this implementation

Table 3.1 The Ising and XY spin Hamiltonians are minimised with *relative* and *absolute* coupling models on unweighted MaxCut problems of size 25 and 49 with edge density 0.5. The median accuracy of both models is calculated for 20 random initial conditions per each coupling matrix which was further averaged over 20 random coupling matrices with coupling strength  $J_0 = 0.04$ . The number in parentheses indicates how many problems with different coupling matrices were globally optimised. The ground state solutions are calculated with the gain-dissipative and the basin-hopping algorithms for the XY Hamiltonians and the gain-dissipative and CIM algorithms for the Ising Hamiltonians.

Problem Size	Relative		Absolute	
	XY	Ising	XY	Ising
25 ( $5 \times 5$ lattice)	99.3% (20)	87.8% (20)	96.8% (20)	72.9% (14)
49 ( $7 \times 7$ lattice)	98.2% (20)	81.7% (4)	93.3% (3)	52.3% (0)

as *all-optical* implementation. In the second approach, the frequency and phase of the condensate emission are read out and fed forward to an additional resonant excitation. Such resonant excitation will have to be iteratively updated based on the phase and energy of the emission until the polariton network synchronises. Consequently, the time-performance of the second scheme would be dependent on the operational frequency of the reading system and the SLM, which could be on the order of a few kHz [176].

The comparable or better time-performance can be achieved with the digital micromirror devices, which have a similar millisecond operational time-scale, or with electro-optical modulators that can operate at a nanosecond scale. We will refer to this implementation as *hybrid-classical* since the condensate must first form to acquire a well-defined phase that is read out and passed to other nodes. Note that in both implementations, we consider symmetric interactions  $J_{ij} = J_{ji}$  for any two condensates in a network, though directional interactions can be readily constructed, e.g. by using an optical isolator.

In addition to two possible experimental implementations of the remote coupling control, we propose two kinds of couplings: *absolute* and *relative*. The *absolute* coupling scheme implies the exchange of equal amounts of photons (identical signals' intensities) between  $i$ -th and  $j$ -th nodes, which guarantees that the occupation of the condensates pumped with equal intensities remains the same. In the *relative* coupling scheme, the condensates are coupled at the rate defined by relative intensities of emission and, therefore, a further density adjustment is required [20]. This adjustment is crucial for the operation of nonequilibrium condensates, lasers or DOPOs as the density heterogeneity changes the values of the coupling strengths. Since the equilibration of densities will be done at the operation frequency of the SLM, the *relative* coupling model shares the same limitations as the *hybrid-classical* implementation.

Thus, the *absolute* coupling scheme with the *all-optical* implementation may lead to a *pure* polaritonic XY-Ising machine for optimising spin Hamiltonians since it doesn't require any external control: all couplings of a given spin Hamiltonian can be programmed on the SLM in advance. By approaching the condensation threshold from below, the polariton network will condense at one of the lowest energy states corresponding to a local or global minimum of the spin Hamiltonian. The term "pure" indicates that the system can operate at its physical time-scale, i.e. picosecond scale for the polariton condensation. Among other pure physical simulators are the time delay CIM [177] and the recently proposed pure molecular simulator [178]. The *absolute* coupling scheme with the *hybrid-classical* implementation as well as the *relative* coupling scheme with either of the proposed implementations would lead to the classical hybrid polariton simulators with an operational time limited by the frequency of the SLM. These approaches would be reminiscent of the CIM with measurement feedback via FPGAs [58, 179] or hybrid molecular simulator [178].

The potentially advantageous performance of the polaritonic machine in optimising spin Hamiltonians stems from the nature of polariton quasiparticles. Polariton condensates have a much stronger nonlinearity (coming from self-interactions between polaritons) than any of the purely photonic or laser-based optimisers. The stronger interactions should allow easier and faster exploration of phase configurations during the condensation process and narrower line width for the final measurement. In addition, the Bose-condensation process itself may facilitate the efficient low-energy sampling of spin Hamiltonians in a polariton simulator thanks to quantum effects present during the coherence formation.

### 3.6 Conclusions

The optical approach of imprinting two-dimensional regular polariton lattices can offer the potential for rapid scalability to several thousands of condensates. For several simple configurations of spatially interacting condensates discussed in this Chapter, the observed phase configurations realise ferromagnetic and antiferromagnetic configurations or their mixture. The spatially varied dissipation profile and additional resonant pumping could allow one to study the rich dynamics of unequally coupled oscillators of different nature, continuous and discrete. With the addition of the density equilibration framework, the Ising and XY models can be possibly minimised for graphs of spatially coupled oscillators with nearest neighbour interactions. Moreover, *relative* and *absolute* remote coupling schemes could be considered to tackle arbitrary graphs. These theoretical and numerical elucidations, together with experimental results, create the foundations for the further development of a scalable polaritonic XY-Ising machine.

## **Chapter 4**

# **Nature-inspired algorithms for evaluating unconventional computing machines**

## 4.1 Gain-dissipative approach for minimising spin Hamiltonians

It is no wonder that the advent of unconventional ways of finding ground states of spin Hamiltonians is accompanied by the development of new classical algorithms. In this Section, motivated by the operation of gain-dissipative physical systems, we develop a new class of classical gain-dissipative algorithms for solving continuous and discrete optimisation problems. The robustness of such iterative algorithms is demonstrated by solving problems of various sizes and coupling structures. Most importantly, these algorithms can be used as a benchmark for the performance of the physical gain-dissipative simulators.

Operational principles of the gain-dissipative simulator with  $N$  coherent centres were formulated for minimisation of the spin Hamiltonians in Section 3.2. The following set of rate equations summarises them:

$$\frac{d\Psi_i}{dt} = \Psi_i(\gamma_i - |\Psi_i|^2) + \sum_{j,j \neq i} \Delta_{ij} K_{ij} \Psi_j + f_{\text{Res}} \Psi_i^*, \quad (4.1)$$

$$\frac{d\gamma_i}{dt} = \varepsilon(\rho_{\text{th}} - \rho_i), \quad (4.2)$$

$$\frac{dK_{ij}}{dt} = \hat{\varepsilon}(J_{ij} - \Delta_{ij} K_{ij}), \quad (4.3)$$

where  $\Psi_i(t)$  is the complex-valued function that describes the state of the  $i$ -th site,  $\gamma_i$  is the effective gain rate at site  $i$ ,  $f_{\text{Res}}$  represents the strength of the resonant force. As shown in the previous Chapter, the individual control of injection rates is required for the steady-state solutions to coincide with the minima of a given spin Hamiltonian. Hence, gain rates  $\gamma_i$  have to be dynamically adjusted to bring all sites to the specified number density  $\rho_{\text{th}}$ . This density equilibration is achieved by Eq. (4.2) where  $\varepsilon$  controls the speed of gain adjustments.

Coupling strengths are represented by  $\Delta_{ij} K_{ij}$  in Eq. (4.1). In these couplings, the gain rates changing interaction strengths are incorporated in  $\Delta_{ij}$  and separated from other coupling mechanisms represented by  $K_{ij}$ . The case of  $\Delta_{ij} = 1$  physically corresponds to the site-dependent dissipative coupling. In this case, we assign  $K_{ij} = J_{ij}$  and equations simplify to

$$\frac{d\Psi_i}{dt} = (\gamma_i - |\Psi_i|^2)\Psi_i + \sum_{j \neq i} J_{ij} \Psi_j + f_{\text{Res}} \Psi_i^*, \quad (4.4)$$

$$\frac{d\gamma_i}{dt} = \varepsilon(\rho_{\text{th}} - \rho_i). \quad (4.5)$$

We shall refer to the numerical realisation of Eqs. (4.4, 4.5) as the gain-dissipative algorithm ('GD'). In contrast,  $\Delta_{ij} = \gamma_i^{\text{inj}}(t) + \gamma_j^{\text{inj}}(t)$  is appropriate for the description of geometrically coupled condensates. For that case, the coupling strengths change in time and have to be dynamically reconfigured depending on injection rates so that the minimum of a given spin Hamiltonian with interaction strengths  $J_{ij}$  can be achieved. This procedure is realised via Eq. (4.3) where  $\hat{\epsilon}$  controls the rate of the coupling strengths adjustments. We will refer to the model based on Eqs. (4.1-4.3) as the modified gain-dissipative algorithm ('GD-mod').

After substituting  $\Psi_i = \sqrt{\rho_i} \exp[i\theta_i]$  and separating real and imaginary parts in Eq. (4.1), the equations on the number density  $\rho_i$  and phase  $\theta_i$  become

$$\frac{1}{2}\dot{\rho}_i(t) = (\gamma_i - \rho_i)\rho_i + \sum_{j:j \neq i} \Delta_{ij}^{\text{inj}} K_{ij} \sqrt{\rho_i \rho_j} \cos \theta_{ij} + f_{\text{Res}} \rho_i \cos(2\theta_i), \quad (4.6)$$

$$\dot{\theta}_i(t) = - \sum_{j:j \neq i} \Delta_{ij}^{\text{inj}} K_{ij} \frac{\sqrt{\rho_j}}{\sqrt{\rho_i}} \sin \theta_{ij} - f_{\text{Res}} \sin(2\theta_i), \quad (4.7)$$

where  $\theta_{ij} = \theta_i - \theta_j$ . The fixed point of Eqs. (4.3, 4.6, 4.7) are

$$\rho_i = \rho_{\text{th}} = \gamma_i + \sum_{j:j \neq i} J_{ij} \cos \theta_{ij} + f_{\text{Res}} \cos(2\theta_i), \quad (4.8)$$

with the total number of particles in the system given by

$$\mathcal{N} = N\rho_{\text{th}} = \sum_i \gamma_i + \sum_{i,j:j \neq i} J_{ij} \cos \theta_{ij} + f_{\text{Res}} \sum_i \cos(2\theta_i). \quad (4.9)$$

Such value of the total number of particles will be first reached at the minimum of  $\sum_i \gamma_i$  and, therefore, at the minimum of the spin Hamiltonian given by

$$H_s = - \sum_{i,j:j \neq i} J_{ij} \cos \theta_{ij} - f_{\text{Res}} \sum_i \cos(2\theta_i). \quad (4.10)$$

This equation represents the general functional that the GD and GD-mod algorithms optimise. The nonzero term  $f_{\text{Res}}$  represents the penalty forcing phases to be 0 or  $\pi$ , which implies that the minima of Eq. (4.10) coincide with the minima of the Ising Hamiltonian. If  $f_{\text{Res}} = 0$ , then Eq. (4.10) represents the XY Hamiltonian.

The NP-hardness assumption suggests that not only any classical algorithm but also any physical simulator cannot escape the exponential growth in the number of operations with the size of the problem. To find the global minimum of a spin Hamiltonian with either of the introduced gain-dissipative methods, one would need to span an exponentially growing number of various phase configurations. This can be achieved by an exponentially slow

increase of gain rates when approaching the threshold or exponential growth in the number of runs when exploring different noise seeds. Here we focus on the second option as it is more practical and corresponds to the operation of the actual physical simulators. We further demonstrate the performance of these gain-dissipative algorithms on the medium scale Ising and XY models.

#### 4.1.1 Minimisation of the XY Hamiltonian

We illustrate operational principles of the gain-dissipative algorithm by minimising the XY Hamiltonian for a fully connected coupling matrix of small size  $N = 20$  with randomly distributed coupling strengths between  $-10$  and  $10$ . We simulate the GD algorithm governed by Eqs. (4.4, 4.5) with  $f_{\text{Res}} = 0$  using the 4th-order Runge-Kutta integration scheme. At the first stage of the time evolution, i.e. when  $t < 120$  in Figure 4.1(a), the densities are well below the threshold and phases span various configurations in Figure 4.1(b) with all injection rates being similar, as shown in Figure 4.1(c). When certain nodes reach and overcome the prescribed density threshold, the injection rates are individually adjusted to bring all the node densities to the same value. At the same time, phases stabilise and realise the minimum of the XY Hamiltonian.

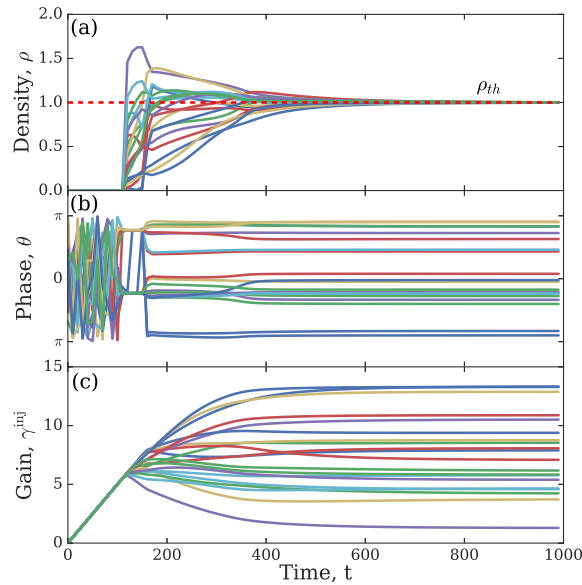


Fig. 4.1 The operational principle of the gain-dissipative algorithm: the number densities  $\rho$  (a), the phases  $\theta$  (b), and the injection rates  $\gamma$  (c) are shown as functions of time for all network elements by simulating Eqs. (4.4, 4.5) with  $f_{\text{Res}} = 0$ . The interactions between elements are given by the fully connected matrix with random coupling strengths taken from the range  $[-10, 10]$ .

We further verify that the proposed gain-dissipative algorithms can find global minima with a sufficient number of runs on small and mid-scale problems. To characterise the performance of these iterative approaches, we compare them to the standard heuristic solvers: Monte Carlo sampling (MC) and the basin-hopping (BH) algorithm, which are built-in optimisation methods of the well-known Scipy optimisation library in Python. We generate a random starting point at each run of the MC algorithm and use the local optimisation algorithm to find the nearest local minimum. Applying such a simple MC method allows us to evaluate both the roughness of the energy landscape of problem instances and evaluate the gain-dissipative algorithms' ability to escape from local minima. The BH algorithm is an iterative stochastic algorithm that is known to be efficient for a wide variety of problems in physics and chemistry [175] and outperforms common heuristic methods such as MC sampling or simulated annealing. At each iteration, the BH method performs a random perturbation of the coordinates with a local minimisation followed by the acceptance test of new coordinates based on the Metropolis criterion. Thus, comparing to the BH method allows us to evaluate better the performance of the proposed gain-dissipative algorithms on the minimisation of the XY model.

Both approaches, MC and BH, depend on a local minimisation algorithm for the optimal descent to a local minimum. Among other local optimisation algorithms, the quasi-Newton method of Broyden, Fletcher, Goldfarb, and Shanno (L-BFGS-B) has shown the best performance on the XY model. This method is designed for large-scale problems with a good performance on non-smooth optimisation problems [180, 181]. We use the L-BFGS-B algorithm as a local optimiser at each step of the BH and MC methods for achieving their best performance. In addition, both BH and MC algorithms are supplied with the analytical Jacobian of the objective function for better time performance.

Next, we generate 50 real-valued symmetric coupling matrices of two types for XY minimisation to compare the performance of gain-dissipative algorithms with BH and MC methods. We consider fully connected graphs with elements that are randomly distributed in  $[-10, 10]$  and sparse 3-regular graphs where each node is randomly connected to exactly three other nodes and coupling strengths are randomly generated from the interval with the random bounds from  $\{-10, -3, 3, 10\}$ . For each such matrix, we simulate all algorithms for 500 random initial conditions. The best found minima of the XY model match to ten significant digits across all methods. The average distribution of counts over various dense matrix instances is shown in Figure 4.2(a-d) for  $N = 50$  as a function of proximity to the optimal solution. All methods show similar performance and achieve the proximity of optimal solutions over 97% for the majority of runs, with slightly better results for the GD and BH methods. The difference between methods becomes more noticeable on sparse

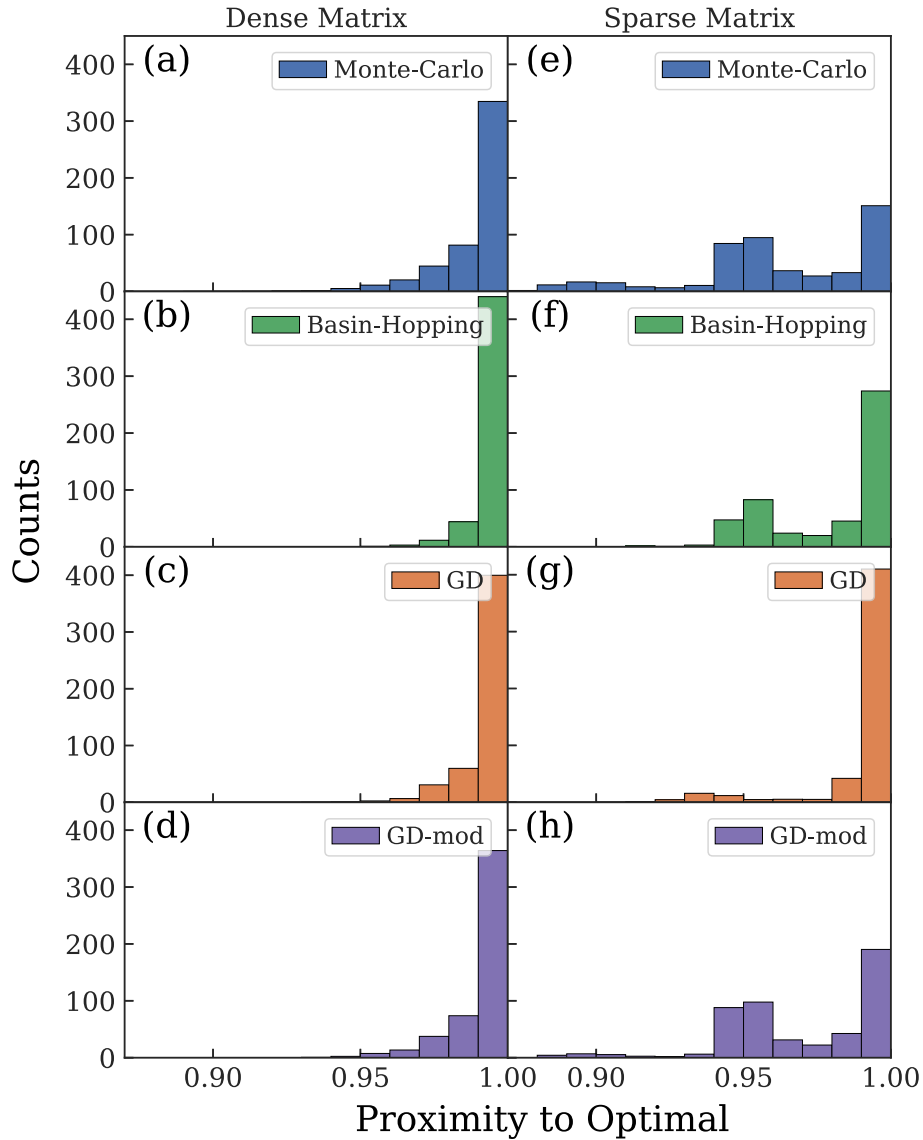


Fig. 4.2 The count number dependence on the proximity to the optimal solutions of the XY Hamiltonian is shown for several methods: (a,e) Monte-Carlo sampling, (b,f) basin-hopping, (c,g) gain-dissipative algorithm (GD) based on Eqs. (4.4, 4.5), and (d,h) the modified gain-dissipative algorithm (GD-mod) based on Eqs. (4.1-4.3). The results of 500 runs are averaged over 50 real symmetric coupling matrices  $J$  of size  $N = 50$  for (a-d) dense and (e-h) sparse matrices described in the main text. The number of internal BH iterations is set to ten.

graphs in Figure 4.2(e-h). Here the GD algorithm demonstrates higher success rates for better solutions' quality than all other methods. In contrast, the performance of the GD-mod method is still similar to that of MC sampling.

Thus, the GD-mod algorithm allows one to find the lowest energy minima of the XY model, albeit the better performance could be achieved with the GD method, which does not include the updates of geometric couplings described by Eq. (4.3).

### 4.1.2 Minimisation of the Ising Hamiltonian

To illustrate the possibility of minimising the Ising model with the gain-dissipative algorithms, we consider the GD algorithm in the presence of the resonance term, i.e. when  $f_{\text{Res}} \neq 0$ . As discussed in the Introduction, the minimisation of the Ising model can be mapped to the MaxCut optimisation problem for which the well-known benchmark set of problems exists, *G-Set*. Hence, we evaluate the GD algorithm on  $G_1 - G_{10}$  instances of size  $N = 800$ . Although the  $G_1 - G_5$  instances are unweighted and  $G_6 - G_{10}$  instances are weighted with elements from  $\{-1, 1\}$ , we simulate the GD method for the same numerical parameters to demonstrate its robustness. For each instance, we perform 100 runs and limit the computational time to 35 – 40s on a single-core CPU. The performance of the GD algorithms is demonstrated in Figure 4.3. The average cuts are within 0.2 – 0.3% for  $G_1 - G_5$  and 1.1 – 1.8% for  $G_6 - G_{10}$  from the optimal MaxCut values [19], which are plotted with coloured rectangles.

The time performance of the standard heuristic methods is highly dependent on a particular instance and for  $G_1 - G_{10}$  varies from 13s to 317s for *breakout local search* algorithms [19] and is within 100 – 854s for *GRASP tabu search* [182], though their average solutions are much closer to the optimal values. The GD algorithm shows similar performance on the problems of bigger sizes. In particular, all found solutions out of 100 runs are within 1.1% of the best known optimal solution for the  $G_{70}$  of size  $N = 10000$ . These results are achieved with an average computational time per run of 530s, equivalent to 1000 time iterations on a single-core CPU, compared to 11365s of the breakout local search algorithm.

The performance of the GD algorithm can be further improved by tuning the parameters  $\rho_{\text{th}}$ ,  $\varepsilon$ , and  $f_{\text{Res}}(t)$  time dependence, which can be done with machine learning techniques such as the M-LOOP algorithm [183]. As a possible modification to the GD algorithm, one can consider individual time-dependent injection rates  $\varepsilon_i(t)$ . For minimising the Ising model, the introduced GD algorithm can be still outperformed by the best available physics-inspired solvers, including the chaotic amplitude control method [184], discrete simulated bifurcation algorithm [185], and parallel tempering [186]. Nevertheless, implementing the gain-dissipative algorithms in physical systems, i.e. GD simulators, will enjoy a super-fast operation and parallelism in processing various phase configurations as the system approaches

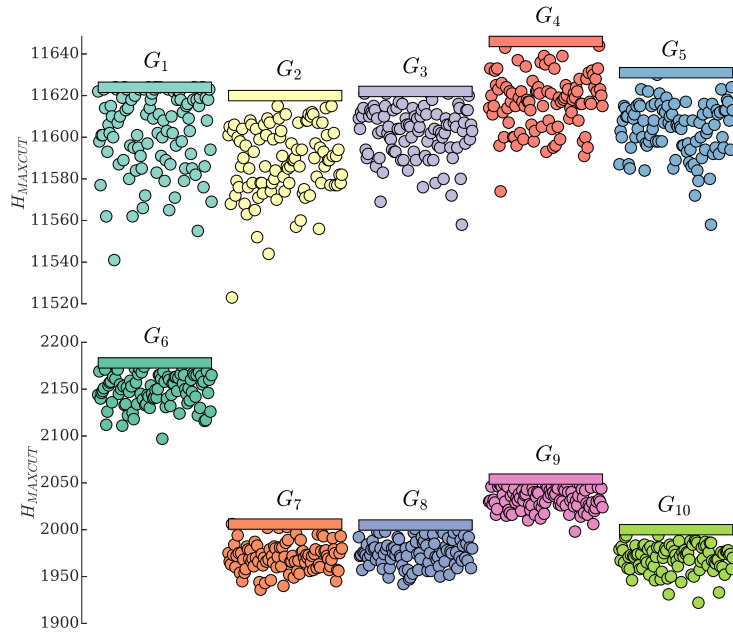


Fig. 4.3 The gain-dissipative algorithm, governed by Eqs. (4.1-4.2), is applied to the MaxCut optimisation problem formulated on  $G$ -Set instances  $\{G_1 - G_{10}\}$  of size  $N = 800$ . The found optimal values are shown with scatter plots for 100 runs on each  $G_i$ . The best known optimal values are plotted with coloured rectangles for each  $G_i$ .

the minima from below even if the system behaves entirely classically. Further acceleration could be expected if quantum fluctuations and quantum superpositions contribute to the processing of phase configurations. Therefore, the proposed GD algorithm shows a promise of physical Ising machines to compete with the classical optimisation techniques.

The operational principles of Ising machines can be suited to the structure of some problems but not others. To develop a standardised procedure for the performance evaluation of emerging physical simulators and physics-inspired algorithms, we evaluate the optimisation complexity of several problems in the next Section.

## 4.2 Computational complexity continuum within Ising formulation of NP problems

A promising approach to achieve computational supremacy over the classical von Neumann architecture explores classical and quantum hardware as Ising machines. Solving the Ising model is  $\mathbb{NP}$ -hard problem with computational hardness proven for certain coupling matrices [16]. From the computational complexity theory perspective, the exponential growth does not necessarily apply to all instances of an optimisation problem, that is shown to be  $\mathbb{NP}$ -hard in general, admitting the worst-case scenario when a mere handful of instances are truly hard to optimise. Selection of the hardest instances within  $\mathbb{NP}$ -hard classes could be the key to determining the computational advantages of small and medium-size simulators and may lead to a reliable generalisation of their optimisation performance to a larger scale.

Given existing small and medium-scale simulators, considerable attention is devoted to problems that can be mapped to the Ising model with zero overhead. A common example includes the MaxCut class of problems in which one looks for the cut of the given graph into two subsets with the largest number of their connecting weighted edges. The subclass of unweighted graphs is attractive for experimental implementation since it only requires the realisation of antiferromagnetic couplings ( $J_{ij} < 0$ ) of the same amplitude, i.e.  $J_{ij} = -1$  if spins  $i$  and  $j$  are connected, and 0 otherwise. Since the unweighted MaxCut problem is  $\mathbb{NP}$ -hard [187], the instances of unweighted  $k$ -regular graphs, in which each spin is randomly connected to  $k$  other spins, are often used to study new and compare existing physical simulators [58, 61, 59, 66, 188]. The 3-regular MaxCut problems are used in the proposal of the quantum approximate optimisation algorithm [189] with its later experimental demonstration on superconducting qubits [190].

Another common practice is to consider the unweighted MaxCut problems on circulant graphs. Circulant graphs are defined by symmetric circulant adjacency matrices where  $(i + 1)$ -th row is a cyclic shift of  $i$ -th row by one element to the right. Subclasses of circulant graphs include complete graphs, cyclic graphs, Möbius ladder and many others [191, 192]. Efficient quantum walks are implemented on circulant graphs with sampling problem shown to be intractable for classical hardware [193]. The complete unweighted graphs with antiferromagnetic couplings can be optimised for large sizes up to 80000 with the photonic Ising machine [66]. The unweighted Ising model on the Möbius ladder graph formally belongs to the MaxCut problem and has the circulant adjacency matrix with nonzero elements of the first row at 0,  $N/2$ , and  $N$ -th positions, where  $N$  is an even number. For the Möbius ladder of size  $N = 100$ , the ground state can be found with a probability of 21% for the coherent Ising machine based on optical parametric oscillators [58, 194, 195]

and a success rate of 34% is demonstrated with optoelectronic oscillators [196]. The 3% ground state probability is reported for the larger Möbius ladder of size 300 on the analogue coupled electronic oscillator machine [197]. The Möbius ladders become typical candidates for evaluating the performance of physical platforms [198, 199] and an exponential time increase on the graphs up to 800 nodes has been reported [200].

Ordinarily, it is tempting to assume that choosing any instance of a general class of  $\text{NP}$ -hard problems is equivalent to considering a hard instance, thereby ignoring the possibility of that instance being in the  $\mathbb{P}$ -class. In this Section, we probe an instance complexity between the two extremes. To detect easy instances within the Ising model, we propose an ‘optimisation simplicity criterion’. We provide numerical evidence of such optimisation simplicity for instances covering a wide range of problems from spin glass models to 3-regular MaxCut problems. As an illustrative example of easy instances of the unweighted 3-regular MaxCut problem, the Möbius ladder graphs are shown to be polynomially solvable. In particular, greater than 99% ground state probability can be ensured with the quadratic increase in the number of time iterations for the Hopfield-Tank algorithm [7] on graphs up to 10000 size. Moreover, the mathematical complexity of the weighted Ising model on the Möbius ladder graphs is shown to be in  $\mathbb{P}$ -class, and the super-linear scaling for its computational complexity is demonstrated with the exact commercial solver, Gurobi. With a simple Möbius ladder at one end and hard random 3-regular graph on the other, the relative computational hardness of intermediate graphs with rearranged edges is investigated. The percentage of rewired edges in the Möbius ladder, that is required to achieve an average hardness of an arbitrary 3-regular graph, depends on the optimisation technique and can vary from 2 – 5% to 40 – 50%, as evidenced by the time performance of several heuristic algorithms and Gurobi solver.

The Ising models satisfying the proposed optimisation simplicity criterion are not limited to circulant matrices and include sparse and dense interaction matrices of various topologies with or without a magnetic field. For some Ising models, such as the Mattis model, unweighted spin glasses on a torus, and biased ferromagnet on Chimera graph, we find that all instances are solvable in polynomial time. There also exists a high probability of finding simple small size random instances of  $\text{NP}$ -hard problems, as we confirm for 3-regular MaxCut, Sherrington-Kirkpatrick, and other spin glass models, with couplings taken from the Gaussian and bimodal distributions. Understanding the average instance complexity of  $\text{NP}$ -hard problems and having a robust way to identify the polynomially easy instances could help evaluate the general potential of small and medium-scale simulators in solving hard combinatorial optimisation problems.

### 4.2.1 Optimisation simplicity criterion for the Ising model

The original work of Hopfield and Tank [7] introduced an analogue computational network for solving difficult optimisation problems. The network, later termed the Hopfield-Tank (HT) model or HT neural network, is governed by the equations:

$$\frac{dx_i}{dt} = -\frac{x_i}{\tau} + \sum_{j=1}^N J_{ij}v_j + I_i^b, \quad v_j = g(x_j), \quad (4.11)$$

where  $x_i(t)$  is a real input that describes the state of the  $i$ -th network element at time  $t$ ,  $\tau$  is the decay parameter,  $\mathbf{J}$  is the symmetric coupling matrix,  $I_i^b$  are the offset biases (external fields) that can be absorbed into  $\mathbf{J}$  by introducing an additional spin,  $N$  is the size of the network, and  $g(x_i)$  is the activation function. The nondecreasing monotonic function  $g(x_i)$  is designed to limit possible values of  $v_i$  to the  $[-1, 1]$  range and is typically chosen as a sigmoid or hyperbolic tangent. The steady states of the HT model (4.11) are the minima of the Lyapunov function  $E$ :

$$E = -\frac{1}{2} \sum_{i,j=1}^N J_{ij}v_i v_j - \sum_{i=1}^N I_i^b v_i + \frac{1}{\tau} \sum_{i=1}^N \int_0^{v_i} g^{-1}(x) dx. \quad (4.12)$$

In the high-gain limit, when  $\tau \rightarrow \infty$  or  $g$  approaches a step function  $g(x) = 1$  ( $g(x) = -1$ ) if  $x \geq 0$  ( $x < 0$ ), the minima of  $E$  occur at  $v_i = \{-1, 1\}$  and correspond to the minima of the Ising model. If the high-gain limit conditions are violated (low-gain limit), the minima of  $E$  are not necessarily at  $v_i = \{-1, 1\}$  and can be inside the hypercube  $[-1, 1]^N$ . By projecting non-integer amplitudes of the steady-state at the end of the simulation, the allowed minimiser of the Ising model is restored at the nearest hypercube corner. Therefore, the HT network tends to locate local minima if it minimises the Ising model at all, as has been recognised in earlier works [8]. Remarkably, there exist simple coupling matrices  $\mathbf{J}$  that can be globally optimised even in this low-gain limit. For zero fields in both limits, the steady states are completely characterised by the coupling matrix eigenvalues  $\lambda_i$  and corresponding orthogonal eigenvectors  $\mathbf{e}_i \in \mathbb{R}^{N \times 1}$  with coupling matrix expressed as  $\mathbf{J} = \sum_{i=1}^N \lambda_i \mathbf{e}_i \mathbf{e}_i^T$ . In the presence of degenerate or zero eigenvalues, the eigenvectors form a subspace of rank lower than  $N$ . Denoting components of  $\mathbf{v}$  in the space of coupling matrix eigenvectors as  $\gamma_i$  and the null

subspace component as  $\mathbf{q}$ , the amplitudes and energy can be written as

$$\mathbf{v} = \sum_{i=1}^N \gamma_i \mathbf{e}_i + \mathbf{q}, \quad (4.13)$$

$$E = -\frac{1}{2} \sum_{i=1}^N \lambda_i \gamma_i^2 + \frac{1}{\tau} \sum_{j=1}^N \int_0^{v_j} g^{-1}(x) dx. \quad (4.14)$$

To minimise  $E$ , the components  $\gamma_i$  should be increased for positive  $\lambda_i$  and decreased otherwise. This observation reveals the nature of how the HT algorithm functions: it changes amplitudes  $v_i$  in a way that gradually favours the larger positive eigenvalues  $\lambda_i$  [9]. Therefore, in the low-gain limit, the HT algorithm finds the minimum of the Ising model that corresponds to the largest positive (dominant) eigenvalue. Suppose this minimum happens to be the global minimum, which is valid for many problems selected for testing the Ising Hamiltonian minimisers. In that case, the corresponding instances should be considered polynomially simple for optimisation, as we further explain.

The choice of the HT algorithm in our analysis is not accidental and is prompted by its ability to replicate the dynamic behaviour of many existing Ising simulators considered in optics, photonics, and electronics. For instance, the recent memristor-based annealing system operates as a Hopfield neural network [201]. Another example is the coherent Ising machine on the optical parametric oscillators that is commonly thought to be similar to HT networks with nonlinear saturation of amplitudes and, therefore, both are often compared [61]. For such gain-dissipative computing machines, the successive better minima toward the dominant eigenmode [202] are achieved via a series of bifurcations [203].

In general, the global minimum of the Ising Hamiltonian would correspond to a nontrivial direction in the eigenspace of  $\mathbf{e}_i$  in Eq. (4.14). This obvious yet substantial observation leads to our proposal for ‘*optimisation simplicity criterion*’ (OSC): the instance of a hard problem should be regarded as computationally simple for optical and electronic analogue machines, if the ground state minimiser  $\mathbf{s}_{\text{gs}}$  of the Ising Hamiltonian  $H_{\text{Ising}}$  is located at the hypercube corner of the projected dominant eigenvector  $\mathbf{e}_{\text{max}}$ , corresponding to one of the largest eigenvalues  $\lambda_{\text{max}}$  of the coupling matrix  $J$ :

$$E_\lambda = \min H_{\text{Ising}} = -\frac{1}{2} \mathbf{s}_{\text{gs}}^T \mathbf{J} \mathbf{s}_{\text{gs}}, \quad \mathbf{s}_{\text{gs}} = \text{sign}(\mathbf{e}_{\text{max}}). \quad (4.15)$$

Without the loss of generality, the fields (the biases in HT networks) are assumed to be zero since they can always be incorporated into the coupling matrix  $\mathbf{J}$  with an additional spin. The OSC provides an upper bound for the ground state energy of the Ising model. Eigenvalue analysis is common to many polynomial-time algorithms that approximate both lower and

upper bounds for optimal solutions to complex combinatorial problems [204, 205]. For the MaxCut problem, the eigenvalue minimisation is known to be equivalent to semidefinite programming [206], which in turn makes it equivalent to the eigenvalue maximisation that the Hopfield-Tank algorithm does for the Ising model.

The standard procedure for verifying whether a particular instance satisfies the OSC would be to compare the upper bound energy  $E_\lambda$ , which corresponds to the dominant eigenvector, with the global minimum obtained with a physical simulator or an optimisation algorithm. If these two energies coincide, the instance should be considered trivial to optimise. The polynomial complexity of instances satisfying the OSC could be recovered with the HT algorithm Eq. (4.11), which is naturally designed to project the input vector into a subspace that is dictated by the eigenvalues of the coupling matrix. For an instance to violate the OSC, it is sufficient to show that it has energy lower than  $E_\lambda$ . The complexity of the instances that do not satisfy the OSC can be further assessed by other means. For example, the optimality gaps could be evaluated using the exact solvers such as Gurobi, or the time to solution metric could be considered for heuristic solvers, as we show below.

### 4.2.2 Minimising Ising model on Möbius ladder graphs

As an illustrative example, we apply the HT algorithm Eq. (4.11) with a hyperbolic tangent activation function to a particular topology of unweighted 3-regular graphs, namely the Möbius ladder graph. The two representations of this cubic circulant graph of size  $N$  are shown in Fig. 4.4A. When  $n = N/2$  is an even number, antiferromagnetic interactions cause lattice frustrations that result in  $N$  degenerate ground states with two frustrated edges (shown in red) between two domains of  $n$  anti-aligned spins and the ground state energy of  $(3n - 4)$ . Figure 4.4B demonstrates a typical simulation of the HT network for the Möbius ladder of size  $N = 1000$ . The ratio of the HT energy, found by associating spins with the signs of amplitudes  $v_i$  at the steady-state, to the ground state energy is defined as the proximity to the ground state. The network operates in the low-gain limit (see Appendix B for parameters) and, hence, the amplitudes  $v_i$  are not binary when the steady-state is reached. Yet, by gradually favouring the eigenvectors with larger eigenvalues, the HT algorithm moves spin states through the hypercube interior over time and achieves the global minimum, although the coupling matrix is modified by non-equal continuous amplitudes  $v_i$  in  $[-1, 1]$ . The necessity of homogeneous amplitudes for minimising non-trivial spin Hamiltonians with gain-dissipative networks was discussed earlier in the Section 3.2. All states of the low energy spectra  $E_{\lambda_i}$  in Fig. 4.4B correspond to the eigenvectors of the largest eigenvalues of the interaction matrix, whose analytical expressions are available for the Möbius ladder as a representative of circulant matrices.

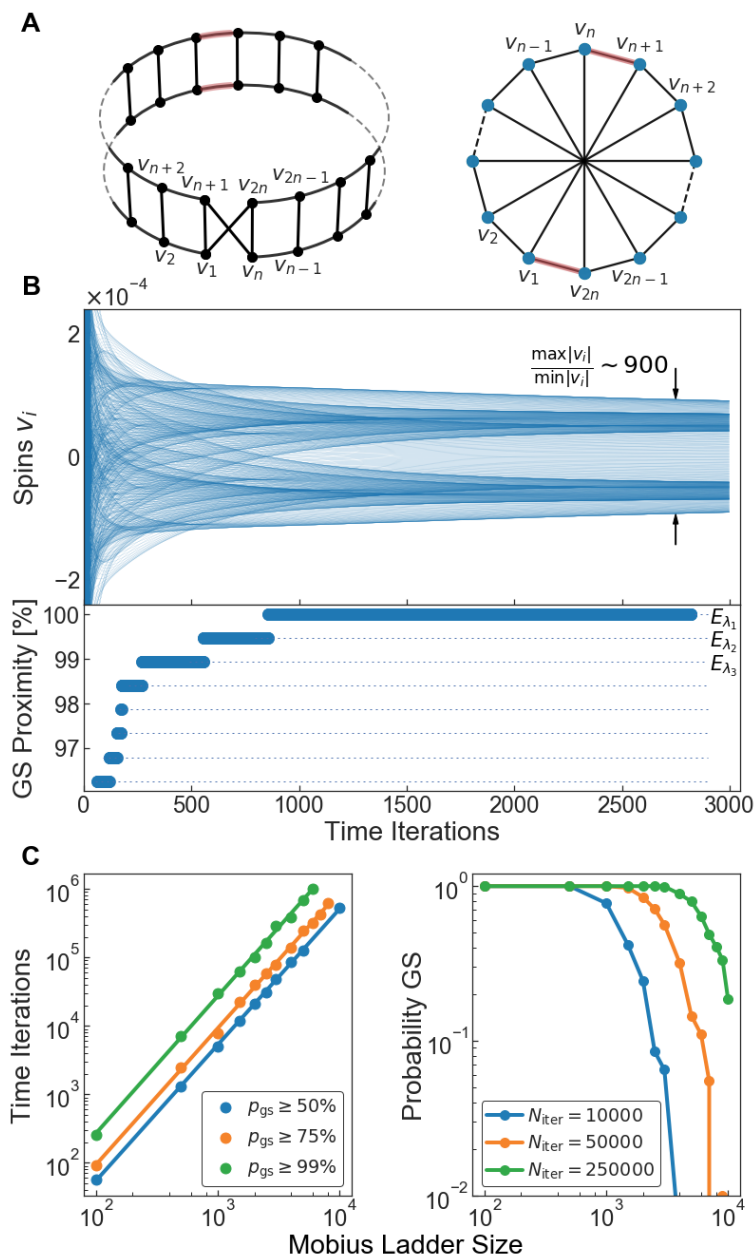


Fig. 4.4 (A) Illustration of the Möbius ladder graph on Möbius strip (left) and on circular graph (right). Two possible frustrated edges in the ground state are highlighted in red. (B) The evolution of amplitudes  $v_i$  (top) for the Möbius ladder graph of size  $N = 1000$  over  $N_{iter} = 3000$  time iterations of the Hopfield-Tank algorithm with the corresponding proximity to the ground state shown below. All low energy levels  $E_{\lambda_i}$  correspond to the projected eigenvectors  $sign(\mathbf{e}_i)$  of the distinct largest eigenvalues  $\lambda_i$ . (C) The number of time iterations  $N_{iter}$  of the Hopfield-Tank algorithm for optimising Möbius ladder graphs of sizes up to  $N = 10000$  with desired ground state probability ranges of  $p_{gs} \in \{50 - 55\%, 75 - 80\%, 99 - 100\%\}$  are shown on the left panel. The solid lines correspond to a quadratic fit confirming that the Ising model on Möbius ladder graphs can be solved in polynomial time. The number of algorithm runs per each graph size is fixed to 250. The ground state probabilities as a function of Möbius ladder size are shown for the fixed number of time iterations  $N_{iter} \in \{10000, 50000, 250000\}$  on the right panel.

To estimate the performance of optical and electronic Ising machines the Möbius ladder graphs, we determine the number of HT time iterations for achieving the ground state with probabilities greater than 50%, 70%, and 99% for problem sizes up to  $N = 10000$ . The ground state probability is defined as the fraction of simulations leading to the global minimum to the total number of simulations. Figure 4.4C(left) shows a polynomial (quadratic) increase in the number of iterations with the graph size, which confirms the optimisation easiness of such problems. The quadratic slope remains the same for each range of the desired ground state probabilities. The ground state probability decreases for the fixed number of iterations as demonstrated in Fig. 4.4C(right), which suggests that the reported quick performance deterioration of the physical Ising machines with the network size [58, 196] may be caused by the fixed amount of internal system loops available in that physical platform. The lack of frustration in the Möbius ladders with odd  $N/2$  does not necessarily mean that the ground state is trivial to reach. We consistently observe that such non-frustrated graphs require larger number of time iterations than frustrated Möbius ladder graphs with even  $N/2$ . Since the complexity of one time iteration of the HT algorithm is determined by the matrix-vector multiplication product as  $\mathcal{O}(kN)$  for  $k$ -regular sparse graphs, the time complexity for globally optimising Ising Hamiltonian on the Möbius ladders scales as  $\mathcal{O}(N^3)$  with the problem size.

Thus, the eigenvalue maximisation principle, which underlies HT algorithm, ignores the energy profile of a simple problem that satisfies the OSC. Even in the absence of a mechanism for exploring the global energy landscape, network elements follow eigenvectors with successively larger eigenvalues. The corresponding consecutive energy states can differ by hundreds of spins, while the Ising Hamiltonian energy monotonically approaches the global minimum. This dynamic behaviour is drastically different from both the Ising machines based on equilibrium systems and optimisation methods, for which the width and height of energy barriers are critical and occasional increases in energy are common once the system escapes local minima. For example, the exponential time scaling for the Ising model on the Möbius ladders was recently reported for the simulated annealing algorithm [200], while unconventional computing platforms based on gain-dissipative networks can efficiently find principal eigenvectors for million size problems [207].

So far we discussed only the computational complexity of the unweighted Ising model on the Möbius ladder graphs. It can be seen that the mathematical complexity of minimising the Ising Hamiltonian on the Möbius ladder topology is in  $\mathbb{P}$ -class. Since the Möbius ladder graph becomes a bipartite graph after removal of two nodes, it belongs to a family of weakly-bipartite graphs [208]. However, the weighted MaxCut problem is in  $\mathbb{P}$ -class for weakly-bipartite graphs [209] and, hence, the Ising model with arbitrary couplings on the Möbius ladder graph is in  $\mathbb{P}$ -class too.

With the understanding of what is essential for an individual instance of the  $\text{NP}$ -hard problem to be counted as simple, we next present a natural approach for restoring complexity and study the continuous complexity transition from simple to hard instances for Ising optimisation on physical Ising machines.

### 4.2.3 Interpolating between simple Möbius ladders and hard 3-regular graphs

We develop a procedure that allows us to continuously ‘tune’ the graph from the Möbius ladders to random 3-regular graphs, the unweighted MaxCut problem on which is known to be  $\text{NP}$ -hard, and thereby to probe the intermediate problem computational complexity. To interpolate between two extremes, we consider the following random rewiring procedure. Starting from the Möbius ladder, we remove and reconnect a pair of edges at random. For each subsequent iteration of the rewiring procedure, a random pair among the original edges (if any) of the Möbius ladder is selected. Hence, intermediate graphs are quantified by the percentage of rewired edges in the Möbius ladder. For the frustrated Möbius ladder graphs to violate the OSC, the rearrangement of two edges is sufficient for any problem size  $N$  as shown in Fig. 4.5A(left) and works for about 85% of the Möbius ladders of size up to 1000 in Fig. 4.5A(right). Both configurations preserve the ground state energy of  $(3n - 4)$  while making the rewired graphs impossible to optimise with the HT algorithm in the low-gain limit even for the smallest problem sizes. For the Möbius ladder with no frustration (odd  $n$ ), the edges  $J_{12}, J_{N-2, N-3}$  could be rewired as  $J_{1, N-3}, J_{2, N-2}$  to violate the OSC for any  $N \geq 10$ . Although satisfying the OSC is sufficient for the certain graph structure to be simple, its violation does not necessarily make the instance hard to solve. Other optimisation approaches have to be tested to estimate the relative hardness.

One way to address the relative complexity is to use exact solvers. For example, the commercial solver Gurobi [210] employs various pre-processing techniques and uses heuristics for accelerating the branch-and-bound algorithm [211] that can be applied to the mixed-integer programming problems. For problems that cannot be exactly solved for a given time limit, Gurobi evaluates the optimality gap defined as:

$$\mathbb{O}_{\text{GAP}} = \frac{E_{\text{best}} - E_{\text{lower bound}}}{E_{\text{best}}}, \quad (4.16)$$

where  $E_{\text{best}}$  and  $E_{\text{lower bound}}$  are the best objective and the lower objective bound, respectively. The size of the optimality gap or the time to reach a particular gap could be used as a performance metric for the problem complexity [212]. Hence, the relative hardness of the

Ising model on the rewired Möbius ladder graphs can be evaluated by the time it takes Gurobi to reach a zero optimality gap.

Another way to evaluate the relative computational hardness is to use heuristic solvers. We consider two physics-inspired algorithms, namely parallel tempering and chaotic amplitude control. The former [213–216] is arguably the current state-of-the-art algorithm that generally shows better or similar performance over other heuristic methods [217, 218, 186], while the latter is inspired by the operation of the Ising machine based on optical parametric oscillators [21, 184]. The operational principles of both algorithms and their optimal parameters are discussed in the Appendix B. The standard quantitative measure of performance of such stochastic algorithms is the time to solution metric [219, 186], which reflects the time it takes to find the ground state with 99% confidence:

$$\text{TTS} = t_{\text{run}} R_{99} = t_{\text{run}} \frac{\log(1 - 0.99)}{\log(1 - p_{\text{gs}})}, \quad (4.17)$$

where  $t_{\text{run}}$  is the time for running an algorithm once,  $R_{99}$  is the number of runs for finding the ground state energy with a probability of 99%, and  $p_{\text{gs}}$  is the ground state success probability.

The computational complexity of the Ising model on 3-regular graphs is interpolated between  $\mathbb{P}$  and  $\mathbb{NP}$  classes in Figure 4.5B, where we use the branch-and-bound, chaotic amplitude control, and parallel tempering methods. For the branch-and-bound algorithm within Gurobi solver, Figure 4.5B(middle) shows the time to zero optimality gap dependence on the percentage of rewired edges in the Möbius ladder graphs of size  $N \in \{100, 200, 300\}$ . For all sizes, the initial exponential increase in time is followed by a plateau starting at about 40–50% of rewired edges. For this percentage of rearranged edges, the still recognisable original four-band structure of the Möbius ladder graph has equivalent complexity of random 3-regular graphs for Ising model minimisation. Such equivalence can be associated with frustrated (unsatisfied) edges, namely edges with different signs of  $s_i s_j$  and  $J_{ij}$ , the number of which is necessarily minimised at the ground state. Rewiring 40% edges in the Möbius ladder for  $N = 100$  introduces about 8% of frustrated edges, which makes its complexity relatively similar to random 3-regular graphs with 8.6% of frustrated edges. For heuristic algorithms, the optimised time to solution metric is shown in Fig. 4.5B(bottom). For each percentage of rewired edges, we minimise the time to solution with the machine-learner online optimisation package [183]. Unlike the branch-and-bound exact solver, the smaller number of rewired edges is required for achieving a time plateau for the considered stochastic algorithms: the relative hardness of the Möbius ladders with around 2% of rewired edges is equivalent to the complexity of random 3-regular graphs. Similar to Gurobi solver, the computational effort scales exponentially with the number of rewired edges for the chaotic

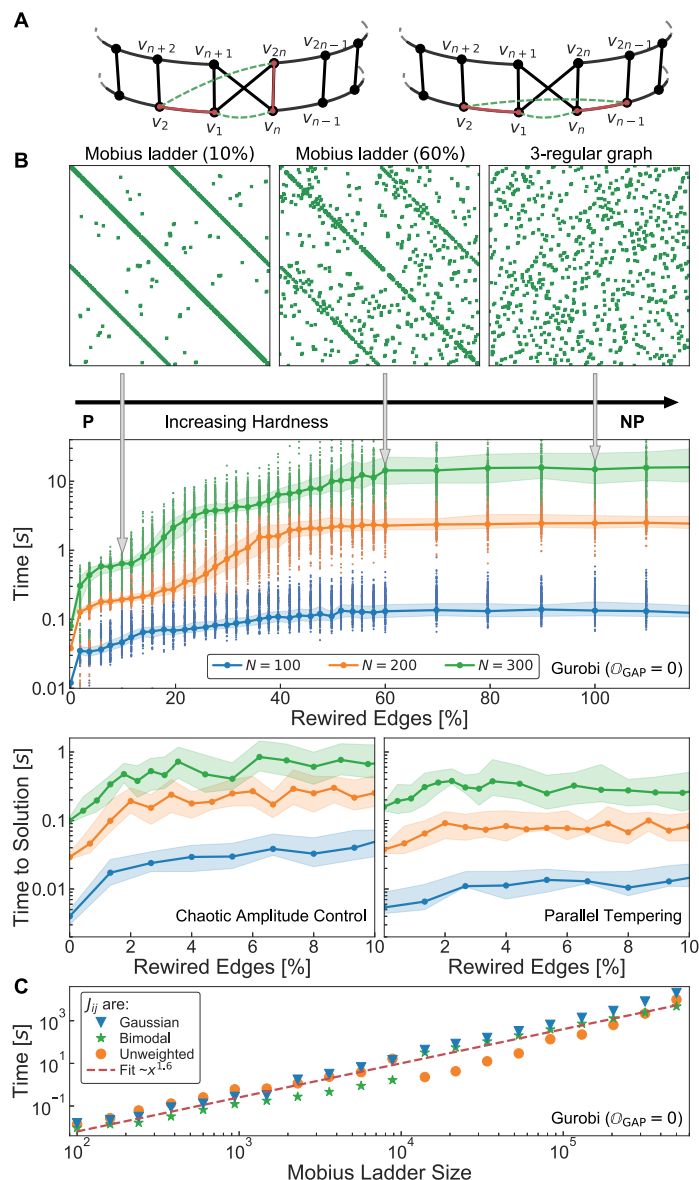


Fig. 4.5 (A) The rewiring procedure of two edges for violating the optimisation simplicity criterion in the Möbius ladder graphs of size  $N = 2n$  for any even  $N$  (left) and most even  $N$  (right). The removed and added edges are shown with red solid and dashed green lines, respectively. (B) The relative computational hardness of the unweighted Ising model on the rewired Möbius ladder graphs is evaluated by the median time required for reaching zero optimality gap with Gurobi solver for problem sizes 100, 200, and 300. The 100 random graphs are optimised for each problem size for every percentage of rewired edges with shaded regions indicating an interquartile range. The median time to solution metric as a function of the percentage of rewired edges in the Möbius ladder graphs is shown at the bottom for chaotic amplitude control and parallel tempering methods. (C) The average computational hardness is evaluated by the median time required for reaching zero optimality gap with Gurobi solver for the Möbius ladder graphs of sizes up to 500000 with couplings from the unweighted, bimodal, and Gaussian distributions. The 10 random graphs are optimised for each problem size.

amplitude control method, although a more modest speed up of 2 – 2.5 times is observed with the parallel tempering.

Evidently, all three considered optimisation techniques can successfully determine the relative easiness of the Möbius ladders for the Ising model. The number of rearranged edges in the Möbius ladder graphs, required for achieving the equivalent computational complexity of random 3-regular MaxCut, depends on the method’s operational principles. As assessed with arguably state-of-the-art heuristics, this relative complexity of rewired graphs leads to a practically significant result. One may consider an existing physical platform that was previously tested on Möbius ladders and construct the graphs with 2-5% of rewired edges with minimal engineering adjustments. The global Ising minimisation of such rewired Möbius ladder graphs would suggest the physical platform’s ability to go beyond the eigenvalue maximisation principle and potentially solve problems that are as hard as random 3-regular MaxCut. Without rewiring, the average computational complexity of the Ising model grows polynomially with the Möbius ladder problem size, as demonstrated for unweighted and weighted graphs with coupling values taken from bimodal and Gaussian distributions in Fig. 4.5C.

#### 4.2.4 General applicability of the optimisation simplicity criterion

Any instance of a problem from the  $\mathbb{P}$ -class is polynomially easy to optimise, while for an arbitrary instance of NP-hard problem, there is no guarantee that the instance is hard. Hardness cannot be guaranteed by violating the proposed OSC, which in itself can only help detect naturally easy instances of NP-hard problems. With the addition of the rewiring procedure proposed above, the relative computational complexity of random graphs can be probed. Till now, the identified simple instances of Ising models were limited to the Möbius ladder graphs. To emphasise the general applicability of the OSC to instances of any NP-hard problem, we show examples of simple graphs in a diverse set of problems that are often chosen to evaluate the performance of the Ising physical machines and computational algorithms.

We apply the OSC to the Ising models with dense, e.g. the Sherrington-Kirkpatrick and the Mattis models, and sparse coupling matrices, where besides 3-regular MaxCut, we examine spin glass models of various topologies including torus, Chimera graph, and 3-regular planar graphs. Where appropriate, in addition to unweighted coupling matrices, we consider commonly chosen probability distributions for interaction strengths such as bimodal, when couplings take values from  $\{-1, 1\}$  with equal probability, and Gaussian, when couplings are distributed around zero mean with unit variance (for the full model descriptions please see Appendix C). Some of these models belong to the  $\mathbb{P}$ -class with all

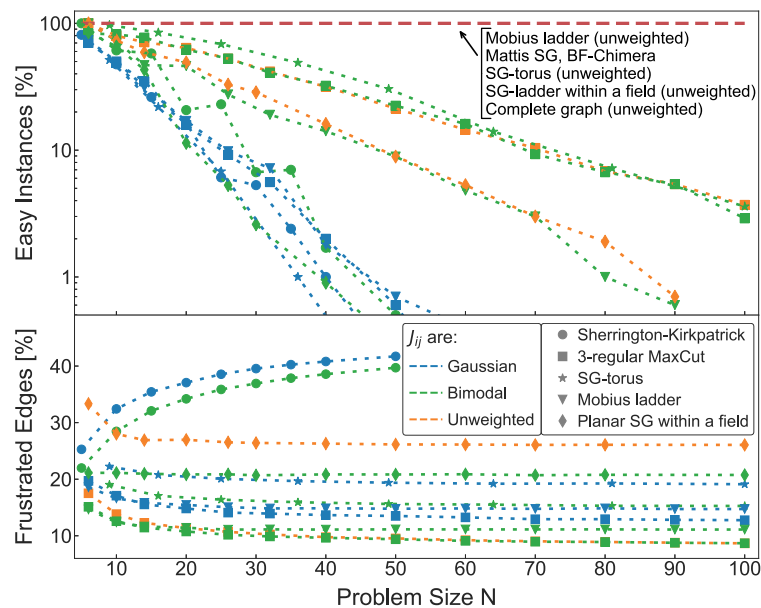


Fig. 4.6 **Probability of finding easy instances for various Ising models.** Fraction of instances, satisfying the optimisation simplicity criterion, is shown as a function of problem size  $N$  for Gaussian, bimodal, and unweighted coupling distributions. The considered Ising models include Sherrington-Kirkpatrick, 3-regular maximum cut, Mattis spin glass, spin glass on a torus, Möbius ladder graphs, biased ferromagnet on Chimera graph, planar spin glass within a magnetic field. The red dashed line represents models which are polynomially easy to optimise across all problem sizes. For each model, 1000 random matrices are generated per each size, and the ground states are verified with the exact Gurobi solver.

instances satisfying the OSC, e.g. the Mattis spin model, unweighted spin glass on a torus, unweighted biased ferromagnet on the Chimera graph, or unweighted ladder graphs with a magnetic field (see Fig. 4.6). For other models, there exist high chances of getting easy to optimise small-size random instances. Across all models, consistently greater probabilities of simple Ising instances are observed for the coupling matrices with values from bimodal and unweighted distributions compared to the Gaussian distribution. Note that in the case of the weighted Möbius ladder graphs, the instances not satisfying the OSC remain easy in terms of both mathematical and computational complexities, as we previously argued.

When testing small-scale Ising simulators, the existence of large fractions of easy instances of NP-hard problems should be taken into account to avoid a misleading assessment of optimisation capabilities of the platform. A hard random instance would possibly be generated for large problem sizes, while small-scale simulators would likely face easy instances satisfying the OSC. As Fig. 4.6 shows, the percentage of frustrated edges in the ground state covers the entire range of possible values confirming that the OSC could help identify simple graphs in low and highly frustrated models.



## **Chapter 5**

# **Other applications for unconventional computing platforms**

## 5.1 Reservoir computing

In addition to a promising Hamiltonian optimisation application, various nonlinear dynamical systems, including electronic [220–222], photonic [223, 224], spintronic [225–227], mechanical [228], and biological [229] systems, have been recently employed as potential reservoirs for reservoir computing (RC) (see [230] and references therein). RC methods, originally referred to as echo state networks [231] or liquid state machines [232], constitute a computational framework for temporal data processing. These methods have been successfully applied to many practical problems involving real data, with most of the studies focused on machine learning applications. The best performance on these applications is usually achieved by applying different reservoir designs to a particular problem and finding an optimal reservoir by evaluating the computational performance, processing speed, power efficiency, and scalability. The role of the reservoir in RC is to nonlinearly map sequential inputs into a higher-dimensional space so that the features can then be extracted from its output with a simple learning algorithm. Therefore, such reservoirs become attractive for experimental implementation in many physical systems. The goal is to design such RC hardware that would perform the high-speed computation for dynamic data and build fast information processing devices with low learning costs.

Networks of non-equilibrium condensates or lasers can serve as interacting nonlinear elements for an efficient network-type reservoir computing system. In particular, many requirements for a physical RC system can be fulfilled by polariton condensates, and indeed the first proposals of such an implementation have appeared [233]. Polariton condensates are scalable to many lattice sites, while high dimensionality is necessary for mapping input data into a high-dimensional space in RC. The polariton network is a strongly nonlinear system which arises from the excitonic part of polaritons. This is necessary for the reservoir to operate as a nonlinear mapping. The presence of short-term memory in polariton systems is supported by many experimental observations of their bistability behaviour [234]. Such memory is necessary to ensure that the reservoir state is dependent on recent-past inputs but independent of distant-past inputs. Thanks to the polariton's photonic component, the rich physical properties of waves such as interference and synchronisation make polariton condensates similar to coupled oscillators (see Section 2.1), and together with a possible on-chip implementation at room temperature with organic materials, they become a compelling candidate for RC [235].

## 5.2 Proof-of-work protocol

This Section suggests a conceptually different scheme of blockchain technology that relies on using unconventional computing platforms. We propose a new generation of proof-of-work protocols that perform a meaningful computation at their core: the minimisation of continuous or discrete spin Hamiltonian problems is completed to add each new block to the blockchain. The modern capabilities of unconventional computing platforms are nearly sufficient for demonstrating computational supremacy over classical computers and, hence, such platforms can provide a greater transaction rate over existing proof-of-work protocols in cryptocurrencies.

### 5.2.1 Introduction to blockchain technology

Blockchain technology with its digital currency, bitcoin, has been introduced a decade ago [236]. Bitcoin is the first decentralised electronic payment system operated by an open peer-to-peer network where a financial transaction happens directly between two willing parties without the need for a trusted intermediary such as banks or other financial institutions. This digital currency initiated the development of many other cryptocurrencies, which attracted significant investments and increased interest in understanding the structure and technological capabilities of the platform. The blockchain platform consists of a publicly accessible database of all transactions arranged into blocks of a certain length in the order preserved by a distributed ledger (see Figure 5.1). Adding each new block of transactions to the blockchain requires solving a computationally demanding problem, i.e. performing a proof-of-work (POW). POW concept is developed initially to prevent junk mails by requiring the sender to solve a moderately complex computational problem to allow the message delivery [237]. The POW concept is implemented in the blockchain by computational nodes that perform complex mathematical calculations and are rewarded with crypto coins. Consequently, the computational nodes are called miners, and the process of completing the computations is called mining.

The common POW problems are based on a function  $H$ , called hash function, which maps an arbitrary sized input data to a fixed size output (called a hash) and is designed to be hard to invert. This means that the hash  $y$  can be easily computed from the initial data  $x$  by calculating  $y = H(x)$  but finding  $x$  from a given  $y$  is computationally hard. The inversion of the hash function requires an exponentially growing computational time of  $\mathcal{O}(2^n)$  where  $n$  is the hash size and can only be completed with brute-force approaches. Still, when  $x$  is found, the validation of the transaction could be quickly done by computing  $H(x)$  and comparing

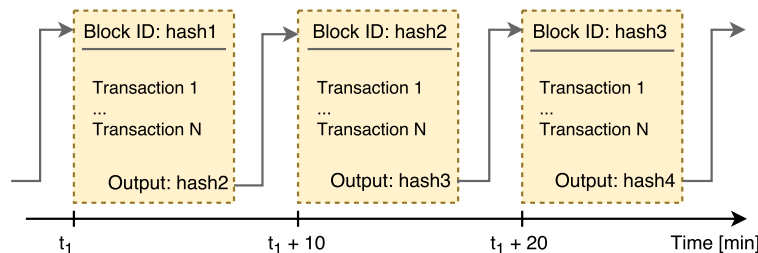


Fig. 5.1 The schematic for blockchain generation by computational nodes in bitcoin cryptocurrency is shown. The block is added to a blockchain with an average interval of ten minutes. The output of each block serves as the name for the next block, thus forming a chain.

the result with the hash  $y$ . This hash is further used as the block header for identifying each block in the blockchain.

The processing time of each new block in a chain depends on the amount of POW performed. The complexity of such work, i.e. mining difficulty for adding a new block, is dynamically controlled to compensate for the increasing computational power and varying interest in running nodes. At the moment, this difficulty target value is updated every 2016 blocks to target the desired block interval accurately, which is set to be ten minutes on average in the case of bitcoin (see Figure 5.1). This ten minutes rate is chosen as an ad hoc tradeoff. If the time is too short, the stability of the blockchain decreases as more forks and longer forks in the blockchain form requiring an increased bandwidth between nodes, so it has to be hard enough for an ordinary CPU to process it instantaneously. On the other side, the time which is too long would increase the block's confirmation time, making it inapplicable for most applications. Other cryptocurrencies can have even shorter times, though their stability and security issues usually remain unclear.

Such a large block's processing time is a major technical obstacle for the broader use of the blockchain, with two main negative consequences. The first is the problem of centralisation. The blockchain is supposed to be insured by distributed computational powers that verify all transactions and agree on what blocks should be in the blockchain. Hence, no specific computer is responsible for a particular transaction. To validate the transaction of a specific block, one can wait until several newer blocks are added to the blockchain, which will automatically validate all of the previously created blocks. Regrettably, about 70% of the cryptocurrencies with the highest capitalisation are currently controlled by a few major computational pools. Such centralised hubs of power lead to a high entry barrier for a new potential computational node since it has to compete with the large computational rate of centralised nodes, which will make the system even more centralised in the nearest future. Possible solutions to such a problem are seemingly mutually exclusive: shortening

the processing time must be accompanied by restrictions on such processing for modest computational powers, but not computational centralisation. Second, a significant block's processing time leads to a considerable transaction confirmation time which prevents traditional payment systems from being replaced by digital cryptocurrencies for routine daily transactions happening in a fraction of a second. These conflicting requirements prevent all of the existing cryptocurrencies from becoming a real electronic payment system.

The growing focus on sustainable practices threatens the existence of rapidly evolving blockchain technologies based on traditional proof-of-work protocols, which consume more than 0.5% of total energy consumption worldwide. Since minimisation of spin Hamiltonians is equivalent to solving practical combinatorial optimisation problems, analogue classical and quantum simulators, based on energy-efficient optical and electronic systems, have the architecture most suitable for realising novel proof-of-work protocols.

### 5.2.2 Proof-of-work through minimisation of spin Hamiltonians

In previous Chapters, we considered several unconventional computing platforms that can potentially outperform classical state-of-the-art algorithms in solving optimisation problems, such as QUBO and QCO. These platforms have either already demonstrated a speedup or can achieve it in the nearest future. Figure 5.2 illustrates the schematics of the POW protocols that are based on solving QUBO or QCO problems using the currently available analogue Hamiltonian simulators.

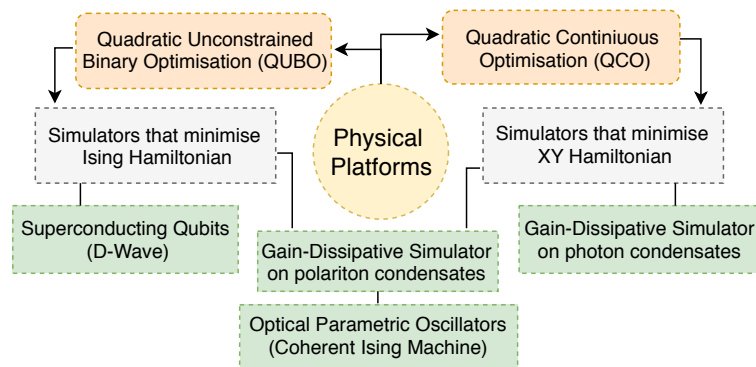


Fig. 5.2 The scheme shows how to use purposely built quantum simulators based on superconducting qubits, optical parametric oscillators, polariton and photon condensates for solving QUBO or QCO problems in the proof-of-work protocol.

The recipe for building a blockchain based on such simulators is essentially the same for all types of simulators. The input for each block will include an additional parameter, namely a matrix of coupling strengths  $J_{ij}$ . The ways of controlling and modifying coupling strengths

are system dependent. For instance, the coupling strengths can be tuned by changing the distance, pumping intensity, and the trap barrier's height in the gain-dissipative simulators. The coupling matrix has to be formed depending on the block content ensuring that nobody can prepare a coupling matrix and solve the corresponding optimisation problem in advance to approve a particular block. For example, the numerical expressions of the order of transactions together with the amount of each transaction could be used to form this matrix. The output of the block consists of the problem optimisers: the resulting "spins"  $s_i$  or phases  $\theta_i$ , that can be further encoded and serve as the next block's name. Verifying whether the block belongs to the chain or not can be done, for instance, by checking that the objective function value for the found optimisers is better than that found by a classical heuristic algorithm.

We schematically demonstrate a simple option for constructing the matrix  $J$  in Figure 5.3(a) where the nodes, i.e. financial parties, are placed around the circle and indexed by  $i$ . Each line corresponds to the transaction between the parties. The transaction amounts  $S_i$  can be used to define the elements of coupling matrix  $J$  as  $J_{i,j>i} = S_i - S_j$  ( $J_{i,j<i} = S_j - S_i$ ) where the nodes are connected using red or blue lines in Figure 5.3(a) for positive and negative  $J_{ij}$ , respectively. The sparsity of such matrix can be fully controlled and regulated by a blockchain protocol allowing, for instance, random connections of each node with up to  $X$  other nodes from at most  $Y$  clusters out of total  $Z$  clusters available. To illustrate the protocol, we randomly generate  $N = 800$  transactions ( $S_i$ ), connect each node with up to 10% of other nodes from at most 50% of clusters out of total 40 clusters and show the resulting matrix in Figure 5.3(b). The lowest excited states of the Ising model are shown in Figure 5.3(c) for three such coupling matrices optimised with the GD algorithm, that has been described in the previous Chapter. The projected performance of a physical GD simulator is shown as an inset in Figure 5.3(c) under an assumption that the pumping feedback mechanism can be physically implemented in  $0.1ms$  (limited by the SLM operational timescale). This inset shows how the average time to find a solution, which is not necessarily the optimal one, increases with a problem size  $N$  for the GD-algorithm much faster compared to its possible implementation in a physical platform. Furthermore, an actual physical simulator will also benefit from simultaneous parallel search through the whole phase space assisted by classical noise and quantum fluctuations. Such results suggest that each block of a blockchain can be processed in a matter of seconds or even less when the POW scheme based on solving NP-hard optimisation problems, e.g. MaxCut problems, will be realised on the real physical simulator.

The above discussion is a simplistic picture of a sophisticated analysis that is yet to be done for designing an actual proof-of-work protocol based on the minimisation of spin

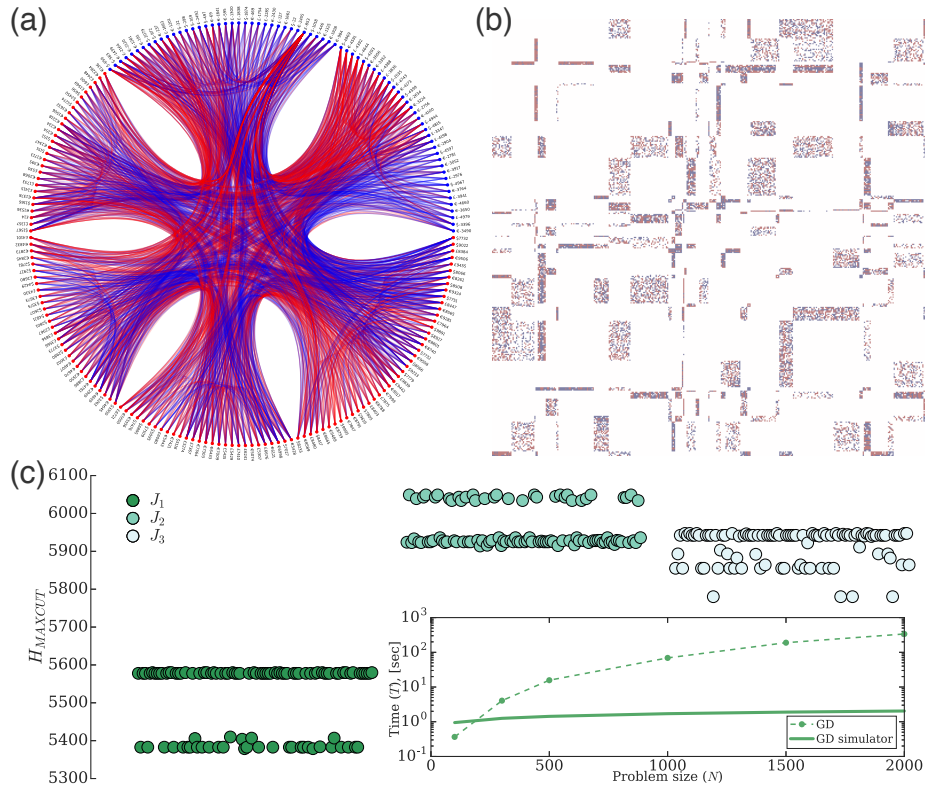


Fig. 5.3 (a) The schematics of mapping the block's information to a coupling matrix  $J$  for solving QUBO or QCO problems as a proof-of-work is shown. Each node is placed around the circle and represents a financial party that transfers (blue dots) or receives (red dots) the money with the nodes being clustered in a few regions, i.e. six regions for 200 nodes shown. The nodes are randomly connected with red or blue lines with respect to positive or negative  $J_{ij}$ , respectively. (b) A typical structure of a random matrix  $J$  of size  $N = 800$  constructed as described in the main text, the positive and negative elements of  $J$  are marked with red and blue colours, respectively. (c) The global and the low energy excited states of QUBO problem for three such randomly generated coupling matrices of size  $N = 800$  denoted by  $J_1$  (dark green),  $J_2$  (green),  $J_3$  (light green). The results show that classical algorithms can often result in finding excited states for such coupling matrices. The inset shows the average time to find a steady-state solution by the GD algorithm as a function of the problem size  $N$  (dashed green line). The projected time of the GD simulator (solid green line) is obtained by multiplying the number of time iterations of the GD algorithm for each size  $N$  with the pumping adjustment time  $0.1ms$ , which is a realistic time for current physical platforms.

Hamiltonians. First, one needs to prove that a coupling matrix constructed in a certain way is not only mathematically difficult, i.e. belongs to  $\text{NP-hard}$ , but also computationally challenging for all state-of-the-art classical optimisation techniques. Second, one needs to ensure that such a coupling matrix corresponds to a practical problem, finding a solution to which is of desire to someone. And third, the minimisation of the spin model on such matrices needs to be performed faster on particular physical platforms than traditional hardware. The first and the last questions could be possibly tackled thanks to the recent advances in artificial intelligence. Inspired by the success of machine learning methods in such games as chess and go, the hardest computational problems of small size could be possibly created with reinforcement learning. For this task, the possible agent policies could be explored for a particular type of interactions between the network elements that, for example, could be taken from the bimodal or Gaussian distributions and certain connectivities, e.g. sparse or dense graphs. The reward procedure could be based on the time performance of the state-of-the-art classical methods, including the traditional simulated annealing and parallel tempering, as well as novel physics-inspired algorithms. Such an approach could help create the hardest problems tailored to a specific optimisation technique, such as quantum annealing, or the most challenging tasks across multiple optimisation algorithms, which would help identify the hardest universal problem. By optimising the performance ratio of classical algorithms and specific physical Ising machines, the hardest Ising instances could be created by taking advantage of a particular physical platform. Finding similar interaction patterns for hard problems of small size would allow one to build the hardest problems of larger sizes for the computational supremacy demonstration of unconventional hardware. Finding connection or mapping of such highly non-trivial problems to solve with real-life tasks could be another interesting challenge.

## 5.3 PageRank algorithm

Access to reliable information has always been and will continue to be critical to people's lives and rights. Diverse ways to retrieve information include text, voice, and image queries to search engines, which systematise human knowledge and provide universal access to hundreds of billions of worldwide web pages (or simply web pages) daily [238]. At a query time, the most relevant pages are returned in a fraction of a second. Behind such impressive time performance lie significant computational resources that can be divided into two categories. First, the semantic meaning of a query is analysed by applying traditional information retrieval techniques, combining advances in computer science and statistics, and machine learning methods, including the latest natural language processing algorithms for context analysis [239]. Millions of pages are retrieved with potentially relevant information to the query. Second, before the search happens, the database of publicly available web pages is precomputed and organised by applying hundreds of ranking metrics covering the linking structure, keywords, location, and content freshness of each page. By combining the ranking scores of these two steps, the final order of the most relevant web pages is determined in response to the query [240].

One ranking algorithm remains in use since the first launch of the Google search engine. The PageRank algorithm [241, 242] evaluates the relative importance of pages by exploiting the web link structure (web graph) solely. The web network is represented as a directed graph, where each page is a node of the graph, and each hyperlink is an edge connecting one page to another. For the entire database of web pages, the PageRank algorithm computes a single score vector, the PageRank vector (or simply PageRank). The algorithm's key underlying assumption is that pages transfer the importance to other pages via links and, hence, the PageRank vector components determine the importance of pages regardless of their textual or visual content and the search query. Mathematically, finding the PageRank vector is equivalent to calculating the principal eigenvector of the link-structure matrix, Google matrix. The general mathematical principles of the PageRank algorithm inspired extensive studies beyond its original use for ranking web search results. A wide range of applications was found in various domains, including social network analysis, recommendation systems, bibliometrics, bioinformatics, DNA sequencing, and distributed computing systems [243, 244].

The ranking of web pages with the PageRank algorithm, which is connectivity-based and query-independent, does not require real-time processing and is computed in advance. Since the principal eigenvectors can be found in polynomial time, the problem of computing the PageRank vector belongs to the  $\mathbb{P}$  complexity class. While being a simple task from the computational complexity theory perspective, the processing of the tens of billions

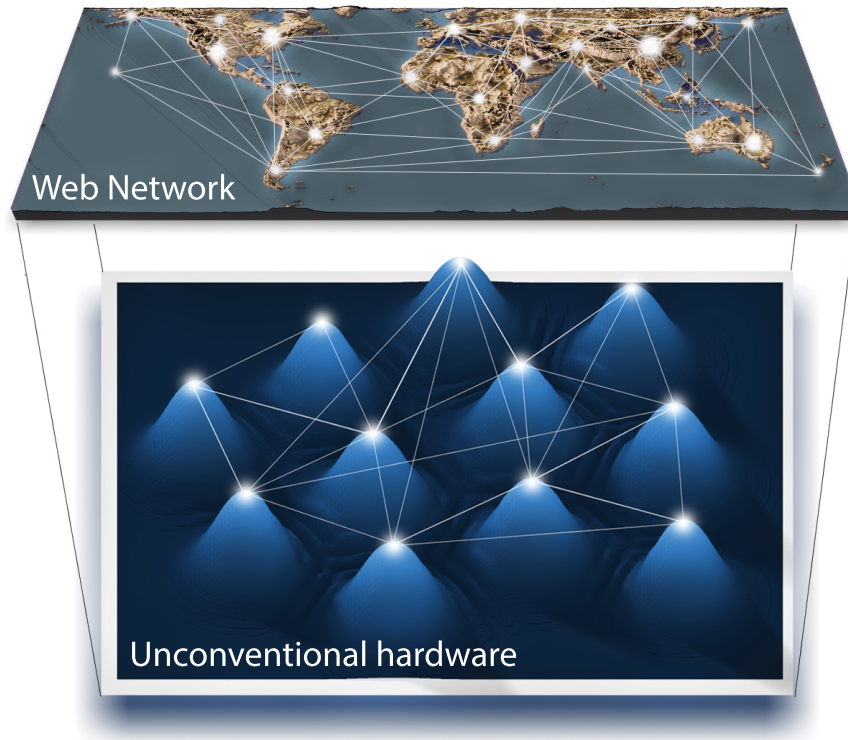
of elements of the link-structure matrix represents a numerical challenge for running the PageRank algorithm on conventional hardware.

Further development of search technologies requires ever-increasing computational resources. Recent advances were achieved with cloud-based tensor processor unit pods with the power of over 100 petaflops and specialised chips designed to accelerate the training of neural networks. Albeit enough computing resources may be available today, the future demand for prodigious amounts of processing power is beyond traditional hardware. The adiabatic quantum algorithm [245] and quantum stochastic walks [246, 247] are considered as potential quantum analogues of the PageRank algorithm. Classical physical systems, such as crosspoint resistive memory arrays [248], are proposed for emulating the original PageRank algorithm based on the power method. In another direction of novel computing, various unconventional physical systems are considered as simulators that can minimise spin Hamiltonians. While the demonstration of the ability of such systems to find the global minima of spin Hamiltonians faster than the classical von Neumann architecture is an ongoing research, many of these disparate physical systems can either efficiently perform matrix-vector multiplication [66, 249–252] or mimic the Hopfield neural networks [253, 201]. For a certain choice of parameters, the time evolution of such networks can be viewed as an eigenvalue maximisation problem [9], which results in finding the energy state dictated by signs of the eigenvector corresponding to the largest eigenvalue of the interaction matrix, i.e. principal eigenvector.

This Section demonstrates that the PageRank algorithm can be naturally simulated on unconventional hardware based on a variety of physical systems. We consider networks of optical parametric oscillators, polariton and photon condensates, coupled lasers, as well as the original Hopfield networks and show their ability to efficiently find principal eigenvectors of the Google matrix (see schematics in Fig. 5.4). We confirm networks' ability to reliably find the PageRank vectors by classifying the importance of pages in actual web graphs with sizes from 500 to 3.5 million, including social and university networks. In addition, the unconventional hardware can offer opportunities for exploring alternative rankings. We show that one of such possible rankings could be based on the minimisation of the XY spin Hamiltonian. We further discuss the feasibility of experimental implementations of the large-scale Google matrices on existing unconventional hardware and argue about the potential improvements in power consumption over classical hardware they could bring.

### 5.3.1 Emulating PageRank algorithm with unconventional networks

*PageRank algorithm.* We start by briefly reviewing the foundations of the PageRank algorithm. The Pagerank algorithm evaluates the importance of web pages based on their connectivity



PageRank:	Alternative Rank:
1 apple	i microsoft
2 google	ii facebook
3 amazon	iii tesla
...	...

Fig. 5.4 The schematics of running ranking algorithms on unconventional hardware is shown. The link-structure of pages is represented as the Google matrix of the web network (top image). This web network is then mapped to unconventional hardware (middle image) that could be based on a variety of physical platforms, including optical parametric oscillators, lasers, polariton and photon condensates. The time-evolution of unconventional networks can mimic the traditional PageRank algorithm and find the principal eigenvector (PageRank) of the Google matrix or offer alternative rankings based on the minimisation of spin Hamiltonians.

via hyperlinks. The web graph is represented by the Google matrix  $\mathbf{G}$  and the power method is used for finding the PageRank vector  $\mathbf{p}$ . In the original algorithm, this method is formulated as [241]:

$$\mathbf{p}^{(k+1)} = \mathbf{G} \cdot \mathbf{p}^{(k)}. \quad (5.1)$$

After a certain number of iterations  $k$ , the power method converges to the principal eigenvector of the matrix  $\mathbf{G}$ , which is known as the PageRank vector. The largest components of the principal eigenvector represent the most relevant pages with ranks given by the indices of ordered decreasing components (the PageRank order  $\mathcal{P}$ ). For a unique stationary solution of the power method in Eq. (5.1) to exist, the Google matrix  $\mathbf{G}$  is constructed as stochastic and irreducible [240, 254, 255]:

$$\mathbf{G} = \alpha \mathbf{P}^T + \mathbf{v}[\alpha \mathbf{d}^T + (1 - \alpha) \mathbf{e}^T] \quad (5.2)$$

where  $\mathbf{P}$  is the transition matrix that represents hyperlink structure of the web,  $\mathbf{d}$  is the dangling vector with  $d_i = 1$  for zero rows of  $\mathbf{P}$  and 0 otherwise,  $\mathbf{v}$  represents a personalisation vector,  $\mathbf{e}$  is the unity vector, and  $\alpha$  is the teleportation (convergence rate) parameter. For  $\alpha \in [0, 1)$ , the Google matrix has a unique principal eigenvector that corresponds to the largest positive eigenvalue  $\lambda_{\max} = 1$  [255]. The details of such construction of the Google matrix are outlined in Appendix D.

To emulate the PageRank algorithm on unconventional hardware, we reformulate the power method of Eq. (5.1) as an iterative scheme on the components  $p_i$ :

$$\frac{dp_i}{dt} = -p_i + \sum_{j=1}^N G_{ij} p_j, \quad (5.3)$$

whose stationary solution realises the principal eigenvector of the Google matrix. As we shall see below, similar dynamic behaviour is reflected by the operation of many physical systems.

*PageRank algorithm on unconventional hardware.* Novel computing paradigms, based on networks of various physical elements from nonlinear oscillators to atoms, may offer a computational advantage over conventional hardware in solving complex optimisation tasks [256], many of which can be reformulated as minimisation of discrete or continuous spin Hamiltonians. Unlike the optimisation of hard optimisation problems, calculating the PageRank vector is a polynomially simple task but of large dimensionality. To determine the requirements for unconventional hardware to simulate the PageRank algorithm or, equivalently, to find the principal eigenvector, we formulate the general dynamic network

description based on physical systems as:

$$\frac{dx_i}{dt} = f_i(x_i) + h_i(x_i) \sum_{j=1}^N \widehat{J}_{ij} g_j \left( \sum_{k=1}^N \widetilde{J}_{jk} x_k \right), \quad (5.4)$$

where  $x_i$  is the real variable that describes a certain measurable physical quantity for each  $i$ -th element of network,  $f_i(\cdot)$  describes the local dynamics,  $h_i(\cdot)$  is an amplification function,  $g_j(\cdot)$  is an activation function,  $\widehat{J}_{ij}$  [ $\widetilde{J}_{ij}$ ] specifies pairwise interactions between  $i$ -th and  $j$ -th elements and  $\widetilde{J}_{ij}$  [ $\widehat{J}_{ij}$ ] is the identity matrix. This generalised class of unconventional networks is reminiscent of two fundamental modelling approaches of neural networks. When  $\widehat{\mathbf{J}}$  is the identity matrix, i.e.  $\widehat{\mathbf{J}} = \mathbf{I}$ , and interactions between elements are governed by  $\widetilde{\mathbf{J}} = \mathbf{J}$ , the time-evolution of Eq. (5.4) represents the static neural network with applications in backpropagation [257]. In the opposite case of  $\widehat{\mathbf{J}} = \mathbf{J}$  and  $\widetilde{\mathbf{J}} = \mathbf{I}$ , the networks of physical elements can be viewed as local field neural models [258]. The latter also represents the Cohen–Grossberg model [259] to which the well-known Hopfield neural networks belong [253]. The ability of both the static and local field neural networks to find the principal eigenvector of the interaction matrix  $\mathbf{J}$  originates from the assumption that their nonlinear dynamics can be linearised to:

$$\frac{dx_i}{dt} = \xi x_i + \beta \sum_{j=1}^N J_{ij} x_j, \quad (5.5)$$

where  $\xi$  and  $\beta$  are the system-dependent parameters. The steady states of the linearised network coincide with the minima of the Lyapunov function, which can be introduced as:

$$\frac{dx_i}{dt} = -\frac{\partial \mathcal{L}}{\partial x_i} \quad \text{where } \mathcal{L} = -\frac{\xi}{2} \mathbf{x}^T \mathbf{x} - \frac{\beta}{2} \mathbf{x}^T \mathbf{J} \mathbf{x}. \quad (5.6)$$

The Lyapunov function can be written for a general asymmetric matrix  $\mathbf{J}$  with a Lyapunov equation although here we assume the matrix to be symmetric for simplicity. The emergence of stable states of Eq. (5.5) can be analysed with the Jacobian matrix with its maximum eigenvalue given by

$$\mathcal{J} = \xi \mathbf{I} + \beta \mathbf{J}, \quad \lambda_{\max}^{(\mathcal{J})} = \xi + \beta \lambda_{\max}^{(\mathbf{J})}. \quad (5.7)$$

The first nonzero stable state occurs when the maximum eigenvalue of the Jacobian is equal to zero, which leads to the critical value  $\xi_{\text{crit}}$ :

$$\xi_{\text{crit}} = -\beta \lambda_{\max}^{(\mathbf{J})}. \quad (5.8)$$

For  $\xi < \xi_{\text{crit}}$ , only the trivial solution  $\mathbf{x} = 0$  exists. At the critical point, the evolution of elements in Eq. (5.5), with time rescaled as  $t \rightarrow \beta t$ , and the Lyapunov function  $\mathcal{L}$  are expressed as:

$$\frac{dx_i}{dt} = -\lambda_{\max}^{(\mathbf{J})} x_i + \sum_{j=1, N} J_{ij} x_j, \quad (5.9)$$

$$\mathcal{L} = \frac{1}{2} \left( \lambda_{\max}^{(\mathbf{J})} \mathbf{x}^T \mathbf{x} - \mathbf{x}^T \mathbf{J} \mathbf{x} \right). \quad (5.10)$$

In this regime, the Lyapunov function is nonnegative, and the network converges toward a stable equilibrium corresponding to the zero minimum value

$$\min_{\xi = \xi_{\text{crit}}} \mathcal{L} = 0 \iff \mathbf{J} \mathbf{x} = \lambda_{\max}^{(\mathbf{J})} \mathbf{x}. \quad (5.11)$$

In case of the Google matrix, the largest eigenvalue is equal to one, namely  $\lambda_{\max}^{(\mathbf{J})} = \lambda_{\max}^{(\mathbf{G})} = 1$ , and the PageRank vector is represented by the network amplitudes at the steady state of equations

$$\frac{dx_i}{dt} = -x_i + \sum_{j=1}^N G_{ij} x_j, \quad (5.12)$$

that is equivalent to the iterative scheme of the power method in Eq. (5.3). Starting with any initial conditions, the solution of Eq. (5.12) will always converge to the equilibrium point of the system corresponding to the principal eigenvector of the Google matrix.

As a demonstration of calculating the PageRank vector on unconventional hardware, we consider networks of elements based on several physical systems, including OPOs, lasers, polariton and photon condensates. These gain-dissipative systems achieve coherent states when the gain exceeds the losses. At the coherence threshold, when  $\xi = \xi_{\text{crit}}$ , the principal eigenvector of the Google matrix can be reconstructed from the network amplitudes of the first stable nonzero steady state. Besides, the PageRank algorithm can be emulated using the Hopfield networks, which can be implemented with photonic [260] and electronic [201] systems. For showing a possible robust emulation of the PageRank algorithm on unconventional hardware, the system-dependent parameter configurations are found analytically for all considered networks whose dynamics at the lowest power consumption regime is equivalent of Eq. (5.12), as discussed in Appendix D.

We consider the Google matrices from small size  $N = 500$  to larger sizes up to  $N = 3.5$  million based on real web graphs of universities, social Networks, frequently co-purchased products, the Wikipedia top categories, and others (see Appendix D for a full description of databases) to show a reliable operation of unconventional hardware for computing the PageR-

ank vectors. For all datasets, the ranking vectors obtained using unconventional networks are compared with the PageRank vectors computed using the original PageRank algorithm based on the power method. We use a standard metric to measure the correspondence between two rankings, namely the Kendall rank correlation coefficient (Kendall's tau):

$$\text{Kendall's tau} = \frac{C - D}{\sqrt{(C + D + T_1)(C + D + T_2)}} \in [-1, 1],$$

where  $C$  is the number of concordant pairs,  $D$  is the number of discordant pairs,  $T_k$  is the number of ties only in the  $k$ -th ranking. Concordant and discordant pairs describe the relationship between pairs of elements from two rankings: the pair  $(i, j)$  is concordant if both methods rate the  $i$ -th element higher than the  $j$ -th. A tie occurs for the pair  $(i, j)$  when a method assigns equal weights to both elements, while the pairs of elements with equal weights in both rankings do not contribute to either number of ties  $T_k$ . The larger positive values of Kendall's tau correspond to the stronger agreement between rankings, larger negative values indicate the reverse order of rankings, and near-zero values reflect no correlation between rankings.

The Kendall's tau between the PageRank order, which corresponds to the indices of the sorted components of the principal eigenvector computed using the power method, and ranks obtained with unconventional networks, is shown in Fig. 5.5A as a function of the number of iterations of all methods. The noticeable discrepancies between rankings of several methods, e.g. networks of OPOs and condensates (lasers), on several datasets, e.g. 'cambridge' and 'wiki-topcats', originate from the elements with the lowest importance as reflected in Fig. 5.5B(top). Computing Kendall's tau between the PageRank vector and amplitude distributions of the steady states in unconventional networks leads to the occasional minor deviations from the perfect agreement with the PageRank algorithm, as shown in Fig. 5.5B(bottom). Despite nonlinearities, the principal eigenvectors of the Google matrices are reconstructed with high accuracy by all networks.

The varying agreement between methods for the PageRank order ( $\mathcal{P}_i$ ) and PageRank vector ( $p_i$ ) is caused by the processing of ties in Kendall's tau calculation. In the latter case, different rankings can have multiple ties for the same pairs of elements that do not contribute to Kendall's tau, while redistributions of these ties into the concordant and discordant pairs decrease the correlation between rankings in the former case. Hence, we conclude that all unconventional networks successfully produce orderings in strong agreement with the PageRank algorithm.

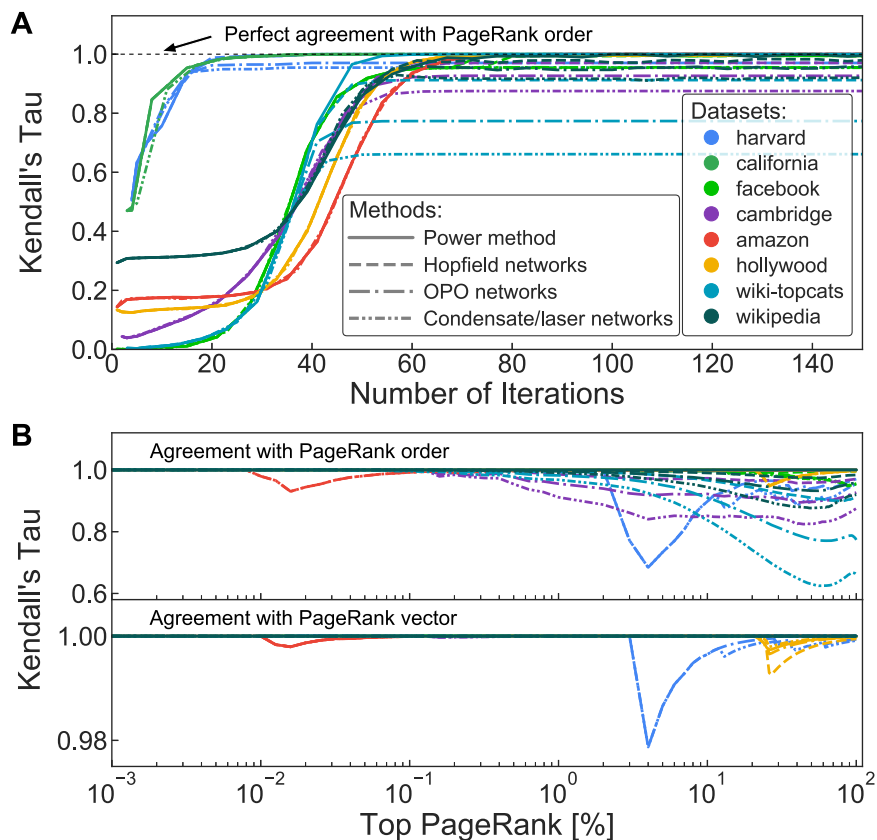


Fig. 5.5 (A) Kendall's tau, as a measure of the agreement between the PageRank order computed with the power method and the rankings obtained using unconventional networks, is shown as a function of the number of iterations for a variety of web graphs. The sizes of graphs vary from  $N = 500$  for the university network ('harvard') to  $N = 3.5$  million for the Wikipedia database ('wikipedia'). The unconventional networks are represented by Hopfield networks and networks of optical parametric oscillators (OPOs), condensates (polariton and photon), and lasers. (B) Kendall's tau distribution is shown as a function of the highest-ranked elements for the PageRank order (top) and the PageRank vector (bottom). The teleportation parameter is fixed across all datasets to  $\alpha = 0.85$ .

### 5.3.2 Alternative ranking through minimisation of the XY Hamiltonian

Physical systems can provide unconventional hardware to mimic the original PageRank algorithm and be used to explore alternative rankings. One of such new rankings could be based on the minimisation of the XY Hamiltonian, i.e. XYRank. As a representative example, we realise the minimisation of the XY model with the gain-dissipative networks that we described in Section 4.1. In the case of the Google matrix  $\mathbf{J} = \mathbf{G}$ , the alternative ranking is based on the individual gains  $\gamma_i$ , which can take negative and positive values. The lower is the gain  $\gamma_i$ , the higher importance is assigned to the  $i$ -th element. We call this alternative ranking the XYRank since the minimum of the total power gain  $\sum_i \gamma_i$  corresponds to the minimum of the XY Hamiltonian.

We show the relation between the traditional PageRank and XYRank distributions in Table 5.1. The highest-ranked elements are simply reshuffled for web graphs ‘harvard’, ‘facebook’, and ‘wiki-topcats’. In the case of the ‘california’ dataset, several of the PageRank positions are given much lower importance with respect to the XYRank, while the top XYRank positions still belong to the highly-rated pages of the PageRank distribution (see Appendix D). Understanding which ranking algorithm is best and whether XYRank can lead to better search results requires a detailed ranking analysis beyond algorithmic methods. In commercial search engines, thousands of trained external raters evaluate search quality results on various datasets and queries, even for small changes in ranking algorithms. The ability to have a platform that emulates the traditional PageRank algorithm and offers alternative rankings could allow unconventional hardware to safely replace traditional computing architectures and facilitate the development of new search algorithms.

*Computing power and energy efficiency.* The evolving nature of the Internet requires regular updates of PageRank distributions. Whereas 20 years ago, almost half of all web pages were updated at weekly intervals, nowadays constant changes in the web structure can occur within an hour or even a minute. As an estimate, the regular updates of the PageRank vector on a minute scale for a 10 billion size matrix would result in the average annual electricity consumption of about  $3.5 \cdot 10^5$  kWh on dedicated hardware, such as the tensor processing units (TPUs), see Fig. 5.6, that is equivalent to charging up about 300 electric cars for one year (see Appendix D for details). In addition to updating the global web network, the monetary success of many other platforms depends on how often similar to the PageRank ratings are calculated. For example, SalesRank needs to be updated hourly to reflect the purchase history of Amazon products.

To keep up with the dynamic changes of the web structure and its growing size, unconventional hardware can offer a time and energy-efficient platform for performing such

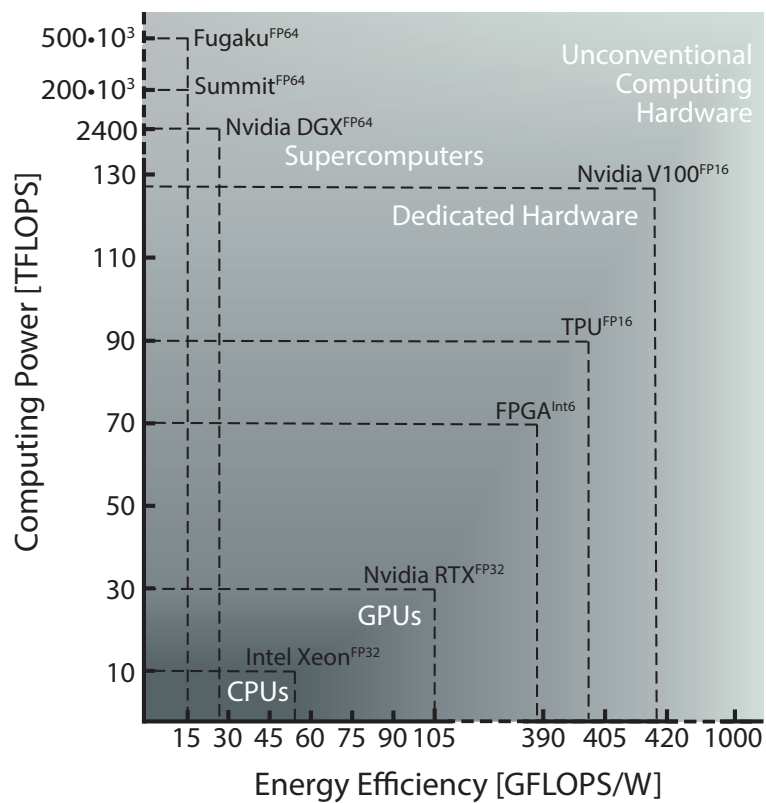


Fig. 5.6 The schematic distribution of the processing power as a function of energy efficiency is shown for several conventional computing devices, including CPUs, GPUs, FPGAs, and supercomputers. Unconventional computing devices based on optical systems could provide orders of magnitude improvements in time and energy performance.

intensive computations. The unconventional hardware typically benefits from inherent computational parallelism and possible quantum speedup. The typical improvements to the power method, such as reduced recalculation of converged pages [261], are naturally embedded in physical systems. In general, the time performance and energy consumption of computing PageRank and alternative ranks on unconventional hardware depend on the type of possible architectures.

For a hybrid (or active) coupling scheme, when interactions in the network are created using traditional devices, the performance of unconventional hardware is dictated by characteristics of the classical counterpart. For example, arbitrary coupling configurations can be implemented in OPO-based networks by matrix multiplication on the FPGA [58], which limits the time and energy performance of the optical system to the operational characteristics of FPGA. For polariton networks discussed earlier in Chapter 3 and other photonic systems [66], couplings could be realised using a spatial light modulator, which also restricts their time and energy performance.

To take full advantage of the capabilities of physical systems underlying unconventional hardware, pure optical architectures with passive schemes for creating interactions could be considered. In such all-optical passive networks, couplings do not require reconfiguration at each iteration, and the performance is determined solely by the characteristics of physical systems. While such coupling schemes are more difficult to engineer, there exist proposals of all-optical OPO and polaritonic machines. The programmable photonic processors provide passive integrated circuits with subnanosecond operation time scale [188].

The presence of inherent nonlinearities in some physical systems requires operation near the coherence threshold to simulate the PageRank algorithm with high accuracy. Nonlinearities are introduced intentionally in other physical computing platforms and can be omitted to model the PageRank algorithm. For example, the PageRank can be calculated by performing optical matrix multiplications that support beyond GHz clock rates [250–252].

To estimate the energy efficiency of unconventional hardware, we note that the power intensity required for creating an element of a network is on the order of milliwatts for most optical systems [251]. For example, a milliwatt laser power is usually required for exciting one micron-sized polariton condensate. Hence, the approximate power scaling with network size could be taken as  $P \sim N$  mW. The computational complexity of the PageRank algorithm is governed by the matrix-vector multiplication product in the power method and can be expressed as  $\mathcal{O}(mnN)$ , where  $m$  is the average connectivity of the web graph, and  $n$  is the number of iterations required for convergence. Then the number of floating-point operations per second (FLOPS) for unconventional hardware operating at picosecond-nanosecond time

scale could be in the range of  $mnN \cdot [10^9, 10^{12}]$  FLOPS with the energy efficiency of

$$\text{Energy efficiency} \approx mn \cdot [1, 10^3] \frac{\text{TFLOPS}}{\text{W}}. \quad (5.13)$$

Evidently, unconventional hardware with passive coupling schemes could provide orders of magnitude more energy-efficient performance than conventional computing architectures, see Fig. 5.6 for their power and efficiency comparison.

Table 5.1 The highest 10 PageRank positions are shown for datasets ‘harvard’, ‘california’, ‘facebook’, and ‘wiki-topcats’ of size  $N = 500$ ,  $N = 9664$ ,  $N = 22470$ , and  $N = 1791489$ . The identical PageRank distributions are found between the original PageRank algorithm based on the power method and simulations of Hopfield networks and networks based on optical parametric oscillators, lasers, polariton and photon condensates. The alternative ranking (XYRank) is computed by minimising the XY Hamiltonian. The difference between the two ratings is indicated by green (red) arrows showing the shift in the XYRank towards a higher (lower) rating by a certain number of positions with respect to the PageRank.

PageRank	Harvard	XYRank	California	XYRank
1	www.harvard.edu	—	www.ucdavis.edu/	↓ 58
2	www.hbs.edu	↓ 6	search.ucdavis.edu/	↓ 421
3	search.harvard.edu:8765/..	↑ 1	www.california.edu/	↓ 22
4	www.med.harvard.edu	↑ 1	home.netscape.com/..	↑ 2
5	www.gse.harvard.edu	—	www.berkeley.edu	—
6	www.hms.harvard.edu	↓ 3	www.linkexchange.com/	↑ 5
7	www.ksg.harvard.edu	↑ 1	www.berkeley.edu/	↑ 3
8	www.hsph.harvard.edu	↑ 4	www.uci.edu/	↓ 173
9	www.gocrimson.com	↓ 5	www.ca.gov	↓ 7
10	www.hsdm.med.harvard.edu	↓ 12	www.lib.uci.edu/	↓ 291
PageRank	Facebook	XYRank	Wikipedia (top categories)	XYRank
1	Facebook	↓ 2	United States	—
2	Sir Peter Bottomley MP	↑ 1	France	—
3	The White House	↓ 9	United Kingdom	↓ 8
4	The Obama White House	↓ 11	Canada	↓ 1
5	U.S. Army	↓ 6	Germany	↓ 5
6	U.S. Army Chaplain Corps	↑ 1	World War II	↓ 18
7	Joachim Herrmann	↑ 5	English language	↓ 16
8	Barack Obama	↓ 1	Australia	↓ 5
9	European Parliament	↓ 5	Italy	↓ 9
10	Manfred Weber	↑ 4	India	↓ 10



# **Chapter 6**

## **Conclusions**

Unconventional computing architectures based on classical and quantum physical systems can become a superior computational paradigm for solving challenging optimisation problems. Analogue simulators are proposed for numerous systems, including superconducting qubits, CMOS hardware, optical parametric oscillators, memristors, lasers, trapped ions, photon and polariton condensates. All these approaches aim to achieve a much faster, more efficient and more accurate way of solving a particular class of optimisation problems.

In this thesis, the possibility of gain-dissipative systems becoming unconventional computing platforms is investigated. As an example of driven-dissipative platforms, polariton condensates are considered throughout the text. Chapter 2 shows that polaritonic networks can be viewed as a paradigm for studying the dynamics of various known coupled oscillators. Intriguing opportunities for entering novel hybrid regimes are revealed as different types of oscillators can be incorporated together in one interaction platform within polaritons. Depending on the identified parameter regimes, various states of matter are possible in such a non-equilibrium system: the classical ferromagnetic and antiferromagnetic models, stationary and non-stationary spin waves, disordered configurations and stable giant vortices.

It is evident that polaritonic networks represent a flexible and robust platform for exploring new regimes and states of matter. Their prospects of optimisation is another discussion on which we are focusing. There are three crucial factors to consider when building a novel computing platform based on physical systems. The first is to ensure that the platform can, in principle, perform a practical computation, which could be minimisation of spin Hamiltonians or any other application of interest. Second is programmability: the platform's flexibility should allow one to realise a diverse set of problems within a chosen application domain. For example, implementations of arbitrary graph connections with controlled amplitudes are required for solving general optimisation problems. And third is the scalability easiness: a platform should be possible to scale to the size needed for tackling practically relevant applications, which should be done preferably with commodity optical and electronic components or, in rare cases, through technological innovation.

Chapter 3 attempts to address all these factors in the context of gain-dissipative systems as an analogue platform for minimising classical spin Hamiltonians. We introduce a new approach for simulating discrete and continuous spin Hamiltonians, e.g. Ising and XY, with polariton networks. The minimisation of the XY Hamiltonian is numerically and experimentally shown for simple building blocks of spatially coupled polariton condensates. For the first time, the scheme to realise discrete spin Hamiltonians, Ising and n-state planar Potts, is demonstrated for lattices of polariton and photon condensates. For minimising arbitrary graphs, the density equilibration feedback mechanism is proposed that applies to a broad family of oscillatory networks, including optical parametric oscillators, lasers, and

---

non-equilibrium condensates. By engineering a spatial variation of a dissipation profile, the localised independent control of individual interactions could be achieved, adding another dimension to the flexibility and tuneability of control parameters in lattice spin models. Finally, we suggest experimental implementations for realising remote phase locking of any two condensates in a micropillar array or in a lattice of trapped condensates with a potential to minimise both the Ising and XY models on fully-connected coupling matrices.

Thus, the proposed polaritonic XY-Ising machine possesses such essential qualities of an analogue optimiser as robust programmability of interactions via SLMs, the ability to simulate sparse and fully-connected matrices, and the implementation of arrays up to a thousand condensates with existing experimental techniques which have great potential for further scale-up. Furthermore, the strong-coupling regime of polariton quasi-particles should be advantageous for the bottom-up optimisation approach. Such strong interactions can facilitate the achievement of low-energy states by a parallel-scanning through all phase configurations near the condensation threshold. The real physical machine would benefit from low noise to signal ratio, ultra-fast operational time-scale, high energy efficiency with a milliwatt excitation power per condensate, and potential room-temperature operation.

Once all three factors are shown to be achievable, at least in theory, for a particular system, one needs to find a way to compare existing physical simulators and decide which approach is worth investing time and money in for further scaling. With dozens of small-size novel machines proposed over the last couple of years, a fair assessment of their optimisation capabilities is a non-trivial task, given the many technological constraints specific to each system. Such evaluation becomes even more difficult since the computational complexity theory operates with limits and tells us that a particular class of problems could be hard to optimise in general, e.g. NP-hard, although this complexity does not immediately apply to all instances of this class. As Leo Tolstoy said in *Anna Karenina*, “All happy families are alike; each unhappy family is unhappy in its own way”, the similar statement seems to be true for the complexity of optimisation problems: all simple problems are alike, but all complex problems are complex in their own way. Therefore, selection of the non-trivial or, even better, the hardest instances available in the NP-hard complexity class could tell more about the general optimisation capabilities of physical machines, even of small size, and could lead to more accurate prediction of their large scale performance.

A compelling approach for distinguishing easy and hard instances within the same NP-hard class of problems is proposed in Chapter 4. To identify computationally simple instances within the Ising model, we present an optimisation simplicity criterion. Neuromorphic architectures based on optical, photonic, and electronic systems can naturally operate to optimise instances satisfying this criterion, which are therefore often chosen to illustrate

the computational advantages of new Ising machines. Significant fractions of polynomially simple instances are further found for a wide range of small-size models from spin glasses to maximum cut problems. The reported simplicity criterion is sufficient but not necessary for an instance to be counted as easy to optimise. Hence, there exist great opportunities for developing other simplicity criteria for identifying easy instances of NP-hard problems.

Analogue optical platforms may become a new class of multi-purpose computing architectures with ultra-low power consumption in the near future. Determining the right architectural design in itself can help in developing new physics-inspired algorithms. Motivated by operational principles of gain-dissipative simulators, a novel gain-dissipative algorithm is proposed in Chapter 4. Its computational advantages over several standard methods are demonstrated for both continuous and discrete problems of various sizes. Besides grand applications of solving challenging optimisation problems on unconventional computing platforms, other possible applications are discussed in Chapter 5. In addition to reservoir computing, we propose to use the analogue Hamiltonian optimisers as a basis for a proof-of-work protocol. Using analogue optimisers at the heart of this protocol to perform valuable computations could help ensure blockchain's sustainable future. Also, these analogue machines could be exploited to accelerate existing search engine techniques and explore novel ranking approaches. Consequently, unconventional hardware based on physical systems may represent an efficient computing and long-term sustainable paradigm for continued innovation in search and other applications.

# References

- [1] Gordon E Moore et al. Cramming more components onto integrated circuits, 1965.
- [2] M Mitchell Waldrop. The chips are down for moore’s law. *Nature News*, 530(7589):144, 2016.
- [3] Giuseppe E Santoro, Roman Martoňák, Erio Tosatti, and Roberto Car. Theory of quantum annealing of an ising spin glass. *Science*, 295(5564):2427–2430, 2002.
- [4] Ryan Babbush, Peter J Love, and Alán Aspuru-Guzik. Adiabatic quantum simulation of quantum chemistry. *Scientific reports*, 4:6603, 2014.
- [5] Alejandro Perdomo-Ortiz, Neil Dickson, Marshall Drew-Brook, Geordie Rose, and Alán Aspuru-Guzik. Finding low-energy conformations of lattice protein models by quantum annealing. *Scientific reports*, 2:571, 2012.
- [6] Edward Farhi, Jeffrey Goldstone, Sam Gutmann, and Michael Sipser. Quantum computation by adiabatic evolution. *arXiv preprint quant-ph/0001106*, 2000.
- [7] John J Hopfield and David W Tank. “neural” computation of decisions in optimization problems. *Biological cybernetics*, 52(3):141–152, 1985.
- [8] GV Wilson and GS Pawley. On the stability of the travelling salesman problem algorithm of hopfield and tank. *Biological Cybernetics*, 58(1):63–70, 1988.
- [9] Sreeram VB Aiyer, Mahesan Niranjan, and Frank Fallside. A theoretical investigation into the performance of the hopfield model. *IEEE transactions on neural networks*, 1(2):204–215, 1990.
- [10] Avrim Blum and Ronald L Rivest. Training a 3-node neural network is np-complete. In *Advances in neural information processing systems*, pages 494–501, 1989.
- [11] Andrew Lucas. Ising formulations of many np problems. *Frontiers in Physics*, 2:5, 2014.
- [12] Botond Molnár, Ferenc Molnár, Melinda Varga, Zoltán Toroczkai, and Mária Ercsey-Ravasz. A continuous-time maxsat solver with high analog performance. *Nature communications*, 9(1):4864, 2018.
- [13] Christopher JC Burges. Factoring as optimization. *Microsoft Research MSR-TR-200*, 2002.

- [14] Magnus Ekeberg, Cecilia Lövkvist, Yueheng Lan, Martin Weigt, and Erik Aurell. Improved contact prediction in proteins: using pseudolikelihoods to infer potts models. *Physical Review E*, 87(1):012707, 2013.
- [15] Michael Sipser. The history and status of the p versus np question. In *Proceedings of the twenty-fourth annual ACM symposium on Theory of computing*, pages 603–618. ACM, 1992.
- [16] Francisco Barahona. On the computational complexity of ising spin glass models. *Journal of Physics A: Mathematical and General*, 15(10):3241, 1982.
- [17] Gemma De las Cuevas and Toby S Cubitt. Simple universal models capture all classical spin physics. *Science*, 351(6278):1180–1183, 2016.
- [18] Richard M Karp. Reducibility among combinatorial problems. In *Complexity of computer computations*, pages 85–103. Springer, 1972.
- [19] Una Benlic and Jin-Kao Hao. Breakout local search for the max-cut problem. *Engineering Applications of Artificial Intelligence*, 26(3):1162–1173, 2013.
- [20] Kirill P Kalinin and Natalia G Berloff. Global optimization of spin hamiltonians with gain-dissipative systems. *Scientific reports*, 8(1):17791, 2018.
- [21] Timothée Leleu, Yoshihisa Yamamoto, Peter L McMahon, and Kazuyuki Aihara. Destabilization of local minima in analog spin systems by correction of amplitude heterogeneity. *Physical review letters*, 122(4):040607, 2019.
- [22] Robert W Harrison. Phase problem in crystallography. *JOSA a*, 10(5):1046–1055, 1993.
- [23] Oliver Bunk, Ana Diaz, Franz Pfeiffer, Christian David, Bernd Schmitt, Dillip K Satapathy, and J Friso Van Der Veen. Diffractive imaging for periodic samples: retrieving one-dimensional concentration profiles across microfluidic channels. *Acta Crystallographica Section A: Foundations of Crystallography*, 63(4):306–314, 2007.
- [24] Jianwei Miao, Tetsuya Ishikawa, Qun Shen, and Thomas Earnest. Extending x-ray crystallography to allow the imaging of noncrystalline materials, cells, and single protein complexes. *Annu. Rev. Phys. Chem.*, 59:387–410, 2008.
- [25] Irène Waldspurger, Alexandre d’Aspremont, and Stéphane Mallat. Phase recovery, maxcut and complex semidefinite programming. *Mathematical Programming*, 149(1-2):47–81, 2015.
- [26] Firas Hamze, Jack Raymond, Christopher A Pattison, Katja Biswas, and Helmut G Katzgraber. The wishart planted ensemble: A tunably-rugged pairwise ising model with a first-order phase transition. *arXiv preprint arXiv:1906.00275*, 2019.
- [27] Michel X Goemans and David P Williamson. Approximation algorithms for max-3-cut and other problems via complex semidefinite programming. *Journal of Computer and System Sciences*, 68(2):442–470, 2004.

- [28] Shuzhong Zhang and Yongwei Huang. Complex quadratic optimization and semidefinite programming. *SIAM Journal on Optimization*, 16(3):871–890, 2006.
- [29] Nathan Krislock, Jérôme Malick, and Frédéric Roupin. Biqcrunch: A semidefinite branch-and-bound method for solving binary quadratic problems. *ACM Transactions on Mathematical Software (TOMS)*, 43(4):32, 2017.
- [30] Dieter Jaksch and Peter Zoller. The cold atom hubbard toolbox. *Annals of physics*, 315(1):52–79, 2005.
- [31] Immanuel Bloch, Jean Dalibard, and Wilhelm Zwerger. Many-body physics with ultracold gases. *Reviews of modern physics*, 80(3):885, 2008.
- [32] Rudolf Grimm, Matthias Weidemüller, and Yurii B Ovchinnikov. Optical dipole traps for neutral atoms. In *Advances in atomic, molecular, and optical physics*, volume 42, pages 95–170. Elsevier, 2000.
- [33] Patrick Windpassinger and Klaus Sengstock. Engineering novel optical lattices. *Reports on progress in physics*, 76(8):086401, 2013.
- [34] Omjyoti Dutta, Mariusz Gajda, Philipp Hauke, Maciej Lewenstein, Dirk-Sören Lühmann, Boris A Malomed, Tomasz Sowiński, and Jakub Zakrzewski. Non-standard hubbard models in optical lattices: a review. *Reports on Progress in Physics*, 78(6):066001, 2015.
- [35] Eugene P Gross. Structure of a quantized vortex in boson systems. *Il Nuovo Cimento (1955-1965)*, 20(3):454–477, 1961.
- [36] LP Pitaevskii. Vortex lines in an imperfect bose gas. *Sov. Phys. JETP*, 13(2):451–454, 1961.
- [37] Lev Pitaevskii and Sandro Stringari. *Bose-Einstein condensation and superfluidity*, volume 164. Oxford University Press, 2016.
- [38] Andrea Trombettoni and Augusto Smerzi. Discrete solitons and breathers with dilute bose-einstein condensates. *Physical Review Letters*, 86(11):2353, 2001.
- [39] RV Mishmash and LD Carr. Ultracold atoms in 1d optical lattices: mean field, quantum field, computation, and soliton formation. *Mathematics and Computers in Simulation*, 80(4):732–740, 2009.
- [40] Julian Struck, Christoph Ölschläger, R Le Targat, Parvis Soltan-Panahi, André Eckardt, Maciej Lewenstein, Patrick Windpassinger, and Klaus Sengstock. Quantum simulation of frustrated classical magnetism in triangular optical lattices. *Science*, 333(6045):996–999, 2011.
- [41] Julian Struck, Malte Weinberg, Christoph Ölschläger, Patrick Windpassinger, Juliette Simonet, Klaus Sengstock, Robert Höppner, Philipp Hauke, André Eckardt, Maciej Lewenstein, et al. Engineering ising-xy spin-models in a triangular lattice using tunable artificial gauge fields. *Nature Physics*, 9(11):738, 2013.

- [42] Mark W Johnson, Mohammad HS Amin, Suzanne Gildert, Trevor Lanting, Firas Hamze, Neil Dickson, R Harris, Andrew J Berkley, Jan Johansson, Paul Bunyk, et al. Quantum annealing with manufactured spins. *Nature*, 473(7346):194, 2011.
- [43] Tadashi Kadowaki and Hidetoshi Nishimori. Quantum annealing in the transverse ising model. *Physical Review E*, 58(5):5355, 1998.
- [44] Damian S Steiger, Bettina Heim, Troels F Rønnow, and Matthias Troyer. Performance of quantum annealing hardware. In *Electro-Optical and Infrared Systems: Technology and Applications XII; and Quantum Information Science and Technology*, volume 9648, page 964816. International Society for Optics and Photonics, 2015.
- [45] Vasil S Denchev, Sergio Boixo, Sergei V Isakov, Nan Ding, Ryan Babbush, Vadim Smelyanskiy, John Martinis, and Hartmut Neven. What is the computational value of finite-range tunneling? *Physical Review X*, 6(3):031015, 2016.
- [46] Ilya Zintchenko, Matthew B Hastings, and Matthias Troyer. From local to global ground states in ising spin glasses. *Physical Review B*, 91(2):024201, 2015.
- [47] Hui Cao, Ronen Chriki, Stefan Bittner, Asher A Friesem, and Nir Davidson. Complex lasers with controllable coherence. *Nature Reviews Physics*, 1(2):156–168, 2019.
- [48] Daniel Brunner, Miguel C Soriano, Claudio R Mirasso, and Ingo Fischer. Parallel photonic information processing at gigabyte per second data rates using transient states. *Nature communications*, 4:1364, 2013.
- [49] Ling Bao, Nam-Heon Kim, Luke J Mawst, Nikolay N Elkin, Vera N Troshchieva, Dmitry V Vysotsky, and Anatolii P Napartovich. Near-diffraction-limited coherent emission from large aperture antiguided vertical-cavity surface-emitting laser arrays. *Applied physics letters*, 84(3):320–322, 2004.
- [50] Vardit Eckhouse, Moti Fridman, Nir Davidson, and Asher A Friesem. Loss enhanced phase locking in coupled oscillators. *Physical review letters*, 100(2):024102, 2008.
- [51] Micha Nixon, Moti Friedman, Eitan Ronen, Asher A Friesem, Nir Davidson, and Ido Kanter. Synchronized cluster formation in coupled laser networks. *Physical review letters*, 106(22):223901, 2011.
- [52] Fabien Rogister, K Scott Thornburg Jr, Larry Fabiny, Michael Möller, and Rajarshi Roy. Power-law spatial correlations in arrays of locally coupled lasers. *Physical review letters*, 92(9):093905, 2004.
- [53] Vishwa Pal, Chene Tradonsky, Ronen Chriki, Asher A Friesem, and Nir Davidson. Observing dissipative topological defects with coupled lasers. *Physical review letters*, 119(1):013902, 2017.
- [54] Yoshiki Kuramoto. *Chemical oscillations, waves, and turbulence*. Courier Corporation, 2003.
- [55] Yoshiki Kuramoto. International symposium on mathematical problems in theoretical physics. *Lecture notes in Physics*, 30:420, 1975.

- [56] Hassan K Khalil. *Nonlinear systems*. Upper Saddle River, 2002.
- [57] C Tradonsky, I Gershenzon, V Pal, R Chriki, AA Friesem, O Raz, and N Davidson. Rapid laser solver for the phase retrieval problem. *Science Advances*, 5(10):eaax4530, 2019.
- [58] Peter L McMahon, Alireza Marandi, Yoshitaka Haribara, Ryan Hamerly, Carsten Langrock, Shuhei Tamate, Takahiro Inagaki, Hiroki Takesue, Shoko Utsunomiya, Kazuyuki Aihara, et al. A fully programmable 100-spin coherent ising machine with all-to-all connections. *Science*, 354(6312):614–617, 2016.
- [59] Ryan Hamerly, Takahiro Inagaki, Peter L McMahon, Davide Venturelli, Alireza Marandi, Tatsuhiro Onodera, Edwin Ng, Carsten Langrock, Kensuke Inaba, Toshimori Honjo, et al. Experimental investigation of performance differences between coherent ising machines and a quantum annealer. *Science advances*, 5(5):eaau0823, 2019.
- [60] Fabian Böhm, Takahiro Inagaki, Kensuke Inaba, Toshimori Honjo, Koji Enbutsu, Takeshi Umeki, Ryoichi Kasahara, and Hiroki Takesue. Understanding dynamics of coherent ising machines through simulation of large-scale 2d ising models. *Nature communications*, 9(1):5020, 2018.
- [61] Yoshitaka Haribara, Hitoshi Ishikawa, Shoko Utsunomiya, Kazuyuki Aihara, and Yoshihisa Yamamoto. Performance evaluation of coherent ising machines against classical neural networks. *Quantum Science and Technology*, 2(4):044002, 2017.
- [62] Andrew D King, William Bernoudy, James King, Andrew J Berkley, and Trevor Lanting. Emulating the coherent ising machine with a mean-field algorithm. *arXiv preprint arXiv:1806.08422*, 2018.
- [63] Kenta Takata, Alireza Marandi, and Yoshihisa Yamamoto. Quantum correlation in degenerate optical parametric oscillators with mutual injections. *Physical Review A*, 92(4):043821, 2015.
- [64] Fabian Böhm, Guy Verschaffelt, and Guy Van der Sande. A poor man’s coherent ising machine based on opto-electronic feedback systems for solving optimization problems. *Nature communications*, 10(1):1–9, 2019.
- [65] Masoud Babaeian, Dan T Nguyen, Veysi Demir, Mehmetcan Akbulut, Pierre-A Blanche, Yushi Kaneda, Saikat Guha, Mark A Neifeld, and N Peyghambarian. A single shot coherent ising machine based on a network of injection-locked multicore fiber lasers. *Nature communications*, 10(1):1–11, 2019.
- [66] D Pierangeli, G Marcucci, and C Conti. Large-scale photonic ising machine by spatial light modulation. *Physical Review Letters*, 122(21):213902, 2019.
- [67] Jacek Kasprzak, M Richard, S Kundermann, A Baas, P Jeambrun, JMJ Keeling, FM Marchetti, MH Szymańska, R André, JL Staehli, et al. Bose–einstein condensation of exciton polaritons. *Nature*, 443(7110):409, 2006.
- [68] NG Berloff and J Keeling. Universality in modelling non-equilibrium pattern formation in polariton condensates. In *Physics of Quantum Fluids*, pages 19–38. Springer, 2013.

- [69] Christian Schneider, Arash Rahimi-Iman, Na Young Kim, Julian Fischer, Ivan G Savenko, Matthias Amthor, Matthias Lermer, Adriana Wolf, Lukas Worschech, Vladimir D Kulakovskii, et al. An electrically pumped polariton laser. *Nature*, 497(7449):348, 2013.
- [70] Michele Saba, C Ciuti, J Bloch, V Thierry-Mieg, R André, Le Si Dang, S Kundermann, A Mura, G Bongiovanni, JL Staehli, et al. High-temperature ultrafast polariton parametric amplification in semiconductor microcavities. *Nature*, 414(6865):731, 2001.
- [71] Kerry Vahala. *Optical microcavities*. World Scientific, 2004.
- [72] Hui Deng, Gregor Weihs, David Snoke, Jacqueline Bloch, and Yoshihisa Yamamoto. Polariton lasing vs. photon lasing in a semiconductor microcavity. *Proceedings of the National Academy of Sciences*, 100(26):15318–15323, 2003.
- [73] R Balili, V Hartwell, D Snoke, L Pfeiffer, and K West. Bose-einstein condensation of microcavity polaritons in a trap. *Science*, 316(5827):1007–1010, 2007.
- [74] Gabriel Christmann, Raphaël Butté, Eric Feltin, Jean-Francois Carlin, and Nicolas Grandjean. Room temperature polariton lasing in a gan/ algan multiple quantum well microcavity. *Applied Physics Letters*, 93(5):051102, 2008.
- [75] S Kéna-Cohen and SR Forrest. Room-temperature polariton lasing in an organic single-crystal microcavity. *Nature Photonics*, 4(6):371, 2010.
- [76] Tien-Chang Lu, Jun-Rong Chen, Shiang-Chi Lin, Si-Wei Huang, Shing-Chung Wang, and Yoshihisa Yamamoto. Room temperature current injection polariton light emitting diode with a hybrid microcavity. *Nano letters*, 11(7):2791–2795, 2011.
- [77] Jan Klaers, Julian Schmitt, Frank Vewinger, and Martin Weitz. Bose–einstein condensation of photons in an optical microcavity. *Nature*, 468(7323):545, 2010.
- [78] Jan Klaers, Frank Vewinger, and Martin Weitz. Thermalization of a two-dimensional photonic gas in a ‘white wall’ photon box. *Nature Physics*, 6(7):512, 2010.
- [79] Jan Klaers, Julian Schmitt, T Damm, F Vewinger, and M Weitz. Bose–einstein condensation of paraxial light. *Applied Physics B*, 105(1):17, 2011.
- [80] Julian Schmitt, Tobias Damm, Frank Vewinger, Martin Weitz, and Jan Klaers. Thermalization of a two-dimensional photon gas in a polymeric host matrix. *New Journal of Physics*, 14(7):075019, 2012.
- [81] Herbert Walther, Benjamin TH Varcoe, Berthold-Georg Englert, and Thomas Becker. Cavity quantum electrodynamics. *Reports on Progress in Physics*, 69(5):1325, 2006.
- [82] Esther Wertz, Lydie Ferrier, DD Solnyshkov, Robert Johne, Daniele Sanvitto, Aristide Lemaître, Isabelle Sagnes, Roger Grousson, Alexey V Kavokin, Pascale Senellart, et al. Spontaneous formation and optical manipulation of extended polariton condensates. *Nature physics*, 6(11):860, 2010.

- [83] Francesco Manni, Konstantinos G Lagoudakis, Timothy Chi Hin Liew, Régis André, and Benoit Deveaud-Plédran. Spontaneous pattern formation in a polariton condensate. *Physical review letters*, 107(10):106401, 2011.
- [84] G Tosi, G Christmann, NG Berloff, P Tsotsis, T Gao, Z Hatzopoulos, PG Savvidis, and JJ Baumberg. Sculpting oscillators with light within a nonlinear quantum fluid. *Nature Physics*, 8(3):190, 2012.
- [85] G Tosi, G Christmann, NG Berloff, P Tsotsis, Tingge Gao, Z Hatzopoulos, PG Savvidis, and JJ Baumberg. Geometrically locked vortex lattices in semiconductor quantum fluids. *Nature communications*, 3:1243, 2012.
- [86] Natalia G Berloff, Matteo Silva, Kirill Kalinin, Alexis Askitopoulos, Julian D Töpfer, Pasquale Cilibrizzi, Wolfgang Langbein, and Pavlos G Lagoudakis. Realizing the classical xy hamiltonian in polariton simulators. *Nature materials*, 16(11):1120, 2017.
- [87] Ch Schneider, K Winkler, MD Fraser, M Kamp, Y Yamamoto, EA Ostrovskaya, and Sven Höfling. Exciton-polariton trapping and potential landscape engineering. *Reports on Progress in Physics*, 80(1):016503, 2016.
- [88] Alberto Amo and Jacqueline Bloch. Exciton-polaritons in lattices: A non-linear photonic simulator. *Comptes Rendus Physique*, 17(8):934–945, 2016.
- [89] David Dung, Christian Kurtscheid, Tobias Damm, Julian Schmitt, Frank Vewinger, Martin Weitz, and Jan Klaers. Variable potentials for thermalized light and coupled condensates. *Nature Photonics*, 11(9):565, 2017.
- [90] Pierre C Hohenberg and Bertrand I Halperin. Theory of dynamic critical phenomena. *Reviews of Modern Physics*, 49(3):435, 1977.
- [91] Leo P Kadanoff. *Statistical physics: statics, dynamics and renormalization*. World Scientific Publishing Company, 2000.
- [92] Iulia M Georgescu, Sahel Ashhab, and Franco Nori. Quantum simulation. *Reviews of Modern Physics*, 86(1):153, 2014.
- [93] Tal Schwartz, Guy Bartal, Shmuel Fishman, and Mordechai Segev. Transport and anderson localization in disordered two-dimensional photonic lattices. *Nature*, 446(7131):52, 2007.
- [94] Daniele Bajoni, Pascale Senellart, Esther Wertz, Isabelle Sagnes, Audrey Miard, Aristide Lemaître, and Jacqueline Bloch. Polariton laser using single micropillar gaas-gaalas semiconductor cavities. *Physical review letters*, 100(4):047401, 2008.
- [95] Edgar A Cerda-Méndez, Dmitry N Krizhanovskii, Klaus Biermann, Rudolf Hey, Maurice S Skolnick, and Paulo V Santos. Dynamic exciton-polariton macroscopic coherent phases in a tunable dot lattice. *Physical Review B*, 86(10):100301, 2012.
- [96] Na Young Kim, Kenichiro Kusudo, Congjun Wu, Naoyuki Masumoto, Andreas Löffler, Sven Höfling, Norio Kumada, Lukas Worschech, Alfred Forchel, and Yoshihisa Yamamoto. Dynamical d-wave condensation of exciton-polaritons in a two-dimensional square-lattice potential. *Nature Physics*, 7(9):681, 2011.

- [97] S Dufferwiel, F Fras, A Trichet, PM Walker, F Li, L Giriunas, MN Makhonin, LR Wilson, JM Smith, E Clarke, et al. Strong exciton-photon coupling in open semiconductor microcavities. *Applied Physics Letters*, 104(19):192107, 2014.
- [98] Karol Winkler, Julian Fischer, Anne Schade, Matthias Amthor, Robert Dall, Jonas Geßler, Monika Emmerling, Elena A Ostrovskaya, Martin Kamp, Christian Schneider, et al. A polariton condensate in a photonic crystal potential landscape. *New Journal of Physics*, 17(2):023001, 2015.
- [99] T Boulier, M Bamba, A Amo, C Adrados, A Lemaitre, E Galopin, I Sagnes, J Bloch, C Ciuti, E Giacobino, et al. Polariton-generated intensity squeezing in semiconductor micropillars. *Nature communications*, 5:3260, 2014.
- [100] Na Young Kim, Kenichiro Kusudo, Andreas Löffler, Sven Höfling, Alfred Forchel, and Yoshihisa Yamamoto. Exciton–polariton condensates near the dirac point in a triangular lattice. *New Journal of Physics*, 15(3):035032, 2013.
- [101] Kenichiro Kusudo, Na Young Kim, Andreas Löffler, Sven Höfling, Alfred Forchel, and Yoshihisa Yamamoto. Stochastic formation of polariton condensates in two degenerate orbital states. *Physical Review B*, 87(21):214503, 2013.
- [102] Thibaut Jacqmin, Iacopo Carusotto, Isabelle Sagnes, Marco Abbarchi, DD Solnyshkov, Guillaume Malpuech, Elisabeth Galopin, Aristide Lemaître, Jacqueline Bloch, and Alberto Amo. Direct observation of dirac cones and a flatband in a honeycomb lattice for polaritons. *Physical review letters*, 112(11):116402, 2014.
- [103] Naoyuki Masumoto, Na Young Kim, Tim Byrnes, Kenichiro Kusudo, Andreas Löffler, Sven Höfling, Alfred Forchel, and Yoshihisa Yamamoto. Exciton–polariton condensates with flat bands in a two-dimensional kagome lattice. *New Journal of Physics*, 14(6):065002, 2012.
- [104] Dimitrii Tanese, Evgeni Gurevich, Florent Baboux, Thibaut Jacqmin, Aristide Lemaître, Elisabeth Galopin, Isabelle Sagnes, Alberto Amo, Jacqueline Bloch, and Eric Akkermans. Fractal energy spectrum of a polariton gas in a fibonacci quasiperiodic potential. *Physical review letters*, 112(14):146404, 2014.
- [105] Jonathan Keeling and Natalia G Berloff. Spontaneous rotating vortex lattices in a pumped decaying condensate. *Physical review letters*, 100(25):250401, 2008.
- [106] Michiel Wouters and Iacopo Carusotto. Excitations in a nonequilibrium bose-einstein condensate of exciton polaritons. *Physical review letters*, 99(14):140402, 2007.
- [107] Iacopo Carusotto and Cristiano Ciuti. Quantum fluids of light. *Reviews of Modern Physics*, 85(1):299, 2013.
- [108] P Cristofolini, A Dreismann, G Christmann, G Franchetti, NG Berloff, P Tsotsis, Z Hatzopoulos, PG Savvidis, and JJ Baumberg. Optical superfluid phase transitions and trapping of polariton condensates. *Physical review letters*, 110(18):186403, 2013.

- [109] Hamid Ohadi, A Dreismann, YG Rubo, F Pinsker, Y del Valle-Inclan Redondo, SI Tsintzos, Z Hatzopoulos, PG Savvidis, and Jeremy John Baumberg. Spontaneous spin bifurcations and ferromagnetic phase transitions in a spinor exciton-polariton condensate. *Physical Review X*, 5(3):031002, 2015.
- [110] Konstantinos G Lagoudakis, Michiel Wouters, Maxime Richard, Augustin Baas, Iacopo Carusotto, Régis André, Le Si Dang, and B Deveaud-Plédran. Quantized vortices in an exciton-polariton condensate. *Nature Physics*, 4(9):706, 2008.
- [111] KG Lagoudakis, B Pietka, M Wouters, Régis André, and Benoit Deveaud-Plédran. Coherent oscillations in an exciton-polariton josephson junction. *Physical review letters*, 105(12):120403, 2010.
- [112] Tiejun Gao, E Estrecho, KY Bliokh, TCH Liew, MD Fraser, Sebastian Brodbeck, Martin Kamp, Christian Schneider, Sven Höfling, Y Yamamoto, et al. Observation of non-hermitian degeneracies in a chaotic exciton-polariton billiard. *Nature*, 526(7574):554, 2015.
- [113] Michael D Fraser, Georgios Roumpos, and Yoshihisa Yamamoto. Vortex-antivortex pair dynamics in an exciton-polariton condensate. *New Journal of Physics*, 11(11):113048, 2009.
- [114] D Sanvitto, FM Marchetti, MH Szymańska, Guilherme Tosi, M Baudisch, Fabrice P Laussy, DN Krizhanovskii, MS Skolnick, L Marrucci, A Lemaitre, et al. Persistent currents and quantized vortices in a polariton superfluid. *Nature Physics*, 6(7):527–533, 2010.
- [115] Michiel Wouters. Energy relaxation in the mean-field description of polariton condensates. *New Journal of Physics*, 14(7):075020, 2012.
- [116] Bryan Nelsen, Gangqiang Liu, Mark Steger, David W Snoke, Ryan Balili, Ken West, and Loren Pfeiffer. Dissipationless flow and sharp threshold of a polariton condensate with long lifetime. *Physical Review X*, 3(4):041015, 2013.
- [117] Kirill P Kalinin and Natalia G Berloff. Networks of non-equilibrium condensates for global optimization. *New Journal of Physics*, 20(11):113023, 2018.
- [118] Pavlos G Lagoudakis and Natalia G Berloff. A polariton graph simulator. *New Journal of Physics*, 19(12):125008, 2017.
- [119] Naoko Nakagawa and Yoshiki Kuramoto. Collective chaos in a population of globally coupled oscillators. *Progress of Theoretical Physics*, 89(2):313–323, 1993.
- [120] Naoko Nakagawa and Yoshiki Kuramoto. From collective oscillations to collective chaos in a globally coupled oscillator system. *Physica D: Nonlinear Phenomena*, 75(1-3):74–80, 1994.
- [121] Hidetsugu Sakaguchi and Yoshiki Kuramoto. A soluble active rotator model showing phase transitions via mutual entertainment. *Progress of Theoretical Physics*, 76(3):576–581, 1986.

- [122] Lars Q English, Zhuwei Zeng, and David Mertens. Experimental study of synchronization of coupled electrical self-oscillators and comparison to the sakaguchi-kuramoto model. *Physical Review E*, 92(5):052912, 2015.
- [123] Giovanni Filatrella, Arne Hejde Nielsen, and Niels Falsig Pedersen. Analysis of a power grid using a kuramoto-like model. *The European Physical Journal B*, 61(4):485–491, 2008.
- [124] Kris Vasudevan, Michael Cavers, and Antony Ware. Earthquake sequencing: chimera states with kuramoto model dynamics on directed graphs. *Nonlinear Processes in Geophysics*, 22(5):499–512, 2015.
- [125] E Estrecho, T Gao, N Bobrovska, D Comber-Todd, MD Fraser, M Steger, K West, LN Pfeiffer, J Levinsen, MM Parish, et al. Measurement of polariton-polariton interaction strength in the thomas-fermi regime of polariton condensation. *arXiv preprint arXiv:1809.00757*, 2018.
- [126] Bruno Eckhardt, Edward Ott, Steven H Strogatz, Daniel M Abrams, and Allan McRobie. Modeling walker synchronization on the millennium bridge. *Physical Review E*, 75(2):021110, 2007.
- [127] István Z Kiss, Yumei Zhai, and John L Hudson. Emerging coherence in a population of chemical oscillators. *Science*, 296(5573):1676–1678, 2002.
- [128] Roy Lang and Kohroh Kobayashi. External optical feedback effects on semiconductor injection laser properties. *IEEE journal of Quantum Electronics*, 16(3):347–355, 1980.
- [129] Juan A Acebrón, Luis L Bonilla, Conrad J Pérez Vicente, Félix Ritort, and Renato Spigler. The kuramoto model: A simple paradigm for synchronization phenomena. *Reviews of modern physics*, 77(1):137, 2005.
- [130] Kirill P Kalinin, Pavlos G Lagoudakis, and Natalia G Berloff. Exotic states of matter with polariton chains. *Physical Review B*, 97(16):161101, 2018.
- [131] Hamid Ohadi, RL Gregory, T Freearde, YG Rubo, AV Kavokin, Natalia G Berloff, and PG Lagoudakis. Nontrivial phase coupling in polariton multiplets. *Physical Review X*, 6(3):031032, 2016.
- [132] IE Dzyaloshinskii. The magnetic structure of fluorides of the transition metals. *SOVIET PHYSICS JETP*, 6(33), 1958.
- [133] Tôru Moriya. Anisotropic superexchange interaction and weak ferromagnetism. *Physical Review*, 120(1):91, 1960.
- [134] Michael Rubinstein, Boris Shraiman, and David R Nelson. Two-dimensional xy magnets with random dzyaloshinskii-moriya interactions. *Physical Review B*, 27(3):1800, 1983.
- [135] Kirill Kalinin, Matteo Silva, Julian D Töpfer, Wolfgang Langbein, Natalia G Berloff, and Pavlos G Lagoudakis. Giant vortices of controlled multiplicity in polariton lattices. *arXiv preprint arXiv:1710.03451*, 2017.

- [136] H Bethe. Eigenvalues and eigenfunctions of the linear atom chain. *Z. Phys*, 71:205–226, 1931.
- [137] Chanchal K Majumdar and Dipan K Ghosh. On next-nearest-neighbor interaction in linear chain. i. *Journal of Mathematical Physics*, 10(8):1388–1398, 1969.
- [138] Chanchal K Majumdar and Dipan K Ghosh. On next-nearest-neighbor interaction in linear chain. ii. *Journal of Mathematical Physics*, 10(8):1399–1402, 1969.
- [139] R Bursill, GA Gehring, Damian JJ Farnell, JB Parkinson, Tao Xiang, and Chen Zeng. Numerical and approximate analytical results for the frustrated spin-1/2 quantum spin chain. *Journal of Physics: Condensed Matter*, 7(45):8605, 1995.
- [140] Yi Zhou, Kazushi Kanoda, and Tai-Kai Ng. Quantum spin liquid states. *Reviews of Modern Physics*, 89(2):025003, 2017.
- [141] Hung T Diep. *Magnetic systems with competing interactions: frustrated spin systems*. World Scientific, 1994.
- [142] Magnus O Borgh, Jonathan Keeling, and Natalia G Berloff. Spatial pattern formation and polarization dynamics of a nonequilibrium spinor polariton condensate. *Physical Review B*, 81(23):235302, 2010.
- [143] Magnus O Borgh, Guido Franchetti, Jonathan Keeling, and Natalia G Berloff. Robustness and observability of rotating vortex lattices in an exciton-polariton condensate. *Physical Review B*, 86(3):035307, 2012.
- [144] Len M Pismen and Len M Pismen. *Vortices in nonlinear fields: from liquid crystals to superfluids, from non-equilibrium patterns to cosmic strings*, volume 100. Oxford University Press, 1999.
- [145] Alexander L Fetter. Rotating trapped bose-einstein condensates. *Reviews of Modern Physics*, 81(2):647, 2009.
- [146] David James Thouless, Ping Ao, and Qian Niu. Transverse force on a quantized vortex in a superfluid. *Physical review letters*, 76(20):3758, 1996.
- [147] DJ Thouless and JR Anglin. Vortex mass in a superfluid at low frequencies. *Physical review letters*, 99(10):105301, 2007.
- [148] EB Sonin. Transverse force on a vortex and vortex mass: Effects of free bulk and vortex-core bound quasiparticles. *Physical Review B*, 87(13):134515, 2013.
- [149] Avraham Klein, Igor L Aleiner, and Oded Agam. The internal structure of a vortex in a two-dimensional superfluid with long healing length and its implications. *Annals of Physics*, 346:195–229, 2014.
- [150] Mikko Möttönen, Ville Pietilä, and Sami MM Virtanen. Vortex pump for dilute bose-einstein condensates. *Physical review letters*, 99(25):250406, 2007.
- [151] Changhyun Ryu, MF Andersen, Pierre Clade, Vasant Natarajan, Kristian Helmerson, and William D Phillips. Observation of persistent flow of a bose-einstein condensate in a toroidal trap. *Physical Review Letters*, 99(26):260401, 2007.

- [152] Pekko Kuopanportti, Emil Lundh, Jukka AM Huhtamäki, Ville Pietilä, and Mikko Möttönen. Core sizes and dynamical instabilities of giant vortices in dilute bose-einstein condensates. *Physical Review A*, 81(2):023603, 2010.
- [153] Robert Dall, Michael D Fraser, Anton S Desyatnikov, Guangyao Li, Sebastian Brodbeck, Martin Kamp, Christian Schneider, Sven Höfling, and Elena A Ostrovskaya. Creation of orbital angular momentum states with chiral polaritonic lenses. *Physical review letters*, 113(20):200404, 2014.
- [154] Benjamin J McMorran, Amit Agrawal, Ian M Anderson, Andrew A Herzing, Henri J Lezec, Jabez J McClelland, and John Unguris. Electron vortex beams with high quanta of orbital angular momentum. *science*, 331(6014):192–195, 2011.
- [155] Yutaka Takeda, Shuhei Tamate, Yoshihisa Yamamoto, Hiroki Takesue, Takahiro Inagaki, and Shoko Utsunomiya. Boltzmann sampling for an xy model using a non-degenerate optical parametric oscillator network. *Quantum Science and Technology*, 3(1):014004, 2017.
- [156] Micha Nixon, Eitan Ronen, Asher A Friesem, and Nir Davidson. Observing geometric frustration with thousands of coupled lasers. *Physical review letters*, 110(18):184102, 2013.
- [157] Shoko Utsunomiya, Kenta Takata, and Yoshihisa Yamamoto. Mapping of ising models onto injection-locked laser systems. *Optics express*, 19(19):18091–18108, 2011.
- [158] Alireza Marandi, Zhe Wang, Kenta Takata, Robert L Byer, and Yoshihisa Yamamoto. Network of time-multiplexed optical parametric oscillators as a coherent ising machine. *Nature Photonics*, 8(12):937, 2014.
- [159] Ricardo A Oliva and Steven H Strogatz. Dynamics of a large array of globally coupled lasers with distributed frequencies. *International journal of Bifurcation and Chaos*, 11(09):2359–2374, 2001.
- [160] S Yu Kourtchatov, VV Likhanskii, AP Napartovich, FT Arecchi, and A Lapucci. Theory of phase locking of globally coupled laser arrays. *Physical Review A*, 52(5):4089, 1995.
- [161] Gregory Kozyreff, AG Vladimirov, and Paul Mandel. Global coupling with time delay in an array of semiconductor lasers. *Physical Review Letters*, 85(18):3809, 2000.
- [162] Hamid Ohadi, Y del Valle-Inclan Redondo, A Dreismann, YG Rubo, F Pinsker, SI Tsintzos, Z Hatzopoulos, PG Savvidis, and JJ Baumberg. Tunable magnetic alignment between trapped exciton-polariton condensates. *Physical review letters*, 116(10):106403, 2016.
- [163] Pierre Coullet and Kjartan Emilsson. Strong resonances of spatially distributed oscillators: a laboratory to study patterns and defects. *Physica D: Nonlinear Phenomena*, 61(1-4):119–131, 1992.
- [164] Arik Yochelis, Christian Elphick, Aric Hagberg, and Ehud Meron. Two-phase resonant patterns in forced oscillatory systems: Boundaries, mechanisms and forms. *Physica D: Nonlinear Phenomena*, 199(1-2):201–222, 2004.

- [165] Fa-Yueh Wu. The potts model. *Reviews of modern physics*, 54(1):235, 1982.
- [166] Daniele Sanvitto and Stéphane Kéna-Cohen. The road towards polaritonic devices. *Nature materials*, 15(10):1061, 2016.
- [167] V May, K Henneberger, and F Henneberger. Renormalization of polaritons due to virtual formation of biexcitons at high densities of excitation. *physica status solidi (b)*, 94(2):611–620, 1979.
- [168] Paola Borri, W Langbein, U Woggon, Jacob Riis Jensen, and Jørn Märcher Hvam. Biexcitons or bipolaritons in a semiconductor microcavity. *Physical Review B*, 62(12):R7763, 2000.
- [169] Masha Vladimirova, Steeve Cronenberger, Denis Scalbert, KV Kavokin, Audrey Miard, Aristide Lemaître, Jacqueline Bloch, Dimitri Solnyshkov, Guillaume Malpuech, and AV Kavokin. Polariton-polariton interaction constants in microcavities. *Physical Review B*, 82(7):075301, 2010.
- [170] Naotomo Takemura, Stéphane Trebaol, Michiel Wouters, Marcia T Portella-Oberli, and Benoît Deveaud. Polaritonic feshbach resonance. *Nature Physics*, 10(7):500, 2014.
- [171] Julian D Töpfer, Helgi Sigurdsson, Lucinda Pickup, and Pavlos G Lagoudakis. Time-delay polaritonics. *Communications Physics*, 3(1):1–8, 2020.
- [172] V Goblot, B Rauer, F Vicentini, A Le Boité, E Galopin, A Lemaître, L Le Gratiet, A Harouri, I Sagnes, S Ravets, et al. Nonlinear polariton fluids in a flatband reveal discrete gap solitons. *Physical review letters*, 123(11):113901, 2019.
- [173] Elisabeth Schlottmann, Steffen Holzinger, Benjamin Lingnau, Kathy Lüdge, Christian Schneider, Martin Kamp, Sven Höfling, Janik Wolters, and Stephan Reitzenstein. Injection locking of quantum-dot microlasers operating in the few-photon regime. *Physical Review Applied*, 6(4):044023, 2016.
- [174] Sören Kreinberg, Xavier Porte, David Schicke, Benjamin Lingnau, Christian Schneider, Sven Höfling, Ido Kanter, Kathy Lüdge, and Stephan Reitzenstein. Mutual coupling and synchronization of optically coupled quantum-dot micropillar lasers at ultra-low light levels. *Nature communications*, 10(1):1–11, 2019.
- [175] David J Wales and Jonathan PK Doye. Global optimization by basin-hopping and the lowest energy structures of lennard-jones clusters containing up to 110 atoms. *The Journal of Physical Chemistry A*, 101(28):5111–5116, 1997.
- [176] Grigory Lazarev, Andreas Hermerschmidt, Sven Krüger, and Stefan Osten. Lcos spatial light modulators: trends and applications. *Optical Imaging and Metrology: Advanced Technologies*, pages 1–29, 2012.
- [177] Takahiro Inagaki, Kensuke Inaba, Ryan Hamerly, Kyo Inoue, Yoshihisa Yamamoto, and Hiroki Takesue. Large-scale ising spin network based on degenerate optical parametric oscillators. *Nature Photonics*, 10(6):415–419, 2016.

- [178] Si Yue Guo, Pascal Friederich, Yudong Cao, Tony C Wu, Christopher J Forman, Douglas Mendoza, Matthias Degroote, Andrew Cavell, Veronica Krasecki, Riley J Hickman, et al. A molecular computing approach to solving optimization problems via programmable microdroplet arrays. *Matter*, 4(4):1107–1124, 2021.
- [179] Takahiro Inagaki, Yoshitaka Haribara, Koji Igarashi, Tomohiro Sonobe, Shuhei Tamate, Toshimori Honjo, Alireza Marandi, Peter L McMahan, Takeshi Umeki, Koji Enbutsu, et al. A coherent ising machine for 2000-node optimization problems. *Science*, 354(6312):603–606, 2016.
- [180] Richard H Byrd, Peihuang Lu, Jorge Nocedal, and Ciyou Zhu. A limited memory algorithm for bound constrained optimization. *SIAM Journal on Scientific Computing*, 16(5):1190–1208, 1995.
- [181] Ciyou Zhu, Richard H Byrd, Peihuang Lu, and Jorge Nocedal. Algorithm 778: L-bfgs-b: Fortran subroutines for large-scale bound-constrained optimization. *ACM Transactions on Mathematical Software (TOMS)*, 23(4):550–560, 1997.
- [182] Yang Wang, Zhipeng Lü, Fred Glover, and Jin-Kao Hao. Probabilistic grasp-tabu search algorithms for the ubqp problem. *Computers & Operations Research*, 40(12):3100–3107, 2013.
- [183] Paul B Wigley, Patrick J Everitt, Anton van den Hengel, John W Bastian, Mahasen A Sooriyabandara, Gordon D McDonald, Kyle S Hardman, Ciaran D Quinlivan, P Manju, Carlos CN Kuhn, et al. Fast machine-learning online optimization of ultra-cold-atom experiments. *Scientific reports*, 6:25890, 2016.
- [184] Timothee Leleu, Farad Khoystatee, Timothee Levi, Ryan Hamerly, Takashi Kohno, and Kazuyuki Aihara. Scaling advantage of nonrelaxational dynamics for high-performance combinatorial optimization. *arXiv preprint arXiv:2009.04084*, 2020.
- [185] Hayato Goto, Kotaro Endo, Masaru Suzuki, Yoshisato Sakai, Taro Kanao, Yohei Hamakawa, Ryo Hidaka, Masaya Yamasaki, and Kosuke Tatsumura. High-performance combinatorial optimization based on classical mechanics. *Science Advances*, 7(6):eabe7953, 2021.
- [186] Maliheh Aramon, Gili Rosenberg, Elisabetta Valiante, Toshiyuki Miyazawa, Hirotaka Tamura, and Helmut G Katzgraber. Physics-inspired optimization for quadratic unconstrained problems using a digital annealer. *Frontiers in Physics*, 7:48, 2019.
- [187] Michael R Garey, David S Johnson, and Larry Stockmeyer. Some simplified np-complete problems. In *Proceedings of the sixth annual ACM symposium on Theory of computing*, pages 47–63, 1974.
- [188] Charles Roques-Carmes, Yichen Shen, Cristian Zanoci, Mihika Prabhu, Fadi Atieh, Li Jing, Tena Dubček, Chenkai Mao, Miles R Johnson, Vladimir Čeperić, et al. Heuristic recurrent algorithms for photonic ising machines. *Nature Communications*, 11(1):1–8, 2020.
- [189] Edward Farhi, Jeffrey Goldstone, and Sam Gutmann. A quantum approximate optimization algorithm. *arXiv preprint arXiv:1411.4028*, 2014.

- [190] Matthew P Harrigan, Kevin J Sung, Matthew Neeley, Kevin J Satzinger, Frank Arute, Kunal Arya, Juan Atalaya, Joseph C Bardin, Rami Barends, Sergio Boixo, et al. Quantum approximate optimization of non-planar graph problems on a planar superconducting processor. *Nature Physics*, 17(3):332–336, 2021.
- [191] AD Mednykh and IA Mednykh. Asymptotics and arithmetical properties of complexity for circulant graphs. In *Doklady Mathematics*, volume 97, pages 147–151. Springer, 2018.
- [192] Mila Widyaningrum and Tri Atmojo Kusmayadi. On the strong metric dimension of sun graph, windmill graph, and möbius ladder graph. In *Journal of Physics: Conference Series*, volume 1008, page 012032. IOP Publishing, 2018.
- [193] Xiaogang Qiang, Thomas Loke, Ashley Montanaro, Kanin Aungskunsiri, Xiaoqi Zhou, Jeremy L O’Brien, Jingbo B Wang, and Jonathan CF Matthews. Efficient quantum walk on a quantum processor. *Nature communications*, 7(1):1–6, 2016.
- [194] Kenta Takata, Alireza Marandi, Ryan Hamerly, Yoshitaka Haribara, Daiki Maruo, Shuhei Tamate, Hiromasa Sakaguchi, Shoko Utsunomiya, and Yoshihisa Yamamoto. A 16-bit coherent ising machine for one-dimensional ring and cubic graph problems. *Scientific reports*, 6:34089, 2016.
- [195] Yoshihisa Yamamoto, Kazuyuki Aihara, Timothee Leleu, Ken-ichi Kawarabayashi, Satoshi Kako, Martin Fejer, Kyo Inoue, and Hiroki Takesue. Coherent ising machines—optical neural networks operating at the quantum limit. *npj quantum information* 3, 1 (2017), 49, 2017.
- [196] Fabian Böhm, Guy Verschaffelt, and Guy Van der Sande. A poor man’s coherent ising machine based on opto-electronic feedback systems for solving optimization problems. *Nature communications*, 10(1):1–9, 2019.
- [197] Jeffrey Chou, Suraj Bramhavar, Siddhartha Ghosh, and William Herzog. Analog coupled oscillator based weighted ising machine. *Scientific reports*, 9(1):1–10, 2019.
- [198] Yoshitomo Okawachi, Mengjie Yu, Jae K Jang, Xingchen Ji, Yun Zhao, Bok Young Kim, Michal Lipson, and Alexander L Gaeta. Demonstration of chip-based coupled degenerate optical parametric oscillators for realizing a nanophotonic spin-glass. *Nature communications*, 11(1):1–7, 2020.
- [199] Qizhuang Cen, Tengfei Hao, Hao Ding, Shanhong Guan, Zhiqiang Qin, Kun Xu, Yitang Dai, and Ming Li. Microwave photonic ising machine. 2020.
- [200] Sourav Dutta, Abhishek Khanna, Hanjong Paik, Darrell Schlom, Arijit Raychowdhury, Zoltan Toroczkai, and Suman Datta. Ising hamiltonian solver using stochastic phase-transition nano-oscillators. *arXiv preprint arXiv:2007.12331*, 2020.
- [201] Fuxi Cai, Suhas Kumar, Thomas Van Vaerenbergh, Xia Sheng, Rui Liu, Can Li, Zhan Liu, Martin Foltin, Shimeng Yu, Qiangfei Xia, et al. Power-efficient combinatorial optimization using intrinsic noise in memristor hopfield neural networks. *Nature Electronics*, pages 1–10, 2020.

- [202] Ryan Hamerly, Kensuke Inaba, Takahiro Inagaki, Hiroki Takesue, Yoshihisa Yamamoto, and Hideo Mabuchi. Topological defect formation in 1d and 2d spin chains realized by network of optical parametric oscillators. *International Journal of Modern Physics B*, 30(25):1630014, 2016.
- [203] Y Yamamoto, T Leleu, S Ganguli, and H Mabuchi. Coherent ising machines—quantum optics and neural network perspectives. *arXiv preprint arXiv:2006.05649*, 2020.
- [204] Svatopluk Poljak and Franz Rendl. Solving the max-cut problem using eigenvalues. *Discrete Applied Mathematics*, 62(1-3):249–278, 1995.
- [205] Charles Delorme and Svatopluk Poljak. Laplacian eigenvalues and the maximum cut problem. *Mathematical Programming*, 62(1-3):557–574, 1993.
- [206] Michel X Goemans and David P Williamson. Improved approximation algorithms for maximum cut and satisfiability problems using semidefinite programming. *Journal of the ACM (JACM)*, 42(6):1115–1145, 1995.
- [207] Kirill P Kalinin and Natalia G Berloff. Large-scale sustainable search on unconventional computing hardware. *arXiv preprint arXiv:2104.02553*, 2021.
- [208] Francisco Barahona. On some weakly bipartite graphs. *Operations Research Letters*, 2(5):239–242, 1983.
- [209] Martin Grötschel and William R Pulleyblank. Weakly bipartite graphs and the max-cut problem. *Operations research letters*, 1(1):23–27, 1981.
- [210] LLC Gurobi Optimization. Gurobi optimizer reference manual, 2020.
- [211] Sanjeev Arora and Boaz Barak. *Computational complexity: a modern approach*. Cambridge University Press, 2009.
- [212] Yuchen Pang, Carleton Coffrin, Andrey Y Lokhov, and Marc Vuffray. The potential of quantum annealing for rapid solution structure identification. *Constraints*, pages 1–25, 2020.
- [213] Robert H Swendsen and Jian-Sheng Wang. Replica monte carlo simulation of spin-glasses. *Physical review letters*, 57(21):2607, 1986.
- [214] Koji Hukushima and Koji Nemoto. Exchange monte carlo method and application to spin glass simulations. *Journal of the Physical Society of Japan*, 65(6):1604–1608, 1996.
- [215] David J Earl and Michael W Deem. Parallel tempering: Theory, applications, and new perspectives. *Physical Chemistry Chemical Physics*, 7(23):3910–3916, 2005.
- [216] Helmut G Katzgraber, Simon Trebst, David A Huse, and Matthias Troyer. Feedback-optimized parallel tempering monte carlo. *Journal of Statistical Mechanics: Theory and Experiment*, 2006(03):P03018, 2006.
- [217] Zheng Zhu, Andrew J Ochoa, and Helmut G Katzgraber. Efficient cluster algorithm for spin glasses in any space dimension. *Physical review letters*, 115(7):077201, 2015.

- [218] Sergei V Isakov, Ilia N Zintchenko, Troels F Rønnow, and Matthias Troyer. Optimised simulated annealing for ising spin glasses. *Computer Physics Communications*, 192:265–271, 2015.
- [219] Sergio Boixo, Troels F Rønnow, Sergei V Isakov, Zhihui Wang, David Wecker, Daniel A Lidar, John M Martinis, and Matthias Troyer. Evidence for quantum annealing with more than one hundred qubits. *Nature physics*, 10(3):218–224, 2014.
- [220] Miguel C Soriano, Silvia Ortín, Lars Keuninckx, Lennert Appeltant, Jan Danckaert, Luis Pesquera, and Guy Van der Sande. Delay-based reservoir computing: noise effects in a combined analog and digital implementation. *IEEE transactions on neural networks and learning systems*, 26(2):388–393, 2014.
- [221] Piotr Antonik. *Application of FPGA to Real-Time Machine Learning: Hardware Reservoir Computers and Software Image Processing*. Springer, 2018.
- [222] Anvesh Polepalli, Nicholas Soures, and Dhireesha Kudithipudi. Digital neuromorphic design of a liquid state machine for real-time processing. In *2016 IEEE International Conference on Rebooting Computing (ICRC)*, pages 1–8. IEEE, 2016.
- [223] Andrew Katumba, Jelle Heyvaert, Bendix Schneider, Sarah Uvin, Joni Dambre, and Peter Bienstman. Low-loss photonic reservoir computing with multimode photonic integrated circuits. *Scientific reports*, 8(1):2653, 2018.
- [224] Laurent Larger, Antonio Baylón-Fuentes, Romain Martinenghi, Vladimir S Udaltsov, Yanne K Chembo, and Maxime Jacquot. High-speed photonic reservoir computing using a time-delay-based architecture: Million words per second classification. *Physical Review X*, 7(1):011015, 2017.
- [225] Jacob Torrejon, Mathieu Riou, Flavio Abreu Araujo, Sumito Tsunegi, Guru Khalsa, Damien Querlioz, Paolo Bortolotti, Vincent Cros, Kay Yakushiji, Akio Fukushima, et al. Neuromorphic computing with nanoscale spintronic oscillators. *Nature*, 547(7664):428, 2017.
- [226] Ryosho Nakane, Gouhei Tanaka, and Akira Hirose. Reservoir computing with spin waves excited in a garnet film. *IEEE Access*, 6:4462–4469, 2018.
- [227] Diana Prychynenko, Matthias Sitte, Kai Litzius, Benjamin Krüger, George Bourianoff, Mathias Kläui, Jairo Sinova, and Karin Everschor-Sitte. Magnetic skyrmion as a nonlinear resistive element: A potential building block for reservoir computing. *Physical Review Applied*, 9(1):014034, 2018.
- [228] Gabriel Urbain, Jonas Degraeve, Benonie Carette, Joni Dambre, and Francis Wyffels. Morphological properties of mass–spring networks for optimal locomotion learning. *Frontiers in neurorobotics*, 11:16, 2017.
- [229] Philippe Vincent-Lamarre, Guillaume Lajoie, and Jean-Philippe Thivierge. Driving reservoir models with oscillations: a solution to the extreme structural sensitivity of chaotic networks. *Journal of computational neuroscience*, 41(3):305–322, 2016.

- [230] Gouhei Tanaka, Toshiyuki Yamane, Jean Benoit Héroux, Ryosho Nakane, Naoki Kanazawa, Seiji Takeda, Hidetoshi Numata, Daiju Nakano, and Akira Hirose. Recent advances in physical reservoir computing: A review. *Neural Networks*, 2019.
- [231] H Jaeger. Technical report gmd report 148. *German National Research Center for Information Technology*, 2001.
- [232] Wolfgang Maass, Thomas Natschläger, and Henry Markram. Real-time computing without stable states: A new framework for neural computation based on perturbations. *Neural computation*, 14(11):2531–2560, 2002.
- [233] Andrzej Opala, Sanjib Ghosh, Timothy CH Liew, and Michał Matuszewski. Neuromorphic computing in ginzburg-landau lattice systems. *arXiv preprint arXiv:1808.05135*, 2018.
- [234] Lucy Pickup, Kirill Kalinin, A Askitopoulos, Zacharias Hatzopoulos, PG Savvidis, Natalia G Berloff, and PG Lagoudakis. Optical bistability under nonresonant excitation in spinor polariton condensates. *Physical review letters*, 120(22):225301, 2018.
- [235] Dario Ballarini, Antonio Gianfrate, Riccardo Panico, Andrzej Opala, Sanjib Ghosh, Lorenzo Dominici, Vincenzo Ardizzone, Milena De Giorgi, Giovanni Lerario, Giuseppe Gigli, et al. Polaritonic neuromorphic computing outperforms linear classifiers. *Nano letters*, 20(5):3506–3512, 2020.
- [236] Satoshi Nakamoto et al. Bitcoin: A peer-to-peer electronic cash system. 2008.
- [237] Cynthia Dwork and Moni Naor. Pricing via processing or combatting junk mail. In *Annual International Cryptology Conference*, pages 139–147. Springer, 1992.
- [238] These and other facts related to the Google Search Engine are taken from the official Google channel on Youtube. 2020.
- [239] Jacob Devlin, Ming-Wei Chang, Kenton Lee, and Kristina Toutanova. Bert: Pre-training of deep bidirectional transformers for language understanding. *arXiv preprint arXiv:1810.04805*, 2018.
- [240] Amy N Langville and Carl D Meyer. Deeper inside pagerank. *Internet Mathematics*, 1(3):335–380, 2004.
- [241] Sergey Brin and Lawrence Page. The anatomy of a large-scale hypertextual web search engine. 1998.
- [242] Lawrence Page, Sergey Brin, Rajeev Motwani, and Terry Winograd. The pagerank citation ranking: Bringing order to the web. Technical report, Stanford InfoLab, 1999.
- [243] Leonardo Ermann, Klaus M Frahm, and Dima L Shepelyansky. Google matrix analysis of directed networks. *Reviews of modern physics*, 87(4):1261, 2015.
- [244] David F Gleich. Pagerank beyond the web. *SIAM Review*, 57(3):321–363, 2015.
- [245] Silvano Garnerone, Paolo Zanardi, and Daniel A Lidar. Adiabatic quantum algorithm for search engine ranking. *Physical Review Letters*, 108(23):230506, 2012.

- [246] Giuseppe Davide Paparo and MA Martin-Delgado. Google in a quantum network. *Scientific reports*, 2:444, 2012.
- [247] Hao Tang, Tian-Shen He, Ruo-Xi Shi, Yan-Yan Zhu, Marcus Lee, Tian-Yu Wang, and Xian-Min Jin. Tensorflow solver for quantum pagerank in large-scale networks. *arXiv preprint arXiv:2003.04930*, 2020.
- [248] Zhong Sun, Giacomo Pedretti, Elia Ambrosi, Alessandro Bricalli, and Daniele Ielmini. In-memory pagerank using a crosspoint array of resistive switching memory (rram) devices. In *2020 2nd IEEE International Conference on Artificial Intelligence Circuits and Systems (AICAS)*, pages 26–30. IEEE, 2020.
- [249] Santosh Kumar, He Zhang, and Yu-Ping Huang. Large-scale ising emulation with four body interaction and all-to-all connections. *Communications Physics*, 3(1):1–9, 2020.
- [250] Yichen Shen, Nicholas C Harris, Scott Skirlo, Mihika Prabhu, Tom Baehr-Jones, Michael Hochberg, Xin Sun, Shijie Zhao, Hugo Larochelle, Dirk Englund, et al. Deep learning with coherent nanophotonic circuits. *Nature Photonics*, 11(7):441, 2017.
- [251] Mihika Prabhu, Charles Roques-Carmes, Yichen Shen, Nicholas Harris, Li Jing, Jacques Carolan, Ryan Hamerly, Tom Baehr-Jones, Michael Hochberg, Vladimir Ćeperić, et al. Accelerating recurrent ising machines in photonic integrated circuits. *Optica*, 7(5):551–558, 2020.
- [252] Liane Bernstein, Alexander Sludds, Ryan Hamerly, Vivienne Sze, Joel Emer, and Dirk Englund. Freely scalable and reconfigurable optical hardware for deep learning. *arXiv preprint arXiv:2006.13926*, 2020.
- [253] John J Hopfield. Neural networks and physical systems with emergent collective computational abilities. *Proceedings of the National Academy of Sciences*, 79(8):2554–2558, 1982.
- [254] Pavel Berkhin. A survey on pagerank computing. *Internet mathematics*, 2(1):73–120, 2005.
- [255] Amy N Langville and Carl D Meyer. *Google’s PageRank and beyond: The science of search engine rankings*. Princeton university press, 2011.
- [256] Kirill P Kalinin and Natalia G Berloff. Nonlinear systems for unconventional computing. In *Emerging Frontiers in Nonlinear Science*, pages 345–369. Springer, 2020.
- [257] Fernando J Pineda. Generalization of back-propagation to recurrent neural networks. *Physical Review Letters*, 59(19):2229, 1987.
- [258] Zong-Ben Xu, Hong Qiao, Jigen Peng, and Bo Zhang. A comparative study of two modeling approaches in neural networks. *Neural networks*, 17(1):73–85, 2004.
- [259] Michael A Cohen and Stephen Grossberg. Absolute stability of global pattern formation and parallel memory storage by competitive neural networks. *IEEE transactions on systems, man, and cybernetics*, (5):815–826, 1983.

- [260] Alexander N Tait, Thomas Ferreira De Lima, Ellen Zhou, Allie X Wu, Mitchell A Nahmias, Bhavin J Shastri, and Paul R Prucnal. Neuromorphic photonic networks using silicon photonic weight banks. *Scientific reports*, 7(1):1–10, 2017.
- [261] Sepandar Kamvar, Taher Haveliwala, and Gene Golub. Adaptive methods for the computation of pagerank. *Linear Algebra and its Applications*, 386:51–65, 2004.
- [262] Sri Krishna Vadlamani, Tianyao Patrick Xiao, and Eli Yablonovitch. Physics successfully implements lagrange multiplier optimization. *Proceedings of the National Academy of Sciences*, 117(43):26639–26650, 2020.
- [263] S Kirkpatrick and D Sherrington. Solvable model of a spin-glass. *Phys. Rev. Lett.*, 35(26):1792–1796, 1975.
- [264] Sanjeev Arora, Eli Berger, Hazan Elad, Guy Kindler, and Muli Safra. On non-approximability for quadratic programs. In *46th Annual IEEE Symposium on Foundations of Computer Science (FOCS'05)*, pages 206–215. IEEE, 2005.
- [265] Andrea Montanari. Optimization of the sherrington-kirkpatrick hamiltonian. In *2019 IEEE 60th Annual Symposium on Foundations of Computer Science (FOCS)*, pages 1417–1433. IEEE, 2019.
- [266] Yaotian Fu and Philip W Anderson. Application of statistical mechanics to np-complete problems in combinatorial optimisation. *Journal of Physics A: Mathematical and General*, 19(9):1605, 1986.
- [267] DC Mattis. Solvable spin systems with random interactions. *Physics Letters A*, 56(5):421–422, 1976.
- [268] John A Tomlin. A new paradigm for ranking pages on the world wide web. In *Proceedings of the 12th international conference on World Wide Web*, pages 350–355, 2003.
- [269] Zhe Wang, Alireza Marandi, Kai Wen, Robert L Byer, and Yoshihisa Yamamoto. Coherent ising machine based on degenerate optical parametric oscillators. *Physical Review A*, 88(6):063853, 2013.
- [270] Timothée Leleu, Yoshihisa Yamamoto, Shoko Utsunomiya, and Kazuyuki Aihara. Combinatorial optimization using dynamical phase transitions in driven-dissipative systems. *Physical Review E*, 95(2):022118, 2017.
- [271] Ben Kassenberg, Mario Vretnar, Shivan Bissesar, and Jan Klaers. Controllable josephson junction for photon bose-einstein condensates. *arXiv preprint arXiv:2001.09828*, 2020.
- [272] Igor Gershenzon, Geva Arwas, Sagie Gadasi, Chene Tradonsky, Asher Friesem, Oren Raz, and Nir Davidson. Exact mapping between a laser network loss rate and the classical xy hamiltonian by laser loss control. *Nanophotonics*, 1(ahead-of-print), 2020.
- [273] Patrick Rebentrost, Thomas R Bromley, Christian Weedbrook, and Seth Lloyd. Quantum hopfield neural network. *Physical Review A*, 98(4):042308, 2018.

- 
- [274] *Harvard database is available at <http://www.math.sjsu.edu/singular/matrices/html/MathWorks/Harvard500.html>, 2002.*
- [275] California database is available at <https://www.cs.cornell.edu/courses/cs685/2002fa/>.
- [276] Jure Leskovec and Andrej Krevl. SNAP Datasets: Stanford large network dataset collection. <http://snap.stanford.edu/data>, June 2014.
- [277] Cambridge university database is available through the academic web link database project at <http://cybermetrics.wlv.ac.uk/database/>. 2006.
- [278] Ryan Rossi and Nesreen Ahmed. The network data repository with interactive graph analytics and visualization. In *Proceedings of the AAAI Conference on Artificial Intelligence*, volume 29, 2015.
- [279] Wikipedia database is available at <https://sparse.tamu.edu/gleich/wikipedia-20070206>. 2007.
- [280] List of the most powerful commercially available computer systems. <https://www.top500.org>, 2020.
- [281] "NVIDIA GeForce RTX 3090 Graphics Card" and "NVIDIA Corporation, "NVIDIA V100 TENSOR CORE GPU" Tech. rep. <https://www.nvidia.com>, 2020.
- [282] Yifan Sun, Nicolas Bohm Agostini, Shi Dong, and David Kaeli. Summarizing cpu and gpu design trends with product data. *arXiv preprint arXiv:1911.11313*, 2019.



# Appendix A

## Parameters for numerical simulations of polaritonic networks

In numerical simulations of polariton lattices throughout the Thesis, until otherwise specified in the main text, we used a Gaussian pumping profile that produces the same width of the condensate as in experiment (FWHM  $2.6\mu\text{m}$ ) and choose the pumping intensity to obtain the correct outflow wavenumber for a single condensate. The *standard* dimensionless integration parameters are  $g = 0.1, b = 1, \gamma = 0.3, \eta = 0.4, p = 9.5 \exp(-0.4r^2)$ . The dimensionless pumping profile of each site of polariton graphs is created by  $P_0 \cdot \exp(-\alpha r^2)$ , where  $P_0 = 9.5, \alpha = 0.4$ . The corresponding dimensional parameters are  $m_{\text{pol}} = 0.4 \text{ meV} \cdot \text{ps}^2/\text{m}^2, \hbar\gamma_C = 0.33 \text{ meV}, \hbar R_R = 0.1 \text{ meV} \cdot \mu\text{m}^2, \hbar g_R = 0.005 \text{ meV} \cdot \mu\text{m}^2, \hbar\gamma_R = 1.5 \text{ meV}, U_0 = 0.036 \text{ meV} \cdot \mu\text{m}^2, \eta_d = 0.037 \mu\text{m}^2$ . These parameters agree with experimental data presented for giant vortices in Chapter 2 and polariton lattices in Chapter 3.

In Section 2.3, the numerical parameters for 1D simulations in Figure 2.5 are  $\eta = 0.4, b = 1.5, \gamma = 1, p_0 = 5, \sigma = 0.4, g = 2.5$ . In Figure 2.6, the pumping intensity is 2.6 times larger to bring about a non-stationary state with the rest of parameters similar to the standard parameters listed above.

In Section 3.1 the numerical simulations are performed for various geometries and distances. All numerical simulations start from initial conditions with phases randomly distributed between the computational modes. The configuration with the largest number of particles,  $N$ , is chosen out of 100 runs for each pumping geometry.

In Section 3.3, the parameters agree with the standard parameters listed above. In addition, the following parameters are used to simulate the resonant pumping:  $P_2(\mathbf{r}, t) = 0.5(\tanh(6t/t_{\text{max}} - 3) + 1) \sum_{i=1}^N p(|\mathbf{r} - \mathbf{r}_i|), P_3(\mathbf{r}, t) = 0.25(\tanh(6t/t_{\text{max}} - 3) + 1) \sum_{i=1}^N p(|\mathbf{r} - \mathbf{r}_i|),$  and to simulate the field  $P_1(\mathbf{r}, t) = 0.25(\tanh(6t/t_{\text{max}} - 3) + 1)(p(|\mathbf{r} - \mathbf{r}_1|) + p(|\mathbf{r} - \mathbf{r}_2|)),$  where  $t_{\text{max}} \approx 100$  is the time when a steady state is achieved.

In Section 3.4, the dimensionless parameters for numerical simulations for Eqs. (3.18, 3.19) in Figure 3.12 and Figure 3.13:  $\eta = 0.01$ ,  $g = 0$  (a small nonzero value of  $g \approx 0.1$  will make the spins less aligned),  $b_0 = 0.2$ ,  $b_1 = 20$ ,  $P = \sum_i P_0 \exp(-\alpha(\mathbf{r} - \mathbf{r}_i)^2)$ ,  $P_0 = 100$ ,  $\alpha = 0.4$ ,  $\gamma_{\text{channel}} = 1$ ,  $\gamma_{\text{barrier}} = 40$ , lattice constant is  $d = 2.8$ , the width and length of channels are 1 and 1.4. In Figure 3.14, the parameters are  $b_0 = 0.1$ ,  $P_0 = 60$ ,  $\gamma_{\text{barrier}} = 60$ ,  $\gamma_{\text{gate}} = 8$ ,  $d = 3$ , while other parameters are the same as in Figure 3.12. The physically meaningful polariton lifetimes of  $5ps$ ,  $20 - 200ps$ , and  $200ps$  (or  $2ps/13ps/100ps$  for simulations in Figure 3.14) are used for barriers, gates, and channels, respectively, with an assumption of the exciton lifetime of  $2ns$ .

# Appendix B

## Algorithms for Ising minimisation

1. *Hopfield-Tank neural networks.* The numerical integration of the Hopfield-Tank algorithm (4.11) is performed in Fig. 5.4 by the Euler scheme with the discrete time step  $dt = 0.9$ . In all numerical simulations, a hyperbolic tangent is used as an activation function  $g = \tanh(x/x_0)$  and the numerical parameters are  $\tau = 1$ ,  $I_b = 0$ ,  $x_0 = 3$ . The polynomial fits are  $0.006x^{1.986}$ ,  $0.01x^{1.993}$ ,  $0.026x^{2.006}$  for ground state probabilities 50%, 75%, and 100%, respectively. We note that for coupling matrices not satisfying the OSC, the Hopfield-Tank neural networks could still find energies lower than the energy corresponding to the largest eigenvector by violating the low-gain limit.

2. *Gurobi solver.* The optimality gaps and times to reach optimal solutions are obtained with the Gurobi solver on a single core of Intel(R) Core(TM) i9-8950HK CPU 2.0GHz in Fig. 5.5.

3. *Chaotic Amplitude Control method.* The chaotic amplitude control method is an iterative scheme that is inspired by the operation of optical parametric oscillators [21] and based on the time evolution of equations:

$$\frac{dx_i}{dt} = (p-1)x_i - x_i^3 + \varepsilon e_i(t) \sum_{j=1}^N J_{ij}x_j \quad (\text{B.1})$$

$$\frac{de_i}{dt} = -\beta(x_i^2 - a)e_i \quad (\text{B.2})$$

where the signs of  $x_i$  represent the Ising spins,  $p$  is the linear gain,  $\varepsilon$  is the coupling strength scaling coefficient,  $e_i$  is the error signal,  $\beta$  is the rate of change of error signal, and  $a$  is the target amplitude. The dynamics of  $x_i$  elements in Eq. (B.1) is similar to a Hopfield network evolution with the addition of nonlinearity, while the amplitude alignment of the network elements as in Eq. (B.2) was first argued to be necessary for minimisation of both discrete and continuous spin Hamiltonians for gain-dissipative simulators in [20]. Following [21],

the parameters  $a$ ,  $p$ , and  $\beta$  are dynamically adjusted as:

$$a = 1 - \tanh(\delta\Delta E) \quad (\text{B.3})$$

$$p = p_0 + \tanh(\delta\Delta E) \quad (\text{B.4})$$

$$\frac{d\beta}{dt} = \begin{cases} \gamma, & \text{if } t - t_c < \tau \\ 0, & \text{otherwise} \end{cases} \quad (\text{B.5})$$

where the baseline of the target amplitude  $a$  is set to one,  $\delta$  is the sensitivity to energy variations,  $\Delta E = E_{\text{best}} - E(t)$  is the difference between the best found Ising energy and the current energy at time  $t$ ,  $p_0$  is the linear gain baseline. The parameter  $\beta$  increases with a positive rate  $\gamma$  for the maximum allowed time  $\tau$ , otherwise is set to zero and  $t_c$  is set to  $t$ , where  $t_c$  is the last time when the best known energy  $E_{\text{best}}$  was updated or  $\beta$  was reset. The numerical simulation of Eqs. (B.1-B.5) could efficiently sample the low energy states of Ising Hamiltonian [21] and was recently implemented on a field-programmable gate array as chaotic amplitude control method [184].

We note that the parameters  $e_i$  in Eq. (B.1) play a critical role in the algorithm's performance and make the local minima escape mechanism of the chaotic amplitude control method somewhat similar to that of parallel tempering. Namely, the error signals  $e_i$  could be seen as a set of inverse temperatures, each applied to individual spin. Hence, the energy landscape exploration within subspaces is performed during network elements' evolution at different temperatures. For spins whose amplitude  $x_i^2$  is much less than the target amplitude  $a$ , the signals  $e_i$  are large and help the system to quickly settle in a local energy minimum within the phase space of these spins (small temperature regime with a rough energy landscape for a subset of spins). For spins with amplitudes close to the target value, the signals  $e_i$  are small and facilitate crossings over energy barriers within this phase subspace (high-temperature regime with a smooth energy landscape for a subset of spins). The global optimisation could be then achieved due to fluctuations of 'inverse temperatures'  $e_i$  in time, which realise a continuous exploration of random spin subspaces at low and high temperatures. The importance of multiplying the interactions by amplitudes  $e_i$  has also been argued in terms of the destabilisation of low energy local minima [184] and due to the energy-conserving rotary motion [262].

*4. Parallel Tempering.* Parallel tempering (PT), or replica exchange Monte Carlo method, takes advantage of the dependence of the energy landscape on the temperature of the system: a rough landscape at low temperatures becomes smooth at high enough temperatures. In this algorithm [213–216], multiple states (replicas) of a particular Ising model are simulated independently at different temperatures with a Monte Carlo algorithm. At low temperatures,

Table B.1 Optimal parameters for chaotic amplitude control method are shown. The individual sets of parameters are selected for each rewiring of 3-regular graphs in Fig. 5.5 by optimising time to solution for ten rewired graphs with the m-loop method. The presented values are averaged over the percentage of rewired edges for each problem size.

Size	$N_{\text{iter}}$	$N_{\tau}$	$\varepsilon$	$\alpha$	$\gamma$	$\delta$	$dt$
100	3100	500	0.25	1.94	0.015	6.1	0.026
200	5500	1250	0.22	1.93	0.007	5.2	0.02
300	6600	1400	0.26	1.22	0.006	5.1	0.031

the local exploration of an energy landscape is realised, and replicas could quickly get trapped in local minima. In contrast, a global exploration of energy profile is facilitated with replicas easily crossing energy barriers at high temperatures. The global optimisation could be then achieved by exchanging replicas at low and high temperatures. For the optimal performance of PT, one needs to ensure the exchange in the reverse direction, which requires a trade-off between two factors. On the one hand, the exchange mechanism is accelerated once the acceptance probabilities for exchanges are high, which can usually be achieved by increasing the number of replicas. On the other hand, the larger number of replicas slows down the algorithm and increases the exchange time between replicas at the lowest and highest temperatures.

*Optimal Parameters.* For parallel tempering and chaotic amplitude control methods, the optimal sets of parameters are determined with the machine-learner online optimisation package (m-loop) [183] over ten random problem instances for each rewiring percentage per each problem size which results in a total of more than 150 graphs optimised for each problem size. The time-to-solution has been used as a target function for optimisation with the success probability calculated by running algorithms 30 times for each instance. The number of m-loop steps was fixed to 200. Both algorithms are implemented in Python and translated to optimised machine code with Numba, while Numba-compiled algorithms are known to approach a performance similar to Fortran. The reported time-to-solution performance is achieved on a single core of Intel(R) Core(TM) i9-8950HK CPU 2.0GHz.

For chaotic amplitude control method, the optimal time-to-solution for a given rewiring percentage for each problem size is determined by optimising the following seven parameters with the m-loop: number of iterations ( $N_{\text{iter}}$ ), maximum number of iterations without energy change ( $N_{\tau}$ ), coupling strength ( $\varepsilon$ ), linear gain baseline ( $p_0$ ), rate of increase of  $\beta$  ( $\gamma$ ), sensitivity to energy variations ( $\delta$ ), and time step ( $dt$ ). The averaged optimised parameters are listed in Table B.1, where linear gain baseline is determined through the parameter  $\alpha$  and the largest eigenvalue  $\lambda_0$  of coupling matrix  $J$  as  $p_0 = 1 - \alpha\lambda_0$ .

Table B.2 Optimal parameters for parallel tempering are shown. The individual sets of parameters are selected for each rewiring of 3-regular graphs in Fig. 5.5 by optimising time to solution for ten rewired graphs with the m-loop method. The presented values are averaged over the percentage of rewired edges for each problem size.

Size	$N_{MC}$	$N_R$	$N_{eq}$	$T_{low}$	$T_{high}$
100	100	4	1.9	0.71	1.18
200	120	4.6	5.3	0.77	1.12
300	230	4.6	5.8	0.77	1.05

For parallel tempering, the optimal time-to-solution for a given rewiring percentage for each problem size is determined by optimising the following five parameters with the m-loop: the number of Monte Carlo sweeps ( $N_{MC}$ ), number of replicas ( $N_R$ ), number of iterations for equilibration ( $N_{eq}$ ), low temperature ( $T_{low}$ ) and high temperature ( $T_{high}$ ). Temperatures at each replica are set based on the geometric schedule [186, 216]. Compared to the pseudocode in [186], our parallel tempering implementation includes an additional extra hyperparameter  $N_{eq}$ , which allows individual replicas to equilibrate over a few Monte Carlo sweeps before exchanging states of neighbouring pairs of replicas. The Metropolis update mechanism is used for the Monte Carlo simulations. The average values of optimal parameters are shown in Table B.2.

# Appendix C

## Ising models

In Fig. 5.6, the non-exhaustive list of problems in which one can find polynomially easy Ising instances includes:

1. *Sherrington-Kirkpatrick (SK) model of spin glasses* [263]. The fully-connected SK instances have a coupling matrix with elements from Gaussian distribution with zero mean and unit variance (Gaussian-SK). The Gaussian-SK model is  $\mathbb{NP}$ -hard [264] though the ground state with precision of  $(1 - \delta)$  can be found in polynomial time for any  $\delta > 0$  when the coupling coefficients are taken from the Gaussian distribution with zero mean and variance  $\sigma = 1/N$  [265]. The probability of finding an easy instance of Gaussian-SK problem with the OSC decreases from 45 – 100% for size  $N = 3 - 10$  to 10 – 20% for 20-25 size. The SK model stays in the  $\mathbb{NP}$ -Hard class [266] when the coupling values are chosen from bimodal distribution (bimodal-SK). In this case, the probability of easy instances drops from 65 – 100% to 20% for problem sizes 3-10 and 20-25, respectively. Both models have 100% simple instances for  $N = 3$  and all instances are simple for  $N = 5$  in case of bimodal distribution. The unweighted SK model coincides with the complete unweighted graphs, which were considered for the complexity continuum transition of  $k$ -regular graphs and argued to be polynomially simple. Both Gaussian-SK and bimodal-SK are commonly chosen for comparing Ising physical machines [59] and computational algorithms [21, 186].

2. *Mattis spin glass (Mattis SG) model* [267]. In the Mattis model, random variables  $\varepsilon$  are generated for each site  $i$  according to a specified probability distribution to build separable spin interactions as  $J_{ij} = f(R_{ij})\varepsilon_i\varepsilon_j$ , where  $f(R_{ij})$  is the adjacency matrix that specifies the topology of a graph. Such a model does not have frustrations, and the ground state is identical to the configuration of the random variables  $s_i = \varepsilon_i$ . Also, one may notice that the Mattis model is equivalent to gauge transformation  $J_{ij}^{\text{gauged}} = J_{ij}^F \varepsilon_i \varepsilon_j$  which conceals the planted ground state of the problem with ferromagnetic couplings  $J_{ij}^F$ . For both Gaussian and bimodal probability distributions of couplings, all Mattis spin models' instances satisfy the OSC,

which generalises to any problem size. Thus, the Mattis SG belongs to the  $\mathbb{P}$ -class. The Mattis model was recently used for evaluating the performance of photonic Ising machines [66].

3. *Maximum cut on 3-regular graphs.* In addition to unweighted 3-regular graphs, we considered 3-regular MaxCut with couplings from bimodal and Gaussian distributions. The bimodal 3-regular MaxCut exhibits a similar probability of easy instances as unweighted 3-regular graphs, while the probabilities for Gaussian 3-regular MaxCut are slightly higher on average than for Gaussian-SK. Besides, the case of 3-regular graphs on Möbius ladder is considered for bimodal and Gaussian coupling distributions. The MaxCut problems are commonly chosen for evaluating physical simulators [61, 59].

4. *Spin glass model on a torus (SG-torus).* A torus is represented by a two-dimensional rectangular lattice with periodic boundaries in both directions and nearest-neighbour interactions. The unweighted SG-torus model satisfies the OSC for any problem size. The Gaussian SG-torus is less likely to have simple graphs compared to Gaussian-SK, while the chances of about 40% hold even for a problem size of  $N = 40$  for bimodal SG-torus. The SG-torus models were recently used for comparing the large-scale performance of optimisation physics-inspired algorithms [186].

5. *Planar spin glass within a magnetic field.* One of the earliest proofs of  $\text{NP}$ -hardness of the Ising model was demonstrated for a three-dimensional spin glass and a planar spin glass within a uniform magnetic field  $h_i = -1$  and unweighted antiferromagnetic interactions [16]. Conveniently for us, the Möbius ladder graphs can be easily rewired to planar cubic graphs by avoiding the twist and becoming ladder graphs. All unweighted ladder graphs with a magnetic field satisfy the OSC. By exploiting the rewiring procedure with an additional planarity constraint, about 50% random planar 3-regular graphs happen to be simple for a problem size of 20. We also note that all found planar graphs of size 6 are simple graphs.

6. *Biased ferromagnet on Chimera graph (BF-Chimera).* The model represents an unweighted ferromagnetic coupling matrix on Chimera graph with fields  $p(h_i = 0) = p_0$  and  $p(h_i = 1) = p_1$  where  $p_0 \gg p_1$  that bias  $s_i = 1$  for all spins as the global optimal solution. This model was introduced as a toy example to get an intuition behind optimisation behaviour of the D-Wave machine and classical algorithms [212]. The BF-Chimera model has no frustration and its instances satisfy the OSC and thus are in  $\mathbb{P}$ -class. Though this is the only model in our list that was not argued to be hard before, its presence here could serve for studying the complexity of other known Ising models with Chimera topology. We note that there could be an additional overhead due to topological embedding in simulators where the long-range interactions are non-trivial to engineer, e.g. the Chimera graphs for some Ising problems.

# Appendix D

## Details of PageRank simulations

### 1. Google Matrix Construction Details

The stages for constructing the Google matrix  $\mathbf{G}$ :

$$\begin{aligned}\mathbf{G} &= (\mathbf{P}'')^T = [\alpha\mathbf{P} + (\alpha\mathbf{d} + (1 - \alpha)\mathbf{e})\mathbf{v}^T]^T \\ &= \alpha\mathbf{P}^T + \mathbf{v}[\alpha\mathbf{d}^T + (1 - \alpha)\mathbf{e}^T]\end{aligned}\tag{D.1}$$

could be divided into the following steps (see [242, 255] for more details):

- i.  $\mathbf{P}$  is the directed (undirected in rare cases) transition matrix, whose nodes represent web pages and the directed edges correspond to hyperlinks, with elements expressed as  $P_{ij} = A_{ij}/deg(i)$  when  $deg(i) > 0$  and  $P_{ij} = 0$  otherwise. Here  $\mathbf{A}$  is the adjacency matrix with  $A_{ij} = 1$  when there is a link from page  $i$  to page  $j$ , and  $A_{ij} = 0$  otherwise, and  $deg(i) = \sum_j A_{ij}$  is the number of outgoing links of a page  $i$  (out-degree). Thanks to such normalisation, the matrix elements  $P_{ij}$  represent probabilities of moving from page  $i$  to page  $j$  in one time-step.
- ii. The stochastic matrix  $\mathbf{P}'$  is constructed from the transition matrix  $\mathbf{P}$  as  $\mathbf{P}' = \mathbf{P} + \mathbf{d}\mathbf{v}^T$ , where  $\mathbf{d}$  is the dangling vector with  $d_i = 1$  for zero rows of  $\mathbf{P}$  and 0 otherwise. The dangling nodes are the nodes without outlinks in the transition matrix. Such nodes commonly occur in practice and can be attributed, for example, to the unexplored ('crawled') web pages that are added to the web graph. The uniform vector  $\mathbf{v}$  adds artificial links by connecting uniformly dangling pages to all pages in the web graph, while the non-uniform choice of  $\mathbf{v}$  represents a personalisation vector. For such nonnegative row-stochastic matrix  $\mathbf{P}'$ , the principal eigenvector corresponds to the eigenvalue  $\lambda = 1$  which could be degenerate, while such degeneracy can prevent the convergence of the power method.

- iii. The stochastic irreducible matrix  $\mathbf{P}''$  is formed as  $\mathbf{P}'' = \alpha\mathbf{P}' + (1 - \alpha)\mathbf{e}\mathbf{v}^T$ , where  $\mathbf{e}$  is the unity vector. The matrix is irreducible (strongly connected) since every page is now directly connected to every other page. The irreducibility adjustment also ensures that  $\mathbf{P}''$  is primitive, which guarantees the existence of the unique stationary PageRank vector for  $\alpha < 1$ , to which the power method will converge regardless of the initial distribution. The parameter  $\alpha$  is known as the damping (teleportation) factor since for a non-dangling page  $i$  a random web surfer can not only follow one of the available outlinks with the probability of  $\alpha$  but can also jump (teleport) to any other page  $j$  with the probability of  $(1 - \alpha)v_j$ . Hence, the probability vector  $\mathbf{v} > 0$  is known as the teleportation vector when chosen to be uniform or personalisation vector otherwise.

For computational efficiency, the Google matrix  $\mathbf{G}$  is never explicitly formed. Instead, the PageRank vector can be calculated with the power method as [? ]:

$$\mathbf{p}^{(k+1)} = \mathbf{G} \cdot \mathbf{p}^{(k)} = \alpha\mathbf{P}^T \cdot \mathbf{p}^{(k)} + \mathbf{v}[\alpha\mathbf{d}^T \mathbf{p}^{(k)} + (1 - \alpha)], \quad (\text{D.2})$$

where the normalisation condition  $\mathbf{e}^T \mathbf{p}^{(k)} = 1$  is assumed and the advantage of the sparse matrix-vector multiplication could be taken of. The PageRank algorithm is also directly linked to the mathematical properties of Markov chains and Perron-Frobenius operators [? 255] and can be viewed as a stationary probability distribution for the Markov chain induced by a random walk on the web graph.

## 2. Feasibility and requirements of embedding the Google matrix in physical systems

To discuss the possibility to embed the Google matrix on unconventional hardware, we comment on all three stages of construction of the Google matrix.

The first step requires an ability to realise a sparse adjacency matrix in a physical platform. It should be possible to create directed interactions between arbitrary nodes in the network with about 10 to 100 connections per node. This requirement is feasible for most of the physical systems considered in this work since the couplings can be usually organised by external means. For example, the field-programmable gate arrays are used for OPOs, and spatial light modulators can be used for polariton condensates. Such number of interactions could be possibly harder to realise in passive coupling schemes.

In the second step, some nodes (dangling nodes) should be equally connected to all other nodes with a small interaction strength. Given the possibly large number of the dangling nodes, this could be an expensive step to complete with purely optical means from the

engineering perspective, although it is straightforward with externally supplied couplings. Alternative ways to create a stochastic matrix may need to be explored to implement such interactions in physical systems efficiently.

In the third step, the irreducible matrix is created. Creating such a strongly-connected matrix may look even more challenging to engineer than a few fully-connected nodes in the second step. Fortunately, there could be a simple way to do this. The method of minimal irreducibility [268] was proven to be equivalent both in theory and in computational efficiency to the maximally irreducible method (that is used in the third step) [240]. An additional node is added to the network and connected to all other nodes in this alternative method. Such an extra node plays the role of a teleportation state: there is a small probability of transitioning to and out of this state. Unlike maximal irreducibility, the minimal irreducibility could be naturally realised in many physical systems by applying a bias, for instance, a small uniform magnetic field to all network elements. Also, a nonuniform magnetic field could allow one to emulate the personalised PageRank algorithm.

### 3. The PageRank algorithm on unconventional hardware

#### Networks of optical parametric oscillators.

Network of coupled optical parametric oscillators (OPOs) represents an unconventional gain-dissipative platform [269, 158] whose simplified dynamics is governed by the equations

$$\frac{dx_i}{dt} = -x_i^3 + (p-1)x_i + \beta \sum_{j=1}^N J_{ij}x_j, \quad (\text{D.3})$$

where  $p$  represents the linear gain,  $J_{ij}$  are the interactions between oscillators, the linear and nonlinear losses are normalised. The OPO-based simulator is proposed initially as a coherent Ising machine since two possible phase states exist for each nonlinear oscillator above a certain pumping threshold, and, hence, these states can be interpreted as binary spins. For degenerate optical parametric oscillators (DOPOs) in a fibre [58], arbitrary coupling connections between any two spins can be realised in the feedback loop on the FPGA.

For mimicking the PageRank algorithm, networks of OPOs should be operating at the lowest loss regime. In the case of the Google matrix, this critical regime corresponds to [269, 270]

$$p_{\text{crit}} - 1 = -\beta \lambda_{\text{max}}^{(\mathbf{G})} = -\beta. \quad (\text{D.4})$$

The linear stability analysis of Eq. (D.3) is similar to that of Eq. (5.5) at  $\xi_{\text{crit}} = p_{\text{crit}} - 1$ . Hence, the PageRank vector is realised by the OPOs amplitudes  $x_i$  in the steady state of

equation:

$$\frac{dx_i}{dt} = -\frac{1}{\beta}x_i^3 - x_i + \sum_{j=1}^N G_{ij}x_j. \quad (\text{D.5})$$

To get this equation, the time is rescaled as  $t \rightarrow \beta t$  in Eq. (D.3).

### Networks of polariton and photon condensates.

Lattices of polariton condensates are another gain-dissipative unconventional hardware that we considered throughout this thesis and whose physics resembles another unconventional computing system based on photon condensates confined in a dye-filled optical microcavity [77, 271]. These networks of gain-dissipative condensates can be realised in experiments using a spatial light modulator [82] with many techniques proposed and engineered for controlling couplings between condensates. The time-evolution of gain-dissipative condensates is derived from the space and time-resolved mean-field equations in Section 2.1 and for certain parameter regimes can be described by the Stuart-Landau equations:

$$\frac{d\psi_i}{dt} = -iU|\psi_i|^2\psi_i + (\gamma - |\psi_i|^2)\psi_i + \sum_{j=1}^N J_{ij}\psi_j, \quad (\text{D.6})$$

For simulating the PageRank algorithm with networks of gain-dissipative condensates, we show the equivalence of stability of linearised equations Eq. (D.6) to Eq. (5.5). By substituting  $\psi_i = \sqrt{\rho_i} \exp[i\theta_i]$  and separating real and imaginary parts in Eq. (D.6), we obtain

$$\begin{aligned} \text{Re} \quad \frac{d\sqrt{\rho_i}}{dt} &= (\gamma - \rho_i)\sqrt{\rho_i} + \sum_{j=1}^N J_{ij}\sqrt{\rho_j} \cos(\theta_j - \theta_i), \\ \text{Im} \quad \frac{d\theta_i}{dt} &= -U\rho_i + \sum_{j=1}^N J_{ij}\sqrt{\frac{\rho_j}{\rho_i}} \sin(\theta_j - \theta_i), \end{aligned} \quad (\text{D.7})$$

where  $\rho_i$  and  $\theta_i$  are the density and phase of the  $i$ -th condensate. When  $J_{ij} = G_{ij}$ , since all the elements of the Google matrix are positive, the condensation threshold is realised at  $\theta_i = \theta_j$  with the  $\cos(\theta_j - \theta_i) = 1$  for all  $i, j$ . By denoting  $x_i = \sqrt{\rho_i}$ , we rewrite the real part of Eqs. (D.7) as:

$$\frac{dx_i}{dt} = -x_i^3 + \gamma x_i + \sum_{j=1}^N G_{ij}x_j. \quad (\text{D.8})$$

This time evolution of polariton and photon condensate amplitudes is similar to the networks of OPOs, described by Eq. (D.3). As the effective pumping rate  $\gamma$  increases from the negative values (linear dissipation dominates), the first nonzero stable state emerges at

$$\gamma_{\text{crit}} = -\lambda_{\text{max}}^{(\mathbf{G})} = -1, \quad (\text{D.9})$$

which corresponds to  $\xi_{\text{crit}} = \gamma_{\text{crit}}$  in Eq. (5.5). Hence, the networks of gain-dissipative condensates emulate the PageRank algorithm in the regime of the lowest gain while the PageRank vector is represented by the absolute values of amplitudes  $|\psi_i|$  at the steady state of equations:

$$\frac{d\psi_i}{dt} = -iU|\psi_i|^2\psi_i - (1 + |\psi_i|^2)\psi_i + \sum_{j=1}^N G_{ij}\psi_j. \quad (\text{D.10})$$

In case of the Google matrix, the nonlinear interactions  $U$  do not affect the dynamics of gain-dissipative condensates. Consequently, the dynamics of Eq. (D.10) is equivalent to that of the networks of coupled lasers, which are considered next.

### Networks of lasers.

The network of the degenerate lasers in a cavity represents a gain-dissipative unconventional computing hardware that was proposed for the minimisation of the XY Hamiltonian [272]. In such networks, the interactions are engineered by mutual light injections from one laser to another, which introduce losses depending on the relative phases of lasers. The dynamics of coupled lasers is governed by the rate equations [52]:

$$\begin{aligned} \frac{dE_i}{dt} &= (\tilde{G}_i - \tilde{\alpha})E_i + \sum_{j=1}^N J_{ij}E_j, \\ \frac{d\tilde{G}_i}{dt} &= \frac{1}{\tau}[\tilde{P} - \tilde{G}_i(1 + |E_i|^2)], \end{aligned} \quad (\text{D.11})$$

where  $E_i$  is the electric field of the  $i$ -th laser,  $\tilde{G}_i$  is the active medium gain,  $\tau$  is the gain medium fluorescence lifetime,  $\tilde{\alpha}$  is the linear loss coefficient, and  $\tilde{P}$  is the active medium pump rate,  $J_{ij}$  are the coupling strengths between the  $i$ -th and  $j$ -th lasers. In the limit of the fast active medium gain relaxation and low amplitude electric fields, the equations simplify to:

$$\frac{dE_i}{dt} = (\tilde{P} - \tilde{\alpha} - \tilde{P}|E_i|^2)E_i + \sum_{j=1}^N J_{ij}E_j. \quad (\text{D.12})$$

Consequently, the stability analysis of the dynamics of polariton and photon condensates, governed by Eq. (D.6), applies to the time evolution of coupled laser oscillators described by Eq. (D.12). For the Google matrix, the first nonzero stable state occurs when the linear losses  $\tilde{\alpha}$  satisfy

$$\tilde{P} - \tilde{\alpha}_{\text{crit}} = -\lambda_{\text{max}}^{(\mathbf{G})} = -1. \quad (\text{D.13})$$

The dynamics of linearised laser networks is equivalent to Eq. (5.5) at  $\xi_{\text{crit}} = \tilde{P} - \tilde{\alpha}_{\text{crit}}$ . Hence, the networks of coupled lasers emulate the PageRank algorithm in the lowest loss regime with the PageRank vector represented by the absolute values of electric fields  $|E_i|$  in the

steady state of equations:

$$\frac{dE_i}{dt} = -(1 + \tilde{P}|E_i|^2)E_i + \sum_{j=1}^N G_{ij}E_j. \quad (\text{D.14})$$

The dynamic of laser networks is reminiscent of gain-dissipative condensates described by Eq. (D.10), where the presence of nonlinear term  $U$  does not affect the system's ability to find the principal eigenvector. Consequently, the emulation of the PageRank algorithm with networks based on either polariton and photon condensates or lasers can be performed with Eq. (D.10).

### Hopfield neural networks.

The Hopfield networks [253] can be realised with unconventional hardware based on electronic [201] and photonic systems [260] with quantum extensions available [273]. These networks are of great importance in many areas with early applications ranging from minimising discrete spin Hamiltonians and associative memory [7] to more recent uses in web information retrieval, pattern recognition, and natural language processing techniques. The evolution of individual neurons is governed by the equations:

$$\frac{dx_i}{dt} = -\frac{x_i}{\tau} + \sum_{j=1}^N J_{ij} \tanh\left(\frac{x_j}{u_0}\right) + I_i^b, \quad (\text{D.15})$$

where  $x_i$  describes the state of the  $i$ -th neuron,  $\tau$  is the leakage parameter,  $J_{ij}$  are the interaction coefficients between neurons,  $I_i^b$  is the external pumping imposed on the  $i$ -th neuron, and the activation function is assumed to be the hyperbolic tangent. In the case of the Google matrix, the first nonzero stable state emerges at

$$\tau_{\text{crit}} = \frac{u_0}{\lambda_{\text{max}}^{(\mathbf{G})}} = u_0. \quad (\text{D.16})$$

The dynamics of the linearised Hopfield networks is equivalent to such of the Eq. (5.5) at  $\xi_{\text{crit}} = -1/\tau_{\text{crit}}$ . Hence, the Hopfield networks emulate the PageRank algorithm in the lowest loss regime with the PageRank vector represented by the amplitudes  $x_i$  in the steady-state of equations:

$$\frac{dx_i}{dt} = -x_i + \sum_{j=1}^N G_{ij} \tanh(x_j) + I_i^b, \quad (\text{D.17})$$

where the time and amplitudes in Eq. (D.15) are rescaled as  $t \rightarrow t/u_0$  and  $x_i \rightarrow x_i/u_0$ .

## 4. Numerical parameters

The numerical results presented in the main text of the article are achieved for the OPO-networks by simulating Eq. (D.5) with  $\beta = 1$ , polariton/photon/laser networks by simulating Eq. (D.10) with  $U = 1$ , Hopfield networks by simulating Eq. (D.17) with  $I_i^b = 0$  for all elements. The Euler iterative scheme is used for all networks with the time step  $dt = 1$ . We note that smaller time steps would work too, and the choice of such large  $dt$  makes the time evolution of the considered networks similar to the power method, albeit in the presence of small nonlinearities, which could affect the components of the PageRank vectors for some datasets. In Fig. 5.5, the L1-norm termination criterion is used for all algorithms with the maximum number of iterations corresponding to the  $10^{-16}$  tolerance.

For the numerical calculations of the XYRank, the numerical parameters are fixed to be  $\rho_{\text{th}} = 10$ ,  $\varepsilon = 60$ ,  $dt = 0.005$ , across datasets ‘*harvard*’, ‘*california*’, and ‘*facebook*’, while for the ‘*wiki-topcats*’ dataset  $\rho_{\text{th}} = 1$ ,  $\varepsilon = 15$ ,  $dt = 0.0005$ . The presented rankings in Table 5.1 and Table D.1 are consistent across different choices of parameters with gain-dissipative networks converging to the similar steady state under the fixed tolerance, although the required number of iterations for convergence greatly depends on a particular choice. The Euler method with L1 norm accuracy of  $10^{-10}$  converges in about 5000, 4000, and 50000 iterations for datasets ‘*harvard*’, ‘*california*’, and ‘*facebook*’, while the maximum limit of 1000000 iterations is reached for the ‘*wiki-topcats*’ dataset. The easiness of the Google matrices for the minimisation of the XY model is caused by the ferromagnetic sign of all couplings.

## 5. The highest XYRank positions

The XYRank is an alternative ranking that is calculated through the minimisation of the XY Hamiltonian on the Google matrix. Similar to the highest PageRank positions in Table 5.1, the highest XYRank positions are shown in Table D.1. The Kendall’s tau between PageRank and XYRank across all positions is 0.74, 0.16, 0.74, 0.61, for the datasets ‘*harvard*’, ‘*california*’, ‘*facebook*’, and ‘*wiki-topcats*’, respectively.

## 6. Web graph datasets

The considered datasets are publicly available and include:

- *Harvard web graph* (‘*harvard*’). The Harvard database is an  $N = 500$  directed graph containing web pages related to Harvard University as of 2002 [274].

Table D.1 The highest 10 alternative ranking positions (XYRank) are shown for datasets ‘harvard’, ‘california’, ‘facebook’, and ‘wiki-topcats’ of size  $N = 500$ ,  $N = 9664$ ,  $N = 22470$ , and  $N = 1791489$ . The XYRank is calculated by minimising the XY Hamiltonian for the Google matrices. The difference between the XYRank and PageRank distributions is indicated by green (red) arrows showing the shift in the PageRank towards a higher (lower) rating by a certain number of positions with respect to the XYRank.

XYRank	Harvard	PageRank	California	PageRank
1	www.harvard.edu	—	www.linkexchange.com/	↓ 5
2	search.harvard.edu:8765/custom/..	↓ 1	home.netscape.com/..	↓ 2
3	www.med.harvard.edu	↓ 1	www.yahoo.com/	↓ 9
4	www.hsph.harvard.edu	↓ 4	www.berkeley.edu/	↓ 3
5	www.gse.harvard.edu	—	www.berkeley.edu	—
6	www.ksg.harvard.edu	↓ 1	www.leginfo.ca.gov/..	↓ 20
7	search.harvard.edu:8765/query	↓ 4	www.creia.com/	↓ 25
8	www.hbs.edu	↑ 6	www.ca.gov/	↓ 11
9	www.hms.harvard.edu	↑ 3	www.adobe.com/..	↓ 15
10	www.gse.harvard.edu/search.html	↓ 7	www.dot.ca.gov/hq/..	↓ 24
XYRank	Facebook	PageRank	Wikipedia (top categories)	PageRank
1	Sir Peter Bottomley MP	↓ 1	United States	—
2	Joachim Herrmann	↓ 5	France	—
3	Facebook	↑ 2	Departments of France	↓ 12
4	Harish Rawat	↓ 7	Communes of France	↓ 14
5	U.S. Army Chaplain Corps	↓ 1	Canada	↑ 1
6	Manfred Weber	↓ 4	Village	↓ 18
7	Home & Family	↓ 9	Powiat	↓ 18
8	Cancillería Argentina	↓ 18	Gmina	↓ 14
9	Barack Obama	↑ 1	Voivodeships of Poland	↓ 14
10	Loïc Hervé	↓ 15	Germany	↑ 5

- *California web graph* (‘california’). The California database is an  $N = 9,664$  directed graph that contains pages matching the query “California” collected in 2002 [275].
- *Facebook web graph* (‘facebook’). The Facebook database is an  $N = 22,470$  undirected graph with nodes representing official Facebook pages and edges corresponding to mutual likes between pages. Pages belong to 4 categories: politicians, governmental organisations, television shows, and companies. The graph is collected in 2017 and is available in Stanford large network dataset collection [276].
- *Cambridge University web graph* (‘cambridge’). The Cambridge University database is an  $N = 212,710$  directed graph containing web pages related to the University of Cambridge as of 2006 [277].

- *Amazon web graph ('amazon')*. The Amazon database is an  $N = 400,727$  directed graph collected in 2003 [276] with nodes representing products and edges corresponding to frequently co-purchased products.
- *Hollywood web graph ('hollywood')*. The Hollywood database is an  $N = 1,139,905$  undirected graph collected in 2009 [278] with nodes representing actors and edges corresponding to the appearance of actors in the same movies.
- *Wikipedia top categories web graph ('wiki-topcats')*. The Wikipedia top categories database is an  $N = 1,791,489$  directed graph collected in 2011 [276] with nodes representing pages from the top Wikipedia categories (have at least 100 pages) with the largest strongly connected component and edges corresponding to hyperlinks.
- *Wikipedia web graph ('wikipedia')*. The Wikipedia database is an  $N = 3,566,907$  directed graph collected in 2007 [279] with nodes representing Wikipedia pages and edges corresponding to hyperlinks between them.

All datasets can also be found on the GitHub page together with the implementations of numerical methods for calculating the PageRank.

## 7. Data for computing power and energy efficiency of classical devices

The numbers in Fig. 5.6 are representative of typical orders of computing power and energy efficiency of contemporary classical computing architectures, although they could be drastically different within one class of computing devices. In the descriptions below, we denote the processing power by  $R$  that is measured in the number of floating-point operations per second (FLOP/s = FLOPS), the power consumption by  $P$  that is measured in watts (W), and energy efficiency is calculated as the ratio  $R/P$  and is measured in units FLOPS/W = [FLOP/J]. The performance for devices is reported for either double-precision (FP64), single-precision (FP32), half single-precision (FP16), or integer precision (int6) calculations.

1. *Supercomputers*. In terms of energy efficiency, the top 10 list of supercomputers [280] starts with

$$\begin{aligned} & \text{NVIDIA DGX SuperPOD (FP64):} \\ & R = 2356 \text{ TFLOP/s, } P = 90 \text{ kW,} \\ & R/P = 26.2 \text{ GFLOPS/W} \end{aligned}$$

and ends with

*Fujitsu's Supercomputer Fugaku (FP64):*

$$R = 442000 \text{ TFLOP/s}, P = 29899 \text{ kW},$$

$$R/P = 14.8 \text{ GFLOP/J}.$$

The latter is also the most powerful supercomputer in terms of processing power, that has overcome the previous best supercomputer

*Summit IBM (FP64):*

$$R = 148600 \text{ TFLOP/s}, P = 10096 \text{ kW},$$

$$R/P = 14.72 \text{ GFLOPS/W}.$$

2. *GPUs.* For an estimate of GPU power efficiency we consider two state-of-the-art cards [281]:

*NVIDIA GeForce RTX 3090 (FP64):*

$$R = 0.556 \text{ TFLOP/s}, P = 0.35 \text{ kW},$$

$$R/P = 1.85 \text{ GFLOPS/W}.$$

*NVIDIA GeForce RTX 3090 (FP32):*

$$R = 36 \text{ TFLOP/s}, P = 0.35 \text{ kW},$$

$$R/P = 103 \text{ GFLOPS/W}.$$

and

*NVIDIA V100 (FP64):*

$$R = 7.8 \text{ TFLOP/s}, P = 0.3 \text{ kW},$$

$$R/P = 26 \text{ GFLOPS/W}$$

*NVIDIA V100 (FP32):*

$$R = 15.7 \text{ TFLOP/s}, P = 0.3 \text{ kW},$$

$$R/P = 52.3 \text{ GFLOPS/W}$$

*NVIDIA V100 (FP16):*

$$R = 125 \text{ TFLOP/s}, P = 0.3 \text{ kW},$$

$$R/P = 417 \text{ GFLOPS/W}.$$

3. *CPUs.* Most CPUs lie within processing power of 2 TFLOP/s and power efficiency of about 10 GFLOPS/W. As an estimate of top CPU power efficiency we use [282]

*Intel Xeon (FP64):*

$$R = 4.8 \text{ TFLOP/s}, P = 0.165 \text{ kW},$$

$$R/P = 29 \text{ GFLOPS/W}$$

*Intel Xeon (FP32):*

$$R = 9. \text{ TFLOP/s}, P = 0.165 \text{ kW},$$

$$R/P = 55 \text{ GFLOPS/W}$$

4. *Dedicated hardware.* FPGAs are reprogrammable hardware devices that provide energy efficient computing tailored specific tasks. One of the high-end FPGA boards is

*Intel Stratix10 (FP32):*

$$R = 10 \text{ TFLOP/s}, P = 0.18 \text{ kW},$$

$$R/P = 56 \text{ GFLOPS/W}$$

*Intel Stratix10 (int6):*

$$R = 70. \text{ TFLOP/s}, P = 0.18 \text{ kW},$$

$$R/P = 389 \text{ GFLOPS/W}$$

The Tensor Processing Unit (TPU) is a custom application-specific integrated circuit (ASIC) designed by Google and used for accelerating machine learning tasks:

*TPU v3 (FP16):*

$$R = 90. \text{ TFLOP/s}, P = 0.225 \text{ kW},$$

$$R/P = 400 \text{ GFLOPS/W}$$

Note that with distributed computing, when the processing power of personal computers is linked together over the Internet, the total computing power over 2.3 exaFLOP could be achieved as of 2020.

As an estimate of the energy consumption of computing the PageRank vector of 10 billion size matrix in the main text, we have assumed that one needs to run 1000 iterations of the power method, and there are around 100 connections per each element in the matrix. The PageRank vector's single computation would then take around 1 PFLOP. To update the ranking on a minute scale, the PageRank vector would need to be recomputed about half a million times over a year. The average annual electricity consumption for computing the PageRank would be around  $3.5 \cdot 10^5$  kWh on dedicated hardware, such as the tensor processing units (TPUs) with the energy efficiency of 400GFLOPS/W. This amount of energy is equivalent to charging up 290 electric cars for one year under the assumption of an average size battery of 30 kWh and 40 charges per year.

